Green Catalytic Process to Achieve Sustainable Products

By Haoyue Sun

A thesis submitted to fulfill requirements for the degree of Doctor of Philosophy.

Faculty of Engineering

School of Chemical and Biomolecular Engineering

The University of Sydney

Supervisor: Professor Jun Huang

February 2025

Table of contents

Table of contents II

Declaration of originality V

Acknowledgements VI

Authorship attribution statement VIII

Attesting authorship attribution statement IX

List of publications X

List of Figures XI

List of Tables XVIII

Table of Abbreviations XIX

Abstract XXIV

1. Chapter 1 – Introduction 26

1.1 Green catalysis and sustainability 26

1.2 Biomass 28

1.2.1 Biomass model compound 28

1.2.2 Biomass upgrading 29

1.3 Future direction: Solar-mediated biomass upgrading 40

1.3.1 Traditional Photocatalysis 41

1.3.2 Plasmonic photocatalysis 52

1.3.3 Photoelectrocatalysis 57

1.4 Summary and outlook 62

2. Chapter 2 – Photo-Enhancement of Reactants Adsorption on AuPd Alloy Surface in Selective Hydrogenation of Ketones 65

Abstract 65

2.1 Introduction 65

2.2 Experimental Section 66

2.2.1 Materials 66
2.2.2 The synthesis of catalysts 67
2.2.3 Photocatalytic hydrogenation test 68
2.2.4 Hot filtration test 68
2.2.5 Characterization 69
2.2.6 DFT calculation 70
2.3 Results 71
2.4 Conclusion 103
3. Chapter 3 – Unbiased Photoelectrochemical Tandem Reaction for Concurrent Oxidations with Ultra-high Overall Faradaic Efficiency 104
Abstract 104
3.1 Introduction 104
3.2 Experimental Section 106
3.2.1 Materials 106
3.2.2 Synthesis Methods 107
3.2.3 Photoelectrocatalysis HMF oxidation 108
3.2.4 Product analysis 109
3.2.5 Characterization 109
3.2.6 DFT calculations 110
3.3 Results 110
3.3.1 Tandem PEC-System for Biomass oxidation 110
3.3.2 Ru-doped CBO ($CuBi_2O_4$) photocathodes 114
3.3.3 NiOOH-modified BVO ($BiVO_4$) photoanodes 128
3.3.4 PEC performance optimization 138
3.3.5 Mechanistic insights 147
3.4 Conclusion 149
4. Chapter 4 – Heterojunction-Engineered photoelectrocatalytic glycerol oxidation coupled with on-site H_2O_2 production 151
Abstract 151
4.1 Introduction 151

4.2 Methods 153
4.2.1 Materials and reagents 153
4.2.2 Synthesis of TiO_2 Photoanode 153
4.2.3 Synthesis of $Bi_2O_{2.33}/TiO_2$ Photoanode 153
4.2.4 Photoelectrochemical measurements 154
4.2.5 PEC glycerol oxidation 155
4.2.6 H_2O_2 quantification 155
4.2.7 DFT calculation 156
4.3 Results 156
4.3.1 Morphology and composition 156
4.3.2 Optical and Electronic Properties 161
4.3.3 Band Structure and Catalytic Mechanism 162
4.3.4 PEC glycerol oxidation performance 169
4.4 Conclusion 178
5. Chapter 5 – Summary and outlook 180
5.1 Summary 180
5.2 Outlook 182
6. Reference 186

Declaration of originality

This is to certify that to the best of my knowledge, the content of this thesis is my own work. This thesis has not been submitted for any degree or other purposes.

I certify that the intellectual content of this thesis is the product of my own work and that all the assistance received in preparing this thesis and sources have been acknowledged.

Signature: Date: 26th Feb 2025

Name: Haoyue Sun

Acknowledgements

As I bring this dissertation to completion, I find myself reflecting on the long, winding, and transformative journey that has brought me here. This milestone is not just a personal achievement; it is a collective triumph shaped by the unwavering support, encouragement, and love of countless individuals who have walked beside me through every challenge and triumph. It is with a full heart and deep gratitude that I take this opportunity to acknowledge them.

First and foremost, I extend my deepest gratitude to my supervisor, Professor Jun Huang. Your mentorship has been a beacon of light throughout this journey, illuminating paths I never imagined I could traverse. You challenged me to think critically, to embrace failure as part of growth, and to persevere with resilience. Your guidance has been both rigorous and compassionate, and you have shown me, by example, the kind of researcher and person I aspire to be. Your expertise and guidance have enriched this work in ways I cannot fully articulate, and I am deeply appreciative of the time and effort you have invested in my growth. Thank you for believing in my potential even when I doubted myself and for always pushing me to reach higher. At the same time, I would like to express my sincere gratitude to Professor Alfons Baiker and Professor Sarina Sarina for their invaluable assistance in revising my research work and their patience in providing insightful guidance. Their meticulous attention to detail and thoughtful suggestions have greatly improved the quality of the research, and I am truly grateful for their generosity in sharing their expertise and time.

I am also profoundly grateful to my lab mates and colleagues, who have been my family in academia. Dr. Weibin Liang, Dr. Lizhuo Wang, Dr. Rui Tang, Dr. Wenjie Yang, Dr. Sibei Zou, Dr. Xingmo Zhang, and Dr. Yuhang Liang, thank you for the countless hours spent brainstorming ideas, troubleshooting experiments, and celebrating small victories. Thanks to Xingxu Liu, Chunjing Su, Ying Shu, Namuersaihan Namuersaihan, Qi Cheng, Zhiqiang Zhao, Yujian Shi, Ziqi Zhou, Binbin Xia, Yawen, Yuqin, Rasmeet, Yihao and Xu Bai, the camaraderie we shared, whether during late nights in the lab, conference road trips, or casual lunches, has been a source of strength and joy. A special thank you to Yu Yang and Yanan Zhao, whose generosity, humor, and unwavering support have left an indelible mark on my life. To the administrative staff, technicians, and collaborators who kept everything running smoothly, thank you for your dedication and kindness.

To my friends, who have been my sanctuary in moments of exhaustion and doubt, thank you for reminding me of life beyond academia. Your laughter, encouragement, and understanding have carried me through the toughest days. Zhan Peng, thank you for always knowing when to listen, when to advise, and when to simply distract me with joy, thank you for being my first cheerleaders and lifelong confidants. Your pride in me has been my greatest motivation. Also, thanks to Yuanhang, Meihui, Yidan, Wenjun, without your encouragement, life will be less happy.

To my family, no words can truly capture the depth of my gratitude. To my parents, thank you for the sacrifices you made to give me opportunities you could only dream of. Your love, wisdom, and belief in me have been the foundation upon which I have built my life.

I would also like to express my gratitude to the countless others whose contributions may seem small but were no less impactful.

Lastly, to the challenges, failures, and moments of self-doubt, thank you for teaching me resilience and humility. This journey has shaped me not only as a researcher but also as a person, and for that, I am eternally grateful.

This dissertation is the culmination of not just my efforts but the love, guidance, and belief of every person who has been part of this journey. To each of you, I owe my deepest gratitude. This work is as much yours as it is mine. Thank you for everything.

Authorship attribution statement

Chapter 2 of this thesis is submitted as " **H. Sun**†, R. Tang†, Y. Shi, Y. Liang, X. Zhang, L. Wang, S. Zou, A. Baiker, Q. Gu, D. S. Sarina, J. Huang*, Photo-Enhancement of Reactants Adsorption on AuPd Alloy Surface in Selective Hydrogenation of Ketones, Angew. Chem., Int. Ed".

As the co-first author, I contributed to catalyst synthesis, material characterization, performance testing, mechanistic studies, and the writing of the manuscript.

Chapter 3 of this thesis is published as "**H. Sun**†**,** R. Tang, X. Zhang, S. Zou, Y. Liang, N. Namuersaihan, Q. Gu, A. Baiker, J. Huang*, Unbiased Photoelectrochemical Tandem Reaction for Concurrent Oxidations with Ultra-high Overall Faradaic Efficiency, J. Mater. Chem. A, 2025, Advance Article".

As the first author, I contributed to catalyst synthesis, material characterization, performance testing, mechanistic studies, and the writing and revision of the manuscript.

Chapter 3 of this thesis is published as "**H. Sun**†**,** Y. Shu, Y. Liang, J. Huang*, Unbiased Photoelectrochemical Tandem Reaction for Concurrent Oxidations with Ultra-high Overall Faradaic Efficiency, Energy Fuels, 2025, 39, 15, 7483-7491".

As the first author, I contributed to catalyst synthesis, material characterization, performance testing, mechanistic studies, and the writing and revision of the manuscript.

Published material distributed through the thesis:

This thesis contains material published in "**H. Sun**†**,** R. Tang, J. Huang*, Considering single-atom catalysts as photocatalysts from synthesis to application, Iscience, 2022, 25, 5, 104232".

This is section 1.3.1.2. As the first author, I contributed to writing and revision of the manuscript.

Attesting authorship attribution statement

In addition to the statements above, in cases where I am not the corresponding author of a published item, permission to include the published material has been granted by the corresponding author.

Student Name: Haoyue Sun

Signature: Date: 26th Feb 2025

As supervisor for the candidature upon which this thesis is based, I can confirm that the authorship attribution statements above are correct.

Supervisor Name: Jun Huang

Signature: Date: 26th Feb 2025

List of publications

1. **Sun H**, Huang J,* et al. Unbiased photoelectrochemical tandem reaction for concurrent oxidations with ultra-high overall faradaic efficiency. J. Mater. Chem. A, 2025, Advance Article.

2. **Sun H**, Huang J,* et al. Heterojunction-Engineered Photoelectrocatalytic Glycerol Oxidation Coupled with On-Site H_2O_2 Production. Energy Fuels, 2025, 39, 15, 7483-7491.

3. **Sun H**, Huang J,* *et al*. Vacancy-engineered bismuth vanadate for photoelectrocatalytic glycerol oxidation with simultaneous hydrogen production [J]. *EES. Catal.,* 2025, Advance Article.

4. **Sun H**, Huang J,* *et al*. Electrocatalysis for Urea Evolution and Oxidation Through Confining Atomic Ni Into In_2O_3 Nanosheet Catalysts[J]. *Adv. Funct. Mater.*, 2024, 2415859.

5. **Sun H**, Huang J,* *et al*. Enhanced solar urea synthesis from CO_2 and nitrate waste via oxygen vacancy mediated-TiO_x support lead-free perovskite[J]. *Appl. Catal., B*, 2025, 360: 124511.

6. **Sun H**, Huang J,* et al. Interfacial energy band engineered $CsPbBr_3$/NiFe-LDH heterostructure catalysts with tunable visible light driven photocatalytic CO_2 reduction capability[J]. *Catal. Sci. Technol.*, 2023, 13(4): 1154-1163.

7. **Sun H**, Huang J,* *et al*. RuCu bimetallic catalyst on N-doped mesoporous carbon for high-performance CO_2 methanation[J]. *Carbon Capture Sci. Technol.*, 2023, 6: 100100.

8. **Sun H**, Huang J,* *et al*. Plasmon-enhanced alcohol oxidations over porous carbon nanosphere-supported palladium and gold bimetallic nanocatalyst[J]. *Appl. Catal., B*, 2021, 292: 120151.

9. **Sun H**, Tang R, Huang J.* Considering single-atom catalysts as photocatalysts from synthesis to application[J]. *Iscience*, 2022, 25(5): 104232.

List of Figures

Figure 1-1. A schematic representation of the potential of biomass in driving green chemistry and renewable energy applications. 28
Figure 1-2. Upgrading biomass via different catalysis methods. 30
Figure 1-3. Biomass thermal conversion via different method. 31
Figure 1-4. (a) Glucose isomerization to fructose on OMC@MgO-1.0.51 (b) Bifunctional carbon-based solid acid catalyst derived from waste bio-tar for glucose upgrading.[52] (c-d) Biomass-Derived compounds upgrading by Hierarchical ZSM-5 zeolites.[53] (e) Glucose dehydration over Sn-containing dendritic mesoporous silica.[54] (f) Brønsted-base and Brønsted-acid catalysts for glucose isomerization into fructose.[55] 32
Figure 1-5. (a) The hydrolysis process of lignocellulosic biomass using magnetically immobilized enzymes.[63] (b) Combined enzymatic and heterogeneous catalysis for one-pot fructose production from glucose.[64] (c) The catalytic mechanism involved in the hydrolysis of a glucuronic acid methyl ester, with the sugar component represented as R, by OtCE15A.[65] 34
Figure 1-6. (a) Conversion of biomass to formic acid from water electrolysis.[83] (b) Mechanisms of electrocatalytic HMF reduction on Ru_1Cu and Cu.[88] (c) Ni_xSe_y nanowire arrays shelled with NiFe LDH nanosheets as a electrocatalyst for efficient upgrading of biomass-derived HMF and furfural.[76] (d) Coupled CO_2 reduction and HMF oxidation system by Cu1Bi cathodic and NiCo LDHs anodic catalysts.[89] (e) Electrochemical cell for the simultaneous production of H_2 and biomass-derived compounds oxidation.[86] (f) Comparison of recent electrolysis performances of biomass-derived compounds oxidation-coupled hydrogen production.[75] (g) Electrocatalysis HMF oxidation over the CF-$Cu(OH)_2$ catalysts.[87] 38
Figure 1-7. Schematic illustration of (a) metal/SnO_2/UiO-66-NH_2.[116] (b) Pt single-atom anchored on TpPa-1-COF over water splitting.[120] (c) Pt SA/Def-s-TiO_2 for photocatalytic H_2 evolution.[122] Copyright 2021, Elsevier. (d) Pd single-atom on CdS over water splitting.[123] (e) Pt/$FAPbBr_{3-x}I_x$ for H_2 evolution.[125] (f) Co_1-G catalyst synthetic procedure.[132]. 45
Figure 1-8. Scheme of photocatalysis mechanism. 46
Figure 1-9. (a) Comparison of ethylene glycol formation rates over different photocatalysts and (b) catalytic performance of RhSA-WZ/$Zn_{0.67}Cd_{0.33}S$.[137] (c) Proposed mechanism of selective photocatalytic HMF oxidation coupled with H_2 evolution over UCNT.[138] (d) Mechanism on the photocatalytic selective oxidation of HMF by $MAPbBr_3$.[139] (e) Schematic mechanism for

photocatalytic selective oxidation of HMF by Ru-CdS.[140] (f) Photocatalytic dehydrocoupling of 2,5-DMF mechanism by Ru-$ZnIn_2S_4$.[141] 49
Figure 1-10. Plasmonic photocatalysis mechanism and LSPR evolution in the LSPR metal nanoparticles (NP) under illumination. 52
Figure 1-11. (a) Schematic of the photocatalytic oxidation of HMF to FDCA by Au/ZnO under irradiation.[177] (b) The interfacial enhanced effect in the photocatalytic selective oxidation of HMF to HMFCA by Ag/TiO_2 catalysts.[178] The FDTD simulated spatial enhancement of the local electric field induced by LSPR effects under irradiation for (c) Au/MCN, (d) Pd/MCN, and (e) Pd-Au/MCN. Conversion of (f) Cinnamyl alcohol, and (g) 3-Methoxybenzyl alcohol over Pd-Au/MCN (red), Pd/MCN (green) and Au/MCN (blue) under light radiation. (h) Schematic mechanism of the oxidation of alcohols over Pd-Au/MCN induced by the spatial local electric field.[179] 56
Figure 1-12. Typical redox reaction of a PEC system, (a) photoanode, (b) photocathode, and (c) dual-photoelectrode tandem configuration. 57
Figure 1-13. (a) PEC selective glycerol oxidation using Bi-rich $BiVO_{4-x}$ photoanode.[203] (b) Schematic diagram of the PEC generation and participation of adsorbed ·OH by NiCo-LDH.[204] (c) Proposed mechanism for the PEC GLY conversion by FeOOH/$BiVO_4$.[205] (d) Band structure of LDH/$BiVO_4$ photoanode and (e) scheme of the TEMPO-mediated PEC oxidation of HMF over 1-LDH/$BiVO_4$ photoanode.[209] 61
Figure 2-1. (a-b) TEM images of AuPd-γ-Al_2O_3 and Au@Pd-γ-Al_2O_3. (c-d) HAADF images (line-scan inserted) of AuPd-γ-Al_2O_3 and Au@Pd-γ-Al_2O_3. (e) XRD pattern. (f) Wavelet-transform (WT) plots for Pd K-edge of AuPd-γ-Al_2O_3, Au@Pd-γ-Al_2O_3, and Pd foil. 72
Figure 2-2. HR-TEM of AuPd-γ-Al_2O_3. 72
Figure 2-3. Large scale range of HAADF-EDS mapping image of Au@Pd-γ-Al_2O_3 (blue is Pd element and yellow is Au element). 73
Figure 2-4. HR-STEM of Au@Pd-γ-Al_2O_3. 74
Figure 2-5. Pd K edge XANE spectra of AuPd-γ-Al_2O_3, Au@Pd-γ-Al_2O_3, and Pd-γ-Al_2O_3 catalysts. 78
Figure 2-6. Au L_3-edge XANE spectra of AuPd-γ-Al_2O_3, Au@Pd-γ-Al_2O_3, and Au-γ-Al_2O_3 catalysts. 78
Figure 2-7. Wavelet-transform (WT) plots for Au L_3-edge of AuPd-γ-Al_2O_3, Au@Pd-γ-Al_2O_3, and Au foil 79
Figure 2-8. (a) Hydrogenation of ACE by different catalysts. Reaction condition: 20 mg catalyst,

0.5 mmol ACE, 10 mL isopropanol (IPA), 3 bar H_2, 4h, light/dark, 20.7±0.6 ºC. TON of ACE hydrogenation as a function of irradiation time using various photocatalysts (calculated based on the surface Pd atoms). (b) UV-vis absorption. (c) Pd K edge XANES spectra of AuPd-γ-Al_2O_3 and Au@Pd-γ-Al_2O_3 tested under dark and light conditions. The charge density difference of (d) Au@Pd-γ-Al_2O_3 and (e) AuPd-γ-Al_2O_3 under dark conditions. The charge accumulation and depletion are represented by yellow and cyan colors, respectively. Color code: Pd: blue; Au: orange..... 82
Figure 2-9. Pd M4 edge EELS spectroscopy of AuPd-γ-Al_2O_3 and Pd-γ-Al_2O_3..... 84
Figure 2-10. (a) Au 4f and (b) Pd 3d XPS spectra of AuPd-γ-Al_2O_3, Au@Pd-γ-Al_2O_3, Pd-γ-Al_2O_3, and Au-γ-Al_2O_3..... 85
Figure 2-11. PL spectra of AuPd-γ-Al_2O_3, Au@Pd-γ-Al_2O_3, Au-γ-Al_2O_3, Pd-γ-Al_2O_3, and γ-Al_2O_3..... 86
Figure 2-12. *In-situ* Pd K-edge XANE spectra of AuPd-γ-Al_2O_3 in H_2-containing isopropanol under (a) dark and (d) light conditions. FT-EXAFS Pd K-edge spectra of AuPd-γ-Al_2O_3 in H_2-containing isopropanol under (b) light and (e) dark conditions. Schematic illustration of (c) sp-d hybridization effect induced electron transfer process under dark conditions, and (f) the plasmonic effect enhanced surface electron transfer process under illumination conditions..... 88
Figure 2-13. (a) *In-situ* Pd K-edge XANE spectra and (b) FT-EXAFS Pd K-edge spectra of AuPd-γ-Al_2O_3 in H_2-containing isopropanol solution with ACE under light conditions. (c) Schematic illustration of the practical electron transfer process under reaction conditions. DFT calculation of ACE adsorbed and C-O bond lengths of adsorbed ACE molecules on AuPd-γ-Al_2O_3 (d) without H atoms adsorbed, and (e) with H atoms adsorbed. (f) WT plots for Pd K-edge of AuPd-γ-Al_2O_3 in H_2-containing isopropanol solution with ACE under light conditions. *In-situ* Pd K-edge XANE spectra of Pd-γ-Al_2O_3, AuPd-γ-Al_2O_3, and Au@Pd-γ-Al_2O_3 in (g) H_2-containing IPA solution, and (h) H_2-containing IPA solution with ACE under light condition at 4 min and 12 min. 89
Figure 2-14. (a) *In-situ* Pd K-edge XANE spectra of AuPd-γ-Al_2O_3 under illumination in IPA solution of ACE without H_2. (b) The corresponding Pd K-edge R-space for (a). 90
Figure 2-15. Free energy diagram for adsorbed H atoms and ACE hydrogenation to form 1-phenylethanol on the AuPd alloy surface of AuPd-γ-Al_2O_3 catalyst and Pd surface of Pd-γ-Al_2O_3 catalyst. 91
Figure 2-16. (a) Apparent quantum yield (AQY) of AuPd-γ-Al_2O_3 and Au@Pd-γ-Al_2O_3. (b) The corresponding TON of AQY. Reaction condition: 20 mg catalyst, 0.5 mmol ACE, 10 mL

IPA, 3 bar H_2, 4 h, light irradiation with different wavelengths, 20.7±0.6 ºC. 91
Figure 2-17. Thermal camera images showing the temperature of the reaction mixture after 1 and 4 hours of reaction under light and dark conditions. Figures (a) and (b) show local temperatures after 1h and 4h of reaction under light conditions. Figures (c) and (d) present corresponding temperatures under dark conditions. (20 mg catalyst, 0.5 mmol ACE, 10 mL IPA, 3 bar H_2). 92
Figure 2-18. (a) Proposed mechanism of ACE hydrogenation over AuPd nanoalloy under visible light/dark conditions. (b) Light irradiation induced reactant concentration change on AuPd nanoalloy in the light-on and light-off cycle. GC results of ACE concentration for (c) 30 min light irradiation and (d) 30 min dark..... 94
Figure 2-19. Comparison of the reaction temperature, pressure, and carbonyl group selectivity of previously reported ketone hydrogenation reaction and this work..... 96
Figure 2-20. ACE hydrogenation cycling test of AuPd-γ-Al_2O_3. Reaction condition: 20 mg catalyst, 0.5 mmol ACE, 10 mL isopropanol (IPA), 3 bar H_2, 4h per cycle, light with full spectrum. 98
Figure 2-21. Hot filtration test of AuPd-γ-Al_2O_3 catalyst. Reaction conditions: 20 mg catalyst, 0.5 mmol ACE, 10 mL IPA, 3 bar H_2, 4h, light irradiation..... 98
Figure 2-22. XRD pattern of AuPd-γ-Al_2O_3 catalyst before and after hydrogenation reaction. 99
Figure 2-23. The core-level Au 4f and Pd 3s spectra of the fresh and cycled AuPd-γ-Al_2O_3. 99
Figure 2-24. TEM image of cycled AuPd-γ-Al_2O_3. 100
Figure 2-25. (a) HAADF and (b-e) the corresponding elemental mapping images of the cycled AuPd-γ-Al_2O_3. 100
Figure 2-26. HR-HAADF image of the cycled AuPd-γ-Al_2O_3. 101
Figure 3-1. (a) Schematic illustration of the tandem HMF oxidation device comprised of the Ru-2/CBO photocathode and the NO-2/BVO photoanode, (b) LSV plots of the Ru-2/CBO photocathode and the NO-2/BVO photoanode under illumination in 1 M KOH electrolyte with 10 mM HMF (pH = 13). (c) The yield of the tandem HMF oxidation device (left part) and the yield of the self-powered system (right part) for Ru-2/CBO photocathode and NO-2/BVO photoanode. (d) The FE_{HMFCA} and $Sel._{HMFCA}$ of tandem HMF oxidation device (left) and self-powered system (right part) for Ru-2/CBO photocathode and NO-2/BVO photoanode. (e) Equivalent circuit of the self-powered PEC HMF oxidation system. Reaction conditions: 1 M KOH electrolyte with 10 mM HMF (pH = 13) under illumination with a flow rate of 10 mL

min^{-1}. 112
Figure 3-2. Photograph of tandem HMF oxidation device. 112
Figure 3-3. Long-term I–t curve of the tandem device. 113
Figure 3-4. The corresponding current through the self-powered PEC HMF oxidation when using the 1.25 V solar panel. 113
Figure 3-5. Schematic illustration of the self-powered PEC system equipped with a solar panel (∼1.25 V) for HMF oxidation. 114
Figure 3-6. Synthesis scheme of Ru-*x*/CBO (*x*=1, 2 and 3). 114
Figure 3-7. (a) The cross-section SEM image and (b) top-view SEM image of Ru-2/CBO. (c) XRD pattern of Ru-x/CBO (x=1, 2 and 3) and CBO, (d) HR-TEM image of Ru-2/CBO, (e) DFT-based optimized atomic structure model of the Ru-2/CBO photocathode (red, green, yellow, and blue colored balls represent Ru, Cu, Bi, and O atoms, respectively). (f) Ru K-edge XANES spectra and (g) FT-EXAFS Ru K-edge spectra of Ru-2/CBO, Ru foil, and RuO_2 reference. Wavelet-transform (WT) plots for Ru K-edge of (h) Ru foil, (i) RuO2 reference and (j) Ru-2/CBO. 116
Figure 3-8. Top-view SEM image of CBO. 117
Figure 3-9.Top-view SEM image of Ru-1/CBO. 117
Figure 3-10. Top-view SEM image of Ru-3/CBO. 118
Figure 3-11. HR-TEM image of CBO. 118
Figure 3-12. (a) HAADF image and (b-e) the corresponding EDS elemental mapping of Ru-2/CBO. 119
Figure 3-13. Formation of Ru-2/CBO by Ru replacing Bi. Red, green, yellow, and blue colored balls represent Ru, Cu, Bi, and O atoms, respectively. 120
Figure 3-14. Raman spectra of the as-prepared Ru-*x*/CBO (*x*=1, 2, and 3) and CBO photocathodes. 120
Figure 3-15. XPS survey spectra of Ru-*x*/CBO (*x* =1, 2, and 3) and CBO photocathodes. .. 121
Figure 3-16. XPS spectra of Ru 3p peaks of (a) Ru-1/CBO and (b) Ru-3/CBO. 122
Figure 3-17. XPS spectra of O 1s peaks of (a) CBO, (b) Ru-1/CBO, (c) Ru-2/CBO, and (d) Ru-3/CBO. 123
Figure 3-18. XPS spectra of Cu 2p peaks of (a) CBO, (b) Ru-1/CBO, (c) Ru-2/CBO, and (d) Ru-3/CBO. 123
Figure 3-19. XPS spectra of Bi 4f peaks of (a) CBO, (b) Ru-1/CBO, (c) Ru-2/CBO, and (d) Ru-3/CBO. 124

Figure 3-20. (a) UV-vis absorption spectra, (b) PL spectra, (c) MS curves, (d) LSV curves under light illumination and dark (dashed lines), (e) chronoamperometry curves, and (f) Nyquist plot of CBO and Ru-*x*/CBO (*x*=1, 2 and 3).....126
Figure 3-21. Tauc plots of CBO, Ru-1/CBO, Ru-2/CBO, and Ru-3/CBO. 127
Figure 3-22. Synthesis scheme of NO-*x*/BVO (*x*=1, 2 and 3). 130
Figure 3-23. (a) The cross-section SEM image and (b) top-view SEM image of NO-2/BVO. (c) XRD pattern of NO-*x*/BVO (*x*=1, 2 and 3) and BVO, (d) TEM image and (e) HR-TEM image of NO-*2*/BVO, (f) HAADF image and (g-j) the corresponding EDS mapping of NO-2/BVO. (k) UV-vis absorption spectra, (l) LSV curves under light illumination and dark (dashed lines), and (m) chronoamperometry curves. 130
Figure 3-24. Top-view SEM image of BVO. 131
Figure 3-25. Top-view SEM image of NO-1/BVO.....131
Figure 3-26. Top-view SEM image of NO-3/BVO.....132
Figure 3-27.HR-TEM image of BVO. 132
Figure 3-28. XPS survey spectra of (a) BVO, (b) NO-1/BVO, (c) NO-2/BVO, and (d) NO-3/BVO. 133
Figure 3-29. XPS spectra of Ni 2p peaks of (a) NO-1/BVO, (b) NO-2/BVO, and (c) NO-3/BVO. 133
Figure 3-30. XPS spectra of O 1s peaks of (a) BVO, (b) NO-1/BVO, (c) NO-2/BVO, and (d) NO-3/BVO. 134
Figure 3-31. XPS spectra of Bi 4f peaks of (a) BVO, (b) NO-1/BVO, (c) NO-2/BVO, and (d) NO-3/BVO. 134
Figure 3-32. XPS spectra of V 2p peaks of (a) BVO, (b) NO-1/BVO, (c) NO-2/BVO, and (d) NO-3/BVO. 135
Figure 3-33. Tauc plot corresponding to UV-Vis absorption spectra of NO-*x*/BVO (*x*=1, 2 and 3) and BVO. 136
Figure 3-34. PL spectra of BVO and NO-*x*/BVO (*x* =1, 2 and 3). 137
Figure 3-35. Mott-Schottky plots of the BVO, NO-1/BVO, NO-2/BVO, and NO-3/BVO photoelectrodes in 10 mM HMF with 1 M KOH (pH=13).....137
Figure 3-36.Nyquist plots of BVO and NO-x/BVO (x =1, 2 and 3). 138
Figure 3-37. HMF oxidation over Ru-2/CBO at 0.7 V, 0.5 V, and 0.2 V vs. RHE under light conditions. 140
Figure 3-38. HMF oxidation over different photocathodes at 0.2 V vs. RHE under light

conditions. 140
Figure 3-39. HMF oxidation over Ru-2/CBO at 0.2 V vs RHE under light conditions with different flow rates. 141
Figure 3-40. HMF oxidation over different photoanodes at 1.2 V vs. RHE under light conditions. 141
Figure 3-41. HMF oxidation over different photoanodes at 1.2 V vs. RHE under light conditions. 142
Figure 3-42. HMF oxidation over NO-2/BVO at 1.2 V vs. RHE under light conditions at different flow rates. 142
Figure 3-43. Wavelength-dependent IPCE of different photocathodes. 143
Figure 3-44. Wavelength-dependent IPCE of different photoanodes. 144
Figure 3-45. Measured ABPE of different photoanodes. 144
Figure 3-46. I-t plots of (a) Ru-2/CBO photocathodes under illumination at 0.2 V vs. RHE, and (b) Ni-2/CBO photoanodes under illumination at 1.2 V vs. RHE. All measurements were conducted in 1 M KOH containing 10 mM HMF solution (pH = 13). 145
Figure 3-47. Ru-2/CBO after the stability test. (a) SEM image, (b) HADDF image, (c) HR-TEM image, (d) HADDF, and the corresponding (e-h) EDS mapping of Ru-2/CBO after stability test. 145
Figure 3-48. NO-2/BVO. (a) SEM image, (b) STEM image, (c) HR-TEM image, (d) HADDF, and the corresponding (e-h) EDS mapping of NO-2/BVO after stability test. 146
Figure 3-49.XRD pattern of (a) Ru-2/CBO and (b) NO-2/BVO after stability test. 146
Figure 3-50. XPS spectra of (a-d) Ru-2/CBO and (e-h) NO-2/BVO after stability test. 147
Figure 3-51.(a) DMPO-$\cdot O_2^-$ adduct spin-trap EPR spectra of the CBO and Ru-2/CBO. (b) proposed mechanism of PEC HMF oxidation at Ru-2/CBO photocathode. (c) DMPO-$\cdot$OH adduct spin-trap EPR spectra of the BVO and NO-2/BVO. (d) proposed mechanism of PEC HMF oxidation at Ru-2/CBO photocathode. 148
Figure 3-52. (a) *In-situ* Ru K-edge XANES of Ru-2/CBO under EC HMF oxidation. (b) FT-EXAFS spectra of Ru-2/CBO under EC HMF oxidation. 149
Figure 3-53. (a) *In-situ* Ru K-edge XANES of Ru-2/CBO under PEC HMF oxidation. (b) FT-EXAFS spectra of Ru-2/CBO under PEC HMF oxidation. 149

List of Tables

Table 1-1. Thermal catalysis for biomass-derived compounds upgrading. 32
Table 1-2. Enzymatic catalysis for biomass-derived compounds upgrading. 35
Table 1-3. Electrocatalytic catalysis for biomass-derived compounds upgrading. 36
Table 1-4. Application of traditional photocatalysts in biomass upgrading. 49
Table 1-5. Application of plasmonic photocatalysts in biomass upgrading. 56
Table 1-6. Application of photoelectrocatalytic catalysts in biomass upgrading. 62
Table 2-1. Summary of elemental concentration of Au and Pd in different catalysts measured by ICP-OES. 74
Table 2-2. Fit results of the $k^3\chi(k)$ spectra at the Pd K-edge of each catalyst and PdO reference. 80
Table 2-3. Fit results of the $k^3\chi(k)$ spectra at the Au L_3-edge of each catalyst. 81
Table 2-4. Amounts of product and TONs for different catalysts in ACE hydrogenation. 83
Table 2-5. Reaction data of heterogeneous Pd-based catalysts, which were reported for the selective carbonyl bond hydrogenation. 97
Table 2-6. Ketone hydrogenation of AuPd-γ-Al_2O_3 under visible-light irradiation (in red colour) and in the dark (shown in the parentheses).[a] 102
Table 3-1. DFT calculation of the formation energy of Ru doping at different sites. 120
Table 3-2. Bader charges analysis for Ru doping at different sites. 124
Table 3-3. EXAFS fitting parameters at the Ru K-edge for Ru-2/CBO. 125
Table 3-4. Summary of the carrier density for CBO and Ru-*x*/CBO (*x*=1, 2 and 3). 127
Table 3-5. Summary of the carrier density for BVO and NO-*x*/BVO (*x*=1, 2, and 3). 138

Table of Abbreviations

ABPE	Applied bias photon-to-current efficiency
ACE	Acetophenone
AEM	Anion exchange membranes
ANSTO	Australian Synchrotron
AQY	Apparent quantum yield
BO	$Bi_2O_{2.33}$
BVO	$BiVO_4$
CB	Conduction band
CBO	$CuBi_2O_4$
COF	Covalent organic frameworks
DFF	Diformylfuran
DFT	Density functional theory
DHA	Dihydroxyacetone
DMF	2,5-Dimethylfuran
DMPO	5,5-Dimethyl-1-Pyrroline-N-Oxide
EC	Electrocatalysis

EDS	Energy-dispersive X-ray spectroscopy
EDTA	Ethylenediaminetetraacetic acid
EELS	Electron energy-loss spectroscopy
EIS	Electrochemical impedance spectroscopy
EPR/ESR	Electron paramagnetic resonance / Electron spin resonance
EXAFS	Extended X-ray absorption fine structure spectroscopy
FA	Formic acid
FDCA	2,5-Furandicarboxylic acid
FDTD	Finite-difference time-domain
FE	Faradaic efficiency
FFCA	5-Formyl-2-furandicarboxylic acid
FSP	Flame spray pyrolysis
FT	Fourier-transformed
FTO	Fluorine-doped tin oxide
GA	Glycolic acid
GC	Gas chromatography

GGA	Generalized gradient approximation
GLA	glyceraldehyde
GLD	Glyceraldehyde
GLY	Glycerol
HAADF	High-angle annular dark-field
HER	Hydrogen evolution reaction
HMF	5-Hydroxymethylfurfural
HMFCA	5-Hydroxymethyl-2-furancarboxylic acid
HPLC	High-performance liquid chromatography
HRTEM	High-resolution transmission electron microscopy
ICP	Inductively coupled plasma-atomic emission spectrometry
IPA	Isopropanol
IPCE	Incident photon-to-current conversion efficiency
LSPR	Localized surface plasmon resonance
LSV	Linear sweep voltammograms
MCN	Mesoporous carbon nanospheres

MOF	Metal-organic frameworks
NHE	Normal hydrogen electrode
NO	NiOOH
NP	Nanoparticle
OCV	Open circuit voltage
OCVD	Open circuit voltage decay
OER	Oxygen evolution reaction
ORR	Oxygen reduction reaction
PC	Photocatalysis
PEC	Photoelectrocatalysis
PEM	Proton exchange membrane
PL	Photoluminescence
RHE	Reversible hydrogen electrode
ROS	Reactive oxygen species
SA	Single-atom
SEM	Scanning electron microscope
SPR	Surface plasmon resonance

STEM	Scanning transmission electron microscopy
TEM	Transmission electron microscopy
TEMPO	2,2,6,6-Tetramethylpiperidine 1-oxyl
TO	TiO_2
TOF	Turnover frequency
TON	Turnover number
VASP	Vienna ab initio simulation package
VB	Valence band
WT	Wavelet-transform
XANE	X-ray absorption near-edge structure
XAS	X-ray absorption spectroscopy
XPS	X-ray photoelectron spectroscopy
XRD	X-ray diffraction
ZSM	Zeolite

Abstract

The transition toward sustainable and green chemical processes is crucial for addressing the environmental, economic, and societal challenges associated with fossil-based production. Green catalysis plays a fundamental role in reducing greenhouse gas emissions, lowering energy consumption, and fostering a circular economy by utilizing renewable feedstocks and optimizing resource efficiency. Among renewable carbon sources, biomass offers significant potential for producing high-value chemicals, fuels, and materials, supporting the shift toward carbon-neutral industrial practices. However, achieving efficient and selective biomass valorization requires the development of advanced catalytic strategies that maximize energy efficiency while minimizing byproduct formation.

This dissertation explores innovative green catalytic processes, with a focus on integrating light-enhanced catalysis into scalable technologies for sustainable chemical production. Chapter 1 provides a comprehensive overview of biomass valorization, highlighting key platform chemicals such as ketones, aldehydes, and biofuels. Various catalytic approaches, including thermal catalysis, enzymatic catalysis, electrocatalysis, and photocatalysis, are analyzed for their potential to enhance biomass upgrading efficiency. The role of solar-driven catalysis in utilizing renewable solar energy for selective transformations is also discussed, setting the foundation for subsequent chapters.

Chapter 2 investigates the photoinduced enhancement of reactant adsorption on AuPd alloy surfaces for the selective hydrogenation of ketones. Through surface plasmon resonance effects, this study demonstrates improved adsorption and reaction kinetics, leading to increased catalytic efficiency and selectivity under mild conditions.

Chapter 3 presents an unbiased tandem photoelectrochemical (PEC) system designed for simultaneous biomass oxidation. This system integrates a Ru-doped $CuBi_2O_4$ photocathode with a NiOOH-modified $BiVO_4$ photoanode, achieving ultrahigh Faradaic efficiency for the selective conversion of 5-hydroxymethylfurfural (HMF) into value-added products. The synergistic interaction between hydroxyl radicals and superoxide species, combined with a continuous-flow configuration, enhances scalability and minimizes undesired byproduct formation.

Chapter 4 focuses on heterojunction-engineered PEC glycerol oxidation, coupled with on-site hydrogen peroxide (H_2O_2) production. By designing an optimized heterojunction architecture, this work demonstrates improved charge carrier separation and redox efficiency, enabling the simultaneous generation of high-value chemicals and H_2O_2 under ambient conditions. This strategy offers a cost-effective and sustainable approach to biomass upgrading, with implications for industrial applications.

Chapter 5 presents the summary and outlook of this dissertation, highlighting advancements in green catalysis through the integration of light-enhanced catalytic processes with scalable reaction systems. By leveraging photocatalysis, photoelectrocatalysis, and heterojunction engineering, this work explores new pathways for sustainable chemical production with high efficiency, selectivity, and minimal environmental impact. These findings contribute to the ongoing development of carbon-neutral technologies and provide a scientific foundation for the future implementation of green catalytic processes in industrial applications.

Chapter 1 – Introduction

1.1 Green catalysis and sustainability

The transition to sustainable and green chemical processes is an urgent and pivotal response to the growing environmental, economic, and societal challenges posed by traditional chemical production.[1-3] the global population and industrial activities continue to expand, the environmental impacts of conventional processes, characterized by their reliance on fossil fuels, high energy demands, and significant waste generation, have become increasingly untenable.[4] These processes contribute to greenhouse gas emissions, resource depletion, and ecosystem degradation, necessitating the adoption of more sustainable approaches that align with the principles of green chemistry and the circular economy.[5]

Sustainable chemical processes emphasize the use of renewable feedstocks, such as biomass and waste materials, to replace finite resources like fossil fuels.[6] By integrating atom economy and selectivity into process design, these approaches minimize byproducts and reduce waste, leading to more efficient utilization of materials.[7] This resource efficiency not only mitigates the depletion of nonrenewable inputs but also addresses critical issues of waste management and environmental contamination.[8] Moreover, the adoption of green chemical processes is essential for achieving global climate targets, as they significantly reduce carbon emissions by improving energy efficiency and transitioning to renewable energy-powered reactions.[9]

The depletion of finite natural resources further underscores the necessity for sustainable approaches. Green chemical processes provide innovative solutions by leveraging abundant and renewable resources, enhancing reaction efficiency, and fostering closed-loop systems through recycling and upcycling technologies.[10,11] These innovations are particularly important in the context of a circular economy, where the focus is on maximizing resource recovery, minimizing waste, and ensuring the continuous reuse of materials.[12] By implementing these strategies, industries can significantly reduce their dependence on virgin materials while aligning with societal demands for sustainable production and consumption.

Economic considerations also play a critical role in driving the adoption of sustainable chemical processes.[13,14] While the initial transition to green technologies may require substantial investment, the long-term benefits are profound. Improved process efficiency

reduces operational costs, particularly in terms of energy consumption and waste management. Furthermore, the utilization of low-cost renewable feedstocks and the creation of value-added products from waste streams open new economic opportunities.[15,16] Industries adopting green chemistry principles gain a competitive edge in emerging markets for bio-based and carbon-neutral products,[17] ensuring economic resilience in a rapidly evolving global landscape.

Advances in technology have made sustainable chemical processes increasingly feasible and scalable.[18] Innovations in catalysis, including the development of biocatalysts, electrocatalysts, photocatalysts, and photoelectro-catalysts, enable selective and energy-efficient transformations.[19,20] The integration of renewable energy sources, such as solar and wind power, into chemical production processes reduces reliance on fossil fuels and lowers the carbon footprint of industrial activities.[21,22] Technologies for CO_2 capture and utilization transform a major greenhouse gas into valuable products,[23,24] while engineered microbes and enzymes enable the sustainable production of chemicals and fuels from bio-based resources.[25,26] These technological breakthroughs are not only critical for reducing environmental impacts but also for addressing the growing demand for sustainable industrial solutions.

Policy and regulatory frameworks further accelerate the transition to sustainable chemical processes.[27] Governments and international organizations are implementing stringent environmental regulations, carbon pricing mechanisms, and climate action plans to incentivize the adoption of green technologies.[28] Subsidies and grants for renewable energy integration, alongside commitments under international agreements such as the Paris Agreement, encourage industries to align with global sustainability goals.[29,30] These policy measures create a conducive environment for innovation and ensure that the chemical industry remains a key player in achieving a low-carbon, sustainable future.

The transition to sustainable and green chemical processes is not merely an environmental imperative but a fundamental transformation that redefines the chemical industry's role in a sustainable global economy. By integrating renewable resources, innovative technologies, and robust regulatory frameworks, green chemical processes offer a path toward reducing environmental impacts, conserving resources, and fostering economic resilience. This shift represents a profound opportunity to achieve a balance between industrial progress and ecological preservation, ensuring a sustainable and equitable future for generations to come.

1.2 Biomass

Biomass, a renewable and abundant source of carbon-based materials, has emerged as a pivotal feedstock for sustainable chemical production and energy applications.[31,32] Derived from plant, animal, and microbial origins, biomass provides a diverse array of compounds, including ketones, aldehydes, and biofuels, which serve as intermediates for producing high-value chemicals, materials, and energy carriers.[33,34] Biomass valorization—converting these feedstocks into useful products—aligns with global efforts to reduce dependence on fossil fuels, mitigate greenhouse gas emissions, and promote a circular economy.[35] Among the various components of biomass, ketones,[36,37] aldehydes,[38,39] and biofuels[40,41] play distinct roles in driving innovation in green chemistry (Figure 0-1).

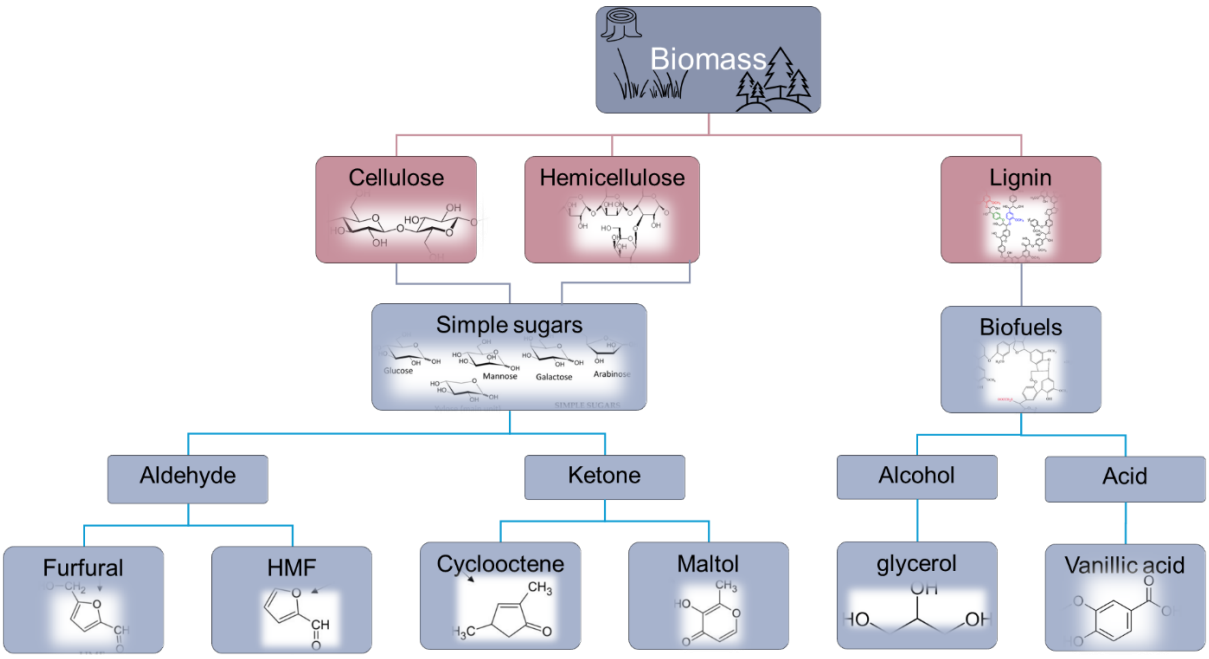

Figure 0-1. A schematic representation of the potential of biomass in driving green chemistry and renewable energy applications.

1.2.1 Biomass model compound

1.2.1.1 Ketones: Acetophenone as a model compound

Ketones derived from biomass, such as acetophenone, represent a versatile class of compounds with significant industrial applications.[42] Acetophenone, a key intermediate in the production of fragrances, pharmaceuticals, and resins, is typically obtained through the oxidative degradation of lignin, a major component of lignocellulosic biomass.[43] The selective

hydrogenation of acetophenone to produce alcohols, or its functionalization to synthesize fine chemicals, highlights its value in green chemistry. The reactivity of ketones, particularly their susceptibility to hydrogenation and oxidation, makes them ideal candidates for exploring catalytic and upgrading strategies, demonstrating the potential to replace fossil-derived feedstocks with renewable alternatives.

1.2.1.2 Aldehydes: 5-Hydroxymethylfurfural (HMF) as a platform chemical

Aldehydes, exemplified by 5-hydroxymethylfurfural (HMF), are critical intermediates in biomass conversion.[44] HMF is derived from the dehydration of hexose sugars found in cellulose and hemicellulose and is considered one of the most promising platform chemicals for producing bio-based materials and fuels.[44] Its versatility lies in its ability to be further oxidized to produce 2,5-furandicarboxylic acid (FDCA), a precursor to bio-based polymers, or reduced to yield 2,5-dimethylfuran (DMF), a high-energy-density biofuel.[45] The selective oxidation or reduction of HMF presents challenges in terms of catalyst design and reaction optimization, but its potential as a renewable intermediate for high-value products underscores its importance in biomass valorization.[46]

1.2.1.3 Biofuels: Glycerol as a Key Byproduct of Biodiesel Production

Biofuels are central to the energy transition, and glycerol, a byproduct of biodiesel production, stands out as a valuable resource for further upgrading.[47] As the biodiesel industry grows, the surplus of glycerol presents an opportunity to convert this low-cost, renewable feedstock into high-value chemicals such as dihydroxyacetone (DHA), glyceric acid, and glycolic acid.[48] The selective oxidation of glycerol is particularly attractive, as it allows for the production of fine chemicals under mild and sustainable conditions. Moreover, glycerol can be transformed into hydrogen and syngas through reforming processes, contributing to the development of renewable energy carriers.[49] The versatility of glycerol highlights its dual role as a biofuel and a platform for chemical synthesis, making it a cornerstone of biomass valorization.

1.2.2 Biomass upgrading

Biomass upgrading is a transformative strategy in sustainable chemistry that focuses on converting low-value or waste materials into high-value products such as fuels, chemicals, and advanced materials.[36,50] This approach addresses critical global challenges, including resource scarcity, environmental degradation, and the need for sustainable industrial practices. By utilizing renewable feedstocks, chemical upgrading not only reduces dependence on finite

fossil resources but also promotes circular economy principles, enabling waste materials to be reused in value-added applications (Figure 0-2).

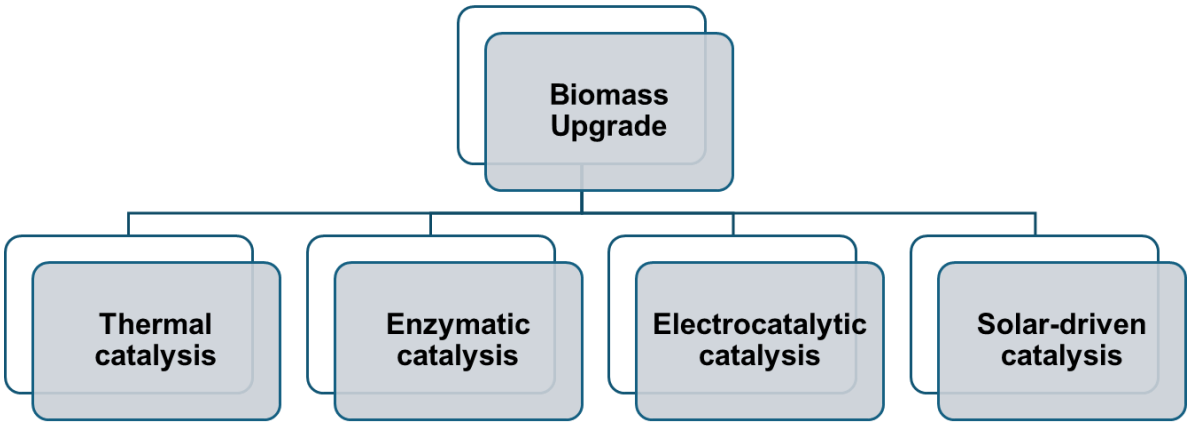

Figure 0-2. Upgrading biomass via different catalysis methods.

1.2.2.1 Catalytic Technologies for Biomass Upgrading

1. Thermal catalysis

Thermal catalysis represents a vital approach to biomass upgrading, enabling the transformation of low-value feedstocks into high-value fuels, chemicals, and materials through the application of heat and catalysts. By leveraging processes such as catalytic pyrolysis, hydrothermal liquefaction, hydrogenation, and reforming, this technology provides versatile solutions for addressing global challenges related to resource scarcity and sustainability (Figure 0-3). Catalysts play a crucial role in enhancing reaction rates, improving product selectivity, and reducing energy consumption, making thermal catalysis an industrially relevant and efficient strategy for biomass valorization.

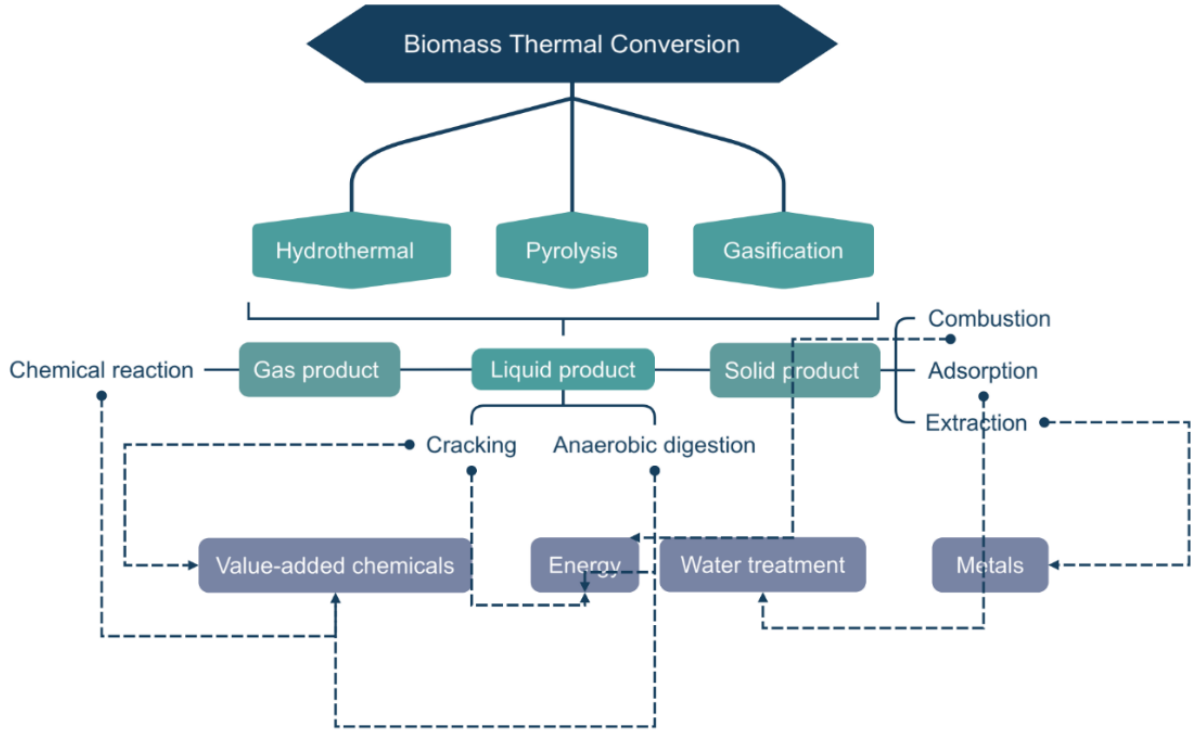

Figure 0-3. Biomass thermal conversion via different methods.

This review explores the diverse materials employed in the hydrothermal valorization of biomass, focusing on their catalytic performance and limitations in converting biomass-derived compounds (Table 0-1). In Figure 0-4, carbon-based catalysts, with their high surface area and porosity, excel in reactant adsorption and product desorption.[51] However, they are prone to fouling from humin formation, which blocks active sites and reduces durability.[52] Zeolite-based catalysts offer high thermal stability and dual-acid sites suitable for sugar isomerization and dehydration, but they are sensitive to harsh reaction environments and suffer from humin deposition over time.[53] Similarly, silica-based catalysts, particularly those functionalized with acidic or basic groups, provide excellent selectivity and activity in reactions like HMF production but are prone to leaching of active components and structural degradation under prolonged use.[54] Metal oxide-based catalysts leverage their Lewis/Brønsted acid sites and oxygen vacancies to facilitate redox reactions, such as glucose oxidation and sugar hydrogenation, but are often limited by metal leaching or aggregation.[55] Other catalysts, such as hydrotalcite, resins, and natural minerals, bring diverse active sites and tailored properties for specific reactions but vary in stability and regeneration efficiency. Across all categories, deactivation due to fouling, leaching, and structural instability remains a critical challenge.

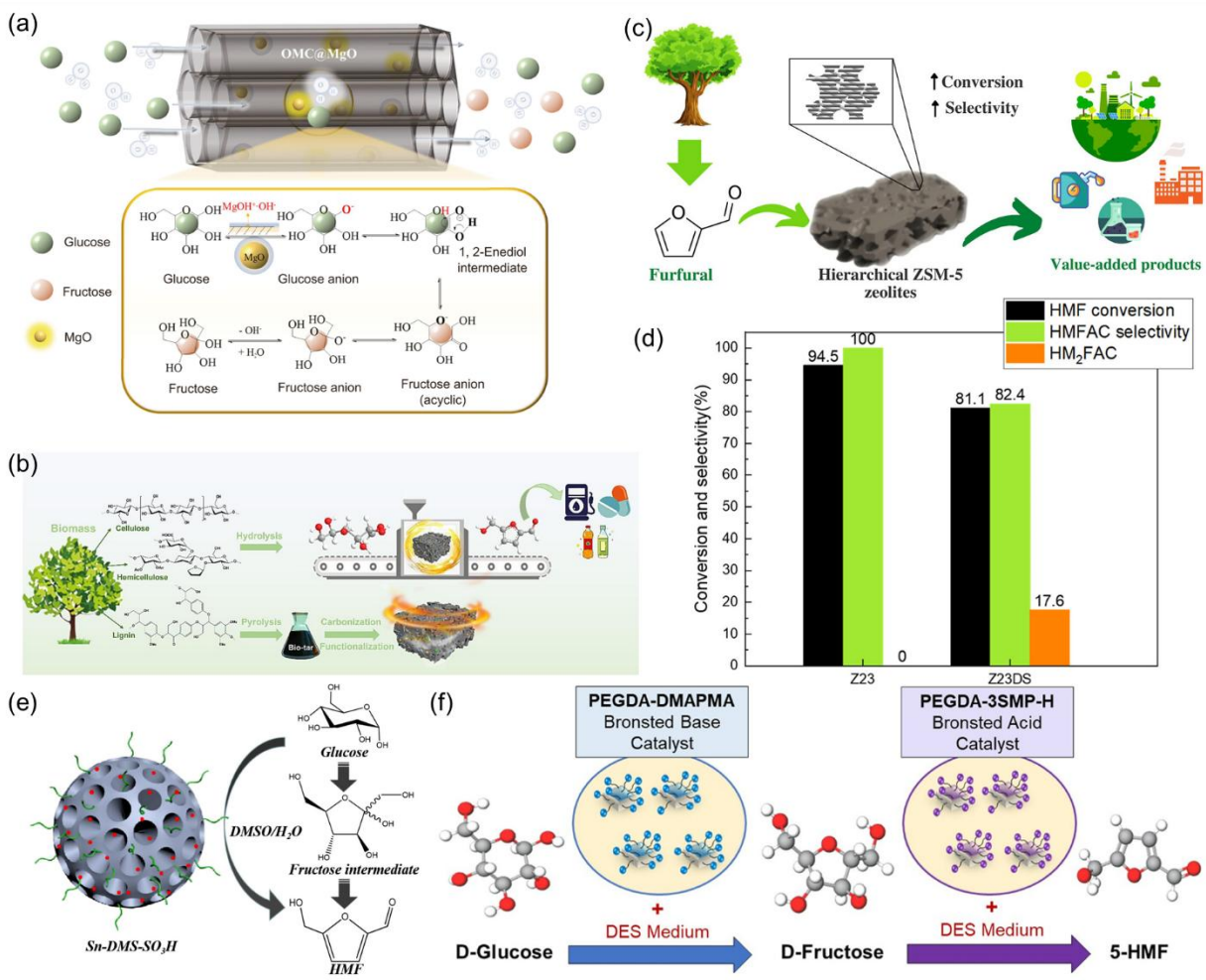

Figure 0-4. (a) Glucose isomerization to fructose on OMC@MgO-1.0.51 (b) Bifunctional carbon-based solid acid catalyst derived from waste bio-tar for glucose upgrading.[52] (c-d) Biomass-derived compounds upgrading by Hierarchical ZSM-5 zeolites.[53] (e) Glucose dehydration over Sn-containing dendritic mesoporous silica.[54] (f) Brønsted-base and Brønsted-acid catalysts for glucose isomerization into fructose.[55]

Table 0-1. Thermal catalysis for biomass-derived compounds upgrading.

Catalyst	Biomass substrate	Reaction	Ref.
Al-Ti/SAPC	Glucose	Oxidation	52
ZSM-5	5-Hydroxymethylfurfural	Oxidation	53
Sn-20DMS-SO_3H	Glucose	Dehydration	54
Ti-Al_2O_3	Glucose	Oxidation	56

Ru/α-HfP	Lignocellulose	Reduction	[57]
$Mn_4Ce_{0.05}O_x$	Xylose	Oxidation	[58]
$Yb(OTf)_2/PhSO_3H$-MPR	Glucose	Oxidation	[59]
Nb-MMT	Glucose	Oxidation	[60]
Au/R-CeO_2	Glucose	Oxidation	[61]
LDMCC-900	Fructose	Dehydration	[62]

Future advancements in thermal catalysis lie in the development of robust, selective, and cost-effective catalysts that resist deactivation, as well as in integrating renewable energy sources to minimize carbon footprints. Innovations in process intensification, such as combining pyrolysis and upgrading in a single step, and the exploration of hybrid systems that merge thermal catalysis with photocatalysis or electrocatalysis, hold promise for further enhancing efficiency and sustainability. By addressing these challenges, thermal catalysis can continue to evolve as a cornerstone of green chemistry, contributing significantly to the global transition toward a circular economy and carbon-neutral industrial practices.

2. Enzymatic catalysis

Enzymatic catalysis stands as a highly selective and environmentally friendly approach for biomass upgrading, leveraging the unique catalytic properties of enzymes to convert renewable feedstocks into high-value products such as biofuels, bioplastics, and fine chemicals. Operating under mild conditions, enzymatic processes significantly reduce energy consumption and minimize environmental impact compared to traditional catalytic methods.[63] As shown in Figure 0-5a, hydrolysis of lignocellulosic biomass using magnetically immobilized enzymes, enhances enzyme stability and reusability while maintaining high catalytic efficiency. In addition, fructose was efficiently produced by one-pot enzymatic oxidation of glucose, combined with Ni/C-catalyzed hydrogenation, with a fructose yield of 77% (Figure 0-5b). This method can be extended to α-cellulose and starch, providing a selective and efficient route for synthesizing fructose from biomass.[64] Zong *et al.* pointed out that glucuronoyl esterases (GEs) play a key role in reducing lignocellulose recalcitrance through their unique catalytic machinery (Figure 0-5c). These studies reveal deacylation as the rate-limiting step and

highlight the critical roles of enzyme, offering insights for enzyme engineering to enhance biomass conversion efficiency.[65]

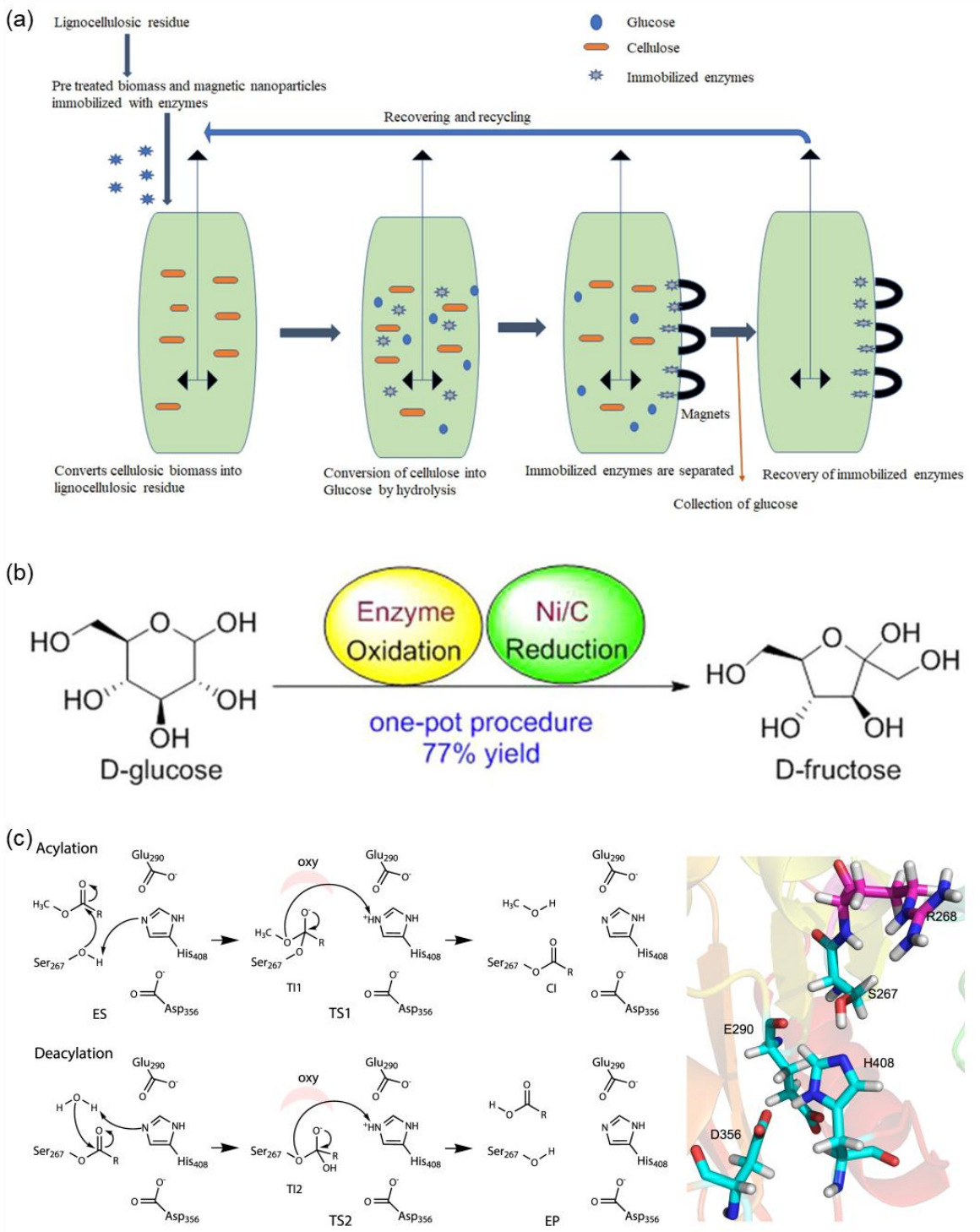

Figure 0-5. (a) The hydrolysis process of lignocellulosic biomass using magnetically immobilized enzymes.[63] (b) Combined enzymatic and heterogeneous catalysis for one-pot fructose production from glucose.[64] (c) The catalytic mechanism involved in the hydrolysis of a glucuronic acid methyl ester, with the sugar component represented as R, by OtCE15A.[65]

Key applications include the enzymatic hydrolysis of lignocellulose into fermentable sugars, lipase-catalyzed biodiesel production, and the synthesis of aromatic compounds and biopolymer precursors, showcasing the versatility of this technology in sustainable chemistry (Table 0-2).

Table 0-2. Enzymatic catalysis for biomass-derived compounds upgrading.

Catalyst	Biomass substrate	Reaction	Ref.
NAD	Glycerol 3-Phosphate	Dehydrogenase	66
Glucose isomerase	Glucose	Reduction/Oxidation	67
DyP-type peroxidases	Lignin	Oxidation	68
Glutathione-dependent β-etherases	Lignin	Oxidation	69
Cellobiohydrolase	Lignocellulose	Oxidation	70

Enzyme catalysis technology presents a highly promising approach for biomass conversion, offering environmentally friendly, energy-efficient processes with high substrate specificity and reduced by-product formation. Enzymes operate under mild conditions, avoiding the use of corrosive chemicals and minimizing energy consumption. Enzyme immobilization techniques further enhance their potential by improving enzyme stability, reusability, and tolerance to inhibitors such as furans, phenolics, and organic acids, commonly derived during biomass pretreatment. This also facilitates continuous processing, which reduces costs and enables efficient production of biofuels and high-value bioproducts from lignocellulosic feedstocks, including agricultural residues and industrial waste.[71] Despite these advantages, several challenges hinder broader industrial implementation. The high cost of enzyme production and immobilization materials, such as nanoparticles or 3D-printed supports, remains a significant economic barrier.[71] Additionally, mass transfer limitations in the hydrolysis of complex lignocellulosic substrates reduce efficiency, particularly with fixed-bed and encapsulated systems.[72] Immobilization may also lead to partial enzyme inactivation due to suboptimal interactions with support materials. Furthermore, most current studies use simplified substrates, such as carboxymethyl cellulose, which do not fully represent the structural and compositional complexities of real lignocellulosic biomass. Future

advancements should focus on developing cost-effective immobilization strategies using novel materials with open porous structures, enhancing enzyme activity and stability under industrial conditions, and designing tailored bioreactors capable of addressing the rheological challenges of high-viscosity, solid-laden biomass suspensions.

3. Electrocatalytic catalysis

Electrocatalytic technologies offer a transformative approach to biomass upgrading, leveraging electrical energy to convert renewable feedstocks into high-value products such as biofuels, fine chemicals, and advanced materials. By enabling selective redox reactions under mild conditions, these systems combine energy efficiency with precision, addressing the limitations of traditional thermal and chemical processes. Key applications include the oxidation of biomass-derived compounds like glycerol to dihydroxyacetone, and the hydrogenation of furfural to furfuryl alcohol (Table 1-3).

Table 0-3. Electrocatalytic catalysis for biomass-derived compounds upgrading.

Catalyst	Biomass substrate	Reaction	Ref.
Au/C	Furfural	Oxidation	[73]
Ru/RGO	Furfural	Reduction/Oxidation	[74]
Cu_2O/Cu foam	5-Hydroxymethylfurfural	Oxidation	[75]
Ni_xSe_y	5-Hydroxymethylfurfural	Oxidation	[76]
Cu/Cu foam	Furfural	Oxidation	[77]
Ag_2O@Ni foam	Furfural	Oxidation	[78]
Bi-Co_3O_4	Glycerol	Oxidation	[79]
PtSA-NiCo	Glycerol	Oxidation	[80]
Rh/CF	Furfural alcohol	Hydrogenation	[81]
Cu	4-Hydroxybenzaldehyde	Hydrogenation	[82]

In Figure 1-6, carbon-based materials, including functionalized carbon and graphene, improve

catalyst dispersion and stability, making them economically viable options, though fouling can limit their longevity.[83] Noble metal-based catalysts, such as Pt, Au, and Ru, demonstrate exceptional activity and selectivity for reactions like furfural oxidation to 2-furoic acid. However, their high cost and limited availability restrict scalability.[73] Non-noble metal catalysts, Such as Ni-based and Cu-based systems, excel in selective hydrogenation of furfural to furfuryl alcohol or 2-methylfuran but suffer from deactivation due to surface oxidation.[74,75] While noble metals provide unmatched efficiency, non-noble alternatives and emerging materials present opportunities for scalable and sustainable electrocatalytic biomass upgrading. Emerging materials like metal phosphides (e.g., Ni_2P) and selenides (e.g., Ni_xSe_y) enhance performance by increasing active sites and promoting electron transfer, offering cost-effective alternatives despite stability challenges.[76,84] Bimetallic systems, such as Ni-Co and Co-Mo, harness synergistic effects to boost activity and durability, requiring precise control over composition.[80,85] By coupling the hydrogen evolution reaction (HER) with value-added oxidation reactions, the electrocatalytic process can become more environmentally friendly. Recent advances in membrane technology, such as anion exchange membranes (AEM), along with innovations in material chemistry and nanotechnology, have enabled the development of dual-chamber electrolyzers (Figure 1-5e).[86] Additionally, metal oxides (e.g., MnO_2) and layered double hydroxides show promise due to their oxygen vacancies and catalytic activity but remain sensitive to harsh reaction environments.[75,87] Future efforts should focus on enhancing catalyst stability, optimizing composition, and advancing regeneration techniques to enable industrial applications.

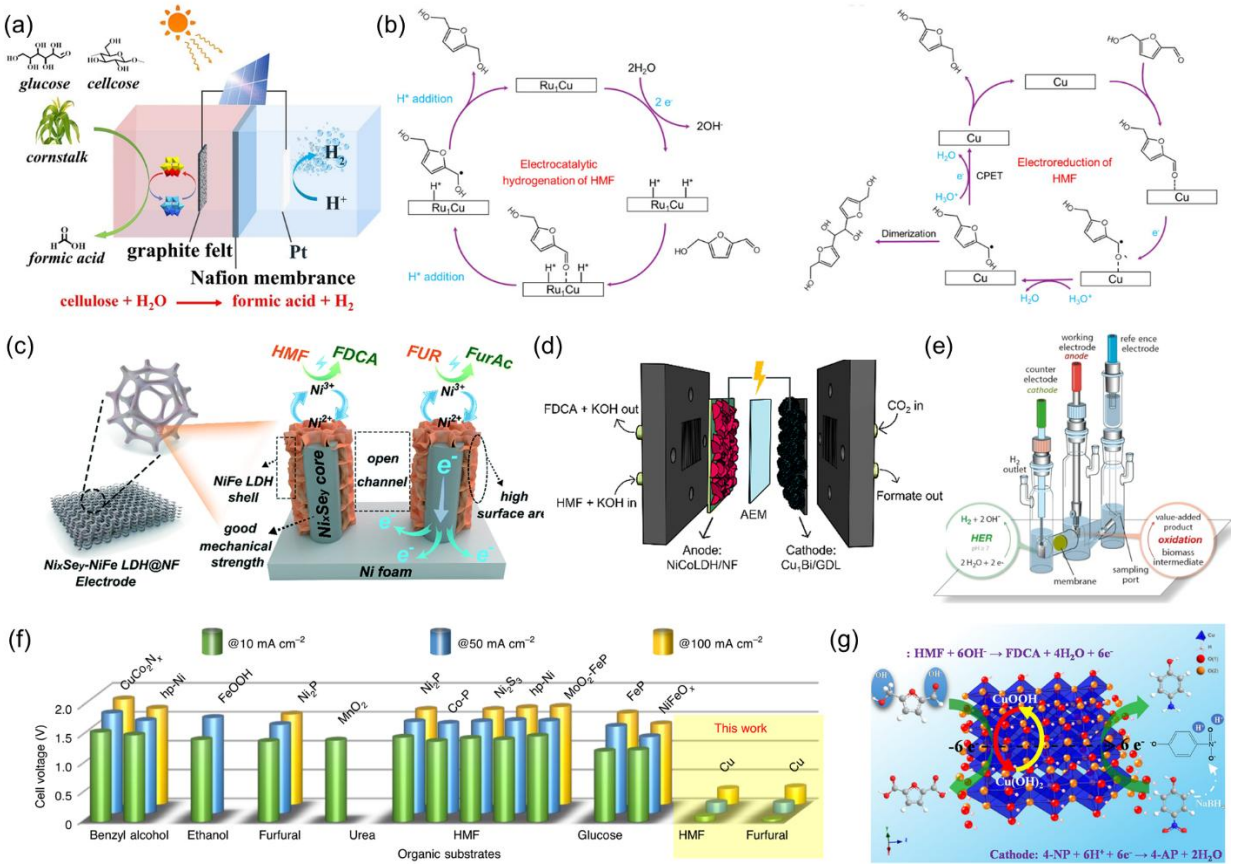

Figure 0-6. (a) Conversion of biomass to formic acid from water electrolysis.[83] (b) Mechanisms of electrocatalytic HMF reduction on Ru_1Cu and Cu.[88] (c) Ni_xSe_y nanowire arrays shelled with NiFe LDH nanosheets as an electrocatalyst for efficient upgrading of biomass-derived HMF and furfural.[76] (d) Coupled CO_2 reduction and HMF oxidation system by Cu1Bi cathodic and NiCo LDHs anodic catalysts.[89] (e) Electrochemical cell for the simultaneous production of H_2 and biomass-derived compounds oxidation.[86] (f) Comparison of recent electrolysis performances of biomass-derived compounds oxidation-coupled hydrogen production.[75] (g) Electrocatalysis HMF oxidation over the CF-$Cu(OH)_2$ catalysts.[87]

4. Solar-driven catalysis

The growing demand for sustainable and green chemical processes has catalyzed the development of innovative strategies that address environmental challenges, resource limitations, and the need for scalable, energy-efficient solutions. Among these, solar-mediated catalytic strategies have emerged as a transformative alternative, leveraging the abundant, renewable energy of sunlight to drive chemical reactions. These approaches present an opportunity to not only reduce the dependency on fossil fuels and lower greenhouse gas emissions but also align with the principles of green chemistry by enabling highly selective and efficient reactions under mild, environmentally friendly conditions. In the following

session, this part will be explained in detail.

1.2.2.2 Challenges in biomass upgrading

Biomass upgrading offers immense potential for sustainable chemical and energy production; however, existing technologies face significant limitations that demand innovative solutions. Thermal catalysis, despite its high efficiency and compatibility with diverse feedstocks, is hindered by substantial energy requirements, catalyst deactivation due to fouling and impurities, and challenges in optimizing processes for variable biomass compositions. These energy-intensive processes often rely on non-renewable sources, leading to concerns about greenhouse gas emissions and environmental sustainability.

Similarly, enzymatic catalysis, known for its high specificity and environmentally friendly operation, encounters challenges such as enzyme instability, slow reaction rates, and high production costs.[90] The heterogeneous nature of biomass feedstocks necessitates extensive pretreatment, further increasing complexity and cost. While advances in enzyme engineering and immobilization have improved enzyme performance and recyclability, scalability remains a critical barrier to industrial adoption.[91]

Electrocatalytic technologies, which leverage renewable electricity for redox transformations, face hurdles such as catalyst deactivation, sluggish reaction kinetics, and reliance on expensive noble metals.[92] Feedstock variability complicates reaction control, and the high cost of catalysts limits scalability. However, advancements in the use of earth-abundant materials and hybrid catalytic systems combining electrocatalysis with other methods offer promising improvements.

These challenges across thermal, enzymatic, and electrocatalytic processes highlight the need for alternative approaches that combine efficiency with environmental sustainability. Solar-driven biomass conversion emerges as a green and transformative solution, directly harnessing abundant and renewable solar energy to drive catalytic processes. By utilizing photocatalysis, photoelectrocatalysis, or hybrid solar systems, this approach minimizes reliance on fossil fuels, reduces greenhouse gas emissions, and lowers energy inputs. Solar-driven technologies not only address the limitations of existing methods but also pave the way for an eco-friendly and economically viable pathway for biomass valorization, aligning with global efforts toward carbon neutrality and sustainable development.

1.3 Future direction: Solar-mediated biomass upgrading

The growing demand for sustainable and green chemical processes has catalyzed the development of innovative strategies that address environmental challenges, resource limitations, and the need for scalable, energy-efficient solutions.[93] Among these, solar-mediated catalytic strategies have emerged as a transformative alternative, leveraging the abundant, renewable energy of sunlight to drive chemical reactions.[94] These approaches present an opportunity to not only reduce the dependency on fossil fuels and lower greenhouse gas emissions but also align with the principles of green chemistry by enabling highly selective and efficient reactions under mild, environmentally friendly conditions.

Solar-mediated catalysis encompasses a range of techniques, including traditional photocatalysis, plasmonic photocatalysis, and photoelectrocatalysis, each harnessing solar energy in unique ways to power chemical transformations. Traditional photocatalysis utilizes semiconductor materials to absorb sunlight and generate charge carriers that directly participate in chemical reactions.[95,96] PEC combines photoactive electrodes with an external bias to drive energy-intensive processes like water splitting and CO_2 reduction.[97] Plasmonic photocatalysis, on the other hand, exploits solar energy to generate localized hot electrons, enhancing reaction rates and improving catalyst efficiency.[98] Together, these approaches provide a versatile platform for tackling some of the most pressing challenges in chemical synthesis and energy conversion.

The potential of solar-mediated catalytic strategies is particularly significant in addressing issues of resource efficiency and environmental sustainability. By utilizing sunlight, a virtually limitless and clean energy source, these technologies offer a pathway to reduce the carbon footprint of industrial processes.[99] Solar-driven systems also enable the utilization of renewable feedstocks to produce valuable chemicals and fuels.[100] For instance, the photocatalytic conversion of biomass into fine chemicals offers a dual benefit of valorizing waste materials while reducing dependence on nonrenewable resources.[101] Similarly, solar-assisted biomass upgrading directly contributes to the development of sustainable energy carriers like hydrogen and carbon-neutral fuels.[102]

In addition to the environmental benefits, solar-mediated strategies are well-suited to address the economic and scalability challenges associated with traditional catalytic processes.[103] The integration of solar energy reduces reliance on costly external energy sources, while advances

in material design, such as heterojunction catalysts and plasmonic nanostructures, improve the efficiency and durability of solar-driven systems.[104,105] These innovations enhance light absorption, charge separation, and catalytic performance, ensuring that solar-mediated processes can meet the rigorous demands of industrial applications.

The development and optimization of solar-mediated catalytic systems are also closely aligned with global climate and sustainability goals. By providing carbon-neutral and resource-efficient solutions, these technologies support international efforts to achieve net-zero emissions and transition to a circular economy. Moreover, the versatility of solar-mediated catalysis makes it applicable across a wide range of reactions, from energy conversion to the selective synthesis of high-value chemicals, highlighting its potential as a cornerstone technology in the future of green chemistry.

1.3.1 Traditional Photocatalysis

Photocatalysis upgrading utilizes light energy to induce and facilitate chemical reactions, leading to the production of valuable chemical compounds.[106] This approach offers unique advantages, including the ability to operate under mild conditions and achieve high selectivity in the production of target products.[107] In this section, we will explore the mechanisms, benefits, and diverse applications of solar-mediated biomass upgrading.

1.3.1.1 Principles of Photocatalysis

Photocatalysis is a light-driven chemical process that accelerates reactions through the use of a photocatalyst, typically a semiconductor, without the catalyst itself undergoing permanent changes.[108] The process involves the absorption of light with energy equal to or greater than the bandgap of the photocatalyst, resulting in the generation of electron-hole pairs. These charge carriers play a crucial role in initiating redox reactions.[109] Upon light absorption, an electron is excited from the valence band to the conduction band, leaving behind a positively charged hole. The separation and migration of these charge carriers to the photocatalyst's surface are critical to their participation in reduction and oxidation reactions. Electrons in the conduction band reduce adsorbed species such as oxygen or protons, while holes in the valence band oxidize adsorbed species like water or organic compounds, producing reactive intermediates such as hydroxyl radicals or superoxide radicals.[110] Efficient photocatalysis requires optimal bandgap energy for light absorption, effective charge carrier separation to minimize recombination, and a high surface area with active sites to enhance reactant

adsorption and reaction kinetics.

The efficiency of photocatalysis depends on various factors, including the photocatalyst's material properties, the light source, and the reaction environment. The bandgap energy determines the wavelength of light that the photocatalyst can absorb, with narrow bandgap materials being able to utilize visible light, while wide-bandgap materials are restricted to ultraviolet light.[111] Effective charge carrier dynamics are essential, as the recombination of electrons and holes reduces the efficiency of the reaction.[112] Surface properties, such as morphology, porosity, and the density of active sites, significantly influence the adsorption of reactants and the desorption of products.[113] Additionally, the intensity and wavelength of the light source, along with environmental conditions such as pH, temperature, and the presence of co-catalysts, play vital roles in determining photocatalytic performance.

By utilizing renewable solar energy, photocatalysis operates under mild conditions and eliminates the need for harsh chemical reagents, making it an environmentally friendly alternative to conventional chemical processes. This combination of renewable energy utilization, broad applicability, and operational efficiency underscores photocatalysis as a promising solution for addressing global challenges in energy, environment, and industrial sustainability.

1.3.1.2 Key components and mechanisms in solar-driven chemical transformations

Solar-driven chemical transformations harness sunlight to drive reactions that convert biomass derivatives into high-value products like fuels, chemicals, or materials. These transformations rely on the interplay of key components, including light-absorbing materials, catalytic systems, and reaction interfaces, which work together to ensure efficient light capture, charge separation, and reaction pathways.[113] The mechanisms underpinning solar-driven transformations involve multiple interconnected processes, from photon absorption to product formation. A detailed examination of the key components and mechanisms is outlined below.

1. Light-absorbing materials

(1) Organic materials

Currently, organic materials have been widely used in photocatalysis, such as metal-organic frameworks (MOFs) and covalent organic frameworks (COFs). For the MOF substrates, the selection criteria are mainly based on the following three aspects [114,115]: a) possessing a large

specific surface area, which is conducive to the adsorption of reactants; b) exhibiting optical activity, which can generate photo-induced carriers to participate in the photocatalytic reaction; c) providing pore confinement, which can prevent the aggregation of metal with a relatively high metal loading. For example, the $Pt_1/SnO_2/UiO\text{-}66\text{-}NH_2$ catalysts were successfully synthesized by Sui *et al.*, applying for the visible-light-driven HER.[116] The obtained $Pt_1/SnO_2/UiO\text{-}66\text{-}NH_2$ photocatalysts showed a superior H_2 evolution rate of 2167 μmol g^{-1} h^{-1}. Further, Li *et al.* synthesized MOF-808-EDTA with implanted Pt single-atoms (SAs),[117] which exhibited an excellent photocatalytic H_2 evolution rate (68.33 mmol g^{-1} h^{-1}) under visible light irradiation (Figure 1-7a).

As for the COFs, SAs can be confined within the COF through the coordination interaction between the metal atom and the binding groups in COF.[118] Moreover, COFs possess heteroatom-rich pore walls that can facilitate reactant adsorption and charge transfer, resulting in more efficient photocatalytic reactions.[119] Therefore, the utilization of COFs as the substrates to capture SAs is expected to bring new opportunities for the development of photocatalysts. For example, Dong *et al.* reported a two-dimensional β-ketoenamine-linked COF supporting Pt SAs (Pt_1@TpPa-1) for photocatalytic HER.[120] TpPa-1-COF showed special holes and dispersed unsaturated coordinating nitrogen atoms, which made the Pt SAs highly dispersed. The optimal 3% Pt_1@TpPa-1 showed the best H_2 evolution rate of 99.86 mmol g_{Pt}^{-1} h^{-1} (Figure 1-7b). Besides Pt, the active Mo SAs were also impregnated in the TPBPY-type COF to get Mo-COF, realizing an efficient photocatalytic reduction of CO_2 to produce C_2H_4 (3.57 μmol g^{-1} h^{-1}) [121].

(2) Inorganic materials

To date, metal oxides are the most used inorganic substrate for photocatalysis. The SAs can also be anchored on metal oxides through the metal-oxygen bonds or be stabilized through oxygen vacancies, contributing to the enhanced stability of the photocatalysts. For instance, Hu *et al.* demonstrated that the Pt SAs could incorporate defective TiO_2 nanosheets (Pt SA/Def-s-TiO_2) for photocatalytic water splitting (Figure 1-7c).[122] The surface oxygen vacancies could efficiently stabilize the Pt SAs by forming a three-center Ti-Pt-Ti structure, which also contributed to the enhanced charge transfer processes. As a result, greatly enhanced photocatalytic HER was evidenced. Notably, the Pt SA/Def-s-TiO_2 SAPs exhibited an enhanced H_2 evolution performance (13460.7 μmol h^{-1} g^{-1}), which was 29.0 times higher than that of TiO_2 nanosheets.

Similar to metal oxides, the unsaturated coordinates sulfur atoms in metal sulfides could also bond with metal SAs to form photocatalysts. For instance, Li *et al.* synthesized CdS-Pd SAPs through the photoreduction method.[123] It was demonstrated that the CdS-Pd SAPs exhibited considerable structural stability and photocatalytic HER performance due to the synergistic interaction between CdS and Pd, achieving an efficient charge transfer process to the catalysts' surface. The obtained H_2 evolution rate (947.93 μmol g^{-1} h^{-1}) was about 110 times higher than that of pure CdS NPs (8.64 μmol g^{-1} h^{-1}).

Besides the metal oxides and sulfides, recently, halide perovskite materials are also demonstrated to be a potential substrate material to synthesize the photocatalysts. Halide perovskites possess fascinating properties such as broad light absorption, long charge carrier migration lengths, *etc.* [124]. Currently, the halide perovskites are demonstrated with excellent photocatalytic performance, besides being applied in the photovoltaic fields. In this regard, synthesizing halide perovskites-based photocatalysts is promising to obtain extraordinary catalytic performance. For instance, Wu *et al.* successfully anchored Pt SAs onto $FAPbBr_{3-x}I_x$ (Pt/$FAPbBr_{3-x}I_x$) with high dispersibility and stability (Figure 1-7e).[125] The obtained Pt/$FAPbBr_{3-x}I_x$ SAPs showed enhanced photocatalytic hydrogen production activity, reaching 682.6 μmol h^{-1} (100 mg). In addition, Hu *et al.* demonstrated that the Pt SAs could be deposited onto the $CsPbBr_3$ NCs (Pt-SA/$CsPbBr_3$) through the formation of Pt-O and Pt-Br bonds.[126] Compared to pristine $CsPbBr_3$ NCs, the trap levels exhibited in the Pt-SA/$CsPbBr_3$ were ascribed to the deposition of Pt SAs, leading to an enhanced separation capability of the photogenerated carriers. Due to the fast carrier transfer from $CsPbBr_3$ to Pt SAs, the Pt-SA/$CsPbBr_3$ exhibited a superior activity towards the photocatalytic propyne semi-hydrogenation (TOF=122.0 h^{-1}).

(3) Carbon-based materials

Because of the excellent conductivity of graphene, carbon-based substrates have been widely used not only in electrocatalysis,[127-130] but also in the photocatalysis field.[131] Similar to organic and inorganic substrates, structurally modified graphene can bind with SAs through coordination interactions with oxygen or nitrogen-containing functional groups. For instance, Gao *et al.* used oxidized graphene nanosheets as the substrates to immobilize the isolated Co SAs (Co_1-G). Under this circumstance, the graphene acted as a bridge to connect the $Ru(bpy)_3$ photosensitizer and the Co SAs, thereby realizing effective charge transfer and CO_2 reduction.[132] It was demonstrated that the Co SAs were coordinated with the carbon and residue

oxygen on the graphene surface and exhibited outstanding TON (678) and TOF (3.77 min^{-1}) towards photocatalytic CO_2 reduction. In addition, N-doped carbon substrates are also widely applied in photocatalysis, which provide rich coordination sites for the anchoring of the SAs.[133] For instance, Zhao *et al.* demonstrated that the Ni SAs decorated N-graphene/CdS (Ni-NG/CdS) could be efficient for photocatalytic HER.[134] As a result, the Ni-NG/CdS received an outstanding photocatalytic HER performance with a quantum efficiency of 48.2% at 420 nm.

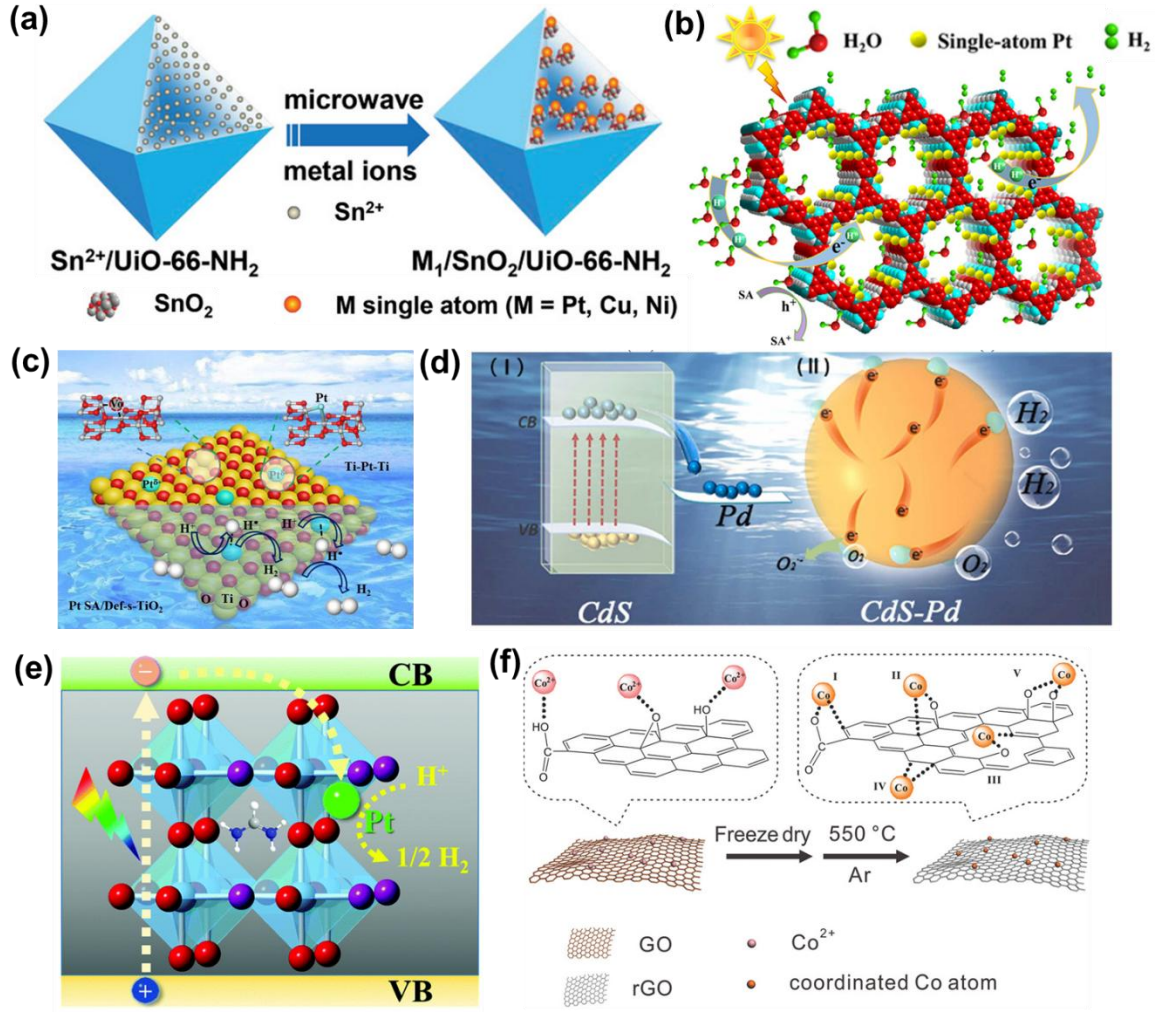

Figure 0-7. Schematic illustration of (a) metal/SnO_2/UiO-66-NH_2.[116] (b) Pt single-atom anchored on TpPa-1-COF over water splitting.[120] (c) Pt SA/Def-s-TiO_2 for photocatalytic H_2 evolution.[122] Copyright 2021, Elsevier. (d) Pd single-atom on CdS over water splitting.[123] (e) Pt/$FAPbBr_{3-x}I_x$ for H_2 evolution.[125] (f) Co_1-G catalyst synthetic procedure.[132].

2. Mechanisms in traditional photocatalytic transformations

The process begins with the absorption of solar photons by light-harvesting materials. Photons with energy equal to or greater than the material's bandgap excite electrons from the valence

band (VB) to the conduction band (CB), leaving behind holes in the VB. This process generates electron-hole pairs (e^-/h^+), which are the primary energy carriers for subsequent reactions (Figure 1-8).

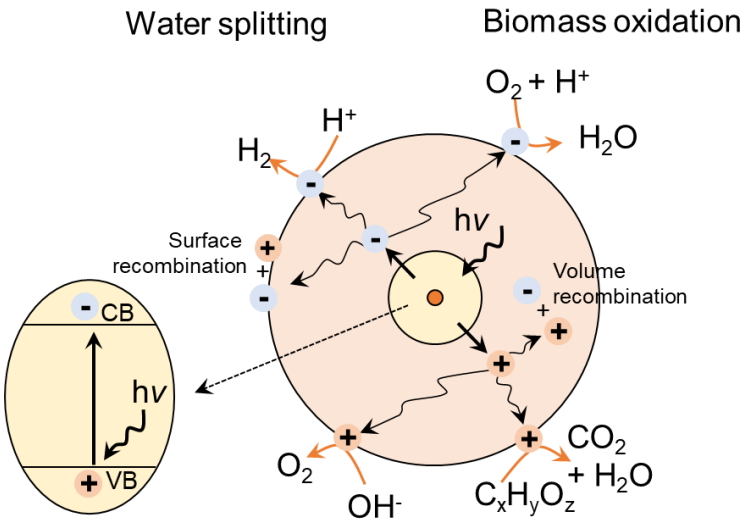

Figure 0-8. Scheme of photocatalysis mechanism.

(1) Charge Separation and Transport

Efficient charge separation is critical to preventing recombination, which would release energy as heat or light. Electrons and holes must migrate to the surface of the material or catalytic sites to participate in redox reactions. Transport efficiency is influenced by the conductivity of the material and the presence of defects or grain boundaries.[135] In materials like heterojunctions or Schottky junctions, internal electric fields separate electrons and holes, directing them to different reaction sites.[136]

(2) Surface Adsorption and Activation

Reactants must adsorb onto the catalyst surface for activation.

Electron Reduction Sites: Electrons in the CB reduce species such as CO_2, protons (H^+), or oxygen (O_2).

Hole Oxidation Sites: Holes in the VB oxidize species such as water, glycerol, or organic substrates, generating oxygen or oxygen-containing intermediates like hydroxyl radicals (·OH).

(3) Reaction pathways and selectivity

The pathways and selectivity of solar-driven reactions depend on the catalyst's ability to stabilize reaction intermediates and lower energy barriers.

Besides, several highly reactive oxygen species (ROS) play crucial roles in the upgrading of various biomass derivatives in photocatalysis. Among these, the hydroxyl radical (·OH), with its high oxidative potential, serves as a key component in photodegradation reactions, particularly for species with weak adsorption affinity to the semiconductor surface. ·OH is primarily generated through the oxidation of surface hydroxyl groups or adsorbed water. However, recent studies suggest that the role of ·OH radicals may be underestimated, as for many organic compounds, the primary oxidation pathway is likely initiated by free or trapped holes, highlighting the complex interplay between different reactive species in oxidation processes. Superoxide anions ($\cdot O_2^-$), another important ROS, are produced through the reduction of molecular oxygen by photoinduced electrons. In acidic environments, these anions can be protonated to form hydroperoxide radicals ($HO_2^{\cdot}$), further contributing to the reaction dynamics. Although $\cdot O_2^-$ is less involved in initiating oxidation reactions, it plays a significant role in the overall reaction mechanism. It reacts with organic peroxyl radicals and undergoes disproportionation to produce hydrogen peroxide (H_2O_2), which can act as an intermediate or terminal oxidant in various pathways. Additionally, ozone-like species (O_3^-) form through interactions between photogenerated hole centers on lattice oxygen (O_L) and molecular oxygen, adding another layer of reactivity to the system. Singlet molecular oxygen ($^1O_2$), a highly reactive ROS, is typically produced via energy transfer from the triplet state of dyes to molecular oxygen or through the oxidation of $\cdot O_2^-$ by photogenerated holes on semiconductor surfaces. This species is particularly important in driving selective oxidation reactions, given its strong reactivity and specificity.

The generation, control, and utilization of ROS are central to the success of heterogeneous photocatalysis. Effective regulation of these species is critical for optimizing reaction pathways and achieving selective organic photocatalytic oxidation. Understanding the mechanisms of ROS formation and their roles in the catalytic process provides a foundation for rational catalyst design and the development of more efficient photocatalytic systems.

(4) Product Desorption and Regeneration

After the reaction, products desorb from the catalyst surface, regenerating active sites for the next cycle. Efficient product desorption is essential to maintaining catalyst activity and stability.

1.3.1.3 Biomass upgrading in traditional photocatalysis

Building upon the understanding of mechanisms in solar-driven transformations, biomass upgrading in traditional photocatalysis emerges as a significant avenue for converting renewable biomass feedstocks into valuable chemicals and fuels. Wang *et al.* demonstrated a record-breaking ethylene glycol formation rate of 34 mmol g^{-1} h^{-1} with 84% selectivity using a single-atom catalyst denoted as RhSA-WZ$Zn_{0.67}Cd_{0.33}S$ under illumination.[137] The wurtzite/zinc-blende heterojunction structure enhances charge-carrier separation and migration, while Rh single atoms selectively deposited on wurtzite segments facilitate methanol adsorption and C-H activation. The catalyst achieved a stable EG yield of 37% in 60 hours, surpassing previous reports, highlighting its potential for industrially relevant bulk chemical synthesis via photocatalysis (Figure 1-9a and 1-9b). Solar-driven catalytic oxidation of HMF to DFF coupled with H_2 evolution has been achieved using ultrathin graphitic carbon nitride (UCNT), which demonstrates 95% DFF selectivity and robust cycling stability. The strong interaction between HMF and UCNT, facilitated by its twisted molecular structure, lowers the dehydrogenation energy barrier, enhancing reaction efficiency (Figure 1-9c).[138] Building on advancements in photocatalytic biomass upgrading, Zhang *et al.* utilized $MAPbBr_3$ lead-halide perovskite as an efficient photocatalyst for selective oxidation of HMF to DFF under visible light, achieving 100% conversion and over 90% DFF selectivity (Figure 1-9d).[139] Expanding on advancements in photocatalytic HMF oxidation, *Xia et al.* introduced a Ru complex anchored on CdS quantum dots, enabling highly selective oxidation of HMF to DFF or HMFCA with over 81% conversion and 90% selectivity under different atmospheres (Figure 1-9e). The system leverages the controlled generation of oxygen radicals and achieves tunable product selectivity even under natural sunlight.[140] Luo *et al.* studied the Ru-doped $ZnIn_2S_4$ photocatalyst for visible-light-driven coproduction of H_2 and diesel fuel precursors (DFPs) from lignocellulose-derived methylfurans (Figure 1-9f). The system achieves exceptional DFP selectivity (>96%) and efficient H_2 production by enhancing charge separation and accelerating C-H activation, offering a sustainable pathway for solar fuel and chemical synthesis.[141] In addition to the above, other applications are outlined in Table 0-4.

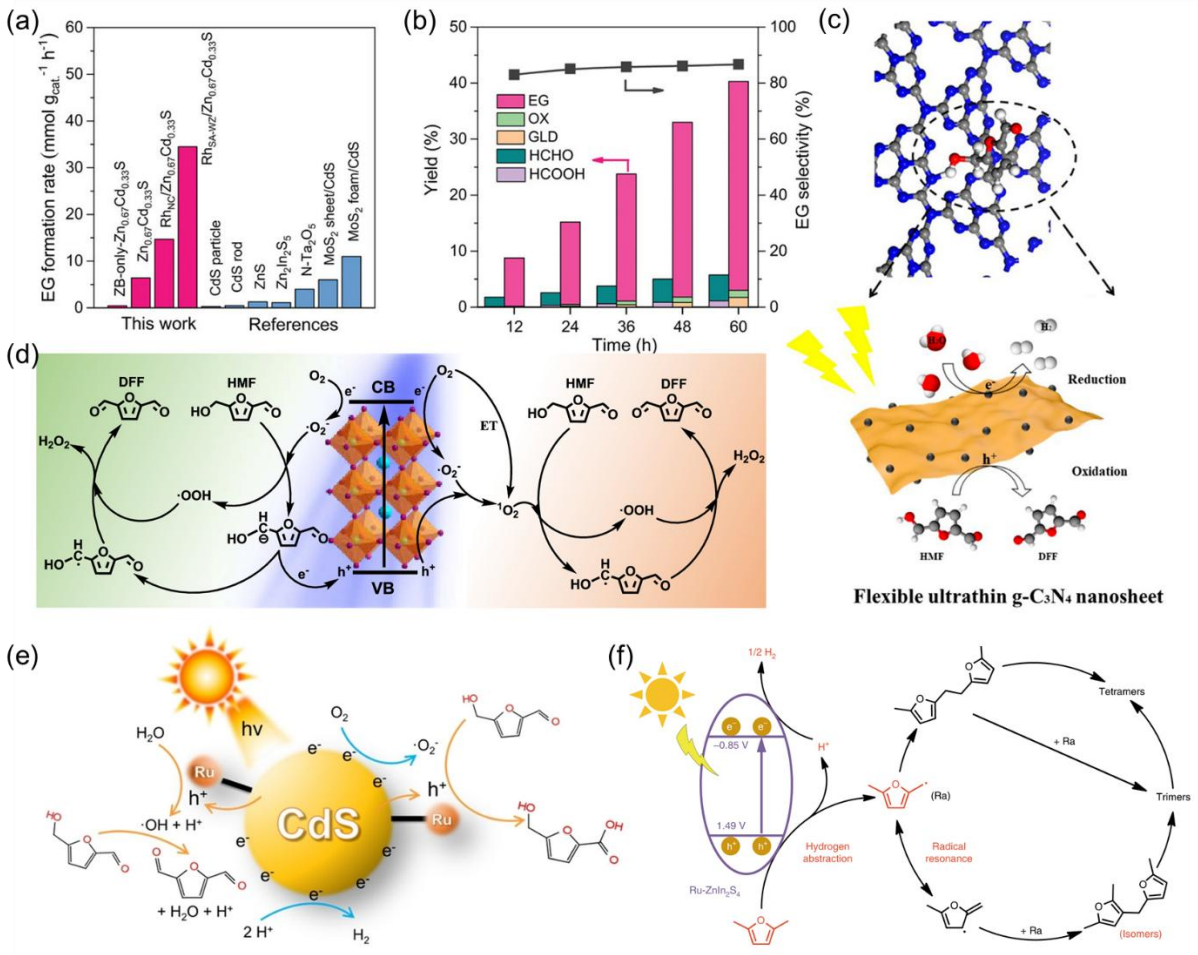

Figure 0-9. (a) Comparison of ethylene glycol formation rates over different photocatalysts and (b) catalytic performance of RhSA-WZ/$Zn_{0.67}Cd_{0.33}S$.[137] (c) Proposed mechanism of selective photocatalytic HMF oxidation coupled with H_2 evolution over UCNT.[138] (d) Mechanism on the photocatalytic selective oxidation of HMF by $MAPbBr_3$.[139] (e) Schematic mechanism for photocatalytic selective oxidation of HMF by Ru-CdS.[140] (f) Photocatalytic dehydrocoupling of 2,5-DMF mechanism by Ru-$ZnIn_2S_4$.[141]

Table 0-4. Application of traditional photocatalysts in biomass upgrading.

Catalyst	Biomass substrate	Reaction	Ref.
MOF-901	HMF	Oxidation	142
COF-Mo	Furfural	Oxidation	143
Ut-OCN	Fructose	Oxidation	144
TiO_2	Furfural	Oxidation	145

MnO_2-NRs	HMF	Oxidation	[146]
$MAPbBr_3$	HMF	Oxidation	[139]
$NiS/Zn_3In_2S_6$	HMF	Oxidation	[147]
$Zn_xCd_{1-x}S$	Glucose	Oxidation	[148]
N-Ta_2O_5	Alcohol	Oxidation	[149]
PdPSA CdS	Bioethanol	Oxidation	[150]

1.3.1.4 Challenges and opportunities in traditional photocatalysis

While solar-driven chemical transformations hold immense potential, challenges such as low photon utilization efficiency, rapid charge recombination, and limited product selectivity remain.[151] To achieve highly selective photo-reforming of biomass, it is essential to explore photocatalyst optimization strategies with broad applicability.

(1) Synthesis methods

The synthesis process significantly impacts photocatalyst performance, influencing crystallinity and particle size.[152] Nguyen *et al.* demonstrated that fabricating g-C_3N_4 from various precursors, such as melamine, urea, and thiourea, showed that melamine-derived g-C_3N_4 exhibited superior photocatalytic stability and the highest hydrogen evolution rates.[153] Its enhanced performance was attributed to improved crystallinity and chemical resistance, emphasizing the importance of precursor selection and structural properties for advancing photocatalytic processes in hydrogen production and plastic waste conversion.

(2) Morphology engineering

Nanomaterials have proven effective in minimizing charge recombination and enhancing photocatalytic efficiency due to their high surface area and reduced charge transport distances. Advances include nanostructures like nanospheres, nanodots, and quantum dots (e.g., CdS/CdO_x),[154] as well as nanosheets like d-$NiPS_3$/CdS, which exhibit notable hydrogen evolution activity.[155] This highlights the critical role of photocatalyst morphology in biomass upgrading.

(3) Material hybrid approaches

Hybridizing semiconductors with materials like carbon-based compounds or metal oxides leverages their combined properties for improved light absorption, catalytic activity, and selectivity. For instance, coupling CN with CNTs enhanced electron transfer due to CNTs' π-conjugative structure. Further improvement was achieved by incorporating NiMo nanoparticles into the CNT-CN system, boosting electron transfer and photocatalytic efficiency.[156]

(4) Cocatalyst integration

Adding metal cocatalysts can enhance charge transfer at interfaces and utilize surface plasmon resonance (SPR) to modulate redox potential. Zerjav *et al.* studied Pt-based cocatalysts on WO_3, revealing their dual role in overall water splitting.[157] This part will detail an explanation in the following session 1.3.2.

(5) Band engineering

Regulating the energy band structure can create an electric field at the photocatalyst surface, improving charge carrier transfer and photocatalytic performance. Techniques such as heterojunction construction are a vital strategy in photocatalysis to enhance the separation and transfer efficiency of photogenerated charge carriers (electrons and holes), directly impacting catalytic performance.[158] By creating a space charge region at the interface of two semiconductors, heterojunctions enable energy band bending, facilitating charge transfer and reducing recombination rates. Band engineering plays a crucial role by aligning the conduction and valence bands of semiconductors, ensuring effective redox reactions and improved light absorption. Most heterojunctions created through synthesis can generally be categorized into two types. Type II heterojunctions, facilitate charge separation where electrons and holes migrate to opposite materials, enhancing redox reactions. For example, composites like $W_{18}O_{49}$/g-C_3N_4 have demonstrated improved efficiency in oxidizing biomass-derived alcohols due to enhanced charge mobility.[159] Another one is Z-Scheme heterojunctions, which enable efficient spatial separation of redox sites, retaining high redox potential. Examples include CdS/g-C_3N_4 composites, which significantly improve photocatalytic hydrogen evolution and selective oxidation.[160]

(6) Surface defect engineering

Introducing surface defects or heteroatoms can increase active sites, optimize energy band structures, and reduce energy barriers, thereby enhancing photocatalytic activity.[161] For

example, defect-rich chalcogenide-coupled photocatalysts like d-$NiPS_3$/CdS demonstrated efficient plastic waste conversion into hydrogen and valuable chemicals through effective electron-hole separation and redox reactions at defect-activated sites.[155]

These strategies provide valuable insights for designing advanced photocatalysts to sustainably convert plastic waste into green fuels and high-value products.

1.3.2 Plasmonic photocatalysis

1.3.2.1 Introduction to plasmonic photocatalysis

Plasmonic photocatalysis is a cutting-edge approach in photocatalysis that leverages localized surface plasmon resonance (LSPR) properties of noble metal nanoparticles (such as gold, silver, or copper) to drive or enhance chemical reactions under light illumination (Figure 1-10).[162] This technique utilizes the unique ability of plasmonic materials to interact with light in a way that produces highly energetic hot electrons, and localized electromagnetic fields, enabling efficient energy conversion and catalytic activity.[163] It represents a powerful and versatile tool for applications in environmental remediation, chemical synthesis, and energy production.

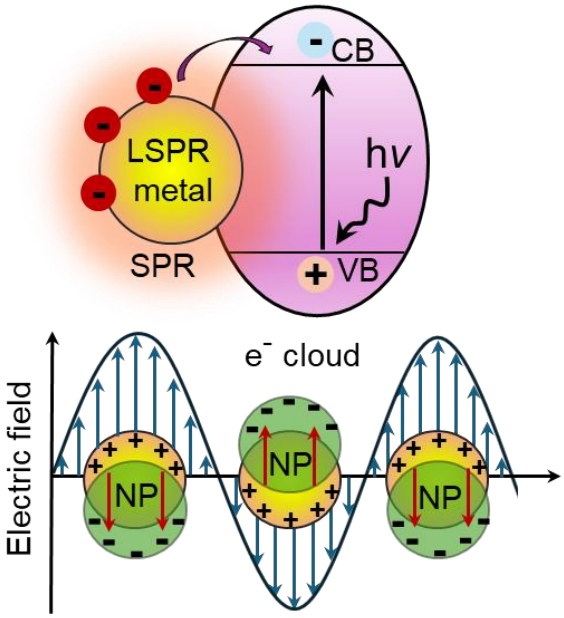

Figure 0-10. Plasmonic photocatalysis mechanism and LSPR evolution in the LSPR metal nanoparticles (NP) under illumination.

1.3.2.2 Benefits of plasmonic photocatalysis

Plasmonic photocatalysis is based on the phenomenon of LSPR, which occurs when conduction

electrons on the surface of metal nanoparticles oscillate collectively in response to incident light.[164] This resonance effect generates unique properties that are exploited in plasmonic photocatalysis as below.

1. Enhanced light absorption

Plasmonic photocatalysts enhance light absorption through the LSPR effect, a phenomenon where conduction band electrons in metallic nanoparticles oscillate collectively upon interaction with light.[165]

2. Generation of hot electrons

Upon light excitation, plasmonic nanoparticles produce high-energy electrons (hot electrons) and holes. These charge carriers can participate directly in redox reactions or be transferred to adjacent catalytic active sites/materials.[166]

3. Localized electromagnetic field enhancement

LSPR creates intense, localized electromagnetic fields near the nanoparticle surface, enhancing the interaction between light and nearby molecules. This effect facilitates the activation of reactants and intermediates.[167]

1.3.2.3 Materials for plasmonic photocatalysis

Gold (Au), silver (Ag), and copper (Cu) are the most prominent plasmonic materials used in photocatalysis due to their distinct optical and catalytic properties, which make them well-suited for driving light-induced chemical transformations.[168] Au is widely recognized for its robust LSPR within the visible spectrum, enabling efficient absorption of solar energy.[169] Its chemical inertness ensures exceptional stability under various reaction conditions, making it highly reliable for long-term applications. Moreover, Au's ability to generate and transfer hot electrons to nearby semiconductors or reactants plays a crucial role in enhancing photocatalytic activity. However, its high cost and scarcity remain significant limitations, restricting its large-scale application.

Ag often considered the most efficient plasmonic material, exhibits the strongest LSPR intensity among noble metals.[170] This results in superior visible light absorption and high rates of hot electron generation, which can significantly boost reaction kinetics. Ag's sharper and more intense plasmon peaks compared to Au make it ideal for applications requiring high light

utilization efficiency. Despite these advantages, Ag's poor chemical stability, particularly its susceptibility to surface oxidation and tarnishing, severely limits its durability, posing challenges for long-term catalytic processes.

Cu is gaining attention as a cost-effective and earth-abundant alternative to Au and Ag for plasmonic photocatalysis. Cu exhibits LSPR in the visible spectrum and is capable of driving light-induced reactions effectively.[171] Its low cost makes it attractive for scalable applications, particularly in large-scale industrial processes. However, Cu's LSPR intensity is weaker than Ag, and its stability is considerably lower due to its high susceptibility to oxidation and corrosion under ambient conditions. These stability issues often necessitate protective coatings or composite designs to mitigate degradation and extend operational lifetimes.

Aluminum (Al) and magnesium (Mg) are emerging as promising non-noble metal candidates for plasmonic photocatalysis due to their abundance and cost-effectiveness, despite some inherent limitations.[172] Al supports strong LSPR in both the ultraviolet (UV) and visible spectral ranges, making it suitable for photocatalytic applications that require high-energy photon absorption.[173] Additionally, its low cost compared to noble metals like gold and silver makes it attractive for scalable industrial applications. However, Al suffers from poor chemical stability and rapid oxidation under ambient conditions, which can diminish its plasmonic performance. Efforts to overcome these challenges include the use of protective coatings, such as oxide layers or encapsulation in inert matrices, to prevent surface degradation while maintaining its plasmonic properties.[174]

Mg is gaining attention as a lightweight, earth-abundant material capable of supporting LSPR in the UV-visible spectrum.[175] Mg offers plasmonic properties, making it a viable candidate for photocatalytic applications such as water splitting and organic transformations. However, its high reactivity and susceptibility to corrosion necessitate protective layers or passivation strategies to prevent degradation in catalytic environments. Recent advancements have demonstrated the incorporation of Mg into hybrid plasmonic-semiconductor systems, where Mg serves as both a plasmonic enhancer and an electron donor, improving charge separation and enhancing catalytic activity.[176]

1.3.2.4 Applications in biomass conversion

Plasmonic photocatalysis has demonstrated significant potential in biomass-derived compound conversion, with several detailed examples showcasing its ability to enhance reaction

efficiency and selectivity through LSPR effects. For instance, a plasmonic Au/ZnO catalyst facilitates the photocatalytic oxidation of HMF to FDCA under visible light irradiation (Figure 1-11 a).[177] The unique integration of LSPR from Au nanoparticles with oxygen vacancies on ZnO significantly enhances light absorption and charge separation, leading to efficient catalytic performance. Specifically, the catalyst achieved a remarkable FDCA selectivity of 96.9% and demonstrated excellent stability over multiple cycles. Similarly, on the photocatalytic oxidation of biomass-derived HMF into high-value HMFCA using Ag/TiO_2 plasmonic photocatalysts under visible light (Figure 1-11b).[178] The Ag nanoparticles (NPs) supported on TiO_2 exhibit an LSPR effect, significantly enhancing visible light absorption and promoting the separation of photogenerated charge carriers. The optimized 2.5%Ag/ TiO_2 catalyst achieves a high HMFCA selectivity of 96.7%, showcasing its efficiency in leveraging LSPR effects for selective biomass conversion

In addition to the above-mentioned mono-metal plasmonic catalysts, bimetallic plasmonic catalyst, comprising palladium (Pd) and Au nanoparticles supported on mesoporous carbon nanospheres (MCN), for the selective photo-oxidation of biomass-derived alcohols under ambient conditions.[179] The Pd-Au/MCN catalyst exploits the LSPR effect of Au to generate hot electrons, which are efficiently transferred to adjacent Pd nanoparticles, enhancing catalytic activity. This finite-difference time-domain (FDTD) simulation gives evidence that the synergistic system demonstrates superior efficiency compared to monometallic catalysts, achieving significantly higher conversion rates for a range of alcohols while maintaining high selectivity. The bimetallic design underscores the advantages of combining plasmonic and catalytic metals, offering a promising route for sustainable solar-driven chemical transformations.

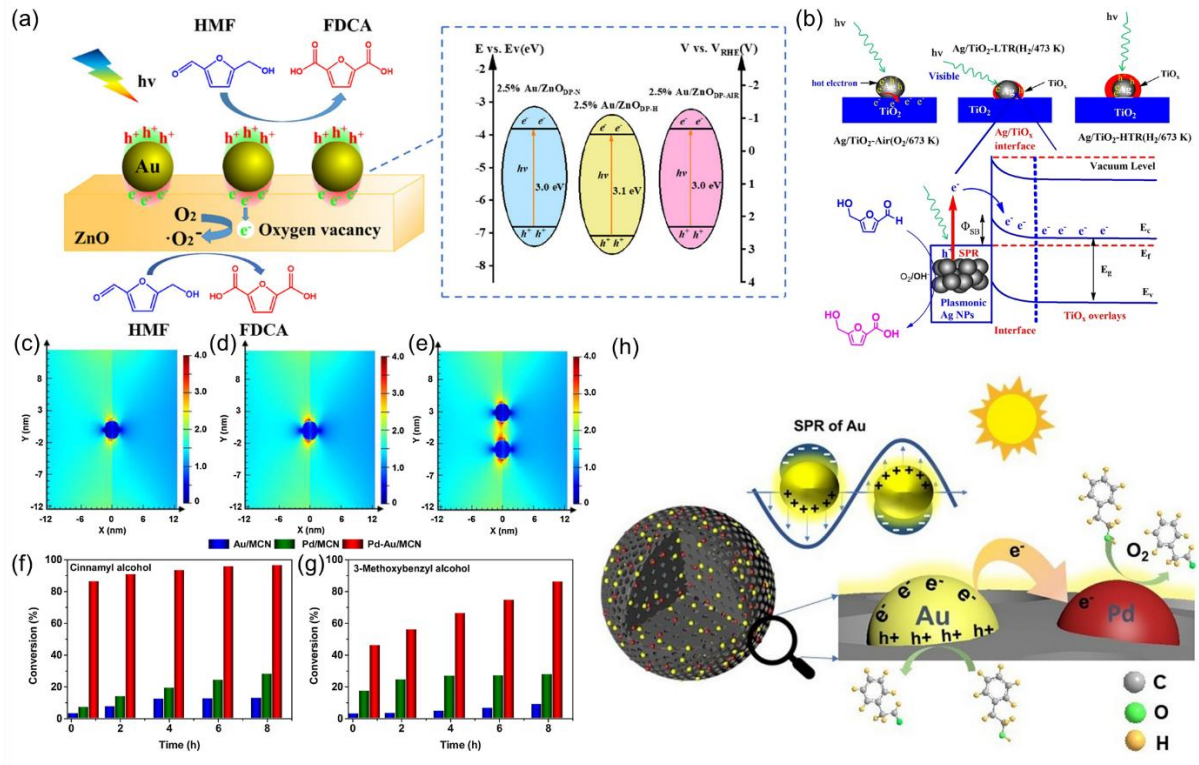

Figure 0-11. (a) Schematic of the photocatalytic oxidation of HMF to FDCA by Au/ZnO under irradiation.[177] (b) The interfacial enhanced effect in the photocatalytic selective oxidation of HMF to HMFCA by Ag/TiO_2 catalysts.[178] The FDTD simulated spatial enhancement of the local electric field induced by LSPR effects under irradiation for (c) Au/MCN, (d) Pd/MCN, and (e) Pd-Au/MCN. Conversion of (f) Cinnamyl alcohol, and (g) 3-Methoxybenzyl alcohol over Pd-Au/MCN (red), Pd/MCN (green) and Au/MCN (blue) under light radiation. (h) Schematic mechanism of the oxidation of alcohols over Pd-Au/MCN induced by the spatial local electric field.[179]

Further summary examples underline the versatility of plasmonic photocatalysis in biomass valorization (Table 0-5), showcasing its ability to optimize light utilization, drive specific reaction pathways, and achieve high yields of value-added products under sustainable and mild conditions.

Table 0-5. Application of plasmonic photocatalysts in biomass upgrading.

Catalyst	Biomass substrate	Reaction	Ref.
Ru/HY-SO_3H	Cellulose	Oxidation	180
3DOM TiO_2-Au	Glucose	Oxidation	181

Ag/TiO_2	Fructose	Oxidation	178
Au/TiO_2	Glycerol	Oxidation	182
$Ni\text{-}Au/g\text{-}C_3N_4$	Furfural-alcohol	Oxidation	183
Au/TiO_2	HMF	Oxidation	184
$AuPt/TiO_2$	Glycerol	Oxidation	185
$Ag/G\text{-}Al_2O_3$	Glucose	Oxidation	186
$Cu\text{-}TiO_2$	Glycerol	Oxidation	187
$Cu\ NPs/CdS/In_2O_3$	Furfural-alcohol	Oxidation	46

1.3.3 Photoelectrocatalysis

Photoelectrocatalytic (PEC) strategies are innovative approaches that combine light-driven photocatalysis with electrocatalysis, leveraging both solar energy and applied electrical bias to enable and enhance chemical transformations.[188] These systems utilize photoactive electrodes to absorb photons, generate charge carriers, and drive redox reactions with high efficiency and precision (Figure 0-12. The typical redox reaction of a PEC system, (a) photoanode, (b) photocathode, and (c) dual-photoelectrode tandem configuration.Figure 0-12). PEC strategies are increasingly recognized as critical tools in the transition to sustainable energy and chemical processes, particularly for applications such as water splitting, CO_2 reduction, pollutant degradation, and fine chemical synthesis.[189,190] By integrating light and electricity, PEC systems overcome the limitations of standalone photocatalysis or electrocatalysis, offering improved control, efficiency, and scalability.

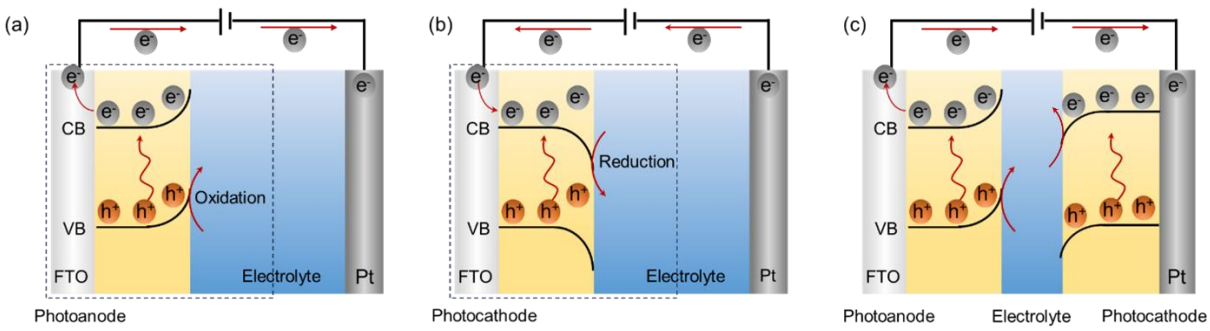

Figure 0-12. The typical redox reaction of a PEC system, (a) photoanode, (b)

photocathode, and (c) dual-photoelectrode tandem configuration.

1.3.3.1 Fundamentals of photoelectrocatalysis

1. Photoelectrodes

Photoelectrodes are the core components of PEC systems, serving as light absorbers and charge transport mediums.[191] These are typically classified into photoanodes and photocathodes.

Photoanodes: Materials such as TiO_2, $BiVO_4$, or α-Fe_2O_3 are commonly used for their wide bandgaps and stability. They absorb light to generate electron-hole pairs, with holes participating in oxidation reactions like water oxidation or organic pollutant degradation.[192]

Photocathodes: Materials like Cu_2O, Si, or MoS_2 are used to reduce species such as CO_2 or protons, generating value-added products like methane, methanol, or hydrogen.[193]

2. Electrolytes

Electrolytes facilitate ionic transport between the photoanode and photocathode, maintaining charge balance in the system.[194] Aqueous electrolytes are commonly used for water splitting, while non-aqueous or ionic liquids are employed for specialized reactions, such as CO_2 reduction.

3. External Bias

An applied electrical bias complements the energy provided by light, facilitating charge carrier separation and enabling reactions that would otherwise require higher activation energy.[195] This external energy input is critical for driving thermodynamically demanding processes.

1.3.3.2 Advantages over traditional photocatalysis

1. Enhanced efficiency

The combination of light and bias improves charge separation, reduces recombination losses, and increases overall reaction rates.[196]

2. Tunable reaction pathways/ selectivity

PEC systems offer precise control over reaction pathways by adjusting the applied bias, light intensity, and catalytic properties.[197] This flexibility extends to regulating the generation of

reactive species, such as radicals, on the catalyst surface, which play a pivotal role in driving selective transformations. For example, photogenerated hydroxyl radicals (·OH) at the photoanode can be tuned to selectively oxidize glycerol to dihydroxyacetone (DHA).[198] Advanced catalyst designs, including bimetallic systems and surface modifications, further enhance radical-mediated reactions and product specificity.[63]

By optimizing reaction environments such as pH, light intensity, and electrolyte composition, photoelectrocatalytic systems effectively suppress side reactions while maximizing selectivity.[199,200] This tunability is particularly advantageous for processing complex biomass-derived feedstocks, enabling efficient conversion into high-value products.

3. Dual Reaction Functionality

Photoelectrocatalysis excels in its dual reaction functionality, enabling simultaneous redox reactions at the photoanode and photocathode, which maximizes resource utilization and enhances overall system efficiency.[201] At the photoanode, oxidation reactions such as the conversion of biomass-derived compounds take place, while the photocathode facilitates reduction reactions like hydrogen evolution, CO_2 reduction, or H_2O_2 production. This integrated process ensures that both photogenerated electrons and holes are actively utilized, minimizing energy loss through recombination and improving the efficiency of solar energy conversion.

This dual functionality not only increases energy utilization but also enables the production of valuable co-products, enhancing the economic viability of the system. For instance, anodic biomass oxidation can yield fine chemicals, while cathodic reduction generates sustainable energy carriers like hydrogen or industrial chemicals like hydrogen peroxide. By integrating two complementary reactions in a single system, photoelectrocatalysis reduces the need for separate processes, aligning with green chemistry principles and promoting scalability. Despite challenges such as reaction coupling and product separation, continued advancements in material design and system integration highlight the transformative potential of this technology for sustainable chemical production and renewable energy applications.

1.3.3.3 Case Studies in biomass upgrading

This introduction systematically explores PEC applications for key compounds such as glycerol, glucose, and HMF, emphasizing how material innovations and tailored designs

address the specific challenges associated with each reaction.

Glycerol oxidation has been extensively studied in PEC systems, with $BiVO_4$-based photoanodes emerging as a leading material due to their strong visible-light absorption and appropriate valence band position.[202] Lu *et al.* developed Bi-rich $BiVO_{4-x}$ photoanodes with engineered bismuth-rich domains and oxygen vacancies, significantly improving glycerol oxidation to DHA (Figure 1-13a).[203] Enhancements such as NiOOH cocatalysts significantly improve reaction kinetics by facilitating hydroxyl radical generation, which is crucial for selective DHA production (Figure 1-13b).[204] Heterojunction structures like $FeOOH/BiVO_4$ further boost charge separation efficiency and photostability, reducing recombination losses and enabling high glycerol oxidation activity (Figure 1-13c).[205]

Glucose oxidation in PEC systems primarily targets the production of gluconic acid, a valuable intermediate for pharmaceuticals and fine chemicals. Materials like WO_3 and $BiVO_4$,[206,207] often combined with cocatalysts or plasmonic nanoparticles (e.g., Au or Ag),[208] enhance catalytic performance by improving surface adsorption of glucose and charge transfer efficiency. Layered double hydroxides (LDHs) also play a key role by providing tunable active sites and improving the stability of the PEC system under operating conditions.[198]

HMF oxidation represents another critical application, with PEC systems enabling its transformation into products such as HMFCA and FDCA. LDH-modified $BiVO_4$ and other hybrid photoanodes have shown remarkable Faradaic efficiencies and product selectivity due to their optimized band alignment and robust catalytic interfaces (Figures 1-13d and 1-13e).[209]

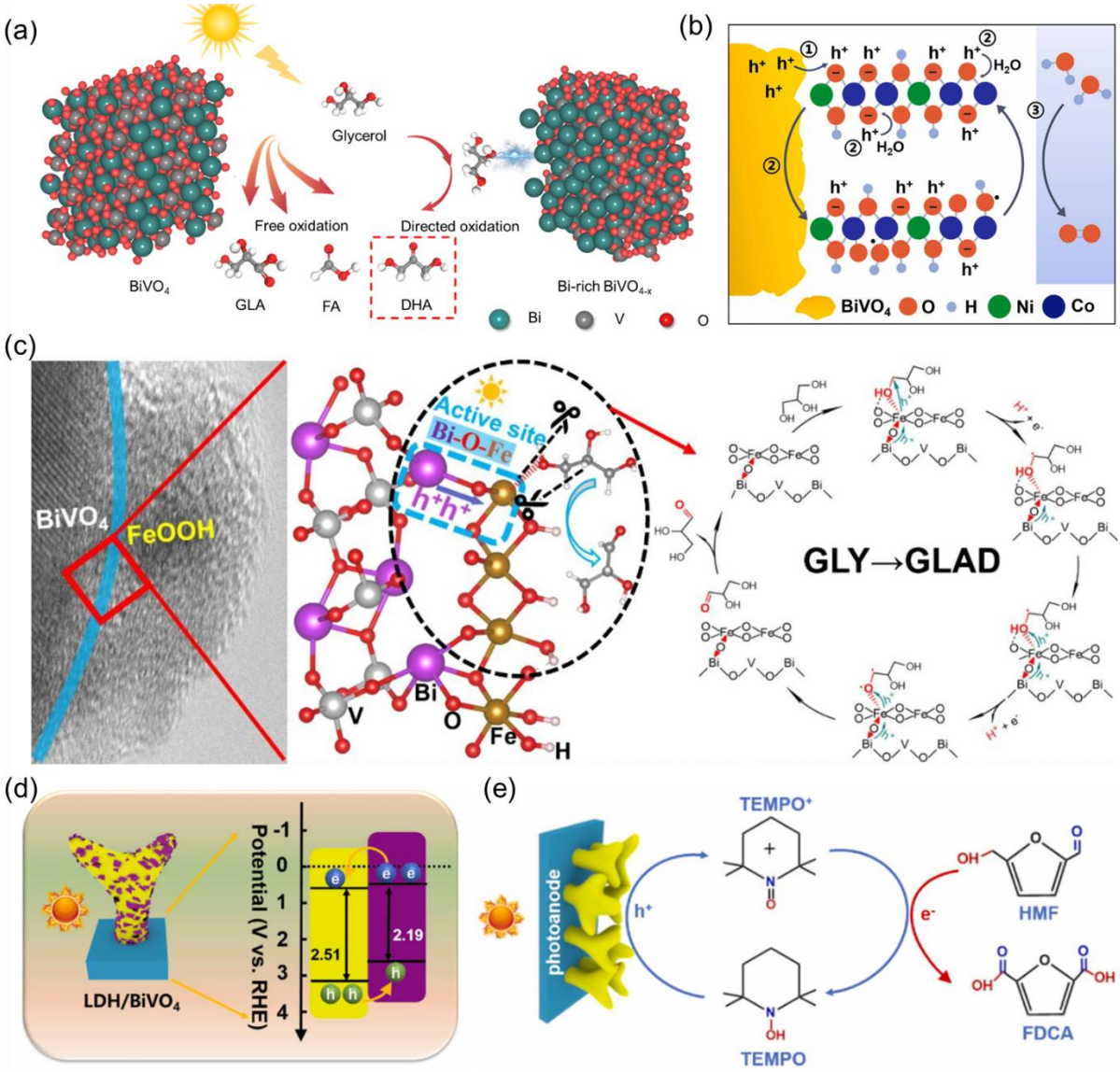

Figure 0-13. (a) PEC selective glycerol oxidation using Bi-rich $BiVO_{4-x}$ photoanode.[203] (b) Schematic diagram of the PEC generation and participation of adsorbed ·OH by NiCo-LDH.[204] (c) Proposed mechanism for the PEC GLY conversion by $FeOOH/BiVO_4$.[205] (d) Band structure of $LDH/BiVO_4$ photoanode and (e) scheme of the TEMPO-mediated PEC oxidation of HMF over 1-$LDH/BiVO_4$ photoanode.[209]

These summary systems effectively address the challenges of overoxidation and low selectivity by stabilizing intermediate products and facilitating efficient charge transfer (Table 0-6). These advancements also position PEC technology as a sustainable and scalable solution for biomass valorization, bridging the gap between renewable energy utilization and green chemical production.

Table 0-6. Application of photoelectrocatalytic catalysts in biomass upgrading.

Catalyst	Biomass substrate	Reaction	Ref.
Au/C_3N_4	Glycerol	Oxidation	210
Bi_2O_3/TiO_2	Glycerol	Oxidation	63
SnO_2/BVO-400	Glycerol	Oxidation	211
Mo–BVO–TiCoNO–$CoFeO_{xy}$	Benzyl alcohol	Oxidation	212
Bi_2MoO_6@TiO_2NTA	Benzyl alcohol	Oxidation	213
FLP-P-BFO	HMF	Oxidation	214
$NiFeO_x$-NF	Glucose	Oxidation	215
α-Fe_2O_3/Nb_2O_5/C	HMF	Oxidation	216
Au/α-Fe_2O_3/RGO	Furfural	Oxidation	217
TiO_2 NTs	Glucose	Oxidation	218

1.4 Summary and outlook

The introduction of this thesis provides a detailed exploration of the critical role of green catalysis in addressing global challenges, including resource depletion, environmental degradation, and the transition toward sustainable energy and materials. Biomass, as a renewable and abundant feedstock, is highlighted for its potential to replace fossil-based resources in producing high-value chemicals, fuels, and materials. The text emphasizes the importance of specific biomass-derived compounds such as ketones (e.g., acetophenone), aldehydes (e.g., 5-hydroxymethylfurfural, HMF), and biofuels (e.g., glycerol), which serve as platform chemicals for developing renewable and sustainable industrial processes. These compounds are noted for their versatility in being transformed into valuable intermediates for bioplastics, bio-based fuels, and specialty chemicals, offering a promising route to decarbonizing the chemical industry.

The discussion also examines advancements in various catalytic technologies tailored for biomass upgrading. Thermal catalysis is recognized for its industrial applicability and high efficiency, but challenges such as energy-intensive operations and catalyst deactivation are highlighted. Enzymatic catalysis, celebrated for its unmatched specificity and ability to operate under mild conditions, faces significant barriers related to enzyme stability and scalability. Electrocatalysis is presented as a promising method that leverages renewable electricity to drive oxidation and reduction reactions, though catalyst durability and reaction kinetics remain areas of active research. Solar-mediated catalysis, including photocatalysis and photoelectrocatalysis, is portrayed as a cutting-edge approach that uses solar energy to drive selective and efficient chemical transformations, significantly reducing environmental impacts. These technologies collectively underscore the potential of advanced catalytic systems in enabling biomass valorization and the broader shift toward carbon-neutral chemical production.

The future of biomass valorization through advanced catalytic technologies holds immense potential for addressing global sustainability challenges, but significant efforts are needed to overcome current limitations. One key direction is the development of robust and cost-effective catalysts with enhanced stability, selectivity, and activity. Innovations such as defect engineering, heterostructure design, and the use of earth-abundant materials are crucial to reducing reliance on expensive or scarce components while improving catalytic performance. Integrating renewable energy sources into catalytic processes will also play a pivotal role. Solar-driven catalytic technologies, such as photocatalysis and photoelectrocatalysis, offer a transformative pathway for biomass upgrading by utilizing abundant sunlight to drive reactions under mild conditions. Coupling these systems with renewable electricity from wind or solar power in electrocatalytic processes can further enhance efficiency and scalability, contributing to the broader goal of achieving carbon-neutral production systems.

The outlook of this thesis emphasizes the need for a multidisciplinary approach to address the limitations of existing catalytic technologies and advance the field of sustainable biomass upgrading. Key methods are included below.

(1) Development of robust catalysts

Designing catalysts with enhanced stability, selectivity, and reusability is critical. This includes the exploration of earth-abundant materials, hybrid catalysts, and defect-engineered surfaces to improve reaction efficiencies and reduce costs.

(2) Integration of Renewable Energy

Combining catalytic processes with renewable energy sources such as solar, wind, or hydropower is essential to achieve carbon-neutral production systems. Solar-driven catalytic technologies, in particular, are positioned as transformative tools for reducing energy demands and enhancing sustainability.

(3) Circular economy and waste valorization

Emphasis is placed on adopting circular economy principles, where waste biomass streams are upgraded into high-value products. This approach not only reduces waste but also contributes to resource efficiency and economic viability.

(4) Advancing reactor design

Innovations in reactor design, including flow reactors and hybrid systems, are needed to improve scalability and operational efficiency. Modular reactor systems that integrate catalytic, electrochemical, and solar processes are highlighted as future directions.

The outlook section proposes future directions, focusing on integrating renewable energy, designing robust and cost-effective catalysts, and adopting circular economy principles. It highlights the need for interdisciplinary collaboration and policy support to drive the industrial adoption of sustainable technologies, positioning solar-driven biomass upgrading as a key player in achieving carbon neutrality and green industrial transformation.

Chapter 2 – Photo-Enhancement of Reactants Adsorption on AuPd Alloy Surface in Selective Hydrogenation of Ketones

Abstract

In heterogeneous catalysis, the adsorption kinetics and the interaction of reactants with the catalyst surface play a crucial role in determining the catalytic performance. In the hydrogenation of ketones, enhancing the adsorption kinetics of both hydrogen and ketone can affect the performance of the hydrogenation reaction and product selectivity. While significant knowledge has been gained about the plasmonic enhancement of AuPd photocatalysts, relatively little is known about the effect of light on the reactants's adsorption. Here we used AuPd alloys for the photocatalytic hydrogenation of ketones to unveil the contribution of light on the adsorption of reactants. We discovered enhanced hydrogen dissociation on the AuPd surface via localized surface plasmon resonance (LSPR) of illuminated Au, forming AuPd-H species on the alloy surface, which increases the charge heterogeneity of the surface. This is followed by an enhanced adsorption of C=O bonds of ketone, which is directly evidenced by in-situ XAS characterization. In-situ XAS provides new insights into the significantly enhanced selective adsorption of C=O bond on the surface AuPd-H species and subsequently induced superior selective hydrogenation reaction at mild conditions. These synergetic effects of merging enhanced electron density and charge heterogeneity and increased hot electron generation upon light irradiation enable AuPd nanoalloys to achieve high conversion and chemoselectivity across various ketone substrates with visible light.

2.1 Introduction

The chemoselective hydrogenation of unsaturated aldehydes and ketones to unsaturated alcohols is essential for producing high-value pharmaceuticals but contributes notably to greenhouse gas emissions. Within the European Union, the healthcare sector alone accounts for 4.7% of total emissions.[219,220] Supported metal catalysts are industrially prevalent for hydrogenating unsaturated carbonyl compounds,[221,222] yet they often suffer from thermodynamic competition between C=C and C=O bond hydrogenation,[223] resulting in

undesired by-products and increased purification costs. Previous research has shown that the presence of base/acid sites on the support material can induce a unique ionic effect (IE) by extracting electrons from the metal nanoparticles, influencing the electronic state of the metal nanoparticles, and regulating the hydrogenation process, which can be tailored to enhance hydrogenation rates without compromising chemoselectivity.[224-226] However, this hydrogenation process needs to be performed generally under heating using fossil fuel resources.

Solar-driven plasmonic metal nanocatalysts present an ideal platform for this,[227,228] as hot electrons can be predominantly generated under solar irradiation of plasmonic metal nanoparticles through localized surface plasmon resonance (LSPR) effect.[229] Plasmonic monometallic photocatalysts like Au, Ag, and Cu often show limited reaction activity due to their deep d-band structure, where antibonding modes reside below the Fermi level, inhibiting the effective adsorption of reactant molecules.[230] To address this, we propose transferring hot electrons generated by the plasmonic metal to the active metal surface via injection into neighboring metal sites within the alloy structure.[231] The homogeneous solid solution alloy catalyst, AuPd, is employed for plasmon-driven hydrogenation, exploring the potential of bimetallic catalysts to enhance activity beyond LSPR amplification. However, the introduction of Pd into Au nanoparticles inherently suppresses the LSPR intensity due to the damping effect of Pd,[232] resulting in reduced light absorption. Despite the weakened plasmon effect, the AuPd alloy shows significantly enhanced efficiency compared to pure Au,[233,234] highlighting that enhancing the LSPR intensity is not the only way to improve photocatalytic activity.

Herein, we design a hydrogenation of the C=O bond of ketones over the AuPd nanoalloy surface, leveraging the mechanism of reactant adsorption enhancement on plasmonic AuPd alloy. The role of light irradiation in the increased reactant adsorption is visualized by *in-situ* X-ray absorption spectroscopy (XAS) experiments, which provide novel insight into the pre-catalytic step of the hydrogenation reaction, especially with the stimulation by light.

2.2 Experimental Section

2.2.1 Materials

Ethanol (Ajax Finechem, 99.5%), aluminum nitrate nonahydrate (Chem-supply, >98%), 30% ammonia aqueous (Chem-supply), Gold (III) chloride trihydrate (Sigma-Aldrich, >99.9%), sodium chloride (Chem-supply, >99.7%), Palladium (II) chloride (Sigma-Aldrich, >99.9%),

sodium borohydride (Aladdin, >98%), isopropanol (Ajax Finechem, 99.8%), acetophenone (Acros Organics, >99.9%), 1-phenylethanol (Sigma-Aldrich, >98.5%), 4'-methylacetophenone (Sigma-Aldrich, >95%), 4'-methoxyacetophenone (Sigma-Aldrich, >99%), 4'-Chloroacetophenone (Sigma-Aldrich, >97%), 4'-bromoacetophenone (Sigma-Aldrich, >98%), 2-Acetonaphthone (Sigma-Aldrich, >99%), benzophenone (Sigma-Aldrich, >99%), 4-Acetylpyridine (Sigma-Aldrich, >97%), cyclohexanone (Sigma-Aldrich, >99.8%), cyclopentanone (Sigma-Aldrich, >99%).

2.2.2 The synthesis of catalysts

2.2.2.1 Preparation of AuPd-γ-Al_2O_3

45g Al $(NO_3)_3 \cdot 9H_2O$ was dissolved in 75 ml deionized water and stirred for 30 min. To the above Al $(NO_3)_3 \cdot 9H_2O$ solution, 10 wt% ammonia aqueous solution was added dropwise at a speed of 5mL/min (~1 drop per second), the titration was ended when the pH value of the mixture reached 5.00, then kept stirring in the air at room temperature for 1 h. The obtained white gel was vacuum filtrated for 2 h to receive a relatively dry gel cake, which weighed 116.22 g, and transferred evenly into 6 glass vials of 20 mL. Then loaded glass vials were transferred into 120 mL Teflon vessels where 2ml ultrapure water was poured to the bottom of each vessel. The Teflon vessels were heated at 170 ºC for 48 h. The resulting white material was washed with ultrapure water 3 times and alcohol once and recovered by centrifuge (3500 rpm, 30 min). The final product was dried at 60°C for two days. The calcined Boehmite in a tube furnace for 4.5 h at 450 ºC called γ-Al_2O_3.

2.0 g of γ-Al_2O_3 powder was dispersed into 49 mL of an aqueous solution containing 0.01 M of $HAuCl_4$ and 49 mL of an aqueous solution containing 0.01 M of $NaPdCl_3$. To prepare the $NaPdCl_3$ solution, 0.05 g of $PdCl_2$ was dissolved in 28.3 mL of an aqueous solution containing 0.02 M of NaCl under stirring. The mixture was then stirred magnetically. Subsequently, 20 mL of an aqueous solution containing 0.53 M of lysine was added to the mixture with vigorous stirring for 30 min. Following this, 10 mL of an aqueous solution containing 0.35 M of $NaBH_4$ was added dropwise over 20 min. The mixture was allowed to age overnight and the solid was then separated, washed twice with water and once with ethanol, and dried at 60 °C to obtain AuPd-γ-Al_2O_3.

2.2.2.2 Preparation of Catalysts Au@Pd-γ-Al_2O_3

The addition of 49 ml of ultra-pure water was stirred magnetically while 2.0 g of γ-Al_2O_3

powder was distributed in 0.01 M $HAuCl_4$ aqueous solution. After vigorously swirling the mixture for 30 min, 20 mL of 0.53 M lysine was added. 10 mL of a 0.35 M $NaBH_4$ solution was added dropwise to this suspension in 20 min. The mixture was aged for an overnight period, after which the solid was separated, three times washed with water and once with ethanol, and finally dried at 60 °C to produce Au-γ-Al_2O_3 powder.

In 49 mL of 0.01 M $NaPdCl_3$ aqueous solution and 49 mL of ultra-pure water, 2.0 g of Au-γ-Al_2O_3 powder was well mixed for 30 min. In 20 min, 10 mL of a 0.35 M $NaBH_4$ solution was added dropwise to this suspension. Au@Pd-γ-Al_2O_3 was produced by aging the combination overnight, separating the solid, and then washing it with water and ethanol.

2.2.3 Photocatalytic hydrogenation test

During the photocatalytic hydrogenation, 20 mg as-synthesized catalysts and 0.5 mmol substrates were dispersed in 10 mL isopropanol (IPA). The mixture was transferred into a 100 mL sealed autoclave, vacuumed, and bubbled with Ar gas to ensure complete degassing. Finally, the autoclave was filled with ultra-high purity H_2 gas to reach 3 bar pressure at ambient temperature. This procedure was performed in complete darkness. An LED light (720 lm, 7.5 W, Osram MR16) was used as the light source to simulate the solar light irradiation. Products were sampled and analyzed by a gas chromatograph (GC-2010, Shimazu) equipped with a flame ionization detector (FID) using high-purity argon (99.99%) as a carrier gas. Five consecutive runs of photocatalytic ACE hydrogenation were used to assess the catalyst stability. Between each cycle, the autoclave was vacuumed and refilled with 3 bar H_2.

$$AQY = \frac{Number\ of\ transformed\ acetophenone}{number\ of\ incident\ photons} = \frac{M \times \mathrm{NA}}{N} \qquad \text{(Equation 2.1)}$$

$$N = \frac{E\lambda}{hc} = \frac{I \times A \times t \times \lambda}{h \times c} \qquad \text{(Equation 2.2)}$$

The number of incident photons (N) was calculated by Equation 2, where I is the light intensity, A is the irradiation area of the catalyst suspension, t is the light incident time, λ is the wavenumber of the incident light, h is the Planck constant, c is the lightspeed, M represents the amount of transformed toluene, and N_A represents the Avogadro's constant.

2.2.4 Hot filtration test

A hot filtration test has been used to investigate the recyclability and stability of the as-prepared

catalyst, Normally, a mixture of ACE (0.5 mmol), catalyst (20 mg), and isopropanol (10 mL) was introduced into the 100 mL stainless-steel autoclave and the reaction mixture was stirred at 21-22 ºC under 3 bar H_2 pressure. After 30 min, the catalyst was separated from the hot reaction mixture, and the as-obtained filtrate solution was analyzed using a Shimazu GC-2010. Then at the same reaction conditions, the hydrogenation reaction was carried out for 4h with sampling at each 1h.

2.2.5 Characterization

Transmission electron microscope (TEM) data were recorded with JEOL 2200FS and Zeiss Sigma VP HD instruments. High-resolution transmission electron microscopy (HRTEM) and high-angle annular dark-field scanning transmission microscopy (HAADF-STEM) images of the samples were acquired using a FEI Themis Z (STEM) equipped with a double spherical aberration corrector operating at 300 kV. Dual electron energy loss spectroscopy (dual-EELS) was conducted on a Themis Z equipped with a double spherical aberration corrector and Gatan magnetic electron prism. The energy dispersion of each channel was 0.1 eV. During the test, the acceleration high tension of the incident electron beam was 300 kV. X-ray diffraction (XRD) measurements were recorded on a Rigaku D max-3C diffractometer using Cu Kα radiation (40 kV, 20 mA, λ = 0.15408 nm). X-ray photoelectron spectroscopy (XPS) measurements were performed using a Thermo Fisher ESCALAB 250Xi spectrometer with a focus monochromatic Al Kα-rays (1486.6 eV) source. The samples were tested under a vacuum below 5.0×10^{-10} Mbar, and energy resolution spectra were collected using a pass energy of 20 eV. Peak fitting of the high-resolution data was carried out using the Thermo Advantage 5.976 surface chemical analysis software. The Solid-state UV–vis absorption spectra of the samples were measured on a SHIMADZU UV-3600i PLUS Spectrophotometer. The Au and Pd contents were analyzed by inductively coupled plasma-atomic emission spectrometry (ICP-OES) on an R4 Perkin Elmer ICP-OES 8300DV. Before analysis, the powder samples were digested by aqua regia dissolved in 70% HNO_3, and diluted by deionized water. The X-ray absorption spectroscopy (XAS) was obtained from the XAS beamline of the Australian Synchrotron, ANSTO, and processed with the Athena program.[235] These powder samples were all probed by the Pd K-edge (24350 eV). XAS was conducted in transmission mode with simultaneous measurements of Pd foil as reference materials for each scan. A photoluminescence (PL) study was recorded on a Horiba Fluoro max-4 spectrofluorometer. The excitation and emission slit width were fixed to 5 nm each with an excitation wavelength of 450 nm. Working electrodes were prepared over a fluorine-doped tin oxide (FTO) glass by the drop-casting method. The FTO glass was cleaned

properly with deionized water and ethanol by ultra-sonication and then dried in the oven. 1 mg photocatalyst along with 400 µL ethanol, 50 µL Nafion and 125 µL distilled water, was sonicated for 30 min, and then the slurry was coated on the conducting surface of the FTO glass. For electrochemical measurements, a three-electrode cell was used, where platinum acted as the counter electrode. An Ag/AgCl electrode was used as the reference electrode and sample-coated FTO acted as the working electrode. All the measurements were carried out with an CHI 660E electrochemical workstation and performed in 0.5 M Na_2SO_4 aqueous solutions. The temperature of the reaction mixture, consisting of catalyst particles suspended in the liquid phase (IPA/ACE) (20 mg catalyst, 0.5 mmol ACE, 10 mL isopropanol (IPA), was measured at three locations using a thermal imaging camera (FLIR ONE Gen 3). The images were taken *in-situ* after 1 and 4 hours of reaction corresponding to different ACE conversions.

2.2.6 DFT calculation

The first-principles calculations were performed based on the spin-polarized density functional theory (DFT) as implemented in the Vienna ab initio simulation package (VASP).[236,237] The Perdew-Burke-Ernzerhof (PBE) form of the generalized gradient approximation (GGA) was employed for describing the exchange and correlation functional,[238] and the spin-orbit coupling (SOC) was included. The van der Waals (vdW) interactions based on the Tkatchenko-Scheffler (TS) scheme were considered for the calculations.[239] The plane wave cutoff was set at 500 eV. The bulk lattice constants were optimized with a Monkhorst–Pack sampling of a $10 \times 10 \times 10$ k-point grid for the face-centered-cubic (FCC) Au, Pd, and AuPd alloy (1:1) unit cell. The 4×4 slab of 3 layers separated by 20 Å of vacuum in periodic cells was adopted for the Au, Pd, and AuPd alloy (111) surface models. Surface calculations were performed with a Monkhorst–Pack sampling of a 2×2×1 k-point grid. All the geometries were fully relaxed until the forces on each atom were less than 0.01 eV/Å. The atomic structures reported in this study were visualized using VESTA, and the post-processing of data was based on VASPKIT.[240] Adsorption energy E_{ads} of A group on the surface of substrates was calculated as follows:

$$E_{ads} = E_{tot} - (E_{sub} + E_A) \qquad \text{(Equation 2.3)}$$

where E_{tot} stands for the total energy of the adsorption system, E_{sub} for the energy of adsorbates (the bare substrates), and E_A for the energy of the A group (catalyst).

The Gibbs free energy of each species was calculated as follows:

$$G = E_{DFT} + E_{ZPE} + \int C_p dT - TS$$

where E_{DFT} is the electronic energy directly obtained from DFT calculations, E_{ZPE} is the zero-point vibrational energy and was computed from the vibrational frequencies of adsorbed species with fixed supports, C_p is the heat capacity, T is the room temperature (300 K), and S is the entropy.

2.3 Results

Figure 1 illustrates the morphology and structure of two types of Au and Pd nanocomposites loaded on alumina nanofiber support: AuPd nanoalloy (AuPd-γ-Al_2O_3) and bimetallic AuPd nanoparticles (Au@Pd-γ-Al_2O_3). The morphology of AuPd-γ-Al_2O_3 and Au@Pd-γ-Al_2O_3 shows the uniform metal nanoparticles distributed on the γ-Al_2O_3 surface with an average size of around 4.5 nm (Figure 0-1a and Figure 0-1b). High-resolution transmission electron microscopy (HR-TEM) imaging (Figure 0-2) confirms successful AuPd nanoalloy formation (lattice spacings of 2.31 Å). Line profile analysis further supports the formation of the AuPd nanoalloy (Figure 0-1c).

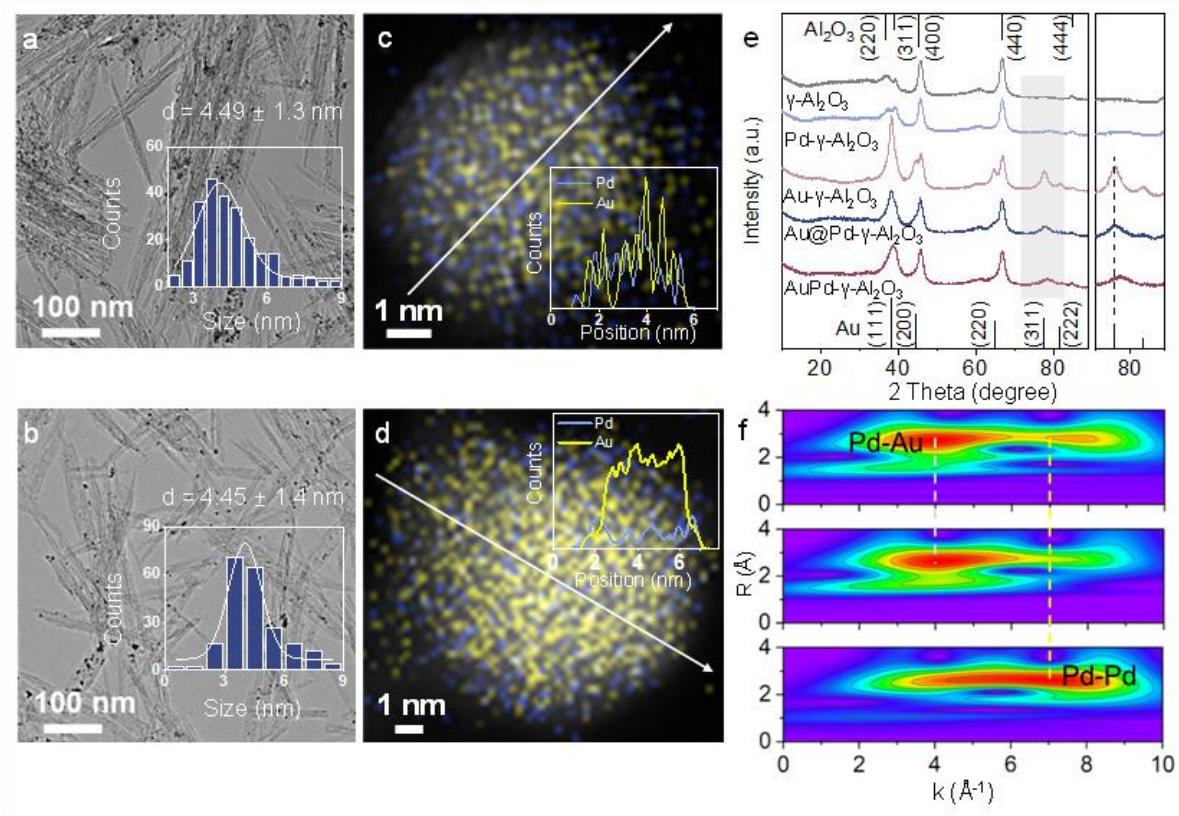

Figure 0-1. (a-b) TEM images of AuPd-γ-Al_2O_3 and Au@Pd-γ-Al_2O_3. (c-d) HAADF images (line-scan inserted) of AuPd-γ-Al_2O_3 and Au@Pd-γ-Al_2O_3. (e) XRD pattern. (f) Wavelet-transform (WT) plots for Pd K-edge of AuPd-γ-Al_2O_3, Au@Pd-γ-Al_2O_3, and Pd foil.

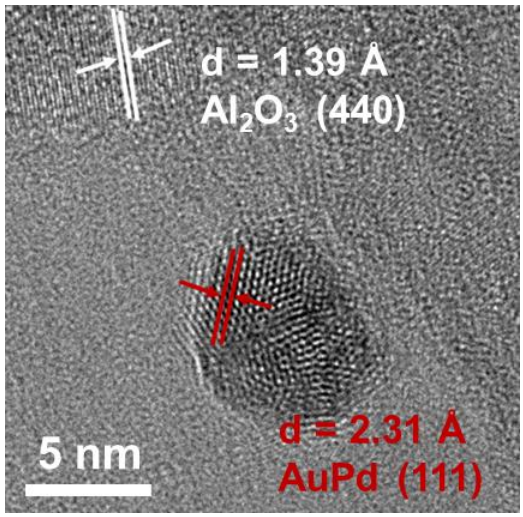

Figure 0-2. HR-TEM of AuPd-γ-Al_2O_3.

In contrast, the scanning transmission electron microscope (STEM) image of Au@Pd-γ-Al_2O_3 reveals surface Pd islands on the Au core (Figure 0-1d), with evident component segregation as shown by high resolution high angle annular dark field STEM (HR-HAADF-STEM) images

(Figure 0-3). Lattice spacings of 2.36 Å and 2.24 Å correspond to the (111) planes of Au and Pd, respectively (Figure 0-4). Component segregation is further evidenced by the line profile of Au@Pd-γ-Al_2O_3 (Figure 0-1d). The Au/Pd ratios were determined through inductively coupled plasma (ICP) measurements for the AuPd nanoalloy, and bimetallic nanoparticles are approximately 1.0 and 0.7, respectively (Table 0-1). X-ray diffraction (XRD) patterns of the AuPd-γ-Al_2O_3, Au@Pd-γ-Al_2O_3, and their monometallic control samples were recorded (Figure 0-1e). Diffraction peaks at 38.01° and 77.28° correspond to the (111) and (311) planes of Au (PDF #04-0784), confirming the presence of nanocrystalline Au. The absence of distinct Pd diffraction peaks suggests the small Pd nanoparticle size in the catalysts. Notably, a positive shift of (311) peak in the AuPd-γ-Al_2O_3 indicates a contracted lattice structure,[241] suggesting that Pd replaces Au[242,243], forming an AuPd alloy.[244]

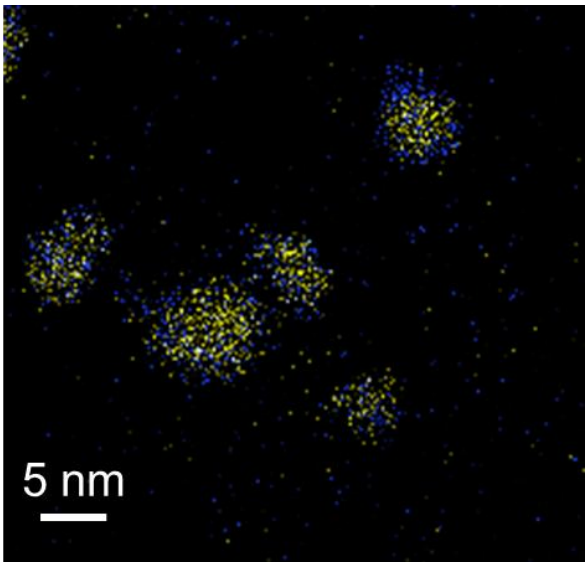

Figure 0-3. Large scale range of HAADF-EDS mapping image of Au@Pd-γ-Al_2O_3 (blue is Pd element and yellow is Au element).

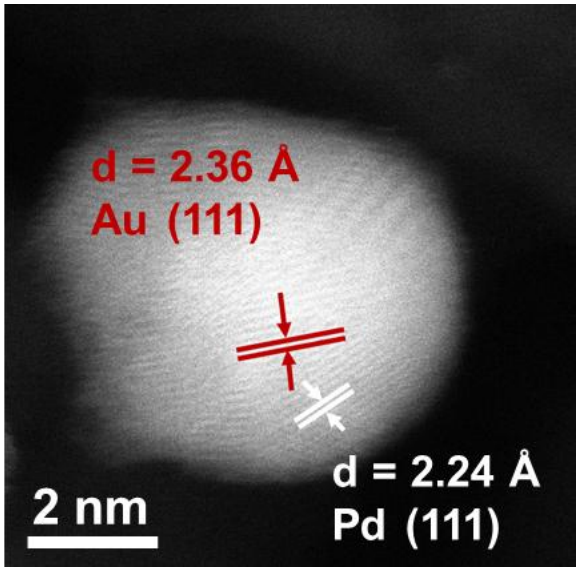

Figure 0-4. HR-STEM of Au@Pd-γ-Al_2O_3.

Table 0-1. Summary of elemental concentration of Au and Pd in different catalysts measured by ICP-OES.

Samples	Au (mol%)	Pd (mol%)
AuPd-γ-Al_2O_3	0.045	0.049
Au@Pd-γ-Al_2O_3	0.032	0.045
Au-γ-Al_2O_3	0.038	/
Pd-γ-Al_2O_3	/	0.049

The X-ray absorption near-edge structure (XANES) reveals a noticeable positive shift in the whiteline edge for both AuPd-γ-Al_2O_3 and Au@Pd-γ-Al_2O_3 compared to Pd foil (Figure 0-5), indicating that both the AuPd nanoalloy and AuPd bimetallic nanoparticles have induced significant alterations in the surface electronic property of the pure Pd lattice.[245,246] Similar shifts at the Au L_3-edge further confirm alloy formation in AuPd-γ-Al_2O_3 (Figure 0-6).[247] Wavelet transform (WT) analysis of the Pd K-edge for Pd foil exhibit maxima at approximately (6.96 $Å^{-1}$, 2.65 Å), representing Pd-Pd scattering (Figure 0-1f). For both AuPd-γ-Al_2O_3 and Au@Pd-γ-Al_2O_3, a new distinct maximum emerged at (3.97 $Å^{-1}$, 2.69 Å), corresponding to the Au-Pd scattering. Particularly, AuPd-γ-Al_2O_3 displays an additional maximum at (7.81 $Å^{-1}$, 2.75 Å), attributed to the alloying effect, which shifted the Pd-Pd scattering maxima. WT

analysis of the Au L_3 edge provides additional confirmation about the AuPd alloy formation (Figure 0-7).[248] The fitting results are shown in

Table 0-2 and

Table 0-3. These XAS results highlight the structural differences between the AuPd nanoalloy and bimetallic Au@Pd, with profound implications for their catalytic behavior, as discussed in subsequent sections. The nanoalloy catalysts, AuPd-γ-Al_2O_3, show a significantly enhanced acetophenone (ACE) conversion (92%) under irradiation with 100 % selectivity for 1-phenylethanol (0.46 mmol) at 21 °C, whereas dark conditions reached only 25% conversion. Au-γ-Al_2O_3 displayed negligible activity, indicating that Au is inactive for the ACE hydrogenation. Pd-γ-Al_2O_3 demonstrated moderate ACE hydrogenation activity, identifying Pd as the active site. Calculating the turnover number (TON) for the catalyst, AuPd-γ-Al_2O_3 showed a remarkably high TON of 2500 under irradiation, 3.7 times higher than that under dark conditions (TON = 679) (Figure 0-8a and

Table 0-4).

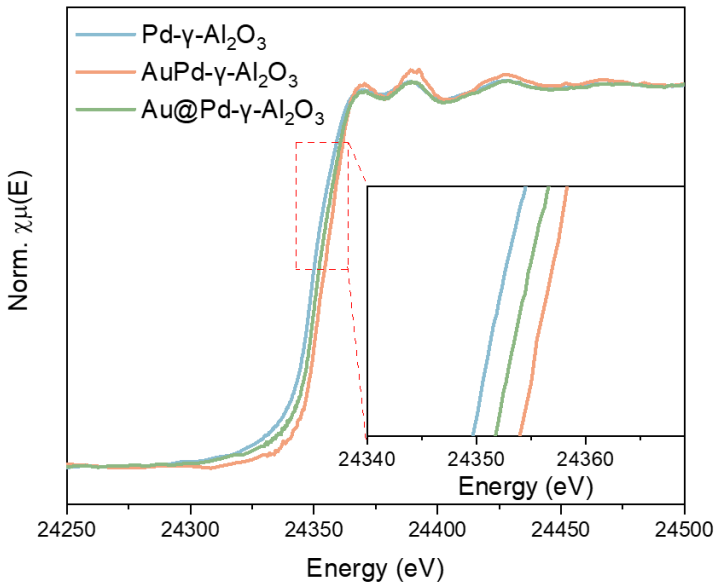

Figure 0-5. Pd K edge XANE spectra of AuPd-γ-Al_2O_3, Au@Pd-γ-Al_2O_3, and Pd-γ-Al_2O_3 catalysts.

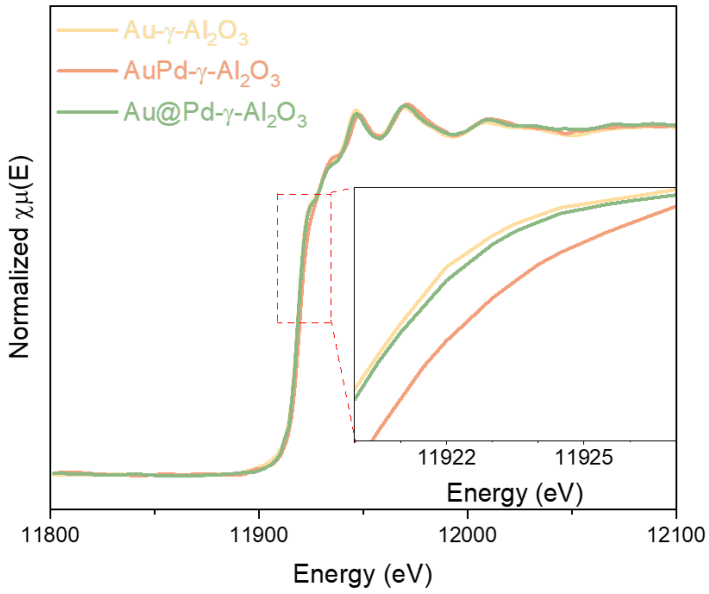

Figure 0-6. Au L_3-edge XANE spectra of AuPd-γ-Al_2O_3, Au@Pd-γ-Al_2O_3, and Au-γ-Al_2O_3 catalysts.

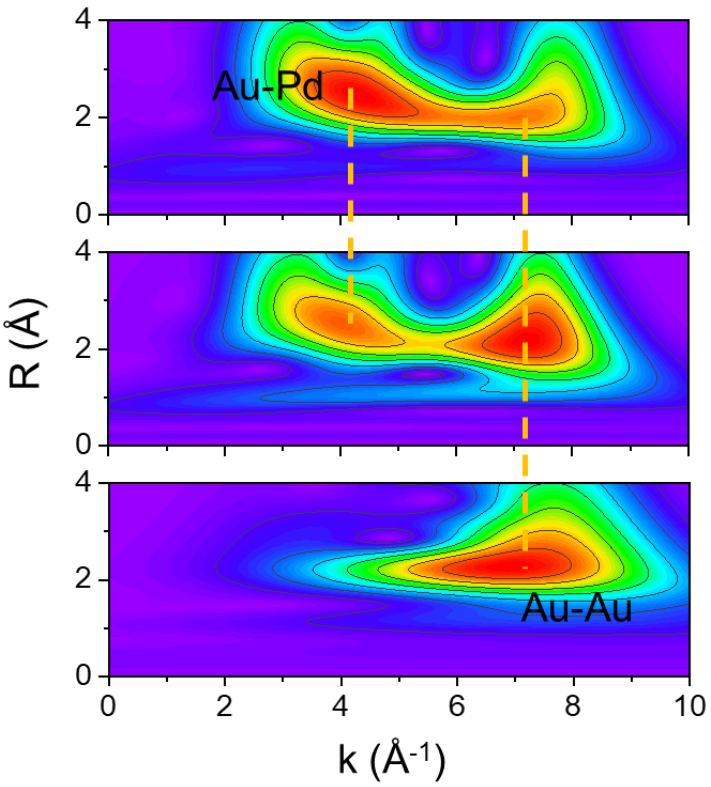

Figure 0-7. Wavelet-transform (WT) plots for Au L_3-edge of AuPd-γ-Al_2O_3, Au@Pd-γ-Al_2O_3, and Au foil.

Table 0-2. Fit results of the $k^3\chi(k)$ spectra at the Pd K-edge of each catalyst and PdO reference.

Catalyst	Bond	N	R (Å)	σ^2	ΔE (eV)	R-factor (%)
AuPd-γ-Al_2O_3	Pd-Pd	4.40±1.85	2.78±0.05	0.016	3.45±1.81	2.3
	Pd-Au	4.42±1.76	2.78±0.03	0.016	3.45±1.81	2.3
Au@Pd-γ-Al_2O_3	Pd-Pd	2.86±1.58	2.73±0.04	0.012	0.92±2.02	2.9
	Pd-Au	1.94±0.94	2.73±0.06	0.012	0.92±2.02	2.9
Pd-γ-Al_2O_3	Pd-Pd	3.28±0.62	2.74 ±0.01	0.017	3.37±1.26	3.3
PdO	Pd-Pd	4.41±0.76	2.02±0.02	0.0004	0.06±2.64	4.8
	Pd-O	6.84±1.45	3.03±0.03	0.0004	0.06±2.64	4.8

Table 0-3. Fit results of the $k^3\chi(k)$ spectra at the Au L_3-edge of each catalyst.

Catalyst	Bond	N	R (Å)	σ^2	ΔE (eV)	R-factor (%)
AuPd-γ-Al_2O_3	Au-Au	7.59±1.84	2.80±0.14	0.008	1.61±1.32	4.6
	Au-Pd	6.49±1.66	3.51±0.43	0.008	1.61±1.32	4.6
Au@Pd-γ-Al_2O_3	Au-Au	5.71±1.27	2.82±0.13	0.006	5.39±0.37	1.1
	Au-Pd	2.49±0.60	3.53±0.41	0.006	5.39±0.37	1.1
Au-γ-Al_2O_3	Au-Au	9.50±1.36	2.85 ±0.09	0.008	4.25±0.79	1.0

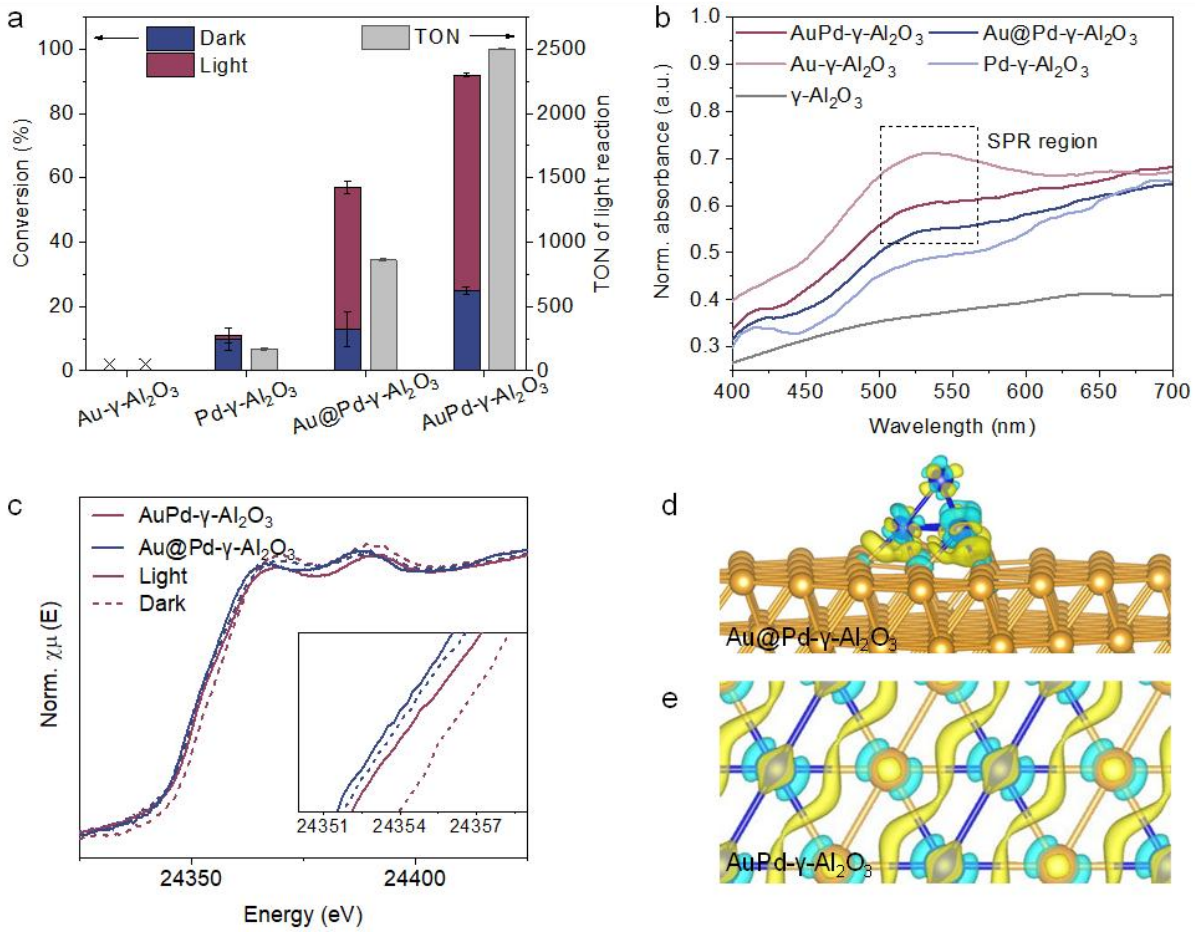

Figure 0-8. (a) Hydrogenation of ACE by different catalysts. Reaction condition: 20 mg catalyst, 0.5 mmol ACE, 10 mL isopropanol (IPA), 3 bar H_2, 4h, light/dark, 20.7±0.6 °C. TON of ACE hydrogenation as a function of irradiation time using various photocatalysts (calculated based on the surface Pd atoms). (b) UV-vis absorption. (c) Pd K edge XANES spectra of AuPd-γ-Al_2O_3 and Au@Pd-γ-Al_2O_3 tested under dark and light conditions. The charge density difference of (d) Au@Pd-γ-Al_2O_3 and (e) AuPd-γ-Al_2O_3 under dark conditions. The charge accumulation and depletion are represented by yellow and cyan colors, respectively. Color code: Pd: blue; Au: orange.

Table 0-4. Amounts of product and TONs for different catalysts in ACE hydrogenation.

Catalyst	Time	Condition	Yield (mmol)	TON
AuPd-γ-Al_2O_3	4 h	Light	0.460	2500
		Dark	0.125	679
Au@Pd-γ-Al_2O_3	4 h	Light	0.285	863
		Dark	0.065	197
Pd-γ-Al_2O_3	4 h	Light	0.055	167
		Dark	0.050	151
Au-γ-Al_2O_3	4 h	Light	0	0
		Dark	0	0

The catalytic activity data demonstrate that the enhanced reaction rate is attributed to the synergistic effect of alloy structure and light excitation. The LSPR effect of the AuPd alloy nanoparticles, induced hot electrons to redistribute Pd sites and enable improved H_2 dissociation since the H_2 dissociation requires electron injection from Au to Pd.[249] The efficiency of hot electron redistribution between Au and Pd sites relies on the extent of Au-Pd interface structures exposed to reactants. AuPd-γ-Al_2O_3 contains abundant homogeneous Au-Pd structures that provide a much more Au-Pd atomic scale interface. In contrast, the Au@Pd-γ-Al_2O_3, where Pd-Pd dominates, as confirmed by HAADF imaging and line profile analysis (Figure 0-1b and Figure 0-1d), has less Au-Pd atomic interface. This explains the comparable conversion of ACE hydrogenation over Au@Pd-γ-Al_2O_3 and Pd-γ-Al_2O_3 (10-13%) under dark conditions, but the enhanced activity of Au@Pd-γ-Al_2O_3 (57%) upon illumination (Figure 0-8a). These results underscore that the homogeneous Au-Pd structure in the nanoalloy is crucial for maximizing photoactivity.

Electron energy-loss spectroscopy (EELS) revealed surface metal composition features in AuPd-γ-Al_2O_3 (Figure S7), showing a 3.7 eV energy loss increase relative to Pd-γ-Al_2O_3 due to unique sp-d electron hybridization in the nanoalloy. Despite Au having a lower work function (5.22 eV) compared to Pd (5.55 eV),[250] a net charge transfer from Pd to Au occurs due to the distinctive sp-d electron hybridization effect in the AuPd alloy.[251,252] Consequently, Pd atoms within the AuPd nanoalloy exhibit an electron-deficient status compared to standalone Pd, necessitating a higher excitation energy.

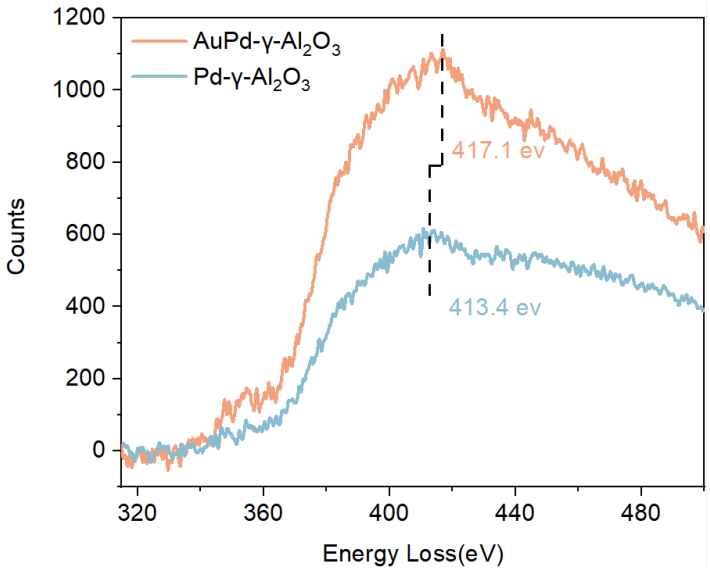

Figure 0-9. Pd M4 edge EELS spectroscopy of AuPd-γ-Al_2O_3 and Pd-γ-Al_2O_3.

Complementing this finding, XANES curves reveal a more pronounced whiteline shift and the increased peak intensity in AuPd-γ-Al_2O_3 compared to Au@Pd-γ-Al_2O_3 (Figure 0-5 and Figure 0-6), signifying its more electron-depleted state.[253-255] This observation suggests that the nanoalloy structure enables a more efficient electron transfer process. X-ray photoelectron spectroscopy (XPS) reveals electronic structure and chemical state differences between AuPd-γ-Al_2O_3 and Au@Pd-γ-Al_2O_3 (Figure 0-10). In comparison to Au-γ-Al_2O_3, the Au 4f core-level spectra show a negative shift of 0.53 eV for AuPd-γ-Al_2O_3 and 0.06 eV for Au@Pd-γ-Al_2O_3, indicating enhanced electron density around Au atoms, with the shift more prominent in AuPd-γ-Al_2O_3.[256,257] Similarly, Pd 3d core-level spectra exhibit positive shifts of 0.43 eV (AuPd-γ-Al_2O_3) and 0.22 eV (Au@Pd-γ-Al_2O_3) compared to Pd-γ-Al_2O_3, suggesting decreased electron density around Pd atoms,[255,258,259] especially in AuPd-γ-Al_2O_3. These findings provide critical insights into the electronic structure and charge distribution in nanoalloy and bimetallic catalysts, clarifying the different roles of Au and Pd in catalytic performance.

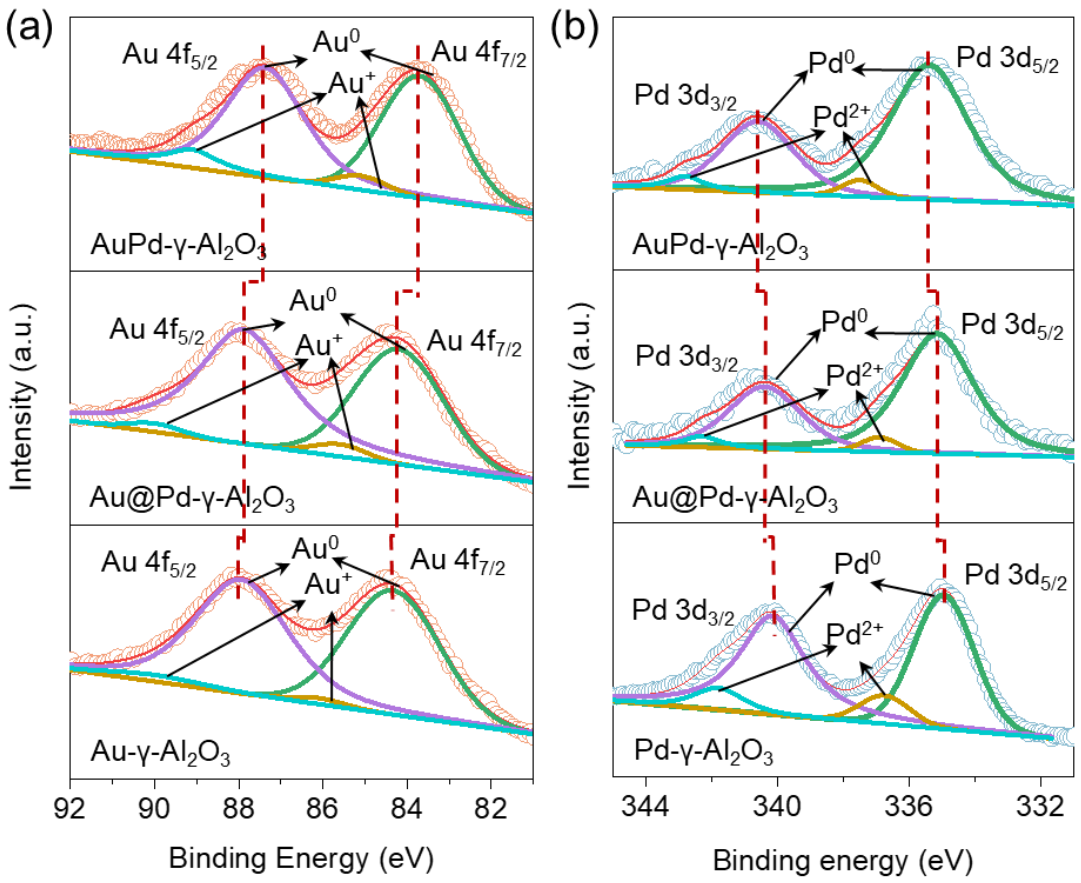

Figure 0-10. (a) Au 4f and (b) Pd 3d XPS spectra of AuPd-γ-Al_2O_3, Au@Pd-γ-Al_2O_3, Pd-γ-Al_2O_3, and Au-γ-Al_2O_3.

UV-vis absorption spectra show that AuPd-γ-Al_2O_3 exhibits apparent SPR-induced light absorption with a slight blue-shift trend, possibly due to the heterogeneous electric field between the Au and Pd.[260,261] However, its SPR peak is weaker than that in Au-γ-Al_2O_3 (around 550 nm), primarily reflecting the microstructure of the AuPd nanoalloy. The SPR peak in Au@Pd-γ-Al_2O_3 is further attenuated, likely due to Pd-induced plasmon damping and uneven Pd distribution, which suppress the plasmon resonance.[262] The support γ-Al_2O_3 shows negligible light absorption,[263,264] while Pd-γ-Al_2O_3 exhibits weak absorption, as Pd lacks a plasmonic effect in the visible light range (Figure 0-8b).[265-267] In contrast, visible light absorption around 550 nm is evident in Au-γ-Al_2O_3, attributable to the SPR effect of Au nanoparticles.[268,269]

Building upon this, we explored the influence of illumination on the surface electron property variation of AuPd-γ-Al_2O_3 and Au@Pd-γ-Al_2O_3 through *in-situ* XAS under light/dark conditions (Figure 0-8c). Under illumination, both AuPd-γ-Al_2O_3 and Au@Pd-γ-Al_2O_3 displayed negatively shifted whiteline edges, indicating increased electron density around Pd

atoms due to hot electrons from Au nanoparticles.[253,254,270] This result indicates that the plasmon effect induced by Au nanoparticles more effectively replenishes Pd atoms with high-energy electrons, attributed to the homogeneous Au-Pd structure within the nanoalloy. This plasmon-induced electron-rich Pd species is expected to enhance the hydrogenation process, as further discussed. Photoluminescence (PL) measurements further support the extensive Au-Pd structure promotes efficient charge transfer (Figure 0-11), consistent with Pd K-edge XANES spectra in Figure 0-8c.

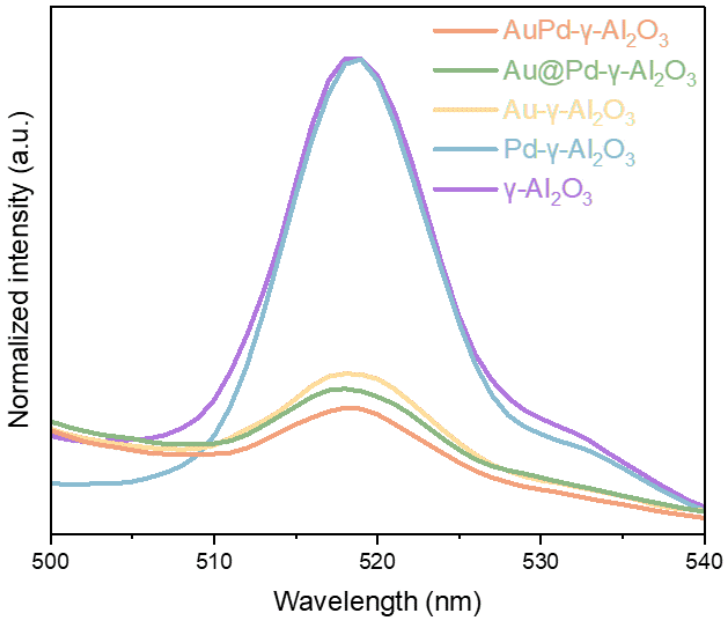

Figure 0-11. PL spectra of AuPd-γ-Al_2O_3, Au@Pd-γ-Al_2O_3, Au-γ-Al_2O_3, Pd-γ-Al_2O_3, and γ-Al_2O_3.

Subsequently, DFT calculations verify the advantages of the homogeneous Au-Pd structure. In comparison to the Au@Pd catalyst, which has fewer electron density Au-Pd structures (Figure 0-8d), the AuPd alloy demonstrates a more uniform and higher electron density distribution at its Au-Pd structures (Figure 0-8e). This enhanced electronic structure facilitates stronger interactions with reactant molecules,[271] thereby explaining the superior performance of the AuPd alloy.

Building on the above observed plasmon-induced electron redistribution at the AuPd nanoalloy surface, we hypothesize that electron-enriched Pd active sites under irradiation could more efficiently activate H_2, thereby enhancing acetophenone (ACE) hydrogenation. *In-situ* XAS was employed under working conditions to study the surface electron property changes of the nanoalloy, bimetallic, and mono-metal catalysts. During the measurement process, the reaction

duration varied from the initial state to 12 min.

Under dark conditions within an H_2-containing isopropanol solution, the Pd K-edge of the AuPd-γ-Al_2O_3 gradually shifted to lower energy (Figure 0-12a), while the Fourier-transformed k^2-weighted extended X-ray absorption fine structure spectroscopy (FT-EXAFS) spectra (Figure 0-12b) revealed an enlarged distance of the Pd-M (M = Pd, Au) interaction, indicating increased electron density near the metal phase. This phenomenon results from ionic interactions and hybridization between Pd antibonding states and unoccupied s and p orbitals of adsorbed hydrogen atoms (Figure 0-12c),[272-274] prompting electron migration from H-atom to the adsorbed M atom (M = Pd, Au), thereby facilitating H_2 dissociation and AuPd-H formation. Given the electronegativity difference between Pd (2.2) and H (2.1),[275-277] electrons are pulled towards Pd, rendering it electron-deficient in H_2-containing isopropanol. Thus, Pd exhibits distinct electron migration behavior compared to thermodynamically equivalent conditions without H_2.

Interestingly, this shifting trend became more pronounced when the catalyst was tested under the same conditions but under illumination (Figure 0-12d). The corresponding FT-EXAFS spectra showed an increased Pd-M (M = Pd, Au) bond distance compared to dark conditions (Figure 0-12e), indicating boosted AuPd-H interaction attributed to plasmonic electron generation/transfer. The LSPR effect of Au generated hot electrons that transferred to adjacent Pd atoms,[278] making Pd electron-rich, which engaged with unoccupied orbitals of adsorbed hydrogen (Figure 0-12f). Consequently, the AuPd nanoalloy exhibited a significantly strengthened AuPd-H interaction driven by plasmon-enhanced surface electron properties.

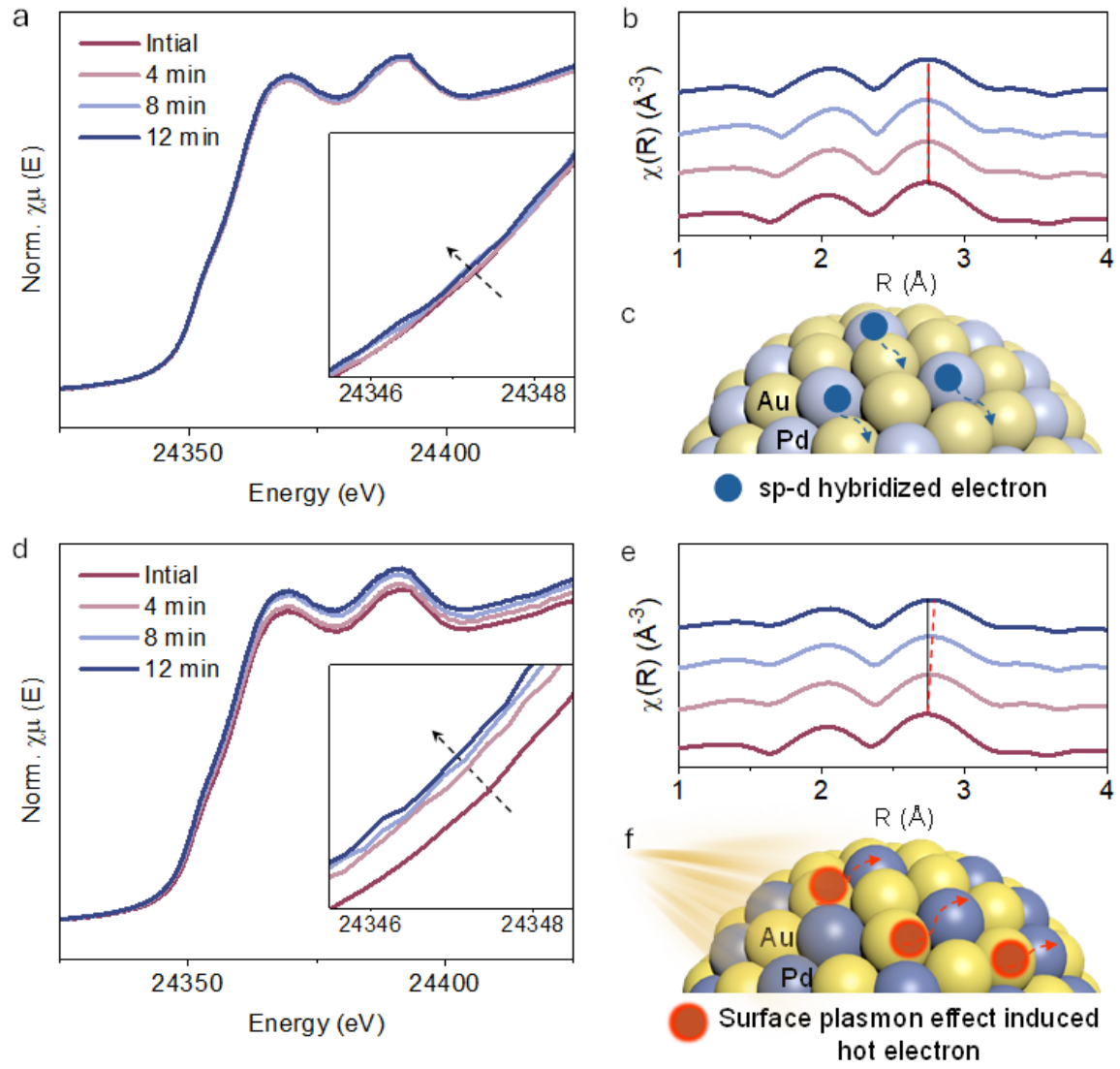

Figure 0-12. *In-situ* Pd K-edge XANE spectra of AuPd-γ-Al_2O_3 in H_2-containing isopropanol under (a) dark and (d) light conditions. FT-EXAFS Pd K-edge spectra of AuPd-γ-Al_2O_3 in H_2-containing isopropanol under (b) light and (e) dark conditions. Schematic illustration of (c) sp-d hybridization effect induced electron transfer process under dark conditions, and (f) the plasmonic effect enhanced surface electron transfer process under illumination conditions.

Upon further adding reactant ACE, the *in-situ* XAS measurement on AuPd-γ-Al_2O_3 revealed a gradual positive shift in the whiteline edge over time (Figure 0-13a), accompanied by a decreased distance for the Pd-M (M = Pd, Au) bond in the FT-EXAFS spectrum (Figure 0-13b). This indicated that the Pd species became electron-deficient as electrons flow from Pd to the C=O bond of ACE upon adsorption (Figure 0-13c). In stark contrast, the spectral shift observed in the absence of H_2 is negligible (Figure 0-14), emphasizing the indispensable role of H_2 in facilitating the adsorption of ACE molecules. This observation was further supported by DFT

simulations, which showed that the oxygen atom in ACE preferentially adsorbs onto AuPd-H (Figure 0-13d and Figure 0-13e). The catalyst exhibited selective adsorption of C=O bonds, enabling efficient electron transfer from Pd to ACE via Pd-O interactions, which was confirmed by WT analysis, revealing a distinct Pd-O interaction peak at (6.01 $Å^{-1}$, 1.32 Å) (Figure 0-13f).

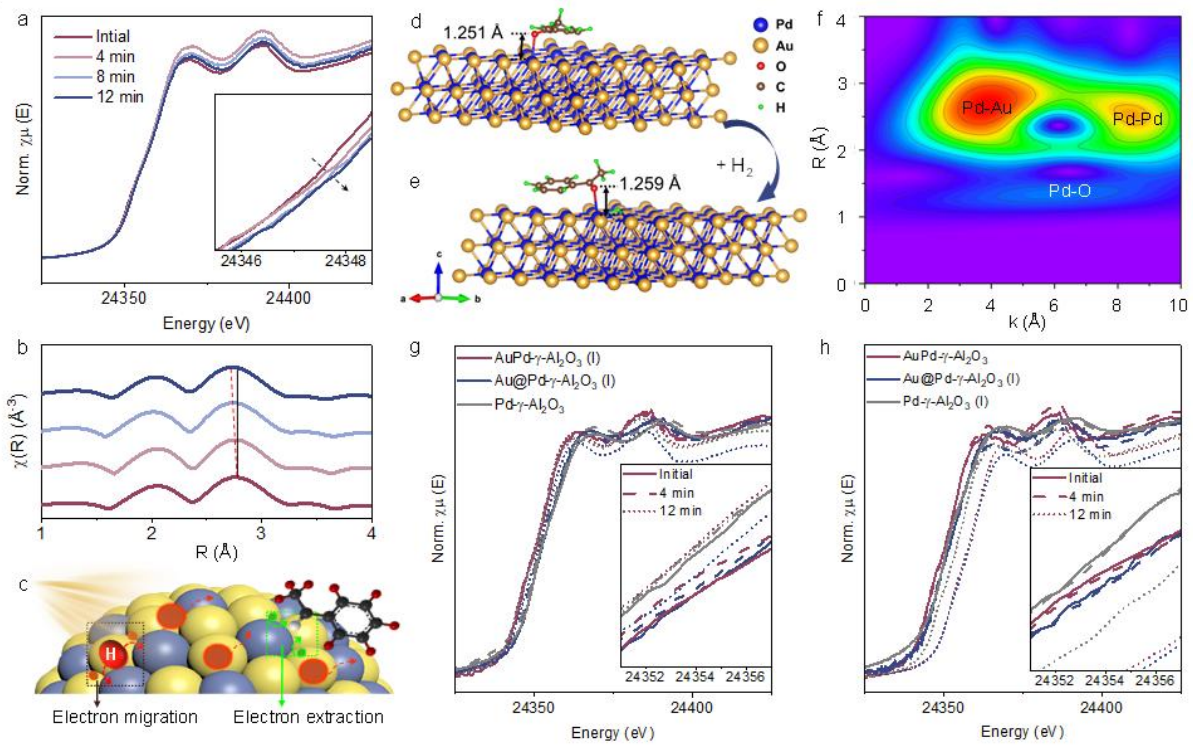

Figure 0-13. (a) *In-situ* Pd K-edge XANE spectra and (b) FT-EXAFS Pd K-edge spectra of AuPd-γ-Al_2O_3 in H_2-containing isopropanol solution with ACE under light conditions. (c) Schematic illustration of the practical electron transfer process under reaction conditions. DFT calculation of ACE adsorbed and C-O bond lengths of adsorbed ACE molecules on AuPd-γ-Al_2O_3 (d) without H atoms adsorbed, and (e) with H atoms adsorbed. (f) WT plots for Pd K-edge of AuPd-γ-Al_2O_3 in H_2-containing isopropanol solution with ACE under light conditions. *In-situ* Pd K-edge XANE spectra of Pd-γ-Al_2O_3, AuPd-γ-Al_2O_3, and Au@Pd-γ-Al_2O_3 in (g) H_2-containing IPA solution, and (h) H_2-containing IPA solution with ACE under light condition at 4 min and 12 min.

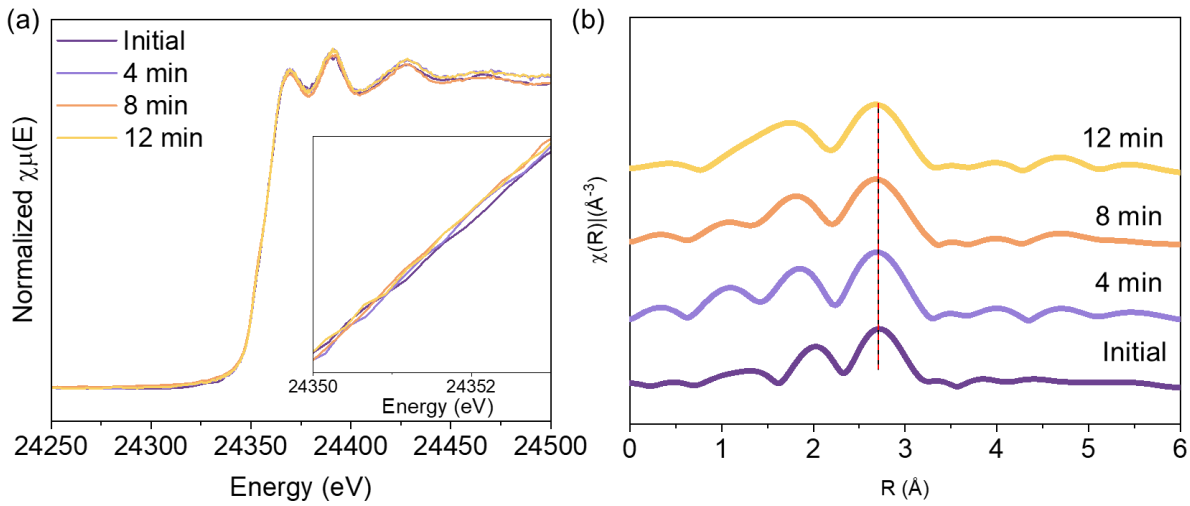

Figure 0-14. (a) *In-situ* Pd K-edge XANE spectra of AuPd-γ-Al_2O_3 under illumination in IPA solution of ACE without H_2. (b) The corresponding Pd K-edge R-space for (a).

Moreover, to compare hydrogenation capability among catalysts with different surface electron properties, the *in-situ* Pd K-edge XANE spectra of Pd-γ-Al_2O_3, AuPd-γ-Al_2O_3, and Au@Pd-γ-Al_2O_3 were recorded during the reaction and at the initial state (Figure 0-13g). Among them, AuPd-γ-Al_2O_3 exhibits the most obvious whiteline shift, highlighting its superior hydrogen adsorption ability. After the introduction of ACE, all catalysts show a positive white line shift, which is attributed to the adsorption of C=O bonds and the Pd-O bonds formation (Figure 0-13h). However, AuPd-γ-Al_2O_3 showed the largest shift, indicating an enhanced interaction with ACE compared to the other catalysts. Notably, the additional Pd K-edge XANES analysis at 12 min revealed a significantly larger shift compared to the shift observed at 4 min, indicating that the plasmon-enhanced electronic properties of AuPd-γ-Al_2O_3 facilitated dynamic electron transfer processes. This Au-Pd structure with high electron density significantly improved hydrogen dissociation promoted the adsorption of C=O bonds in ACE, and led to superior hydrogenation activity and chemoselectivity. These results highlight the critical role of the Au-Pd atomic structure in optimizing catalytic performance, with the AuPd nanoalloy catalyst outperforming bimetallic and mono-metallic catalysts.

The calculated Gibbs free energy on AuPd alloy and single Pd sites further demonstrated that the Au-Pd structure is more favorable for the adsorption of ACE reactants and intermediates (Figure 0-15). The AuPd nanoalloy exhibits significantly lower adsorption enthalpies for intermediates and reduces the energy barrier for the rate-determining step (*$C_6H_5COCH_3$→ *$C_6H_5COHCH_3$), supporting enhanced efficiency for ACE hydrogenation on the AuPd

nanoalloy structure.

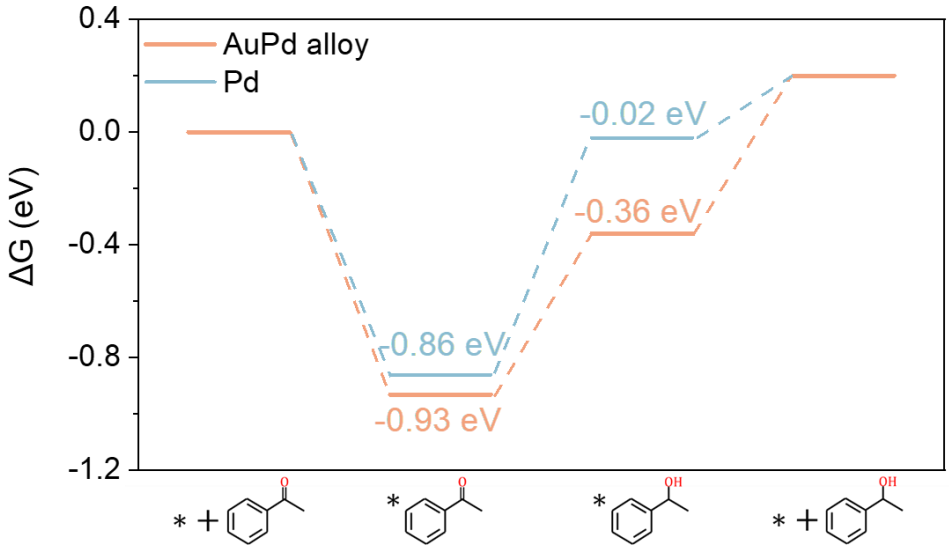

Figure 0-15. Free energy diagram for adsorbed H atoms and ACE hydrogenation to form 1-phenylethanol on the AuPd alloy surface of AuPd-γ-Al_2O_3 catalyst and Pd surface of Pd-γ-Al_2O_3 catalyst.

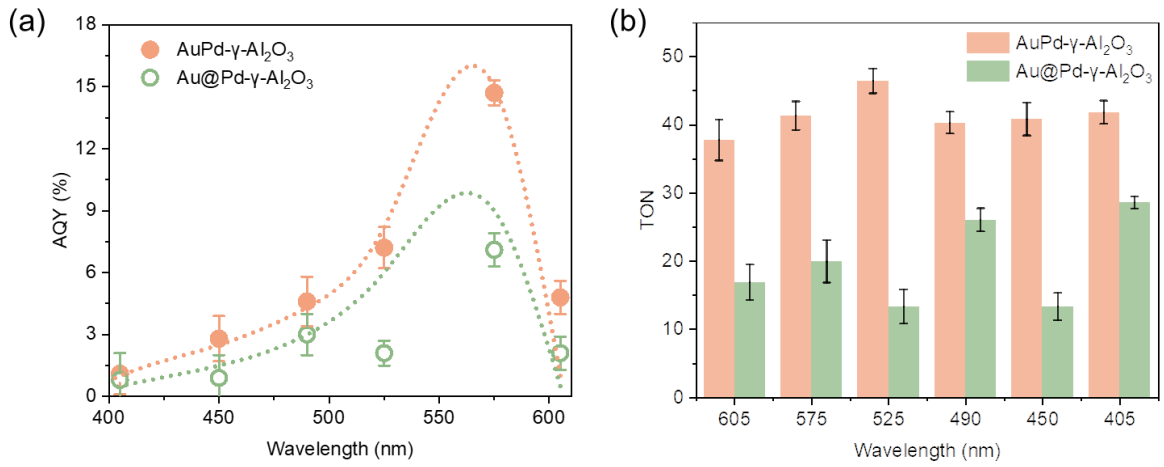

Figure 0-16. (a) Apparent quantum yield (AQY) of AuPd-γ-Al_2O_3 and Au@Pd-γ-Al_2O_3. (b) The corresponding TON of AQY. Reaction condition: 20 mg catalyst, 0.5 mmol ACE, 10 mL IPA, 3 bar H_2, 4 h, light irradiation with different wavelengths, 20.7±0.6 °C.

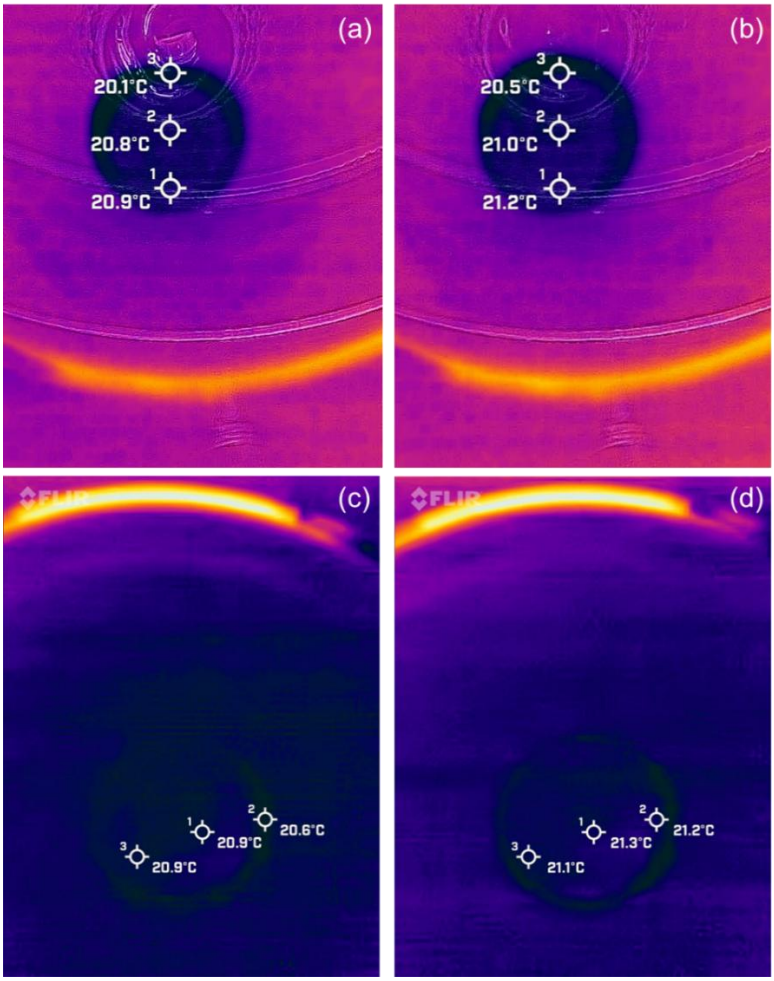

Figure 0-17. Thermal camera images showing the temperature of the reaction mixture after 1 and 4 hours of reaction under light and dark conditions. Figures (a) and (b) show local temperatures after 1h and 4h of reaction under light conditions. Figures (c) and (d) present corresponding temperatures under dark conditions. (20 mg catalyst, 0.5 mmol ACE, 10 mL IPA, 3 bar H_2).

The apparent quantum yield (AQY) efficiencies of AuPd-γ-Al_2O_3 and Au@Pd-γ-Al_2O_3 were assessed (Figure 0-16). TON was calculated at different wavelengths, revealing that AuPd-γ-Al_2O_3 achieved the highest TON of 46.4% at 525 nm, approximately 3.5 times higher than Au@Pd-γ-Al_2O_3. Further studies found that the hydrogenation efficiency under 575 nm irradiation was nearly 3 times greater than at 605 nm. Since the energy input was slightly higher at 650 nm than 575 nm,[279] the results suggest wavelength-sensitive rather than photothermal enhancement. Top thermal imaging of the reaction mixture reveals that the catalytic hydrogenation of ACE at room temperature (20.7±0.6 ºC) is primarily driven by a non-thermal plasmonic effect rather than by a thermal contribution (Figure 0-17).

We investigated the photo-enhanced adsorption of reactants on the catalyst surface through a

light-on/light-off experiment in a mixed solution system, quantitatively analyzing the ketone concentration in the bulk solution via gas chromatography (GC). Our hypothesis posited that light irradiation modulates the interaction between catalyst interfaces and ACE molecules, facilitating adsorption (Figure 5a). Under 30 min of continuous light irradiation, the ketone concentration in the bulk solution decreased from 50 mM to 35.5 mM, reflecting a 30% reduction relative to the initial concentration (Figure 5b). Upon cessation of light exposure, the ketone concentration partially recovered to 42.5 mM, corresponding to 75% of the overall concentration. This reversible concentration change confirms that a significant quantity of ketone molecules adsorbed onto the catalyst surface under illumination and subsequently desorbed into the bulk solution when the light was removed. The observed photoinduced adsorption is attributed to the localized electromagnetic field enhancement generated by AuPd alloy nanoparticles, which facilitates the optical trapping of polar molecules near the catalyst surface. Additionally, the AuPd-H species formation increases surface polarity, introducing localized charge heterogeneity that amplifies the adsorption process. These synergistic mechanisms, electromagnetic field enhancement, and surface polarity modulation simultaneously play a pivotal role in achieving significant and reversible light-enhanced ketone adsorption on AuPd alloy nanoparticles. This indicates that the photo-thermal effect is not the driving force for the enhanced photocatalytic activity.

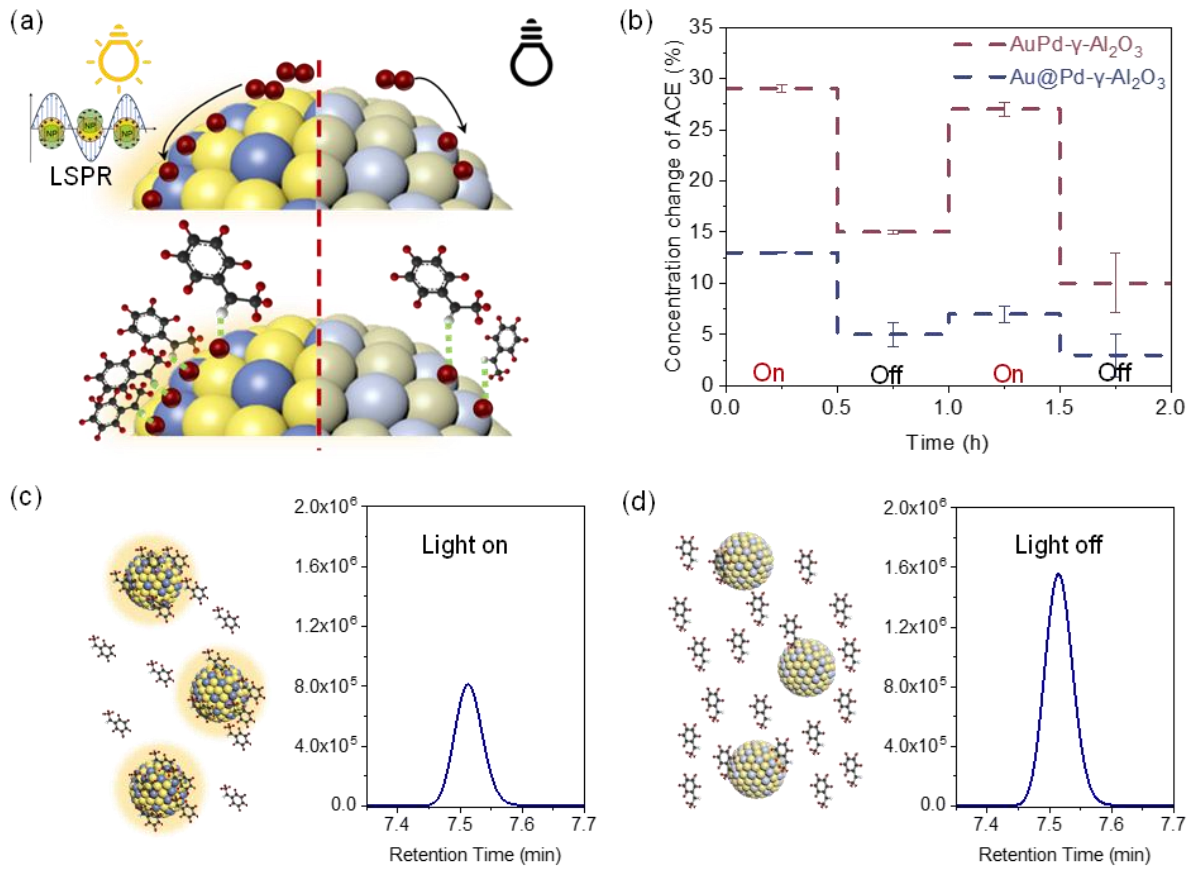

Figure 0-18. (a) Proposed mechanism of ACE hydrogenation over AuPd nanoalloy under visible light/dark conditions. (b) Light irradiation induced reactant concentration change on AuPd nanoalloy in the light-on and light-off cycle. GC results of ACE concentration for (c) 30 min light irradiation and (d) 30 min dark.

AuPd-γ-Al_2O_3 exhibited a more pronounced increase in 1-phenylethanol production under light illumination than Au@Pd-γ-Al_2O_3, indicating a stronger plasmonic enhancement in the AuPd alloy. This enhanced performance is due to the high electron density at the Au-Pd structure, which is more effective in promoting ACE adsorption. In contrast, Au@Pd-γ-Al_2O_3 demonstrated a weaker light-induced adsorption effect, highlighting the superior ability of the AuPd alloy to enhance both the adsorption of reactants and the catalytic activity under light excitation. This emphasizes the enhanced plasmonic properties of the AuPd-γ-Al_2O_3 catalyst, which drives more efficient light-induced adsorption and reaction compared to the bimetallic Au@Pd structure.

In this study, we achieved 100% conversion of acetophenone to 1-phenylethanol under ambient conditions at 20.7±0.6 °C and relatively low H_2 pressure (3 bar). To the best of our knowledge, the performance reported here is comparable to or even better than some of the most recent studies in the field (Figure 0-19 and

Table 0-5).[280-289] The stability of the AuPd-γ-Al_2O_3 catalyst was evaluated over five consecutive ACE hydrogenation cycles, demonstrating negligible activity loss (Figure 0-20). Hot filtration test [290] further confirms the absence of metal leaching for AuPd-γ-Al_2O_3 (Figure 0-21). Post-stability test analyses reveal no phase changes and chemical state variations (Figure 0-22 and Figure 0-23), maintaining structural and compositional integrity throughout cycling (Figure 0-24 to Figure 0-26), highlighting its good stability. Additionally, the AuPd-γ-Al_2O_3 catalyst was tested for other aromatic ketones (

Table 0-6). Light irradiation consistently enhanced conversions for all substrates compared to dark conditions, while selectivity remained 100% under both light and dark conditions.

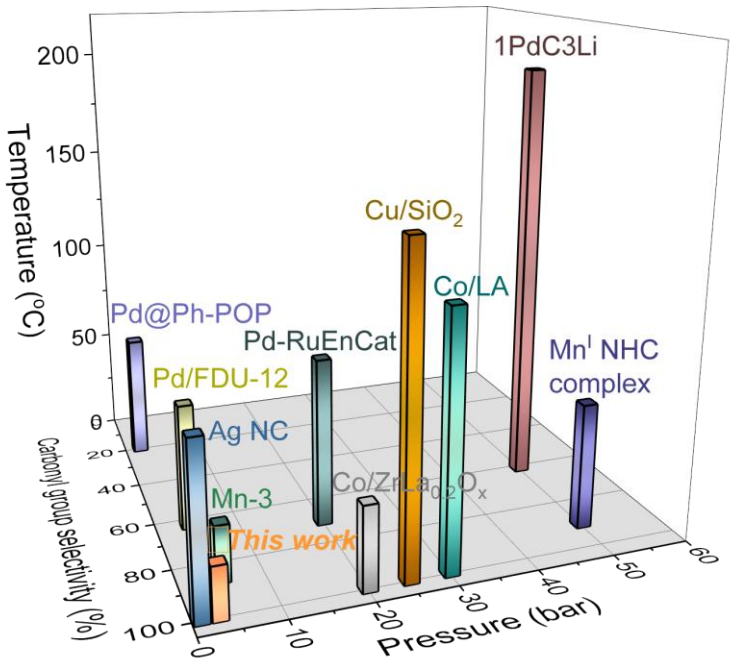

Figure 0-19. Comparison of the reaction temperature, pressure, and carbonyl group selectivity of previously reported ketone hydrogenation reaction and this work.

Table 0-5. Reaction data of heterogeneous Pd-based catalysts, which were reported for the selective carbonyl bond hydrogenation.

Entry[ref]	Catalyst	Conversion % (Selectivity %)	Condition
1[280]	Pd/PPh_3@FDU-12	100 (100)	8×10^{-3} mmol Pd, 0.2 mmol ketone, 2 mL ethanol, 4 bar H_2, 60 °C, 0.5 h.
2[281]	Pd-RuEnCat	97 (71)	20 mg catalyst, 0.05 mol ketone, 20 bar H_2, 80 °C, 4 h.
3[282]	Pd@Ph-POP	100 (≤ 20)	15 mg catalyst, 1 mol ketone, 30 mL isopropanol, 2 bar H_2, 60 °C, 4 h.
4[283]	1PdC3Li	62 (61.6)	20 mg catalyst, 0.2 mL/min ketone, 5 MPa H_2, 200 °C, 8 h.
5[291]	Mn-NHC complex	98(91)	0.1 mol % catalyst, 2.0 mmol ketone, 1.0 mol % base, 2 mL solvent, 50 bar H_2, 60 °C for 20 h.
6[292]	Co/LA	95 (100)	1 mol % Co, 0.25 mmol ketone, 1 mol % Lewis acid in 0.5 mL fluorobenzene,30 bar H_2, 120 °C, 12 h.
7[286]	Ag nanocubes	92 (100)	1 mg catalyst, 1 mmol ketone, 5 mL dioxane, 1 atm H_2, 405 nm (100mW), 80 °C, 24 h.
8[287]	Mn-3	100 (80)	0.01 mmol catalyst, 0.2 mmol ketone, 1 mL MeOH, 30 bar H_2, 0.02 mmol K_3PO_4 base, 50 °C, 20 h.
9[288]	Co/$ZrLa_{0.2}O_x$	100 (100)	50 mg catalyst, 100 mg ketone, 10 mL H_2O, 20 bar H_2, 80 °C, 10 h.
10[289]	Cu/SiO_2	100 (100)	10 mg catalyst, 0.5 mmol ketone, 3 mL toluene, 25 bar H_2, 150 °C, 15 h.
11	**AuPd-γ-Al_2O_3 (this work)**	**92 (100)**	**20 mg catalyst, 0.5 mmol ketone, 10 mL isopropanol, 3 bar H_2, 4h, LED light, 20.7±0.6 °C.**

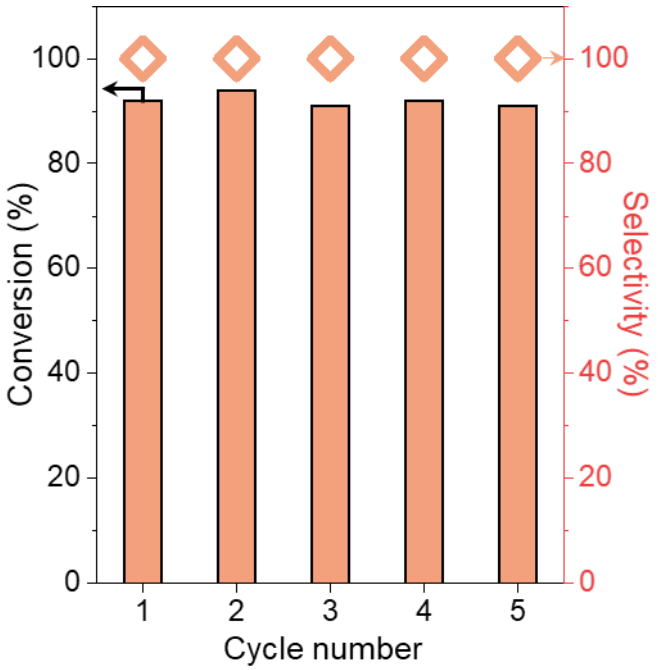

Figure 0-20. ACE hydrogenation cycling test of AuPd-γ-Al_2O_3. Reaction condition: 20 mg catalyst, 0.5 mmol ACE, 10 mL isopropanol (IPA), 3 bar H_2, 4h per cycle, light with full spectrum.

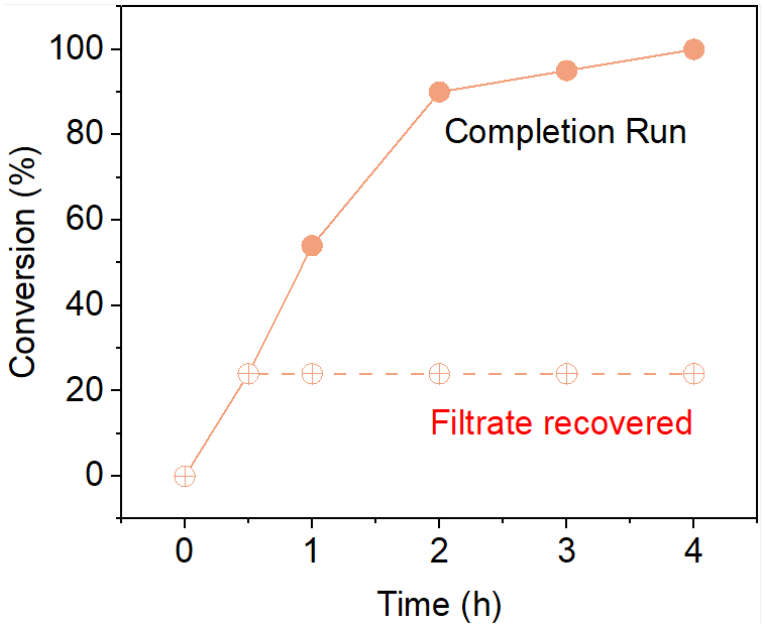

Figure 0-21. Hot filtration test of AuPd-γ-Al_2O_3 catalyst. Reaction conditions: 20 mg catalyst, 0.5 mmol ACE, 10 mL IPA, 3 bar H_2, 4h, light irradiation.

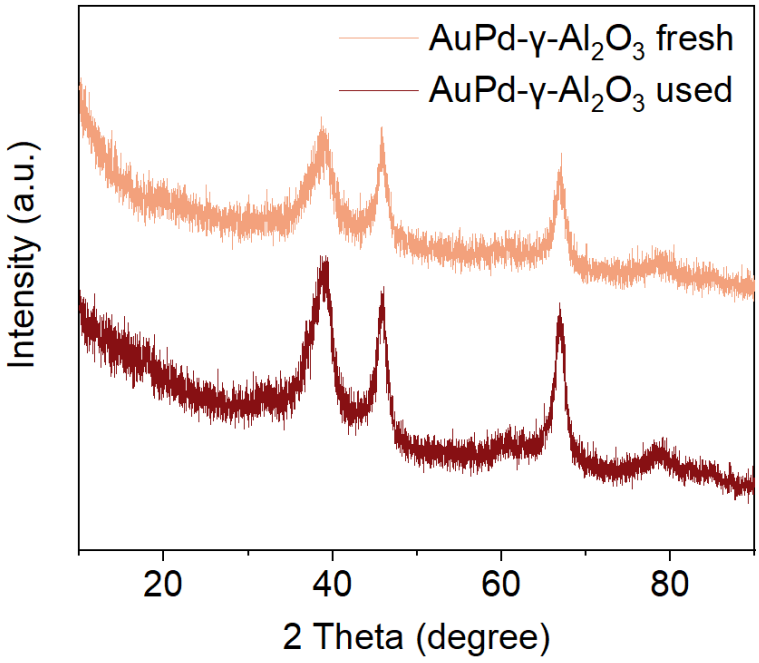

Figure 0-22. XRD pattern of AuPd-γ-Al_2O_3 catalyst before and after hydrogenation reaction.

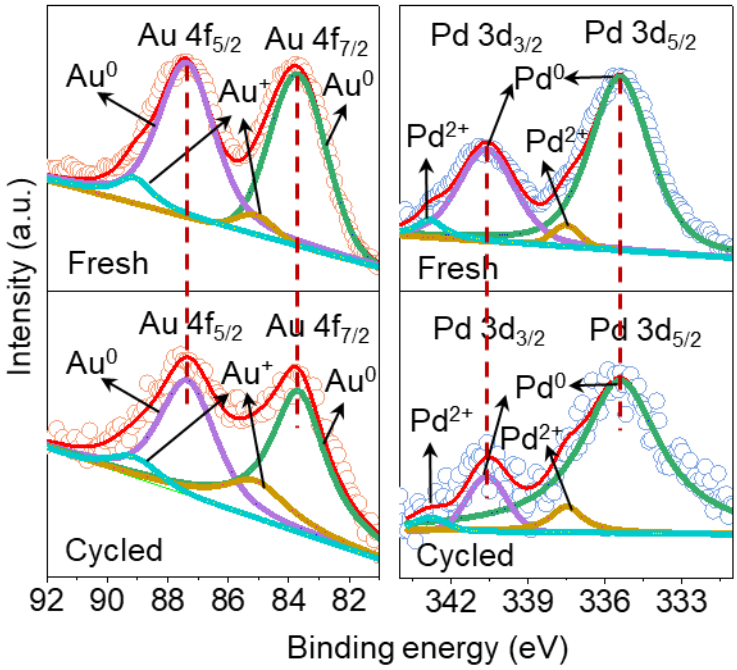

Figure 0-23. The core-level Au 4f and Pd 3s spectra of the fresh and cycled AuPd-γ-Al_2O_3.

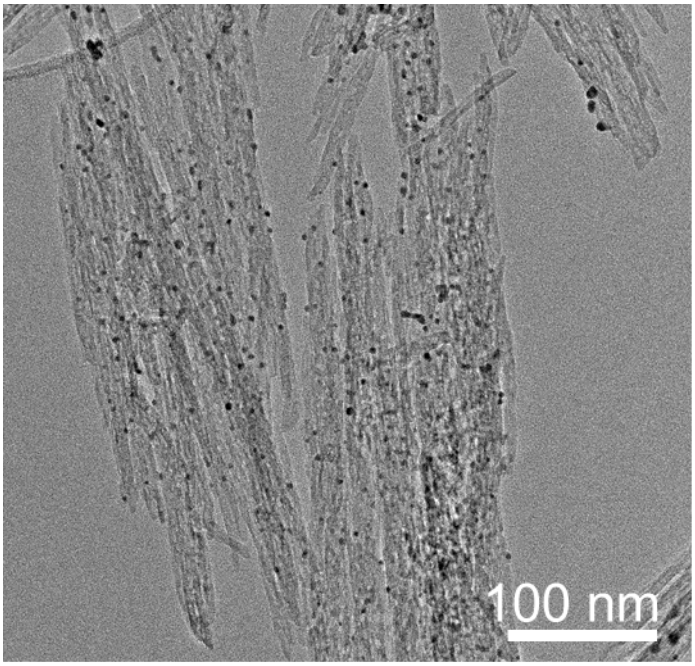

Figure 0-24. TEM image of cycled AuPd-γ-Al_2O_3.

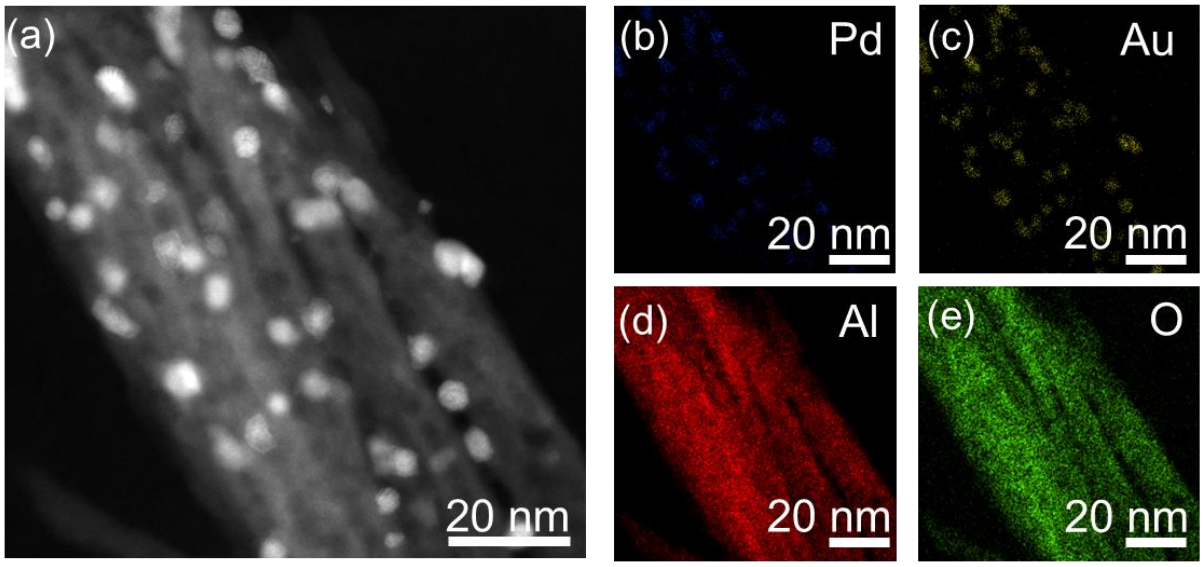

Figure 0-25. (a) HAADF and (b-e) the corresponding elemental mapping images of the cycled AuPd-γ-Al_2O_3.

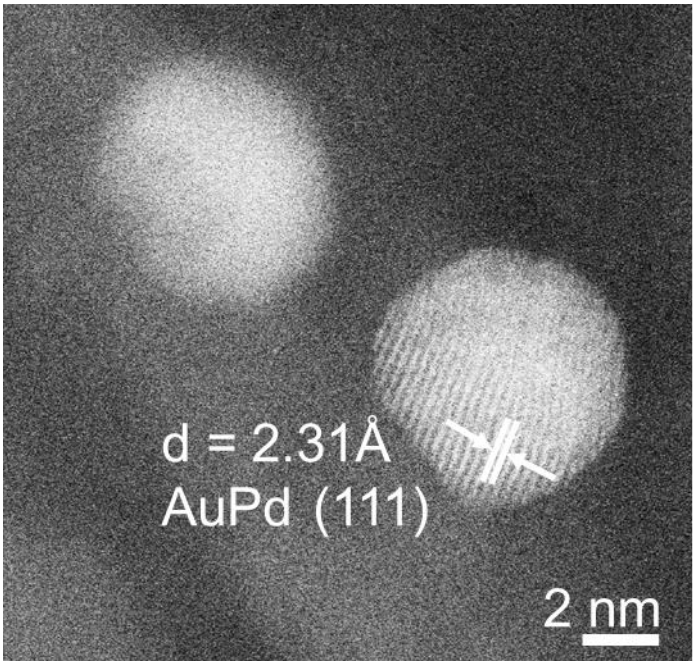

Figure 0-26. HR-HAADF image of the cycled AuPd-γ-Al_2O_3.

Table 0-6. Ketone hydrogenation of AuPd-γ-Al_2O_3 under visible-light irradiation (in red colour) and in the dark (shown in the parentheses).[a]

Entry	Substrates	Products	Time (h)	Conversion (%)	Selectivity (%)
1	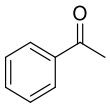	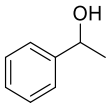	4	92 (25)	100 (100)
2	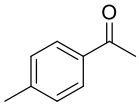	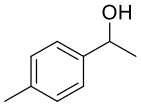	4	98 (69)	100 (100)
3	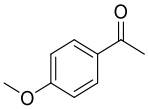	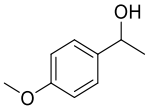	4	91 (57)	100 (100)
4	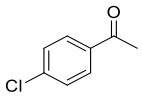	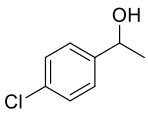	1	93 (58)	100 (100)
5	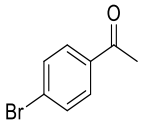	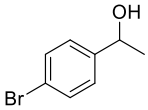	2	97 (63)	100 (100)
6	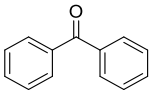	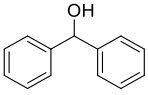	24	94 (32)	100 (100)
7	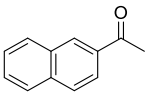	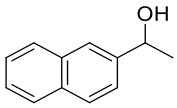	24	51 (13)	100 (100)
8	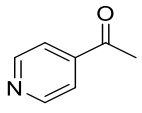	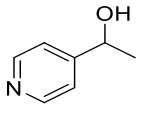	0.67	100 (57)	100 (100)
9		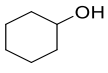	24	41 (9)	100 (100)

10	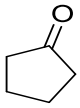	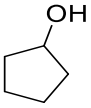	24	31 (2)	100 (100)

[a] Reaction conditions: 20 mg of AuPd-γ-Al_2O_3 catalyst, 0.5 mmol reactants in 10 mL IPA, 3 bar H_2, light/dark.

2.4 Conclusion

In summary, this study unveils a γ-Al_2O_3 supported AuPd nanoalloy catalyst (AuPd-γ-Al_2O_3) that leverages plasmonic-enhanced electron generation and transfer for efficient, chemoselective hydrogenation of unsaturated ketones. Comprehensive spectroscopic analyses reveal that the homogeneous Au-Pd structure of AuPd-γ-Al_2O_3 facilitates significantly more efficient electron transfer compared to bimetallic catalysts (Au@Pd-γ-Al_2O_3), with the LSPR effect of Au nanoparticles enhancing electron migration capabilities. DFT calculations confirm that the enriched electron density within the homogeneous Au-Pd structure is key to its high reaction performance. This research also demonstrates the preferential formation of surface AuPd-H species at the Au-Pd atomic interface, significantly enhanced by plasmon excitation. Consequently, it enables AuPd-γ-Al_2O_3 with a remarkable ability for plasmonic-enhanced hydrogen dissociation, selective adsorption, and activation of C=O bonds in acetophenone, as evidenced by *in-situ* XAS and theoretical calculations. This work underscores the versatility and efficiency of AuPd nanoalloy catalysts in hydrogenating aromatic ketones with excellent conversions and chemoselectivities, advancing sustainable chemical synthesis and offering a model for alloy-based, plasmonic catalyst design in ambient hydrogenation reactions.

Chapter 3 – Unbiased Photoelectrochemical Tandem Reaction for Concurrent Oxidations with Ultra-high Overall Faradaic Efficiency

Abstract

The selective oxidation of biomass-derived compounds remains a critical challenge in sustainable biorefining. With 5-hydroxymethylfurfural (HMF) employed as a model reactant, current solar-driven HMF conversions and efficiencies of single photoelectrode-based photoelectrochemical (PEC) systems are suboptimal. Here, we report an unbiased tandem PEC system that enables concurrent selective oxidation of HMF to 5-hydroxymethyl-2-furancarboxylic acid (HMFCA) at both photoelectrodes, achieving a groundbreaking Faradaic efficiency (FE_{HMFCA}) of 153.4%. The photoanode, composed of NiOOH-modified $BiVO_4$ (BVO), regulates the generation of hydroxyl radicals (·OH) to enhance oxidative reactivity, as demonstrated by ESR spectroscopy. *In-situ* XAS reveals that Ru-doped $CuBi_2O_4$ (CBO) at the photocathode promotes the oxygen reduction reaction (ORR), generating superoxide ($\cdot O_2^-$) that further participates in the selective oxidation of HMF. This synergistic "dual-core processor" mechanism enables the tandem PEC device to achieve a stable photocurrent of 0.68 mA cm^{-2}, with an HMFCA selectivity exceeding 75% for both photoelectrodes. Additionally, a self-powered PEC system driven by solar energy demonstrates industrial scalability, achieving 355.2 mmol m^{-2} HMFCA yield. This work provides foundational insights into the design of highly selective and efficient PEC systems for biomass valorization, setting a new benchmark for carbon-neutral chemical production and industrial scalability.

Keywords: Unbiased, photo-electrochemical tandem device, concurrent selective HMF oxidation, HMFCA, self-powered PEC system

3.1 Introduction

The global pursuit of sustainable energy solutions has underscored the need for carbon-neutral and efficient biomass conversion methods.[293] Biomass oxidation represents a promising route

for producing renewable chemicals and fuels, aligning with global efforts to develop sustainable alternatives to fossil-derived resources. However, achieving selective oxidation of complex biomass substrates presents significant challenges. Conventional oxidation methods often rely on harsh conditions, such as high temperatures and strong oxidants, which limit selectivity and reduce energy efficiency. [294-296]

Electrocatalysis (EC) offers a promising alternative for biomass conversion, often coupling biomass oxidation at the anode with hydrogen evolution (HER) at the cathode to improve energy efficiency over traditional water electrolysis.[297,298] However, solely relying on the anode limits biomass oxidation efficiency. Integrating the cathode to produce value-added chemicals remains challenging, as traditional EC methods typically generate hydrogen peroxide (H_2O_2) via the oxygen reduction reaction (ORR) with inherently slow kinetics.[299] Platinum (Pt) has shown the highest ORR activity[300] but is limited by high cost and scarcity, necessitating alternative materials. Metal-semiconductor cathodes, especially those in photoelectrochemical (PEC) systems, show promise due to their low energy input and environmental benefits.[301,302] In PEC systems, intermediate superoxide radicals ($\cdot O_2^-$) generated during ORR can drive selective biomass oxidation,[303] presenting a compelling strategy for advancing PEC-based biomass conversion.

$CuBi_2O_4$ (CBO), a promising ternary metal oxide, is emerging as an effective photoelectrode material due to its suitable band structure for visible light absorption, stability, and low cost.[304-306] Specifically, the conduction band position of CBO is more negative than the reduction potential of two-electron O_2 to H_2O_2 (0.68 V vs. RHE), suggesting its potential for efficient PEC ORR.[307] Despite these attributes, CBO photocathodes are limited by low carrier separation efficiency and limited selectivity in catalytic product formation. To address these issues, Ru doping (Ru-*x*/CBO, *x*=1, 2, and 3) is explored, leveraging the ORR activity of Ru, comparable to Pt but at a lower cost, to enhance selective biomass oxidation performance by improving ORR kinetics. While photocathodic biomass oxidation has been investigated, coupled anodic simultaneous PEC biomass oxidation remains unexplored. Many biomasses undergo oxidation at potentials lower than that of water oxidation, possibly enhancing PEC performance in onset potential, photocurrent density, and stability.[308] Biomass upgrading could, therefore, be a cost-effective alternative to the PEC oxygen evolution reaction (OER). To realize this potential, we employed NiOOH-modified $BiVO_4$ (NO-*x*/BVO, *x*=1, 2 and 3) as an anodic catalyst,[309] combining excellent light absorption of BVO and stability with improvements of NiOOH in

charge transport and photostability.[310,311] This integrated approach aims to advance sustainable PEC biomass upgrading with enhanced Faradaic efficiency (FE) and overall system performance. The selective oxidation of biomass compounds remains a critical challenge in sustainable biorefining, with 5-hydroxymethylfurfural (HMF) used here as a model reactant due to its importance in producing 5-hydroxymethyl-2-furancarboxylic acid (HMFCA), a key intermediate for biopolymers, pharmaceuticals, and antifungal agents.[312] The aldehyde group (−CHO) in HMF is prone to peroxidation, forming 5-formyl-2-furandicarboxylic acid (FFCA) and 2,5-furandicarboxylic acid (FDCA).

Here, we report for the first time on an unbiased tandem PEC system for concurrent HMF oxidation at both photoelectrodes, integrating Ru-doped CBO (Ru-2/CBO) photocathode and a NiOOH-modified BVO (NO-2/BVO) photoanode in a continuous-flow configuration, effectively minimizing humin formation and maximizing HMFCA yield. Mechanistic investigations using ESR and *in-situ* XAS reveal a synergistic "dual-core processor" mechanism, where hydroxyl radicals (·OH) generated at the NO-2/BVO photoanode and superoxide radicals ($\cdot O_2^-$) generated at the Ru-2/CBO photocathode collectively drive the selective PEC HMF oxidation process. This tandem PEC device demonstrates a stable photocurrent of 0.68 mA cm^{-2}, an ultra-high FE for HMFCA of 153.4%, and selectivity exceeding 75% for HMFCA. Furthermore, a solar-driven, self-powered PEC system showed scalability, achieving an HMFCA yield of 355.2 mmol m^{-2}. This tandem PEC approach holds promising potential for scalable, solar-driven biomass conversion technologies, paving the way for sustainable production of high-value chemicals with enhanced efficiency and selectivity.

3.2 Experimental Section

3.2.1 Materials

The chemicals were used as delivered from the supplier without further purification. 5-Hydroxymethylfurfural (HMF, 99%, 5-Hydroxymethyl-2-furancarboxylic acid (HMFCA, >98%, 2-formyl-5-furancarboxylic acid (FFCA, >98%, 2,5-furandicarboxylic acid (FDCA, 97%, 5,5-Dimethyl-1-Pyrroline-N-Oxide (DMPO, >99%, Bismuth(III) Nitrate pentahydrate ($Bi(NO_3)_3$, ≥99%, and Copper(II) nitrate trihydrate ($Cu(NO_3)_2$, ≥99%, Nickel(II) sulfate ($NiSO_4$, ≥99%, Ammonium metavanadate (NH_4VO_3, ≥99%, Ethylenediaminetetra-acetic acid (EDTA, ≥99%) and potassium hydroxide (KOH, ≥85% were purchased from SIGMA-ALDRICH. 2-Methoxyethanol ($C_3H_8O_2$, ≥99%, and Acetylacetone

($CH_3COCH_2COCH_3$, ≥99%, were from Alfa-Aesar. The fluorine-doped tin oxide conductive (FTO) glasses were thoroughly cleaned with detergent, deionized water, and ethanol.

3.2.2 Synthesis Methods

3.2.2.1 Preparation of $CuBi_2O_4$ (CBO)

The CBO solution was prepared by adding 0.5 mM $Cu(NO_3)_2$ and 1.0 mM $Bi(NO_3)_3$ into an ethylene glycol methyl ether solution successively. The mixture was immediately followed by sonicating and magnetic stirring to obtain a clear, transparent blue solution.

Next, thin-film samples were prepared by spin coating. The specific spin coating steps were as follows: First, a slow-speed spin coating process was carried out. The films were then transferred to a heating plate at 350 °C to pyrolyze for 10 min. After the spin coating, all samples were annealed at 500 °C for 1 h with a ramp of 5 °C/min.

3.2.2.2 Preparation of CBO supported Ru (Ru-*x*/CBO, *x*=1, 2 and 3)

In the photo-deposition session, CBO was dispersed into the liquid mixture of water and isopropanol. Then, a proper amount of 3 mg $RuCl_3$ was added to the solution. The resultant slurry was irradiated by lamp under vigorous stirring for 20 min, 40 min, and 60 min, which is denoted as Ru-*x*/CBO (*x*=1, 2, and 3), respectively.

3.2.2.3 Preparation of $BiVO_4$ (BVO)

1 mmol $Bi(NO_3)_3 \cdot 5H_2O$ and 1.5 mmol EDTA were dissolved in 15 mL deionized water, and under rapid stirring 1 mL of ammonia water was added. This solution was rigorously mixed with another solution prepared by dissolving 1 mmol NH_4VO_3 and 0.5 mmol EDTA in 15 ml deionized water to which 1 mL of ammonia water was added under rapid stirring. Mixing of these two solutions yielded the precursor solution for spin-coating on FTO glass.

0.3 mmol of $Bi(NO_3)_3 \cdot 5H_2O$ and 0.45 mmol of EDTA were dissolved in 30 mL deionized water. Then, 0.75 mL of a 2 M NaOH solution was added under rapid stirring until the solution became clear and transparent. Then 0.3 mmol of ammonium metavanadate was added to this solution. This precursor solution was transferred to a 50 mL Teflon-lined autoclave heated to 180 ºC for 6 h and then calcined at 500 °C for 4 h.

3.2.2.4 Preparation of BVO supported NiOOH (NO-*x*/BVO, *x*=1, 2 and 3)

The electrodeposition of NiOOH on the BVO electrode was carried out in the NiOOH plating

solution containing 0.13 M $NiSO_4$ and 0.2 M Na_2SO_4 solution while gently stirring. An applied potential of 0.8 V, 1.0 V, and 1.2 V was applied to the deposition. As prepared samples were denoted as NO-*x*/BVO (*x*=1, 2 and 3), respectively.

3.2.3 Photoelectrocatalysis HMF oxidation

For the photoelectrocatalysis, the hydroxymethylfurfural (HMF) oxidation reactions were carried out in a H-cell and operated at the electrochemical workstation (CHI660E). Typically, the working HMF oxidation performance of the catalyst under the Xe light source was tested using a three-electrode system, including Ru-*x*/CBO and NO-*x*/BVO working electrode, Pt sheet counter electrode, and Ag/AgCl (saturated potassium chloride electrolyte) reference electrode. A 300 W Xenon lamp was used to simulate the solar light. Linear sweep voltammograms (LSV) at 0.1 V s^{-1} and transient response under chopped light were carried out. Mott-Schottky (MS) plots were tested at 1000 Hz.

According to the MS curves, the charge carrier density (N_d) can be calculated using the following equation:

$$N_d = \frac{2}{e\varepsilon_0\varepsilon} \times \left(\frac{d\left(\frac{1}{C^2}\right)}{dV_s} \right)^{-1} \qquad \text{(Equation 3.1)}$$

The electronic charge (e) is 1.6×10^{-19} C, vacuum permittivity (ε_0) is 8.86×10^{-14} F m^{-1}, and relative permittivity (ε) is 68 for BVO.[313] C (F cm^{-2}) is the space charge capacitance in the semiconductor (obtained from MS curves), and Vs (V) is the applied potential for MS curves.

All the potentials versus reversible hydrogen potential (vs. RHE) were converted from the potentials versus Ag/AgCl according to the Nernst equation:

$$E_{RHE} = E_{Ag/AgCl} + 0.059\ pH + 0.197 \qquad \text{(Equation 3.2)}$$

where E_{RHE} refers to the converted potential versus reversible hydrogen potential. $E_{Ag/AgCl}$ is the obtained potential versus Ag/AgCl, and pH is the pH value of the electrolyte.

The ABPE can be calculated by the photocurrent-potential curves under simulated sunlight using the equation:

$$ABPE\ (\%) = [(1.23 - V) \times J / P_{light}] \times 100\% \qquad \text{(Equation 3.3)}$$

where V is the applied potential, J is the photocurrent density (mA cm^{-2}), and P_{light} is the power density of a 300 W Xe lamp.

The IPCE was obtained using a monochromator coupled with a 300 W Xe lamp as the simulated light source. An applied potential of 1.23 V vs. RHE was supplied by a CHI660e electrochemical workstation, and the power density at a specific wavelength was measured by a Newport power meter. IPCE values were calculated using the following equation:

$$IPCE\ (\%) = [1240 \times J_{light} / \lambda \times P_{light}] \times 100\% \qquad \text{(Equation 3.4)}$$

where J_{light} is the photocurrent density (mA cm^{-2}) obtained from the electrochemical workstation, λ is the wavelength (nm) of incident radiation, and P_{light} is the power density obtained at a specific wavelength (mW cm^{-2}).

3.2.4 Product analysis

The continuous HMF oxidation was conducted at constant potential under light illumination in 1 M KOH and 10 mM HMF. The concentration of HMF and its oxidation products were analyzed by high-performance liquid chromatography (HPLC, Shimazu LC-20AD) equipped with a C18 column and SPD detector. The eluent was a mixture of 5 mM ammonium acetate and methanol at a flow rate of 0.6 mL min^{-1}. The following equations (3.5-3.7) were applied to calculate the selectivity (Sel.) of HMF oxidation products, yield of oxidation products, and the Faradaic efficiency (FE):

$$\text{Yield} = \frac{moles\ of\ oxidation\ product}{moles\ of\ initial\ HMF} \times 100\% \qquad \text{(Equation 3.5)}$$

$$\text{Sel.} = \frac{moles\ of\ oxidation\ product}{moles\ of\ HMF\ reacted} \times 100\% \qquad \text{(Equation 3.6)}$$

$$\text{FE} = \frac{moles\ of\ oxidation\ product \times n}{total\ passed\ charge/F} \times 100\% \qquad \text{(Equation 3.7)}$$

where F is the Faraday constant (96,485 C mol^{-1}).

3.2.5 Characterization

Transmission electron microscopy (TEM) data were recorded with a JEOL 2200FS and a Zeiss Sigma VP HD instrument. The high-resolution transmission electron microscopy (HRTEM) and high-angle annular dark-field scanning transmission microscopy (HAADF-STEM) images

of the samples were acquired using an FEI Themis Z instrument equipped with a double spherical aberration corrector operating at 300 kV. During the test, the acceleration high tension of the incident electron beam was 300 kV. X-ray diffraction (XRD) measurements were recorded on a Rigaku D max-3C diffractometer using Cu Kα radiation (40 kV, 20 mA, λ = 0.15408 nm). X-ray photoelectron spectroscopy (XPS) measurements were performed using a Thermo Fisher ESCALAB 250Xi spectrometer with a focus monochromatic Al Kα-ray (1486.6 eV) source. The samples were tested under a vacuum below 5.0×10^{-10} Mbar, and energy resolution spectra were collected using a pass energy of 20 eV. Peak fitting of the high-resolution data was carried out by Thermo Avantage 5.976 surface chemical analysis software. The Solid-state UV–vis absorption spectra of the samples were measured on a SHIMADZU UV-3600i PLUS Spectrophotometer. X-ray absorption spectroscopy (XAS) was carried out at the XAS beamline of Australian Synchrotron, ANSTO, and processed with the Athena program.[235] These powder samples were all probed by the Ru K-edge (22127 eV). XAS was conducted in transmission mode at room temperature, with simultaneous measurements of Ru foil as reference materials for each scan.

3.2.6 DFT calculations

The spin-polarized density functional theory (DFT) calculations[314] were performed as implemented in the Vienna ab initio simulation package (VASP).[236] The DFT-D3 scheme of Grimme was adopted for describing van der Waals (vdW) interactions.[315] Projector-augmented wave (PAW) pseudopotentials were used to model the valence states and the interactions between core and valence electrons.[316] The Perdew-Burke-Ernzerhof (PBE)[317] form of the generalized gradient approximation (GGA) was employed for describing the exchange and correlation function, and the spin-orbit coupling (SOC) was included. Plane-wave functions were expanded with an energy cutoff of 600 eV, and the Brillouin zone was sampled using a Monkhorst–Pack sampling of 8 × 8 × 8 k-point grid. All the geometries were fully relaxed until the forces on each atom were less than 0.005 eV/Å.

3.3 Results

3.3.1 Tandem PEC-System for Biomass Oxidation

Developing highly efficient, scalable solar-driven chemical processes is one of the most pressing challenges in transitioning to renewable energy sources. Conventional PEC systems often require external bias, reducing energy efficiency and increasing costs. Here, we present

an alternative approach, employing an unbiased tandem PEC system for HMF oxidation, utilizing a Ru-2/CBO photocathode directly wired with a NO-2/BVO photoanode. This device first achieves complete HMF oxidation by harnessing both photoanode and photocathode, operating through a synergistic "dual-core processor" mechanism, where each photoelectrode performs a distinct, yet complementary function to maximize efficiency and selectivity. As shown schematically in Figure 0-1a (photos in Figure 0-2), the device exhibits overlapping anodic and cathodic photocurrents with an intersecting potential of 0.89 V vs. RHE, confirming efficient, bias-free operation (Figure 0-1b). Under illumination, a stable photocurrent density of 0.68 mA cm^{-2} was maintained over 1800 s (Figure 0-3), yielding 168.9 mmol cm^{-2} and 159.0 mmol cm^{-2} of HMFCA at the photocathode and photoanode, respectively (Figure 0-1c, left part). The Faradic efficiencies for HMFCA production (FE_{HMFCA}) are nearly 153.4% during overall HMF oxidation, which is accompanied by an HMFCA selectivity ($Sel._{HMFCA}$) of 75.2% and 76.1% for photocathode and photoanode, respectively (Figure 0-1d, left part). In addition, we aim to implement a self-powered PEC system for HMF oxidation entirely driven by solar energy. Given that the necessary bias voltage could be readily supplied by solar panels, we constructed a practical setup to evaluate the performance of the self-powered PEC HMF oxidation system with a dual-electrode configuration. The system incorporated a solar panel (~1.25 V) to provide a constant bias voltage and featured a continuous-flow PEC H-cell (Figure 0-4). A step-down transformer first reduces the electricity generated by the solar panel and then converts it to direct current through full-wave rectification. The positive electrode of the inverter is connected to the NO-2/BVO photoanode, while the negative electrode is linked to the Ru-2/CBO photocathode. As shown in Figure 0-1c and Figure 0-1d (right part), after 1800 s of PEC HMF oxidation, the Ru-2/CBO photocathode achieved an HMFCA yield of 171.4 mmol cm^{-2} (Sel_{HMFCA}=73.4%) with a FE_{HMFCA} of 73.5%. Meanwhile, the NO-2/BVO photoanode system produced an HMFCA yield of 183.8 mmol cm^{-2} (Sel_{HMFCA}=78.2%) with a FE_{HMFCA} of 78.8%. Figure 0-1e and Figure 0-5 illustrate the equivalent circuit and schematic diagram of the self-powered PEC HMF oxidation system, which utilized a NO-2/BVO photoanode and a Ru-2/CBO photocathode. This self-powered PEC strategy highlights a viable pathway for efficient and selective HMFCA production at both electrodes, demonstrating the substantial potential for solar-driven biomass conversion.

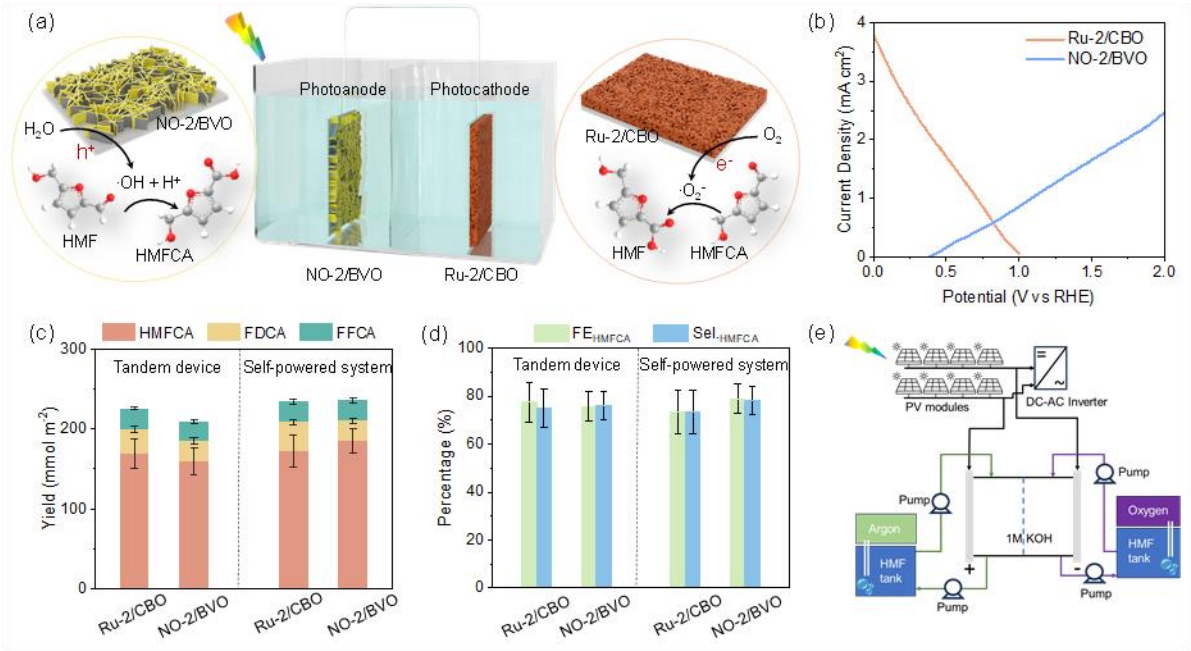

Figure 0-1. (a) Schematic illustration of the tandem HMF oxidation device comprised of the Ru-2/CBO photocathode and the NO-2/BVO photoanode, (b) LSV plots of the Ru-2/CBO photocathode and the NO-2/BVO photoanode under illumination in 1 M KOH electrolyte with 10 mM HMF (pH = 13). (c) The yield of the tandem HMF oxidation device (left part) and the yield of the self-powered system (right part) for Ru-2/CBO photocathode and NO-2/BVO photoanode. (d) The FE_{HMFCA} and $Sel._{HMFCA}$ of tandem HMF oxidation device (left) and self-powered system (right part) for Ru-2/CBO photocathode and NO-2/BVO photoanode. (e) Equivalent circuit of the self-powered PEC HMF oxidation system. Reaction conditions: 1 M KOH electrolyte with 10 mM HMF (pH = 13) under illumination with a flow rate of 10 mL min^{-1}.

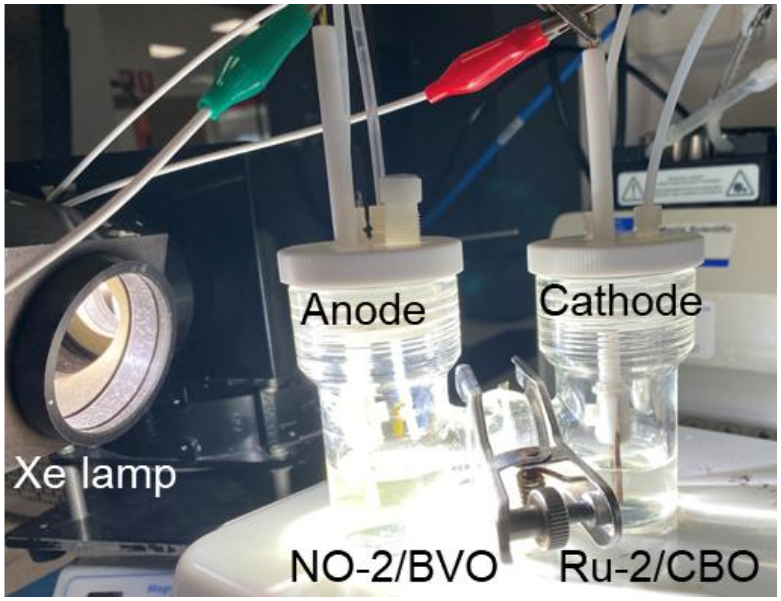

Figure 0-2. Photograph of tandem HMF oxidation device.

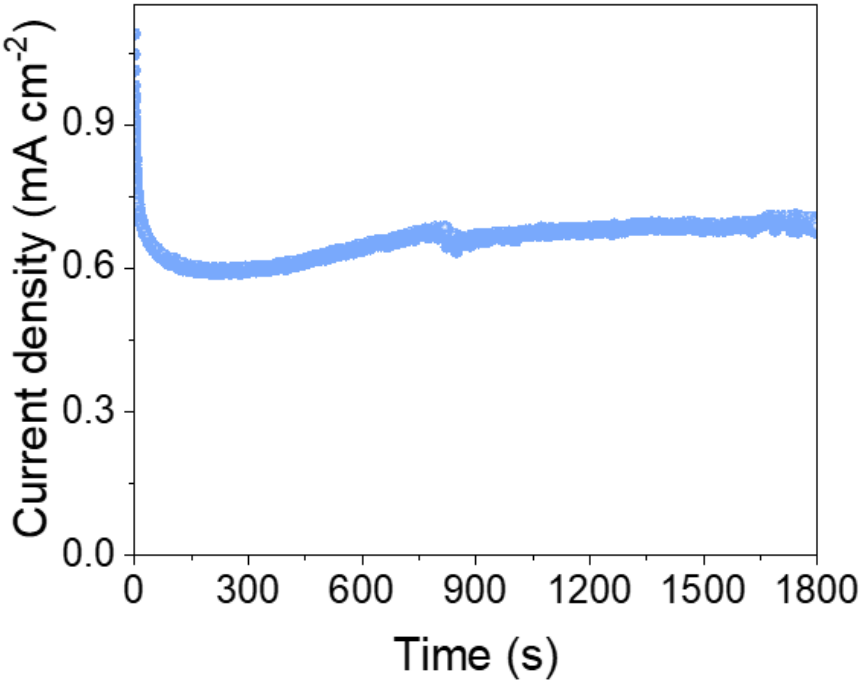

Figure 0-3. Long-term I–t curve of the tandem device.

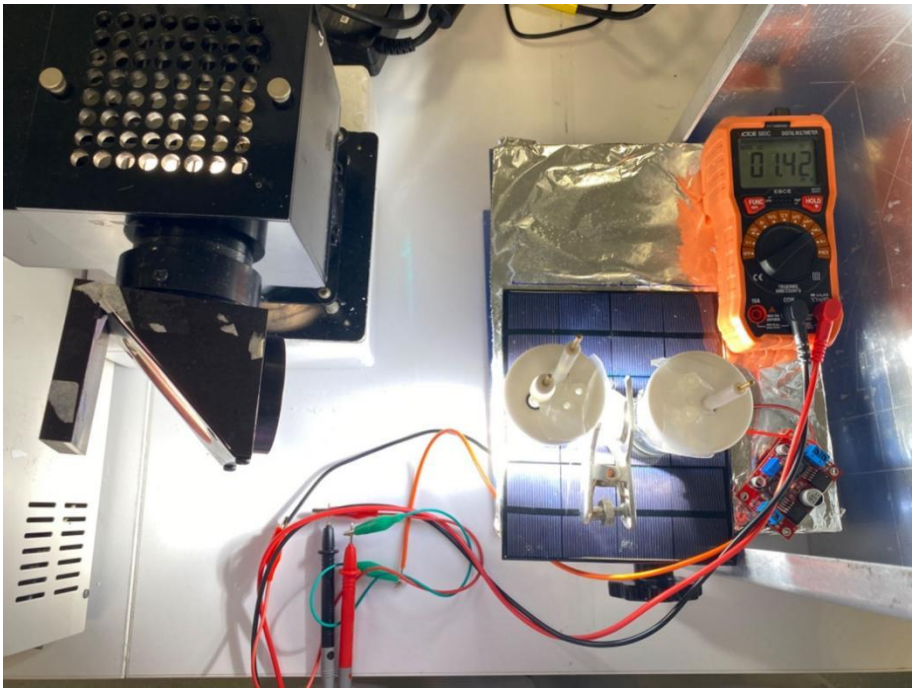

Figure 0-4. The corresponding current through the self-powered PEC HMF oxidation when using the 1.25 V solar panel.

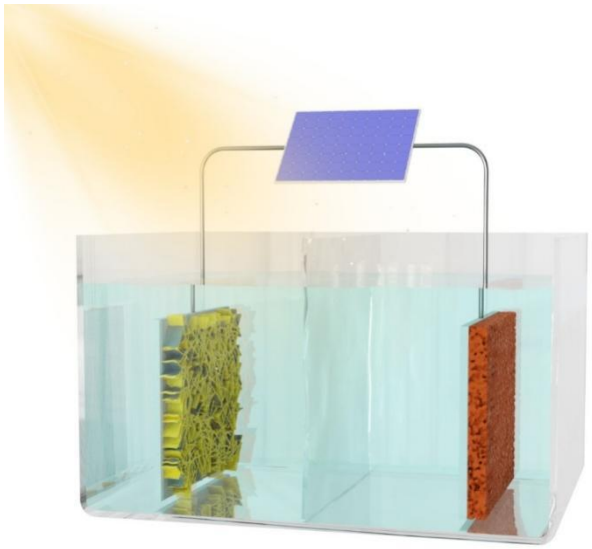

Figure 0-5. Schematic illustration of the self-powered PEC system equipped with a solar panel (~1.25 V) for HMF oxidation.

3.3.2 Ru-doped CBO ($CuBi_2O_4$) photocathodes

We first study the photocathode of Ru-doped CBO. A schematic representation of the fabrication of the CBO photocathode using an evaporation decomposition-controlled method is shown in Figure S5.[318] Ru/CBO was prepared by photo-deposition accompanied by Ru incorporation into CBO. Different Ru contents were obtained by deposition for specific times (20, 40, and 60 min), yielding samples denoted Ru-*x*/CBO (*x*=1, 2, and 3).

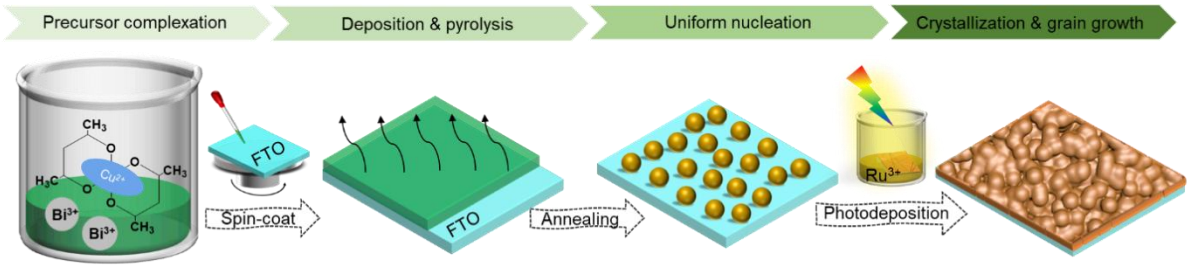

Figure 0-6. Synthesis scheme of Ru-*x*/CBO (*x*=1, 2 and 3).

The cross-sectional SEM image of Ru-2/CBO films in Figure 0-7a revealed a polycrystalline porous morphology with a thickness of around 4 μm, consistent with previously reported CBO films.[319] Compared with the pure CBO (Figure 0-8), the top-view SEM image of Ru-*x*/CBO (Figure 0-9, Figure 0-7b, Figure 0-10) kept the morphology of the CBO, all exhibiting the network morphology consisting of interconnected particles and open channels. X-ray

diffraction (XRD) analysis of Ru-*x*/CBO (x=1, 2 and 3) and pure CBO confirmed a tetragonal CBO phase (PDF #2-0334), with additional diffraction peaks from the SnO_2 in the FTO substrate (PDF #46-1088) (Figure 0-7c). Magnification examination of the (211) diffraction peak revealed a positive shift in Ru-2/CBO and Ru-3/CBO relative to pure CBO, suggesting lattice contraction as Ru^{4+} (62 pm) replaces the larger Cu^{2+} (73 pm).[320,321] Bragg's law ($2d\sin\theta = n\lambda$) implies that the decreased interplanar spacing (d) results in a higher diffraction angle (θ), corroborating this lattice contraction due to smaller Ru dopants. A more pronounced shift in Ru-3/CBO indicates further lattice shrinkage with increased Ru content. High-resolution transmission electron microscopy (HR-TEM) provided additional insight into lattice changes. For pure CBO, a (211) plane d-spacing of 3.2 Å was found to be consistent with the XRD results (Figure 0-11), whereas Ru-doped Ru-2/CBO exhibited a reduced 3.1 Å spacing (Figure 0-7d), further confirming lattice contraction due to Ru incorporation. Scanning transmission electron microscopy (STEM, Figure 0-12a) and elemental mapping (EDS, Figure 0-12b to Figure 0-12e) illustrate the worm-like morphology of Ru-2/CBO, with Cu, Bi, Ru, and O uniformly distributed, confirming the homogeneity of the Ru-doped structure.

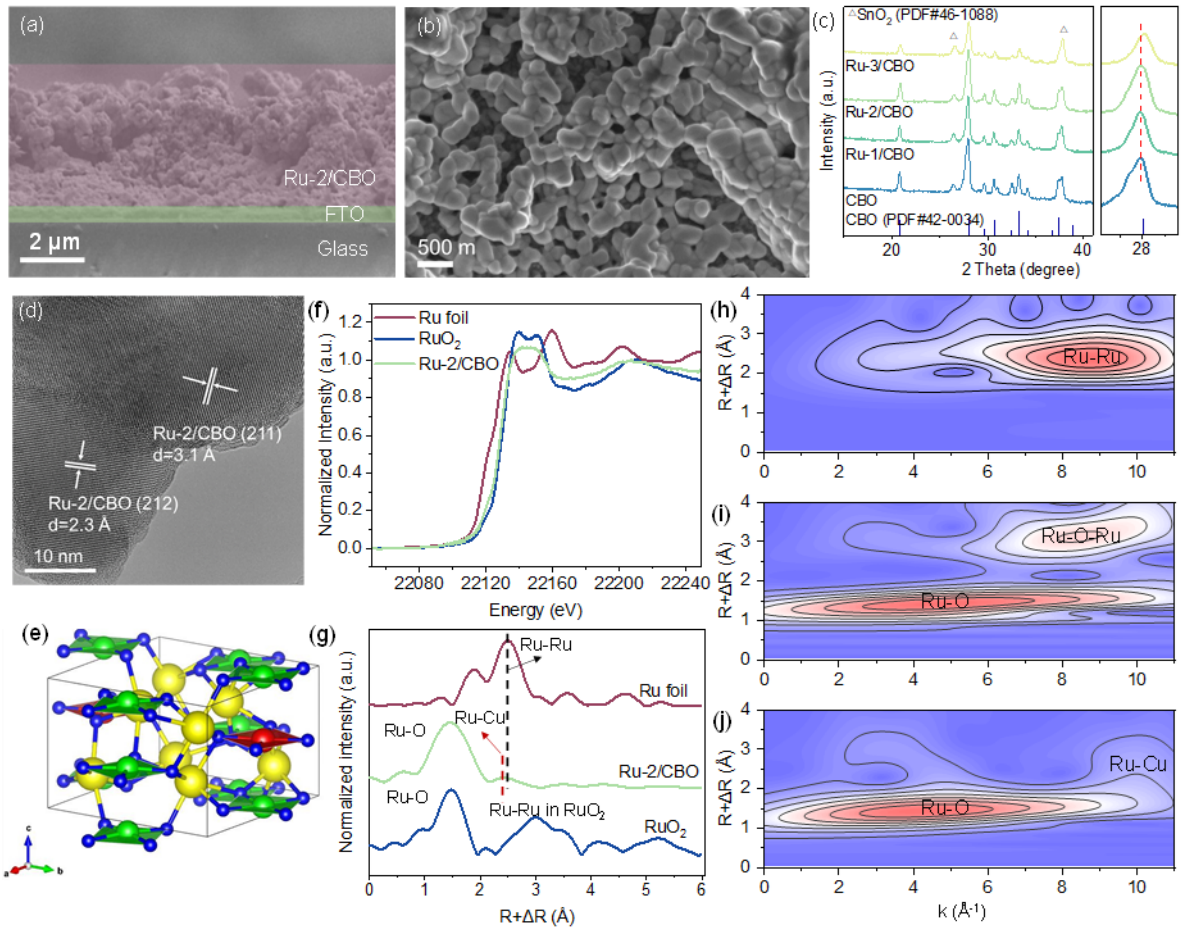

Figure 0-7. (a) The cross-section SEM image and (b) top-view SEM image of Ru-2/CBO. (c) XRD pattern of Ru-x/CBO (x=1, 2 and 3) and CBO, (d) HR-TEM image of Ru-2/CBO, (e) DFT-based optimized atomic structure model of the Ru-2/CBO photocathode (red, green, yellow, and blue colored balls represent Ru, Cu, Bi, and O atoms, respectively). (f) Ru K-edge XANES spectra and (g) FT-EXAFS Ru K-edge spectra of Ru-2/CBO, Ru foil, and RuO_2 reference. Wavelet-transform (WT) plots for Ru K-edge of (h) Ru foil, (i) RuO2 reference and (j) Ru-2/CBO.

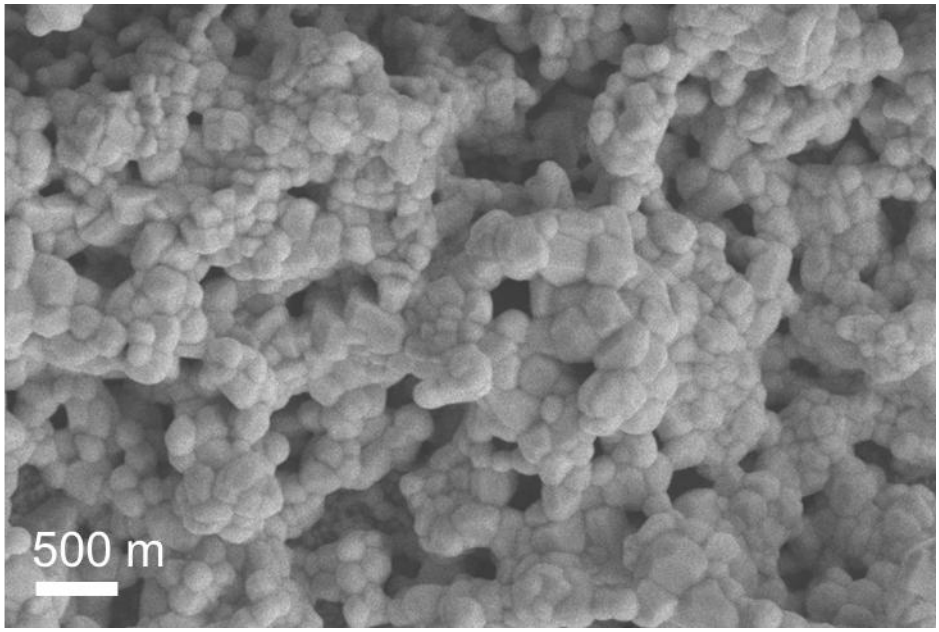

Figure 0-8. Top-view SEM image of CBO.

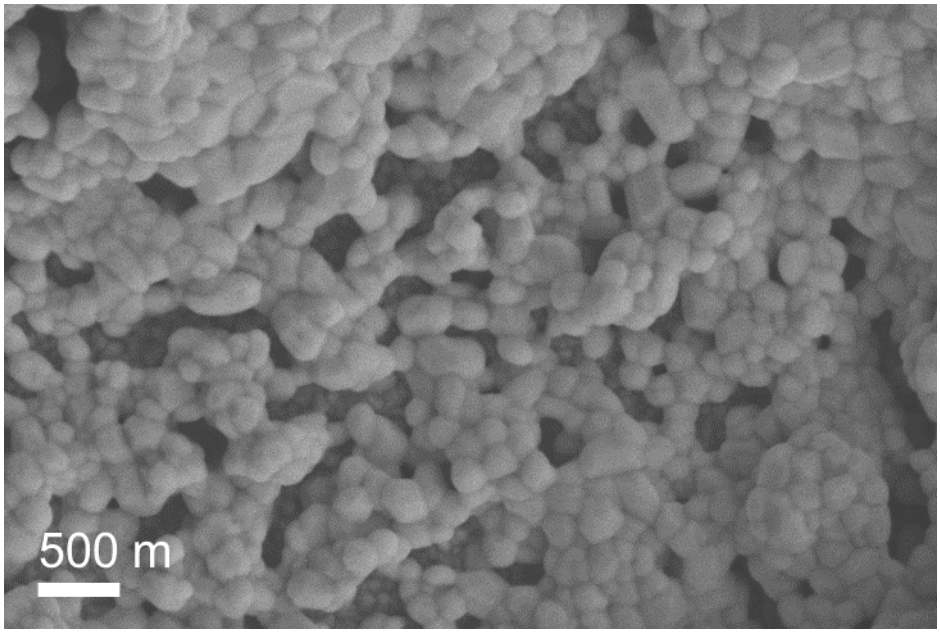

Figure 0-9.Top-view SEM image of Ru-1/CBO.

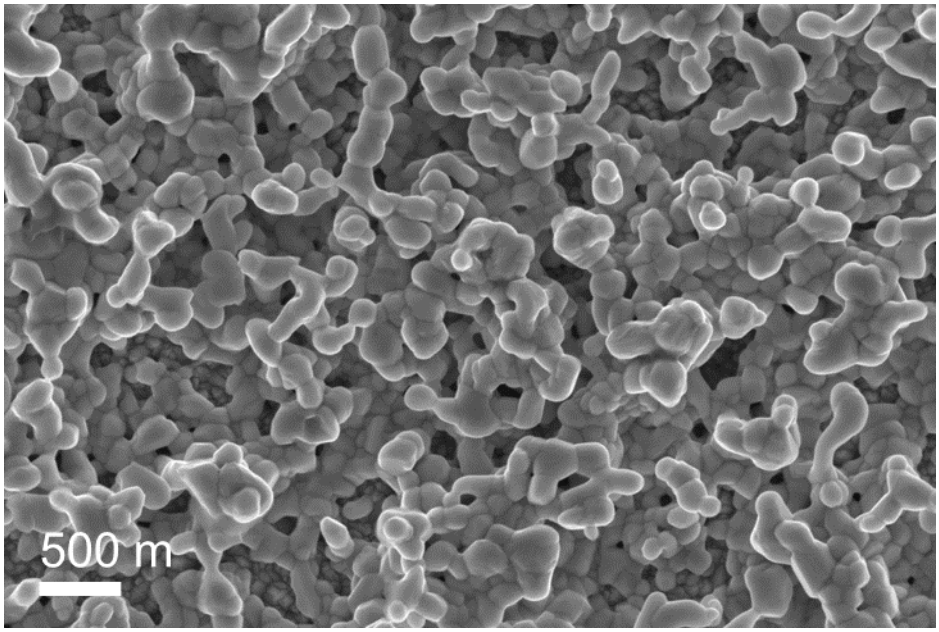

Figure 0-10. Top-view SEM image of Ru-3/CBO.

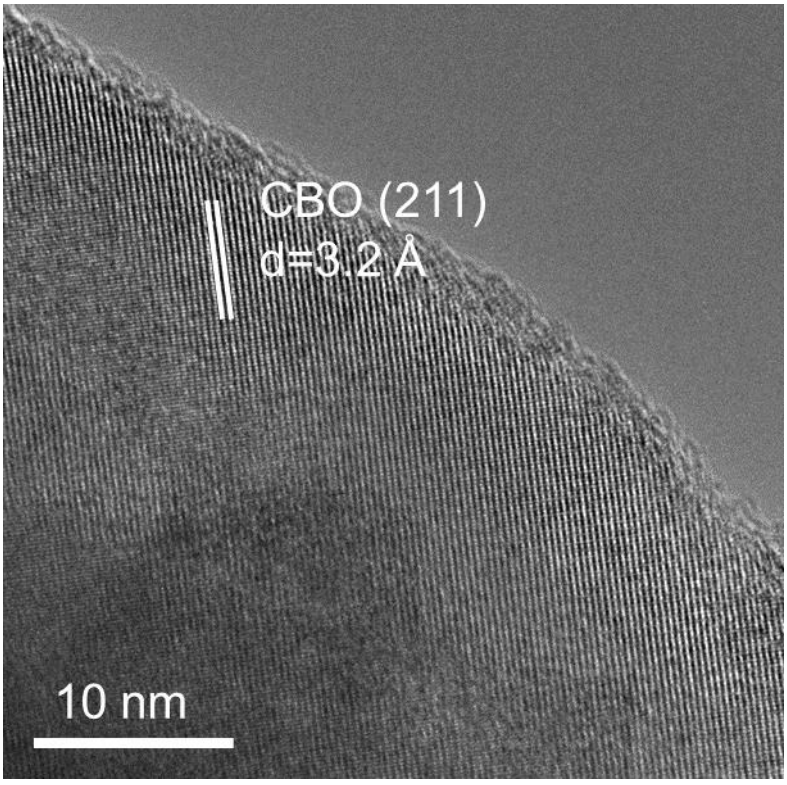

Figure 0-11. HR-TEM image of CBO.

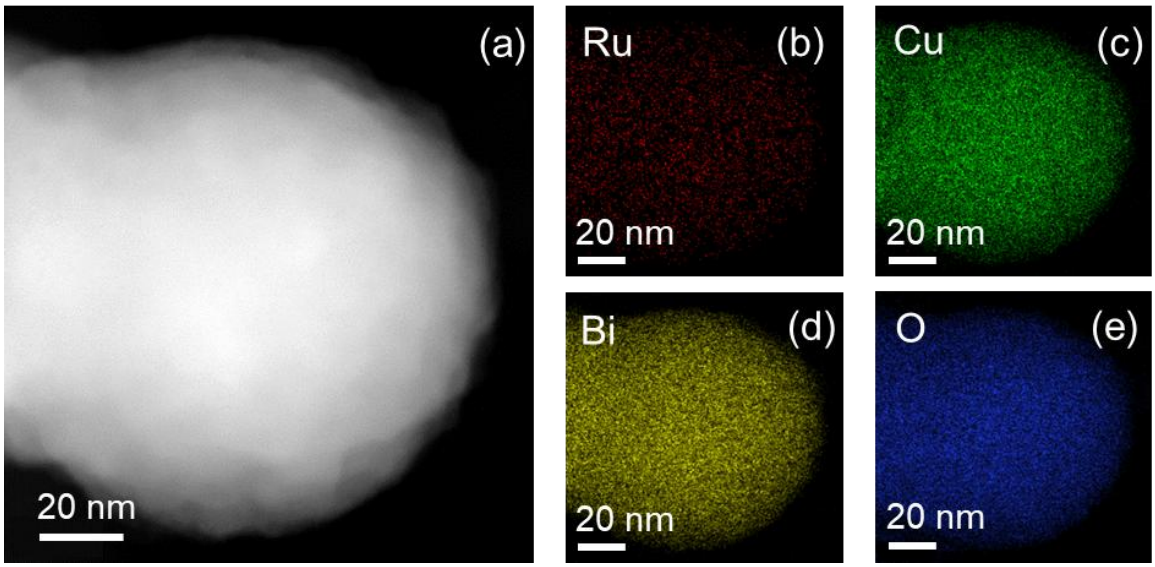

Figure 0-12. (a) HAADF image and (b-e) the corresponding EDS elemental mapping of Ru-2/CBO.

The Ru substitution site in CBO was investigated using density functional theory (DFT) optimization (Figure 0-7e and Figure 0-13). Table 0-1 shows that Ru substitution at the Cu-site has a formation energy of 0.507 eV, significantly lower than the 1.162 eV for substitution at the Bi-site, suggesting a preference for Ru to occupy Cu sites. Ru-doped CBO retains a similar crystal structure to pure CBO due to the comparable ionic radii of Ru (73 pm) and Cu (62 pm). However, slight lattice distortions appeared upon Ru substitution, confirmed by XRD analysis, which is attributed to electron density shifts around O atoms, with Cu and Bi experiencing reduced electron density. Raman spectroscopy of pristine CBO and Ru-doped samples (Ru-*x*/CBO, *x* = 1, 2, 3) showed consistent vibrational peaks (Figure 0-14), [16] indicating successful Ru incorporation.[322,323] The chemical and surface electronic structure of Ru-*x*/CBO (*x* = 1, 2, 3) and pure CBO samples were further characterized by X-ray photoelectron spectroscopy (XPS) (Figure 0-15, Figure 0-16, Figure 0-17, Figure 0-18, and Figure 0-19). The Ru 3p peaks in Ru-2/CBO align with Ru^{3+} and Ru^{4+} species and exhibit a positive shift with increased Ru content, indicating reduced electron density at the Ru site,[324] which is beneficial for ORR.[325] The O 1s spectrum reveals peaks for lattice oxygen and adsorbed oxygen species (e.g., hydroxide), with increased oxygen vacancies following Ru doping. XPS analysis of Cu 2p and Bi 4f spectra further shows shifts toward positive binding energies in Ru-doped CBO, reflecting Ru's oxophilicity[326] and corroborated by Bader charge analysis (Table 0-2).

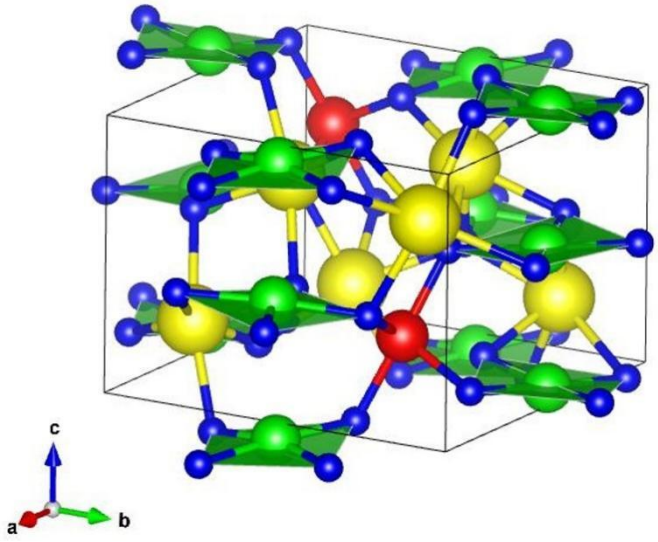

Figure 0-13. Formation of Ru-2/CBO by Ru replacing Bi. Red, green, yellow, and blue colored balls represent Ru, Cu, Bi, and O atoms, respectively.

Table 0-1. DFT calculation of the formation energy of Ru doping at different sites.

	Ru at Cu-site	Ru at Bi-site
Formation energy (eV)	0.507	1.162

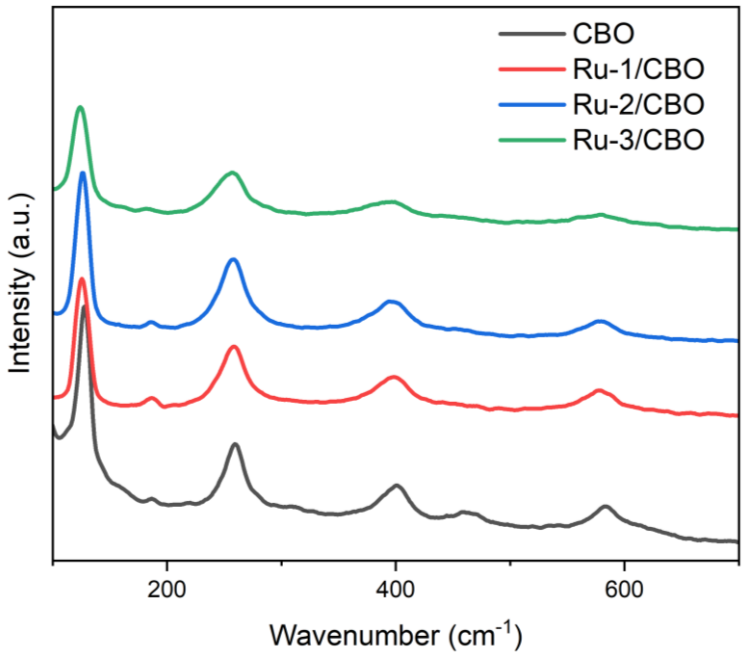

Figure 0-14. Raman spectra of the as-prepared Ru-*x*/CBO (*x*=1, 2, and 3) and CBO photocathodes.

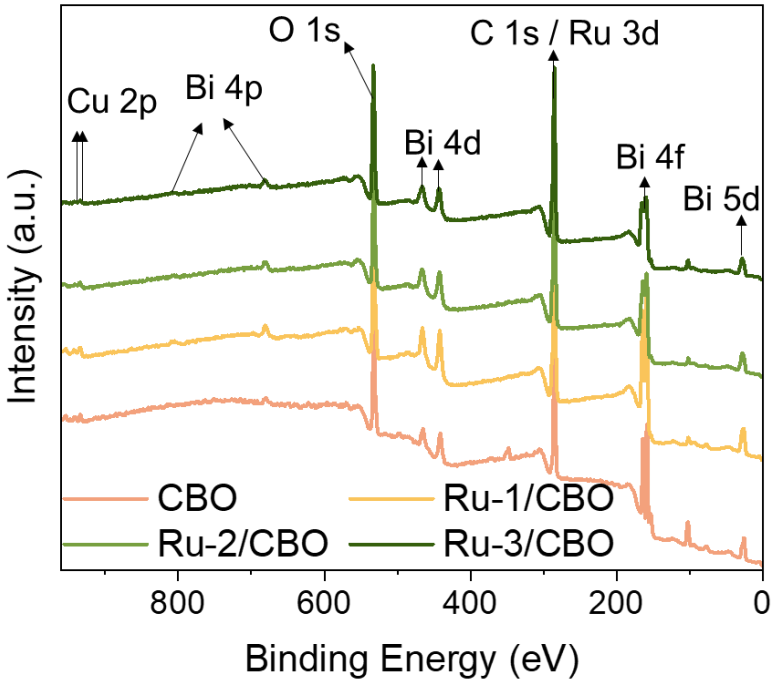

Figure 0-15. XPS survey spectra of Ru-*x*/CBO (*x* =1, 2, and 3) and CBO photocathodes.

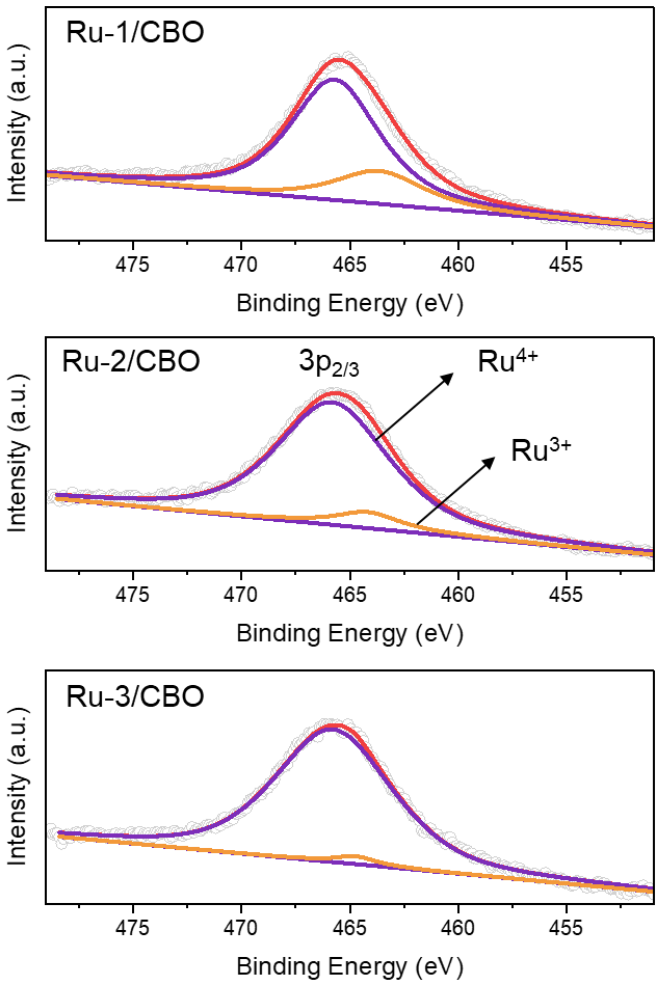

Figure 0-16. XPS spectra of Ru 3p peaks of (a) Ru-1/CBO and (b) Ru-3/CBO.

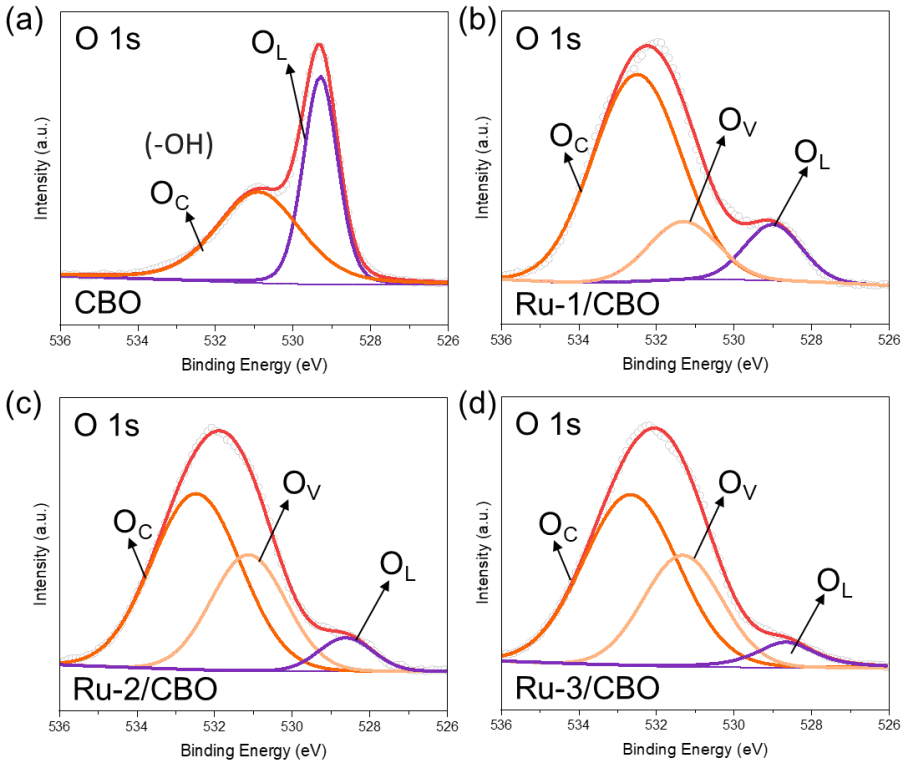

Figure 0-17. XPS spectra of O 1s peaks of (a) CBO, (b) Ru-1/CBO, (c) Ru-2/CBO, and (d) Ru-3/CBO.

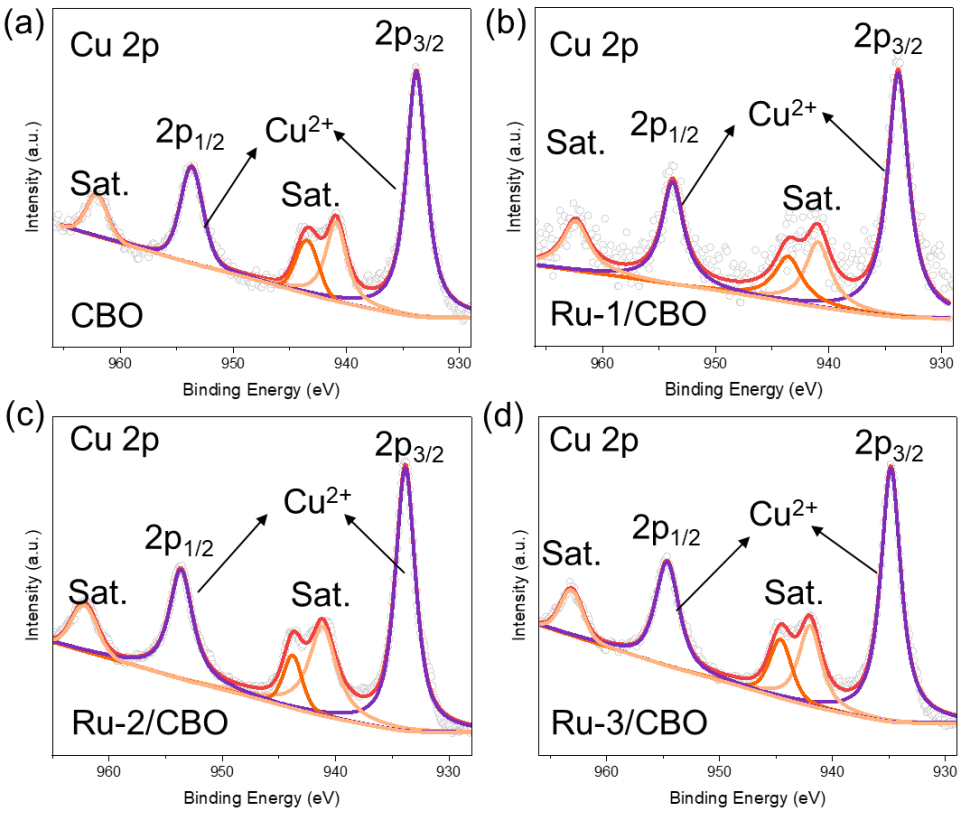

Figure 0-18. XPS spectra of Cu 2p peaks of (a) CBO, (b) Ru-1/CBO, (c) Ru-2/CBO, and

(d) Ru-3/CBO.

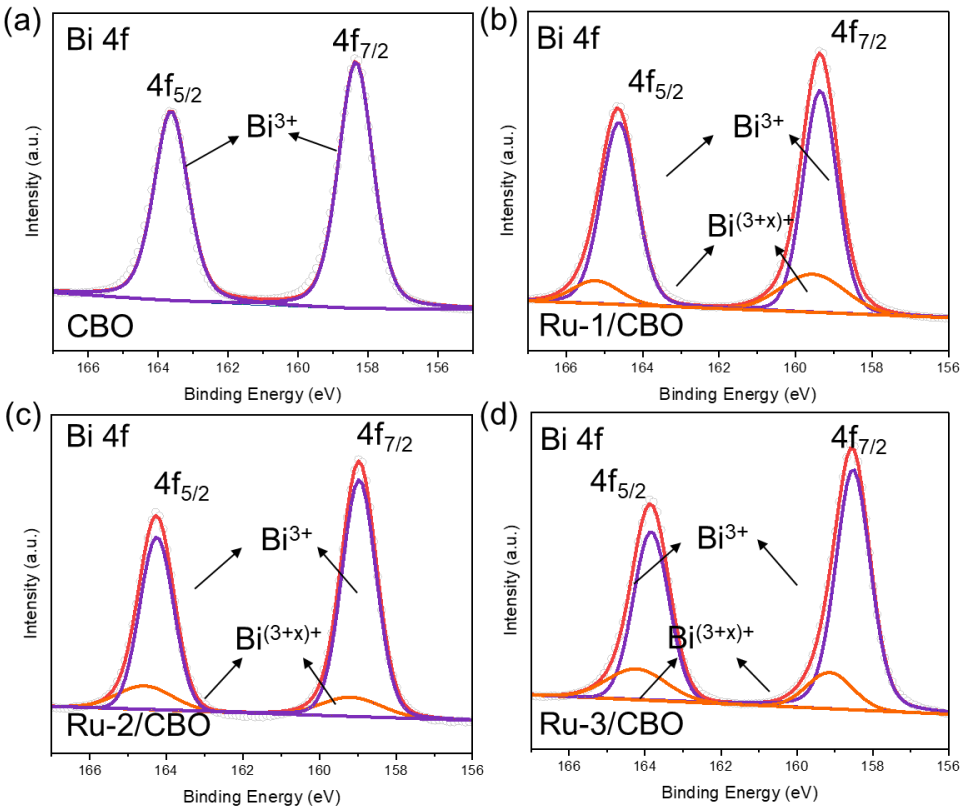

Figure 0-19. XPS spectra of Bi 4f peaks of (a) CBO, (b) Ru-1/CBO, (c) Ru-2/CBO, and (d) Ru-3/CBO.

Table 0-2. Bader charges analysis for Ru doping at different sites.

	Pristine	Ru at Cu-site
O	-0.932 *e*	-1.065 *e*
Cu	+0.966 *e*	+0.872 *e*
Bi	+1.654 *e*	+1.65 *e*
Ru	-	+1.241 *e*

In addition, to further confirm the doped Ru structure, the electronic and coordination structures of Ru-2/CBO are probed using X-ray absorption spectroscopy (XAS). The Ru K-edge extended X-ray absorption near-edge structure (XANES) spectrum shows a slight oxidation of Ru compared to Ru foil and RuO_2 (Figure 0-7f). The FT-EXAFS spectrum of Ru-2/CBO displays two main peaks at 1.46 and 2.50 Å. The obvious peak at 1.42 Å is attributed to the contribution

of Ru-O scattering,[327] which is mainly due to the formation of Ru-O bonds in CBO due to Ru doping. A closer look at the spectra further discloses that the Ru-O bond in Ru-2/CBO is shorter than that in RuO_2,[328] This observation indicated that following Ru doping, there was a discernible migration of O atoms toward the Ru, which also supports the XPS results (Figure 0-7g). The peak at 2.22 Å in Ru-2/CBO is different from the peak in Ru foil (2.39 Å), which could be tentatively attributed to the contribution of Ru-Cu,[327] indicating that Ru doping is dispersed in the CBO after replacing Bi, and no nanoclusters are formed. The wavelet transform (WT) of the Ru EXAFS oscillations further confirms the presence of Ru-Cu scattering (Figure 0-7h, Figure 0-7i and Figure 0-7j). In addition to the Ru-O bond (4.6 $Å^{-1}$), an intensity maximum near 8.1 $Å^{-1}$ is exclusively observed, which is attributed to the Ru-Cu contribution in Ru-2/CBO. This is different from the Ru-Ru bond in Ru foil, again indicating that the Ru doping on the CBO substrate is not due to the presence of Ru atoms.

Table 0-3. EXAFS fitting parameters at the Ru K-edge for Ru-2/CBO.

	Bond	N	R (Å)	σ^2	ΔE (eV)	R-factor (%)
Ru foil	Ru-Ru	4.84±0.81	2.73±0.07	0.001	3.34±1.04	0.9
RuO_2	Ru-O	2.32±0.28	1.94±0.02	0.002	2.69±1.25	1.1
	Ru-Ru	4.50±2.42	3.11±0.05	0.005	2.69±1.25	1.1
Ru-2/CBO	Ru-O	2.38±0.24	1.94 ±0.07	0.002	1.92±1.21	0.4
	Ru-Cu	0.92±0.26	2.76±0.02	0.005	1.09±0.49	2.2

Apart from the structure characterization of the photocathodes, we systematically investigated the optical and electrochemical properties of Ru-doped CBO photocathodes to elucidate the role of Ru doping in enhancing PEC HMF oxidation. The UV-vis absorption spectra reveal that pristine CBO and Ru-*x*/CBO (*x* = 1, 2, 3) exhibit strong absorption in the UV-visible range (Figure 0-20a). The band gap energies (E_g), calculated using the Kubelka-Munk function, show

a reduction from pure CBO to Ru-doped CBO, indicating improved visible-light utilization due to Ru doping (Figure 0-21). Photoluminescence (PL) spectra reveal that Ru-2/CBO exhibits a lower PL intensity, signifying reduced electron-hole recombination and efficient charge separation, attributed to electron transfer from CBO to Ru (Figure 0-20b). Mott-Schottky (MS) analysis confirms that Ru-2/CBO displays a more positive flat-band (E_{fb}) potential than CBO, reflecting heterojunction formation and improved band bending, conducive to charge transfer (Figure 0-20c). All the samples have a negative slope, proving they are p-type semiconductors.[329] The carrier density (Nd) calculated by MS curve (Equation 1 in experimental section),[330] which was significantly higher for Ru-2/CBO (1.4×10^{20} cm^{-3}) compared to CBO and other Ru-doped samples (Table 0-4), facilitated efficient charge separation at the photoelectrode/electrolyte interface.[331]

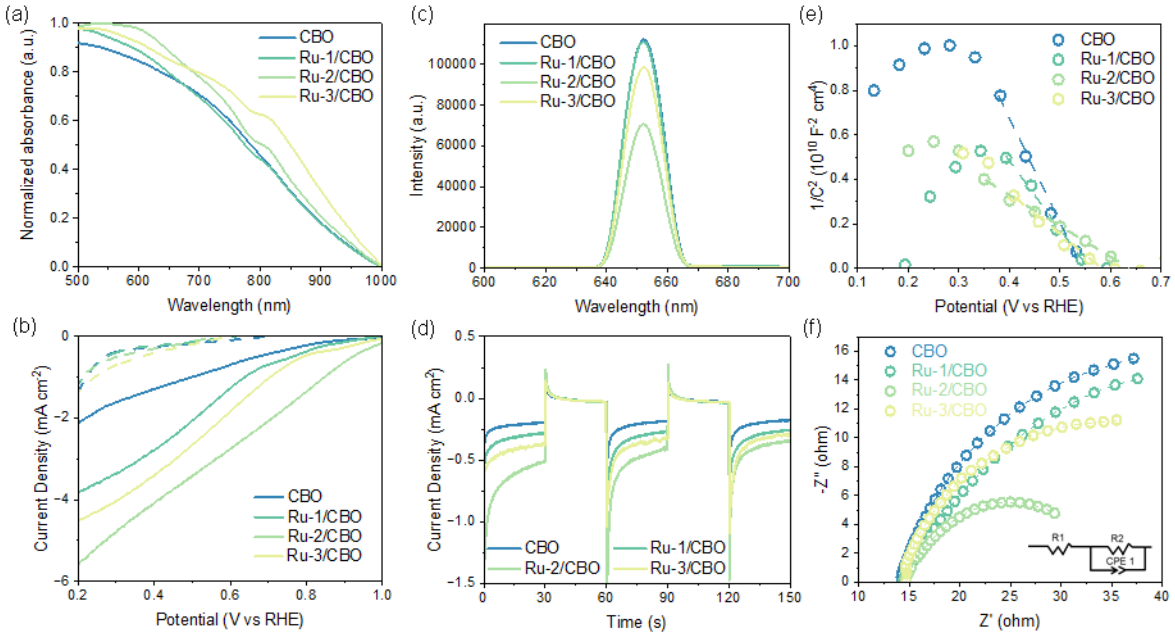

Figure 0-20. (a) UV-vis absorption spectra, (b) PL spectra, (c) MS curves, (d) LSV curves under light illumination and dark (dashed lines), (e) chronoamperometry curves, and (f) Nyquist plot of CBO and Ru-*x*/CBO (*x*=1, 2 and 3).

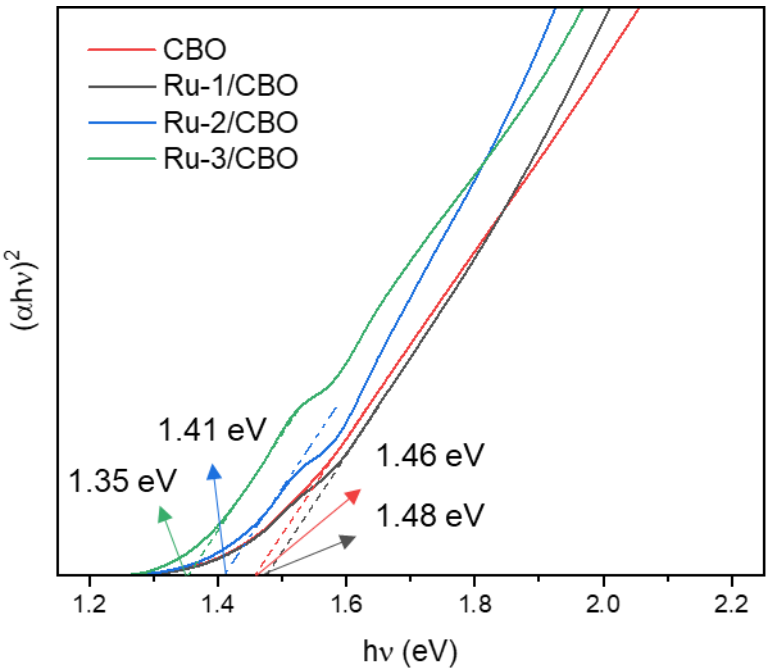

Figure 0-21. Tauc plots of CBO, Ru-1/CBO, Ru-2/CBO, and Ru-3/CBO.

Table 0-4. Summary of the carrier density for CBO and Ru-*x*/CBO (*x*=1, 2 and 3).

Cathode	Nd (cm^{-3})
CBO	3.3×10^{19}
Ru-1/CBO	4.5×10^{19}
Ru-2/CBO	1.4×10^{20}
Ru-3/CBO	9.2×10^{19}

Linear sweep voltammetry (LSV) in 1 M KOH showed that Ru-doped photocathodes achieve notably higher photocurrent densities compared to CBO, with Ru-2/CBO reaching -2.04 mA cm^{-2} at 0.4 V vs. RHE (Figure 0-20d). Excess Ru doping, however, induces structural distortions that create recombination centers, as seen in Ru-3/CBO.[332] The I-t curves further confirm enhanced photocurrent in Ru-2/CBO (Figure 0-20e), whereas electrochemical impedance spectroscopy (EIS) shows a smaller impedance arc for Ru-2/CBO, indicating lower charge-transfer resistance and higher PEC activity compared to CBO (Figure 0-20f). These findings demonstrate that optimal Ru doping in CBO enhances visible light absorption, charge separation, and overall photoelectrochemical performance.

3.3.3 NiOOH-modified BVO ($BiVO_4$) photoanodes

To achieve efficient PEC oxidation of HMF concurrent at the photoanode, we designed NiOOH-modified BVO (NO-*x*/BVO, *x* = 1, 2, 3) photoanodes, harnessing the excellent light absorption of BVO and the catalytic prowess of NiOOH to achieve enhancement in performance. BVO seed layers were first fabricated via spin-coating, followed by hydrothermal synthesis to create BVO films. NiOOH layers were electrodeposited on BVO nanoplates (Figure 0-22), forming vertically oriented nanoplates approximately 3 μm high on FTO substrates (Figure 0-23. (a) The cross-section SEM image and (b) top-view SEM image of NO-2/BVO. (c) XRD pattern of NO-x/BVO (*x*=1, 2 and 3) and BVO, (d) TEM image and (e) HR-TEM image of NO-2/BVO, (f) HAADF image and (g-j) the corresponding EDS mapping of NO-2/BVO. (k) UV-vis absorption spectra, (l) LSV curves under light illumination and dark (dashed lines), and (m) chronoamperometry curves.a). SEM and TEM analyses confirmed the maintenance of rectangular BVO morphology post-NiOOH modification, with the NiOOH layer forming an ultrathin film on the BVO surface (Figure 0-24, Figure 0-25, Figure 0-26, Figure 0-23. (a) The cross-section SEM image and (b) top-view SEM image of NO-2/BVO. (c) XRD pattern of NO-x/BVO (*x*=1, 2 and 3) and BVO, (d) TEM image and (e) HR-TEM image of NO-2/BVO, (f) HAADF image and (g-j) the corresponding EDS mapping of NO-2/BVO. (k) UV-vis absorption spectra, (l) LSV curves under light illumination and dark (dashed lines), and (m) chronoamperometry curves.b and Figure 0-23. (a) The cross-section SEM image and (b) top-view SEM image of NO-2/BVO. (c) XRD pattern of NO-x/BVO (*x*=1, 2 and 3) and BVO, (d) TEM image and (e) HR-TEM image of NO-2/BVO, (f) HAADF image and (g-j) the corresponding EDS mapping of NO-2/BVO. (k) UV-vis absorption spectra, (l) LSV curves under light illumination and dark (dashed lines), and (m) chronoamperometry curves.d). XRD patterns displayed monoclinic scheelite BVO diffraction peaks and weak NiOOH peaks (25.9° and 51.5°), verifying the integration of NiOOH (Figure 0-23. (a) The cross-section SEM image and (b) top-view SEM image of NO-2/BVO. (c) XRD pattern of NO-x/BVO (*x*=1, 2 and 3) and BVO, (d) TEM image and (e) HR-TEM image of NO-2/BVO, (f) HAADF image and (g-j) the corresponding EDS mapping of NO-2/BVO. (k) UV-vis absorption spectra, (l) LSV curves under light illumination and dark (dashed lines), and (m) chronoamperometry curves.c). HR-TEM imaging further confirmed the NiOOH deposition, revealing lattice fringes with a 2.4 Å spacing for NiOOH (101) on BVO (Figure 0-23. (a) The cross-section SEM image and (b) top-view SEM image of NO-2/BVO. (c) XRD pattern of NO-x/BVO (*x*=1, 2 and 3) and BVO, (d) TEM image and (e) HR-TEM image of NO-2/BVO, (f) HAADF image and (g-j) the

corresponding EDS mapping of NO-2/BVO. (k) UV-vis absorption spectra, (l) LSV curves under light illumination and dark (dashed lines), and (m) chronoamperometry curves.e), while HADDF-EDS mapping highlighted the slightly larger Ni and O distributions, indicating NiOOH localization on BVO surfaces (Figure 0-23. (a) The cross-section SEM image and (b) top-view SEM image of NO-2/BVO. (c) XRD pattern of NO-x/BVO (*x*=1, 2 and 3) and BVO, (d) TEM image and (e) HR-TEM image of NO-2/BVO, (f) HAADF image and (g-j) the corresponding EDS mapping of NO-2/BVO. (k) UV-vis absorption spectra, (l) LSV curves under light illumination and dark (dashed lines), and (m) chronoamperometry curves.g, Figure 0-23. (a) The cross-section SEM image and (b) top-view SEM image of NO-2/BVO. (c) XRD pattern of NO-x/BVO (*x*=1, 2 and 3) and BVO, (d) TEM image and (e) HR-TEM image of NO-2/BVO, (f) HAADF image and (g-j) the corresponding EDS mapping of NO-2/BVO. (k) UV-vis absorption spectra, (l) LSV curves under light illumination and dark (dashed lines), and (m) chronoamperometry curves.h, Figure 0-23. (a) The cross-section SEM image and (b) top-view SEM image of NO-2/BVO. (c) XRD pattern of NO-x/BVO (*x*=1, 2 and 3) and BVO, (d) TEM image and (e) HR-TEM image of NO-2/BVO, (f) HAADF image and (g-j) the corresponding EDS mapping of NO-2/BVO. (k) UV-vis absorption spectra, (l) LSV curves under light illumination and dark (dashed lines), and (m) chronoamperometry curves.I and Figure 0-23. (a) The cross-section SEM image and (b) top-view SEM image of NO-2/BVO. (c) XRD pattern of NO-x/BVO (*x*=1, 2 and 3) and BVO, (d) TEM image and (e) HR-TEM image of NO-2/BVO, (f) HAADF image and (g-j) the corresponding EDS mapping of NO-2/BVO. (k) UV-vis absorption spectra, (l) LSV curves under light illumination and dark (dashed lines), and (m) chronoamperometry curves.j). XPS analysis revealed the presence of Bi, V, and O in both BVO and NO-x/BVO photoanodes, along with distinct Ni^{2+} and Ni^{3+} peaks in NO-x/BVO, affirming the presence of NiOOH (Figure 0-28 and Figure 0-29).[333] Deconvoluted O 1s spectra (529.6 eV for lattice oxygen and 531.8 eV for chemisorbed oxygen) further detailed the chemical states of oxygen (Figure 0-30).[334] High-resolution XPS spectra of Bi 4f and V 2p showed low-energy shifts in NO-x/BVO compared to pure BVO, indicating electron redistribution attributed to the higher electronegativity of NiOOH (Figure 0-31 and Figure 0-32). These findings underscore the successful integration of NiOOH on BVO, enhancing electron transfer properties critical for efficient PEC HMF oxidation.

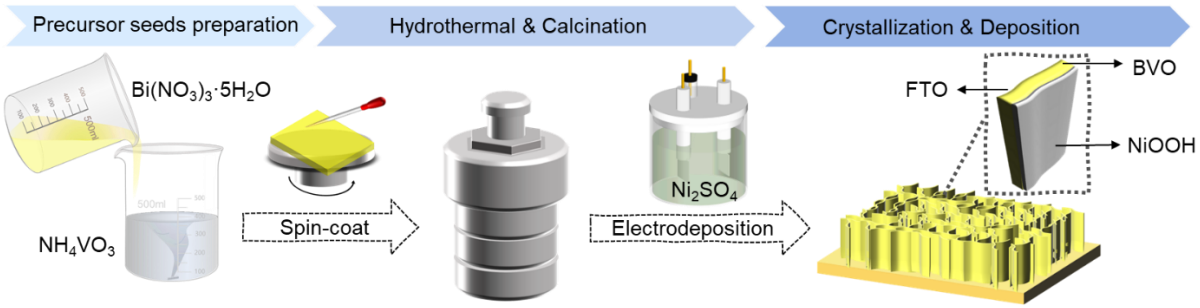

Figure 0-22. Synthesis scheme of NO-*x*/BVO (*x*=1, 2 and 3).

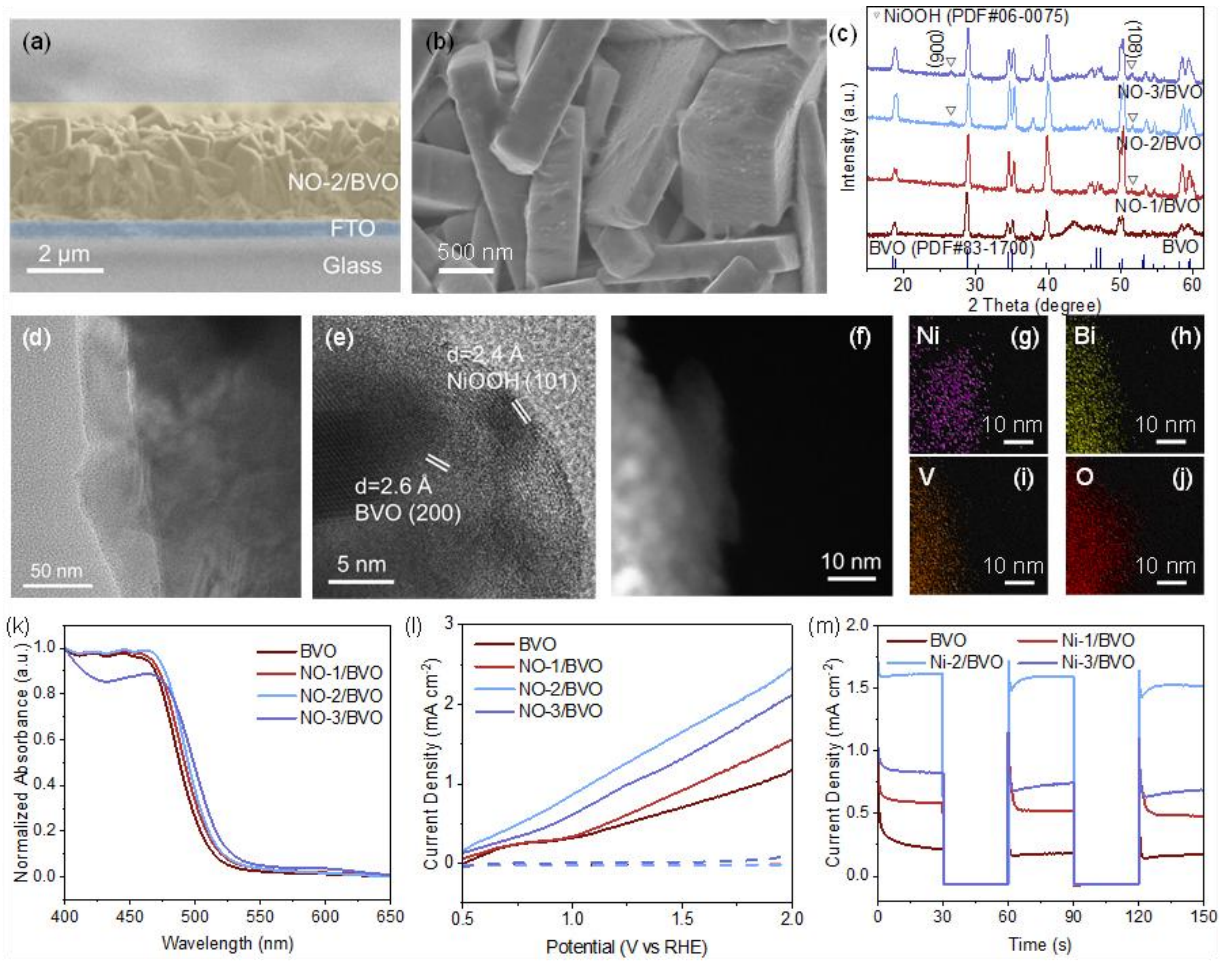

Figure 0-23. (a) The cross-section SEM image and (b) top-view SEM image of NO-2/BVO. (c) XRD pattern of NO-*x*/BVO (*x*=1, 2 and 3) and BVO, (d) TEM image and (e) HR-TEM image of NO-*2*/BVO, (f) HAADF image and (g-j) the corresponding EDS mapping of NO-2/BVO. (k) UV-vis absorption spectra, (l) LSV curves under light illumination and dark (dashed lines), and (m) chronoamperometry curves.

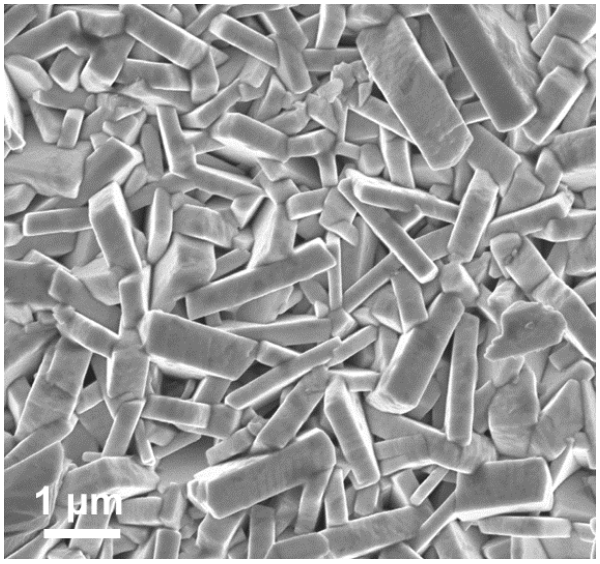

Figure 0-24. Top-view SEM image of BVO.

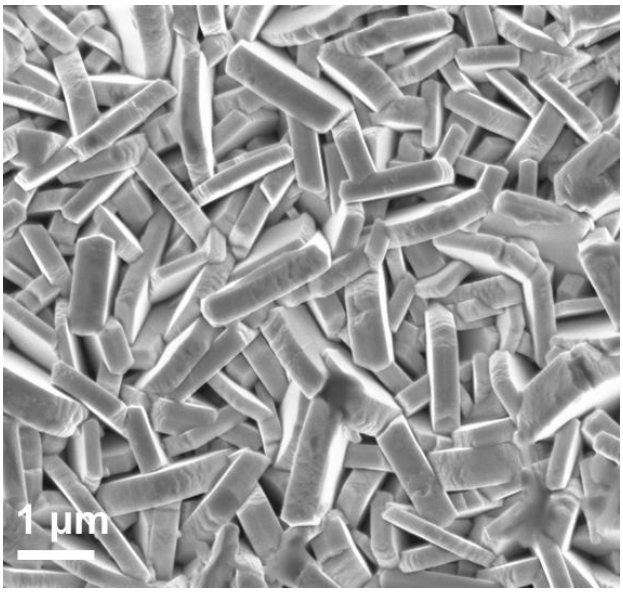

Figure 0-25. Top-view SEM image of NO-1/BVO.

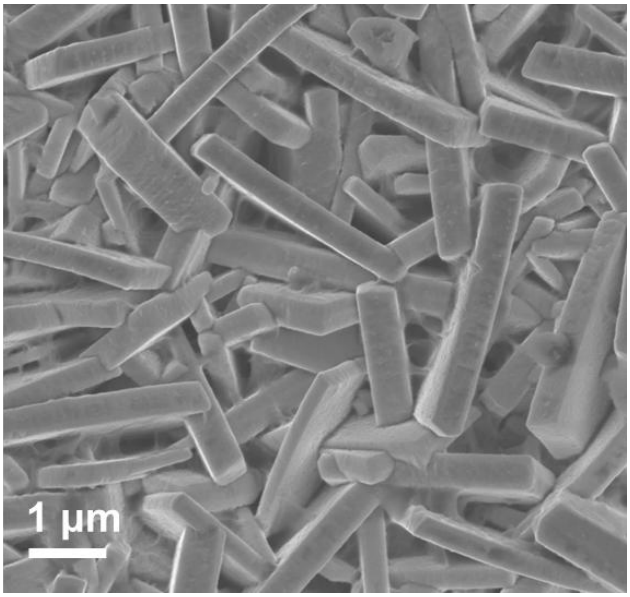

Figure 0-26. Top-view SEM image of NO-3/BVO.

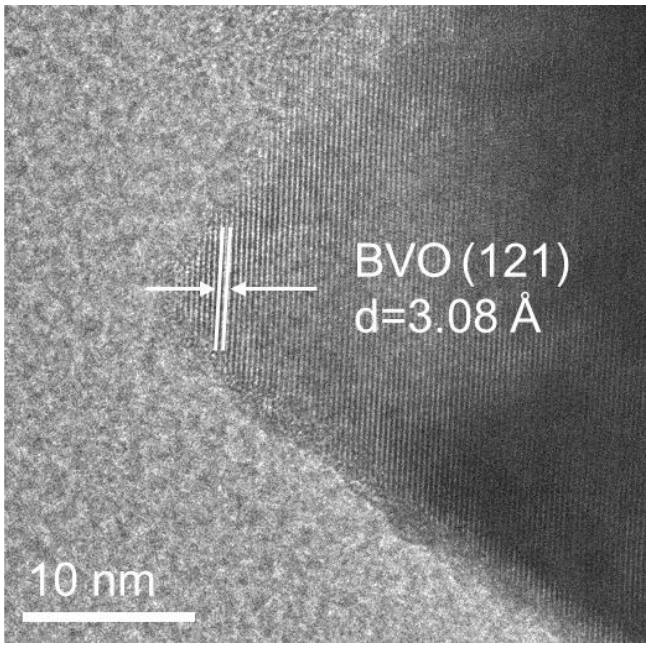

Figure 0-27.HR-TEM image of BVO.

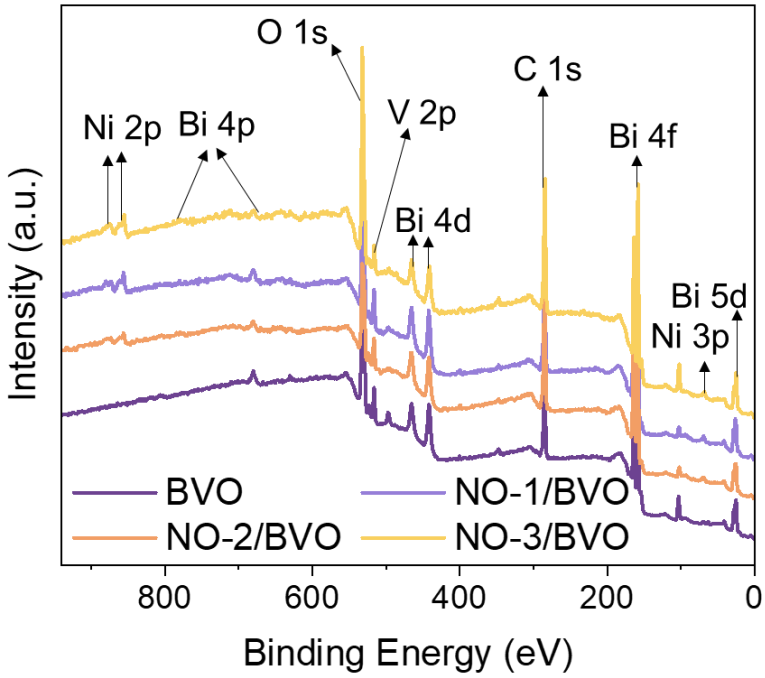

Figure 0-28. XPS survey spectra of (a) BVO, (b) NO-1/BVO, (c) NO-2/BVO, and (d) NO-3/BVO.

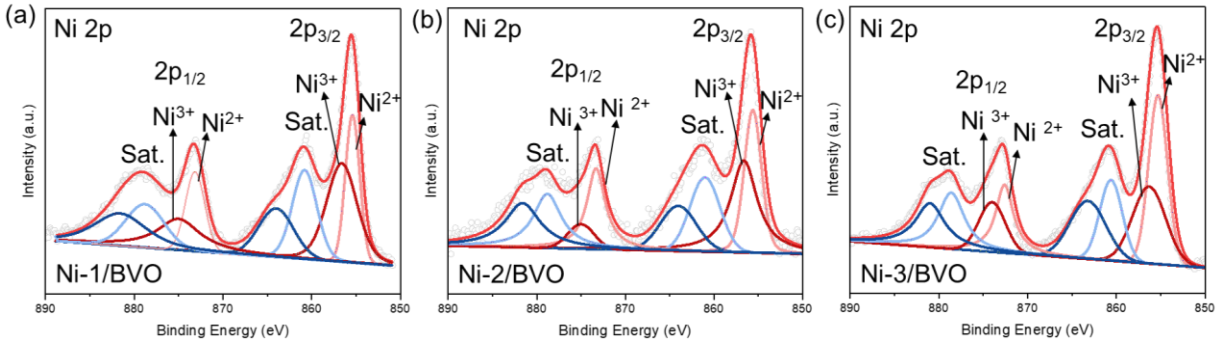

Figure 0-29. XPS spectra of Ni 2p peaks of (a) NO-1/BVO, (b) NO-2/BVO, and (c) NO-3/BVO.

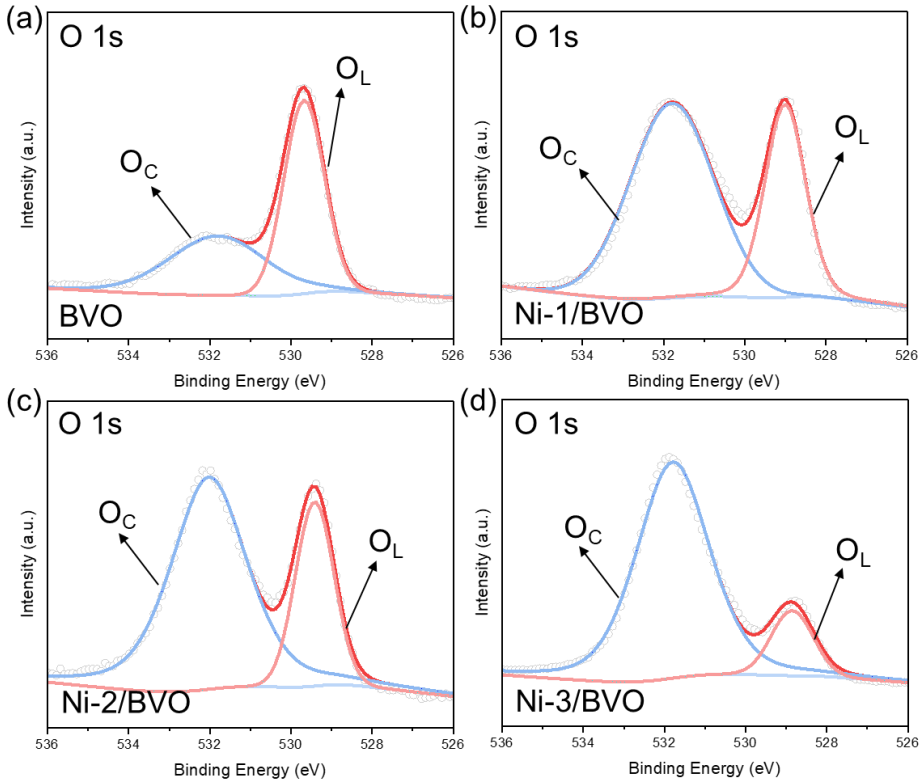

Figure 0-30. XPS spectra of O 1s peaks of (a) BVO, (b) NO-1/BVO, (c) NO-2/BVO, and (d) NO-3/BVO.

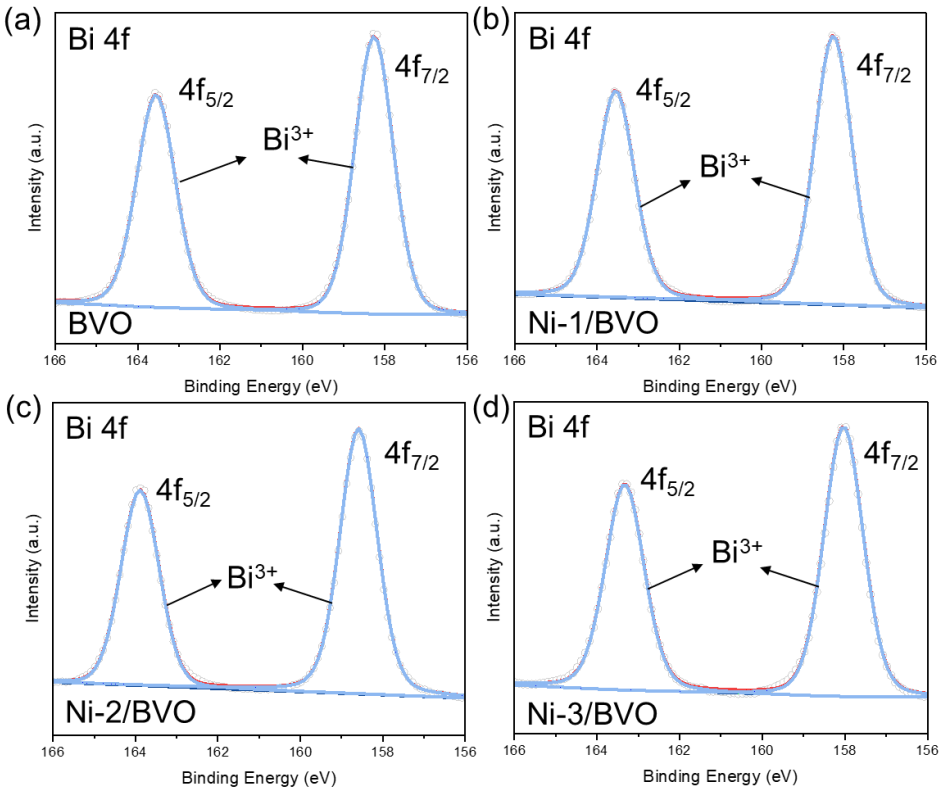

Figure 0-31. XPS spectra of Bi 4f peaks of (a) BVO, (b) NO-1/BVO, (c) NO-2/BVO, and

(d) NO-3/BVO.

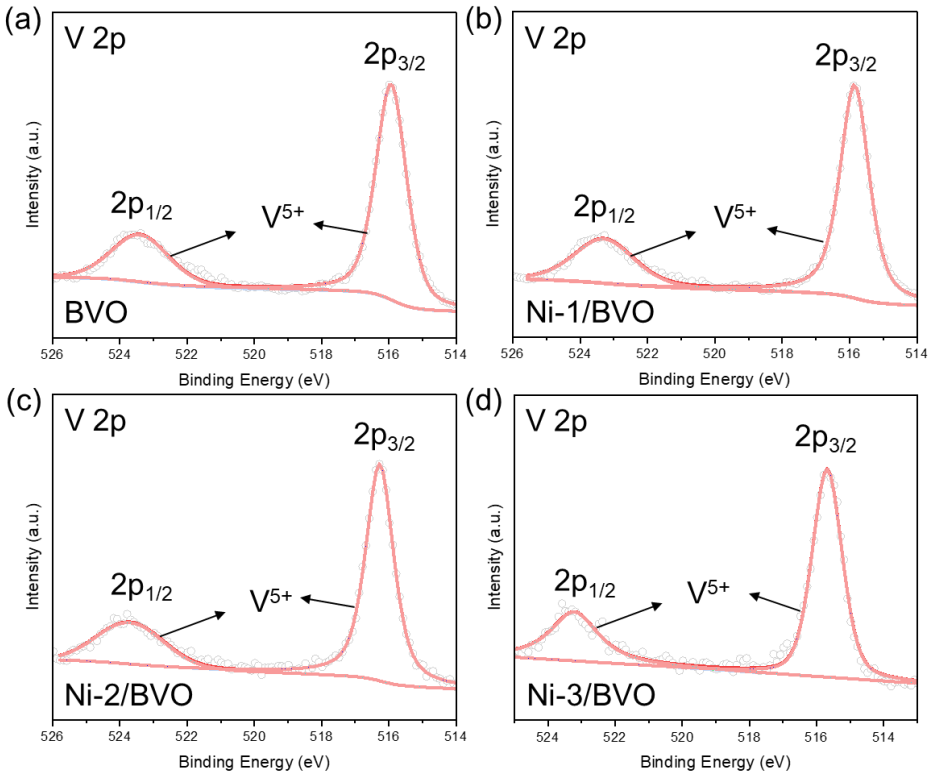

Figure 0-32. XPS spectra of V 2p peaks of (a) BVO, (b) NO-1/BVO, (c) NO-2/BVO, and (d) NO-3/BVO.

In addition to morphology and composition, the optical response and carrier behavior of the photoanodes were further studied. The BVO absorption edge was near 520 nm, whereas NiOOH modification induced a redshift, broadening the light absorption range (Figure 0-23k). As shown in Figure 0-33, bandgap values of NO-1/BVO, NO-2/BVO, and NO-3/BVO were approximately 2.48, 2.47, and 2.44 eV, respectively, compared to 2.50 eV for pristine BVO, indicating that NiOOH reduces the bandgap slightly, enhancing light absorption. To assess carrier recombination, PL spectra show that NiOOH-supported BVO exhibits reduced emission peak intensity at 510 nm compared to pure BVO, suggesting suppressed carrier recombination and improved surface charge transfer for reactions (Figure 0-34).[335] However, excess NiOOH (NO-3/BVO) increases emission intensity, indicating that surplus NiOOH can act as recombination sites, thereby hindering PEC performance. MS analysis determined the E_{fb} and semiconductor type for BVO and NO-x/BVO (x=1, 2, 3), revealing n-type characteristics for all samples (Figure 0-35). The progressively negative shift of E_{fb} in the NO-*x*/BVO heterostructures, with NO-2/BVO possessing the lowest E_{fb}, indicates an enhanced electron density. Carrier densities in Table 0-5 follow the order of NO-2/BVO > NO-3/BVO > NO-

1/BVO > BVO, supporting the superior performance of NO-2/BVO. Consequently, NO-2/BVO emerged as the optimal composite photoanode, achieving a photocurrent density of 1.48 mA cm^{-2} at 1.2 V vs. RHE, nearly three times higher than that of pristine BVO (0.5 mA cm^{-2}, Figure 0-23l). Transient photocurrent response confirmed stability, with minimal current spikes upon light switching[336] reflecting enhanced charge separation and reduced hole accumulation (Figure 0-23m). Nyquist plots further demonstrate NO-2/BVO's smallest arc radius (Figure 0-36), indicative of higher conductivity and faster electron transfer kinetics, critical for improved HMF oxidation performance. These results align with the MS slope data and reinforce that the NiOOH layer's enhanced interfacial charge transfer and conductivity are key factors in NO-2/BVO for improving PEC performance.

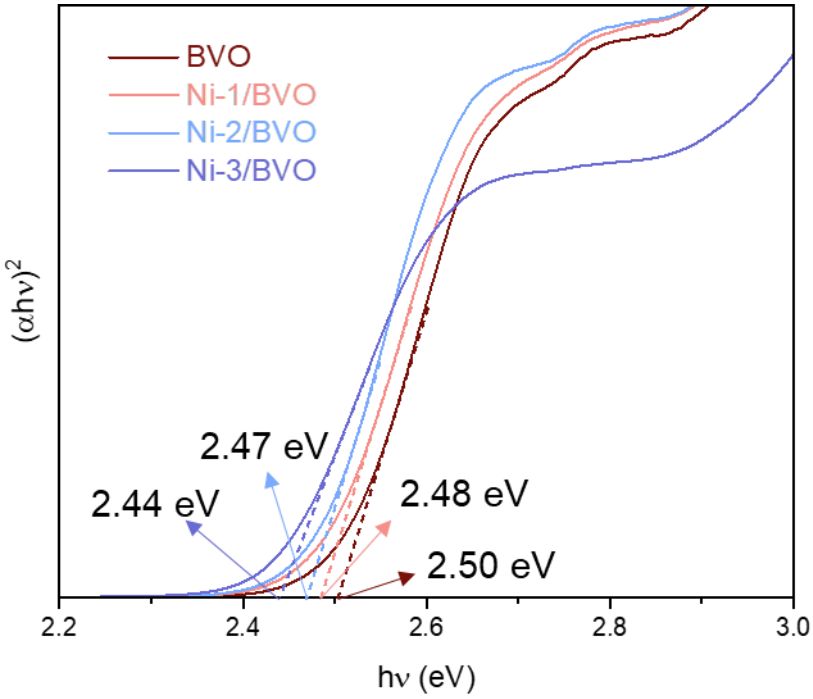

Figure 0-33. Tauc plot corresponding to UV-Vis absorption spectra of NO-*x*/BVO (*x*=1, 2 and 3) and BVO.

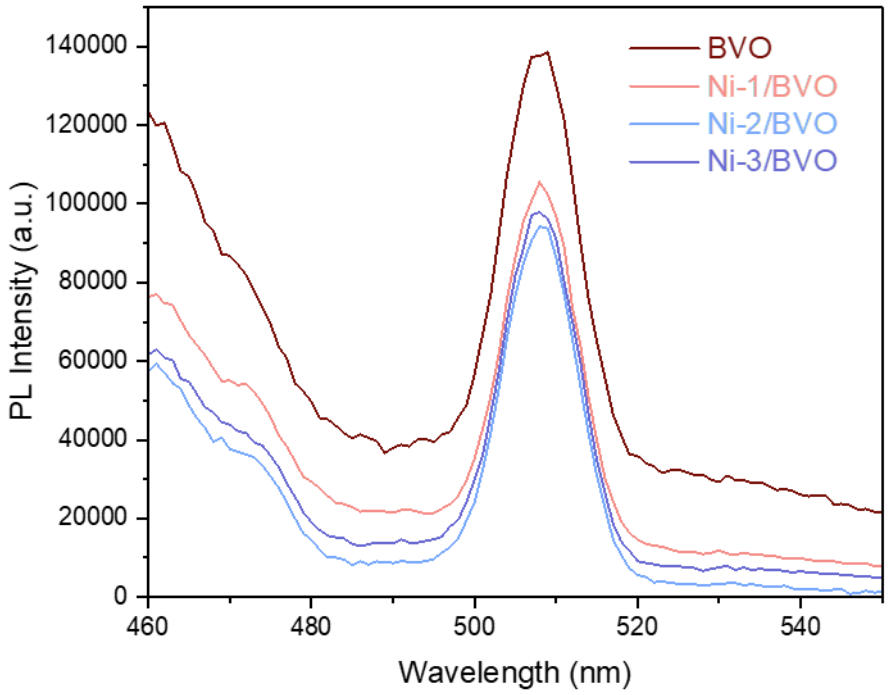

Figure 0-34. PL spectra of BVO and NO-*x*/BVO (*x* =1, 2 and 3).

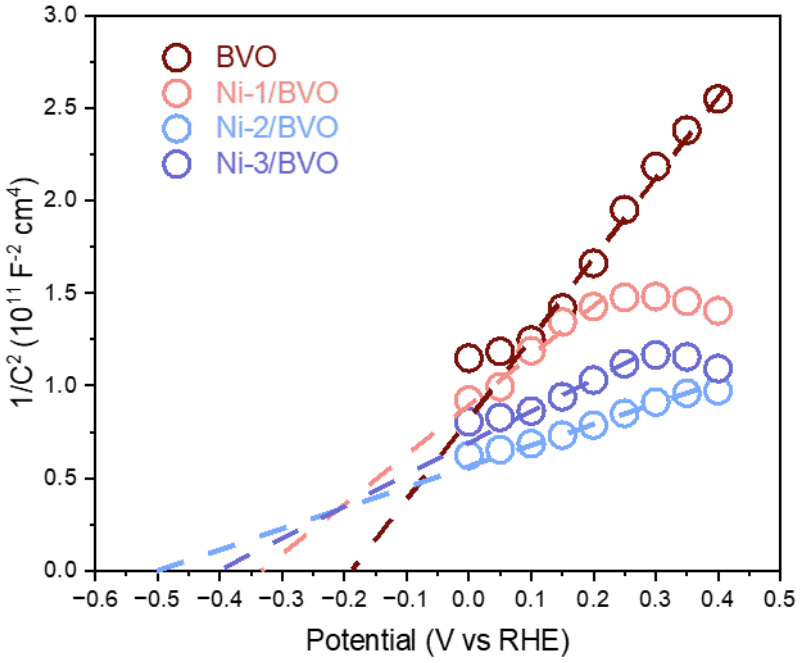

Figure 0-35. Mott-Schottky plots of the BVO, NO-1/BVO, NO-2/BVO, and NO-3/BVO photoelectrodes in 10 mM HMF with 1 M KOH (pH=13).

Table 0-5. Summary of the carrier density for BVO and NO-*x*/BVO (*x*=1, 2, and 3).

Anode	N_d (cm^{-3})
BVO	4.0×10^{18}
NO-1/BVO	5.9×10^{18}
NO-2/BVO	1.8×10^{19}
NO-3/BVO	1.2×10^{19}

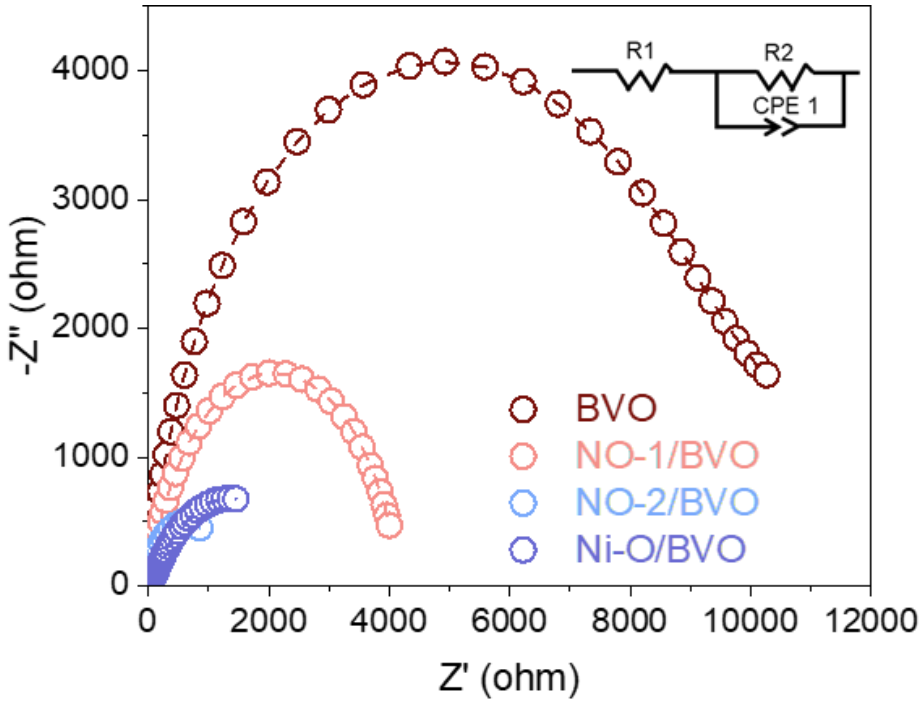

Figure 0-36.Nyquist plots of BVO and NO-x/BVO (x =1, 2 and 3).

3.3.4 PEC performance optimization

Apart from the structural and optical characterization, PEC measurements were optimized for both photocathodes and photoanodes in a 1 M KOH electrolyte (pH = 13) under simulated solar illumination using a standard three-electrode setup. For the Ru-2/CBO photocathode, PEC oxidation of HMF was conducted at 0.7, 0.5, and 0.2 V vs. RHE, yielding primarily HMFCA and FDCA, with a maximum production rate of 303.1 mmol m^{-2} at 0.2 V (Figure 0-37). Testing different Ru-doped photocathodes revealed that HMF oxidation performance increased from

233.8 mmol m^{-2} (Ru-1/CBO) to 303.1 mmol m^{-2} (Ru-2/CBO), with further doping (Ru-3/CBO) inducing charge recombination, thus lowering yields to 270 mmol m^{-2} (Figure 0-38). Significant mass loss due to humin formation at pH ≥ 12. posed limitations by blocking active sites, hindering mass transfer, and reducing efficiency across all systems, necessitating low substrate concentrations to suppress side reactions.[337] To address humin formation, a continuous flow PEC cell was implemented, adjusting flow rates to 50, 20, and 10 mL min^{-1} (Figure 0-39). Although a high flow rate (50 mL min^{-1}) prevented humin formation, short contact times limited yields to 242 mmol m^{-1}. Flow PEC enabled the detection of intermediate FFCA, confirming the oxidation pathway. Reducing flow to 10 mL min^{-1} produced the highest HMF yield of 290 mmol m^{-2} with a FE_{HMFCA} of 63.7%, exceeding batch PEC. Similarly, for the NO-2/BVO photoanode, optimal potentials (0.6, 0.8, and 1.2 V vs. RHE) were explored for PEC HMF oxidation, with yields increasing from 214.9 to 297.6 mmol m^{-2} (Figure 0-40). No oxidation products were detected under dark conditions, confirming solar-assisted electrolysis. Comparative testing of BVO (199.1 mmol m^{-2}), NO-1/BVO, and NO-3/BVO at optimal potentials yielded 231.3 and 267.4 mmol m^{-2}, respectively, with NO-2/BVO achieving the highest performance (Figure 0-41). Adjusting the flow rate on the NO-2/BVO anode further enhanced FE_{HMFCA}, from 65.8% at 50 mL min^{-1} to 79.7% at 10 mL min^{-1} (Figure 0-42), underscoring the advantages of continuous flow PEC in mitigating side reactions and maximizing efficiency.

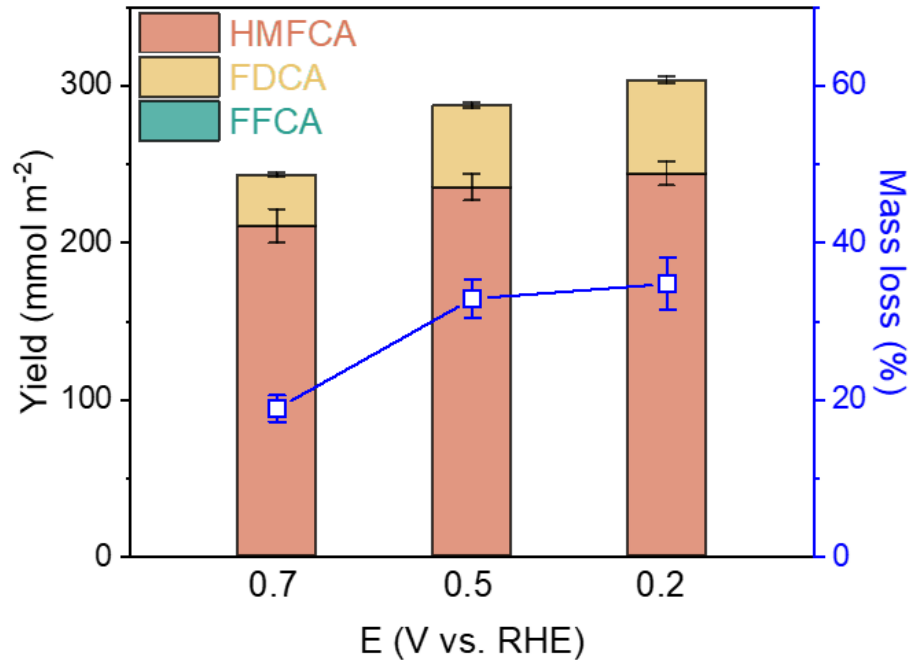

Figure 0-37. HMF oxidation over Ru-2/CBO at 0.7 V, 0.5 V, and 0.2 V vs. RHE under light conditions.

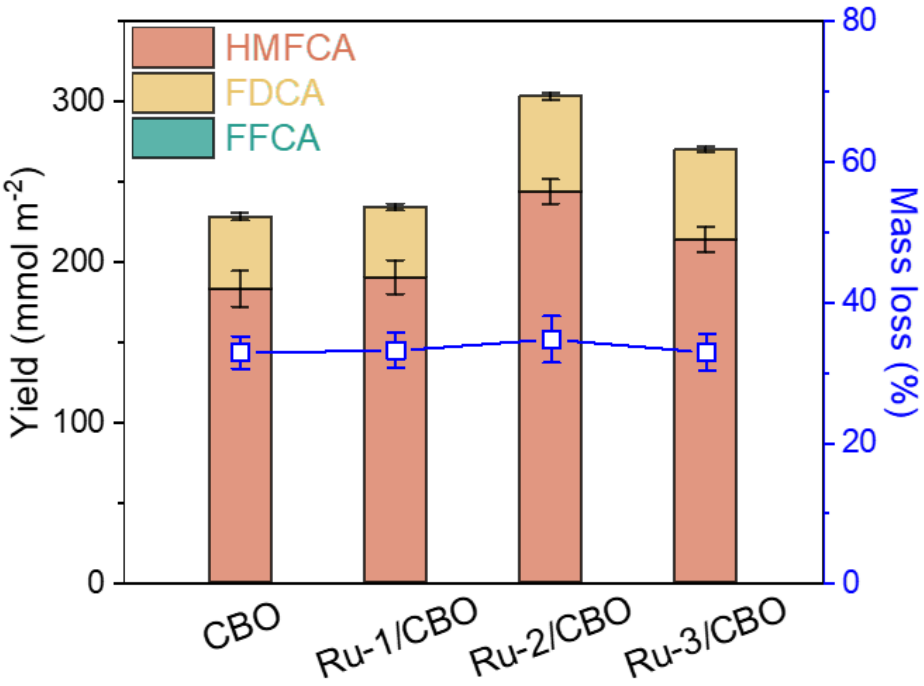

Figure 0-38. HMF oxidation over different photocathodes at 0.2 V vs. RHE under light conditions.

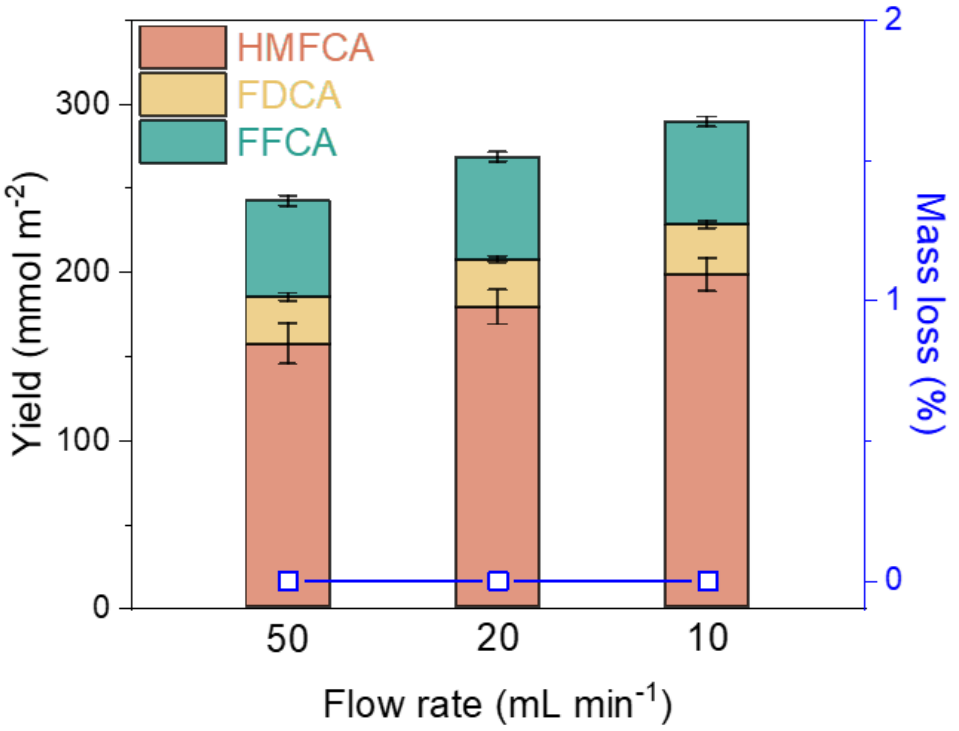

Figure 0-39. HMF oxidation over Ru-2/CBO at 0.2 V vs RHE under light conditions with different flow rates.

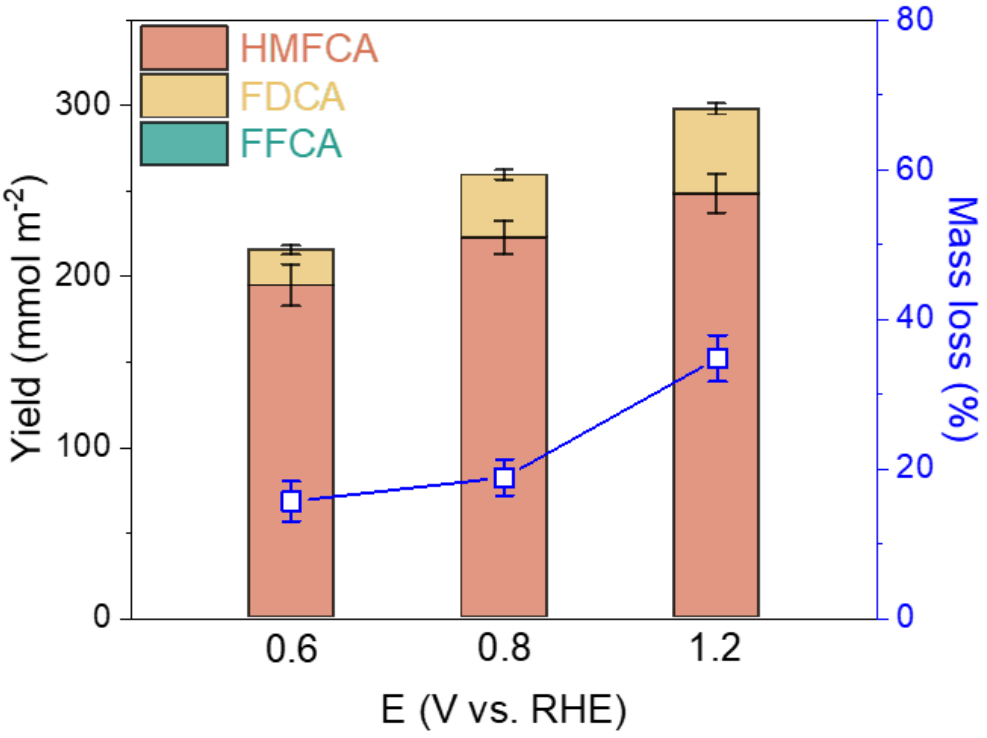

Figure 0-40. HMF oxidation over different photoanodes at 1.2 V vs. RHE under light conditions.

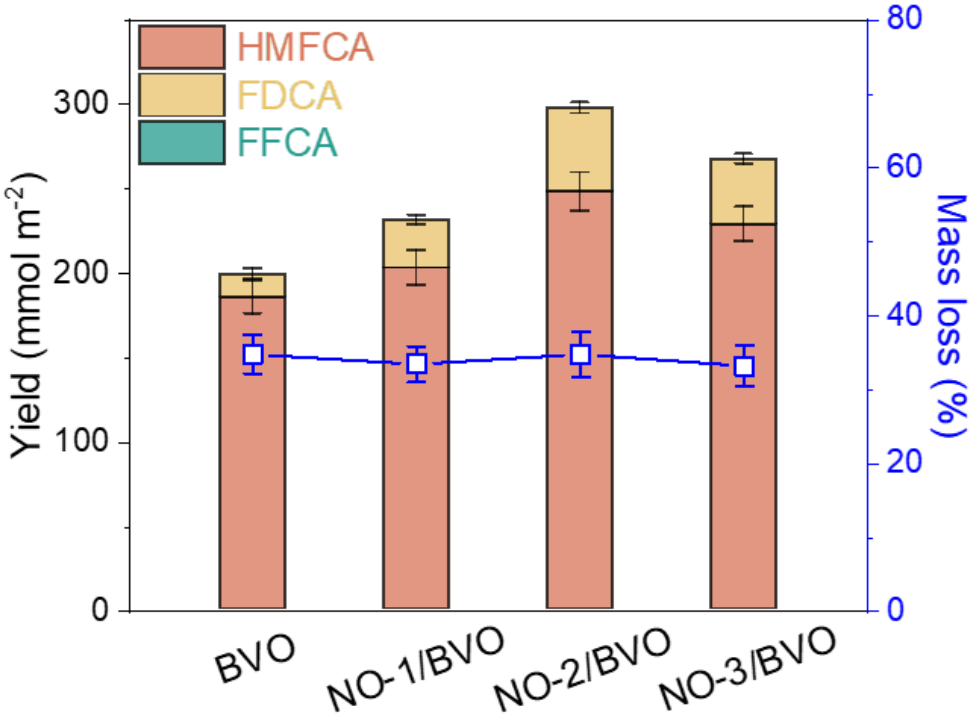

Figure 0-41. HMF oxidation over different photoanodes at 1.2 V vs. RHE under light conditions.

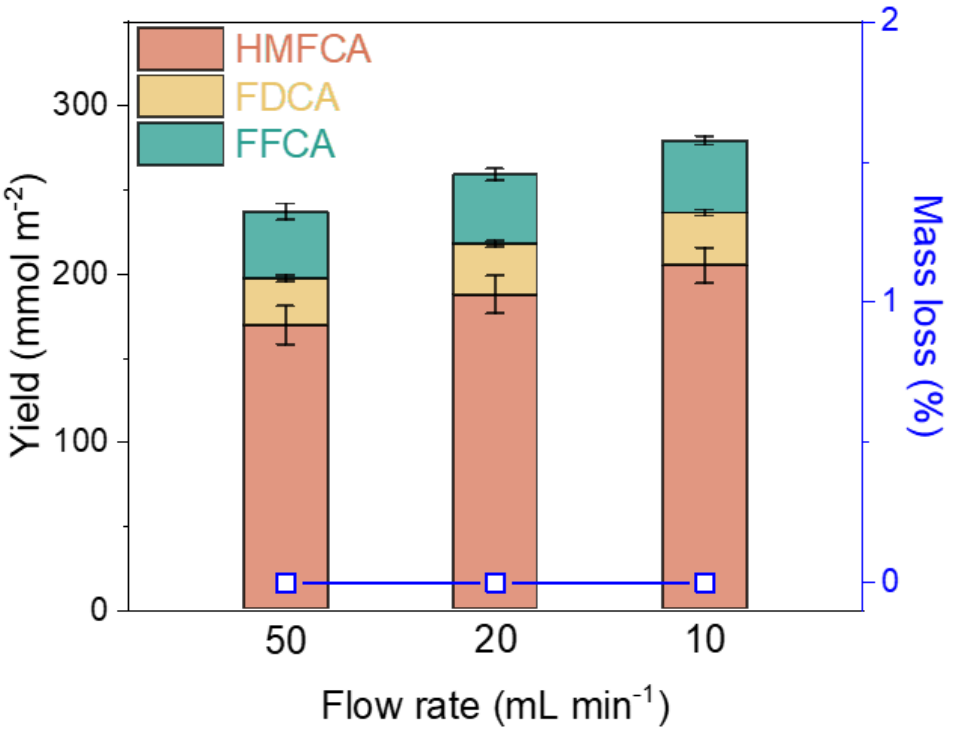

Figure 0-42. HMF oxidation over NO-2/BVO at 1.2 V vs. RHE under light conditions at different flow rates.

The incident photon-to-current conversion efficiency (IPCE) comparisons before and after Ru doping on CBO revealed significant performance enhancements, with Ru-2/CBO reaching a peak IPCE of 54% at 0.2 V vs. RHE, compared to 22% for undoped CBO (Figure 0-43). Similarly, the NO-2/BVO photoanode achieved a maximum IPCE of 60% at 1.23 V vs. RHE, surpassing the 48% of pure BVO (Figure 0-44). Besides, the maximum half-cell applied bias photon-to-current efficiency (HC-ABPE) for NiOOH-modified BVO was also significantly enhanced, with Ni-2/BVO displaying a peak ABPE of 1.25% at 0.73 V vs. RHE, 2.4 times higher than pure BVO, indicating the NiOOH co-catalysts impact on solar energy conversion (Figure S41). These results highlight the improved PEC performance in both Ru-2/CBO and NO-2/BVO photoelectrodes.

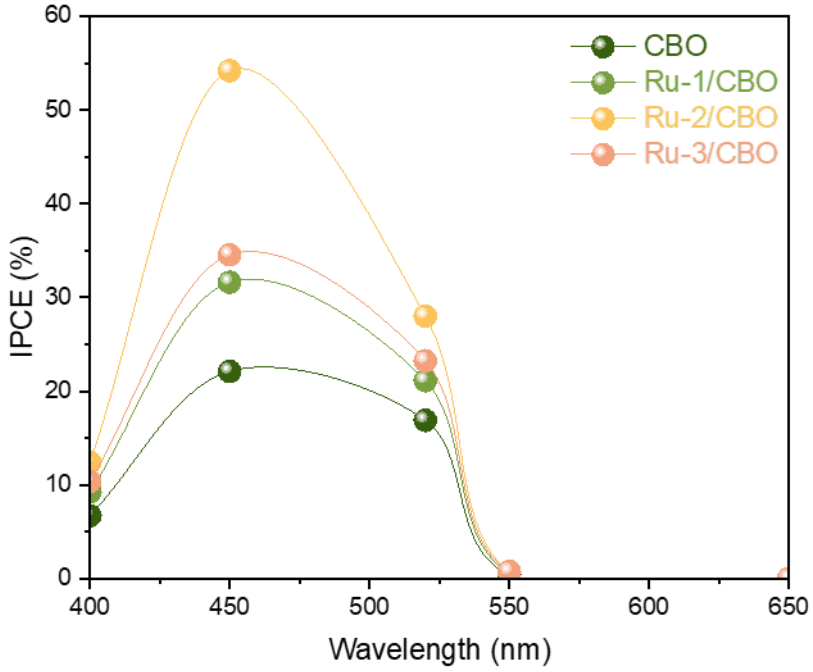

Figure 0-43. Wavelength-dependent IPCE of different photocathodes.

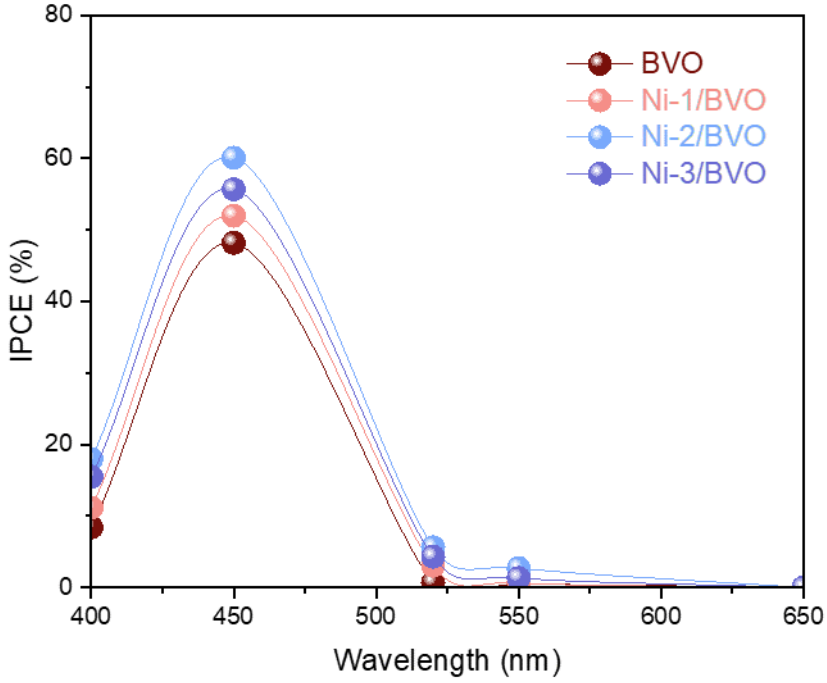

Figure 0-44. Wavelength-dependent IPCE of different photoanodes.

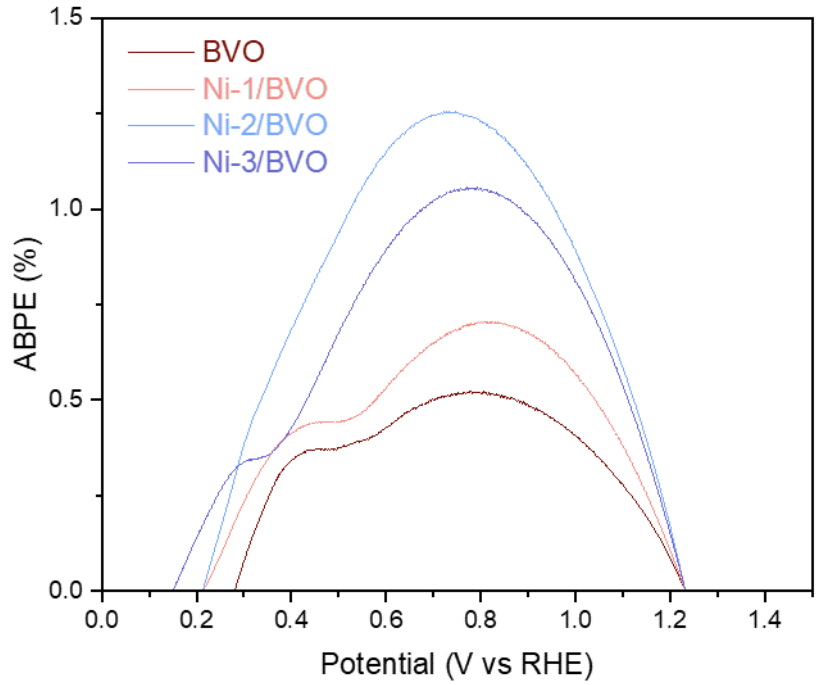

Figure 0-45. Measured ABPE of different photoanodes.

Long-term stability tests showed that Ru-2/CBO and NO-2/BVO retained high PEC HMF oxidation performance (Figure 0-46), with Ru-2/CBO displaying only 13% loss after 1800 s at 0.2 V vs. RHE and NO-2/BVO exhibiting minimal degradation at 1.2 V vs. RHE, aided by

heterojunction formation for improved charge transfer. Post-illumination characterizations (SEM, HRTEM, XRD, XPS; Figure 0-47, Figure 0-48, Figure 0-49 and Figure 0-50) confirmed structural integrity in both Ru-2/CBO and NO-2/BVO.

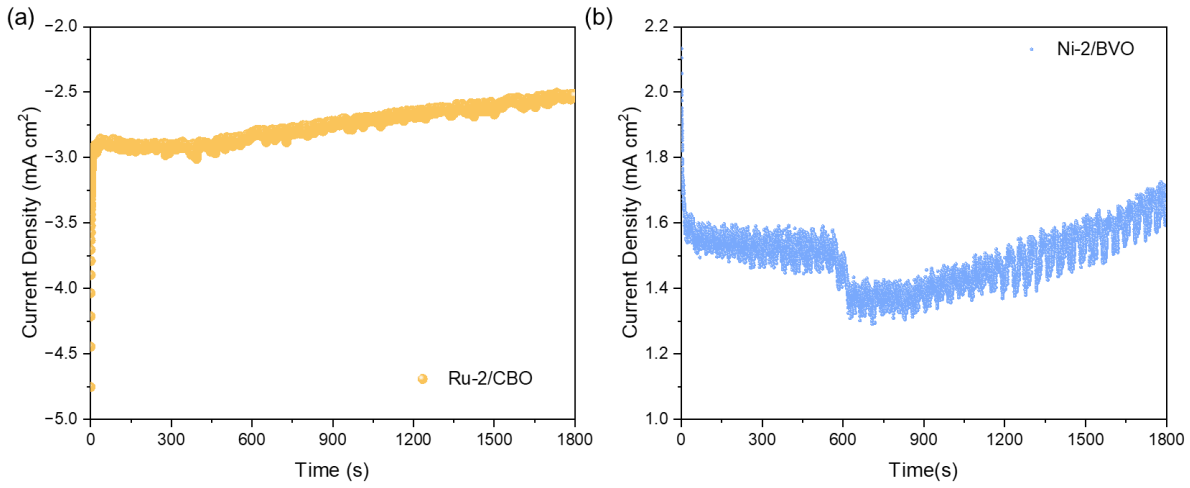

Figure 0-46. I-t plots of (a) Ru-2/CBO photocathodes under illumination at 0.2 V vs. RHE, and (b) Ni-2/CBO photoanodes under illumination at 1.2 V vs. RHE. All measurements were conducted in 1 M KOH containing 10 mM HMF solution (pH = 13).

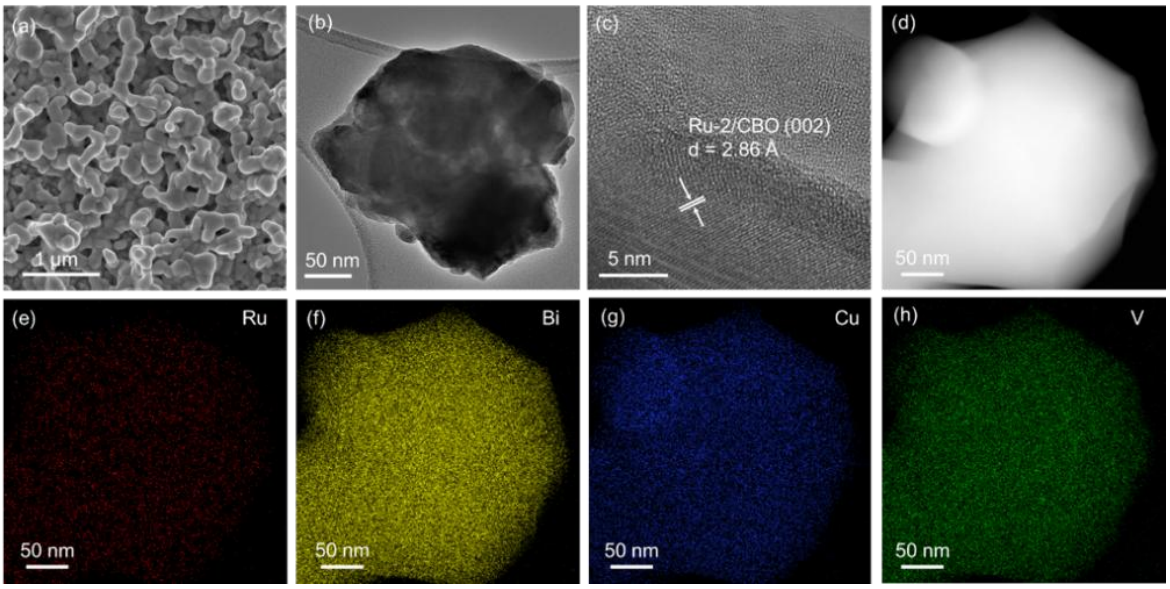

Figure 0-47. Ru-2/CBO after the stability test. (a) SEM image, (b) HADDF image, (c) HR-TEM image, (d) HADDF, and the corresponding (e-h) EDS mapping of Ru-2/CBO after stability test.

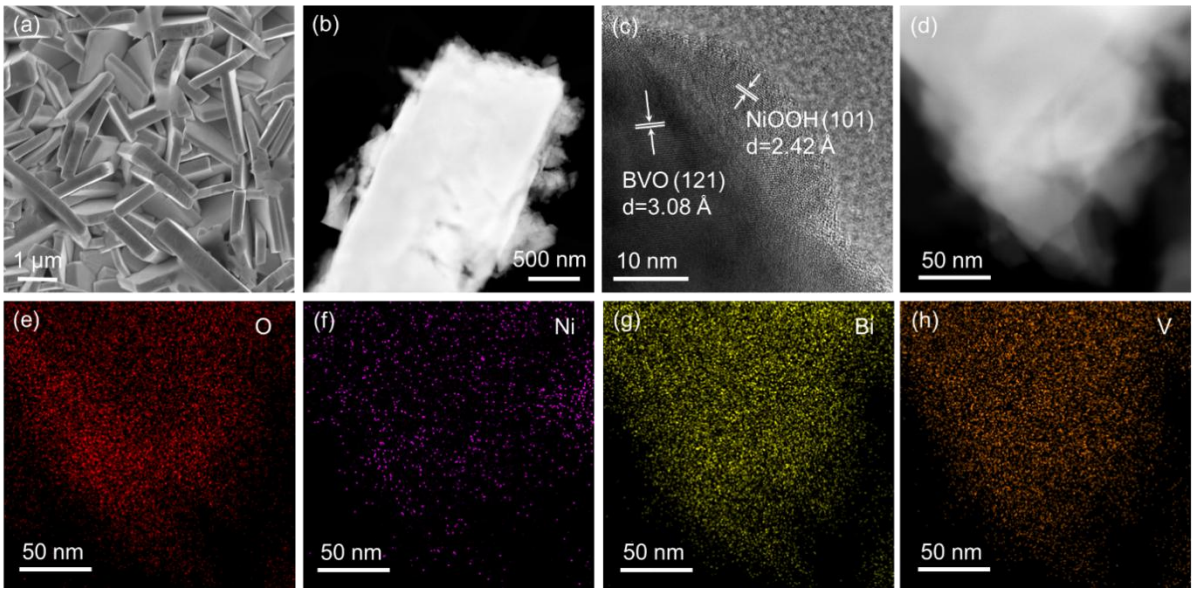

Figure 0-48. NO-2/BVO. (a) SEM image, (b) STEM image, (c) HR-TEM image, (d) HADDF, and the corresponding (e-h) EDS mapping of NO-2/BVO after stability test.

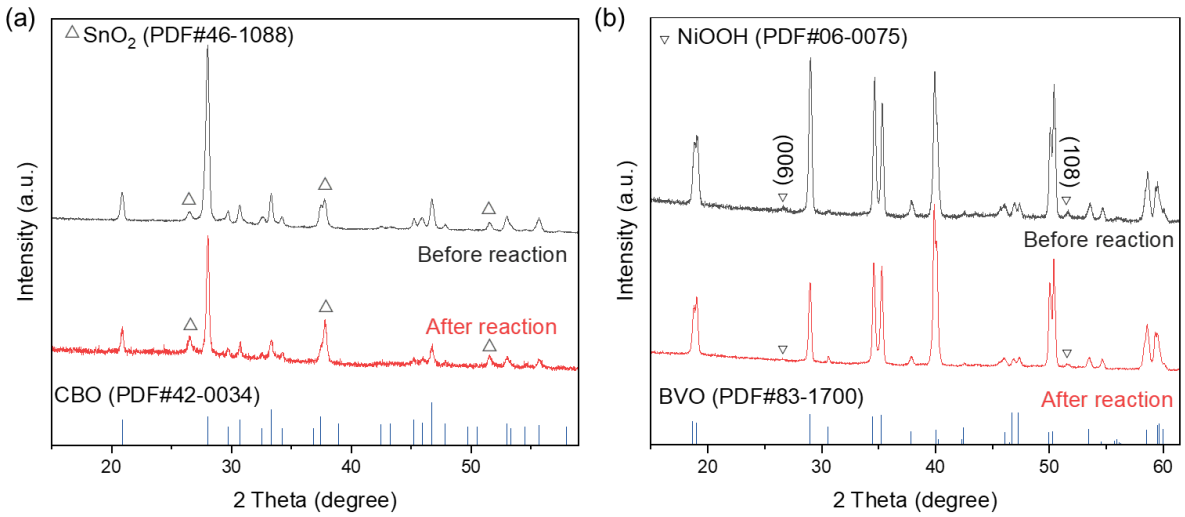

Figure 0-49.XRD pattern of (a) Ru-2/CBO and (b) NO-2/BVO after stability test.

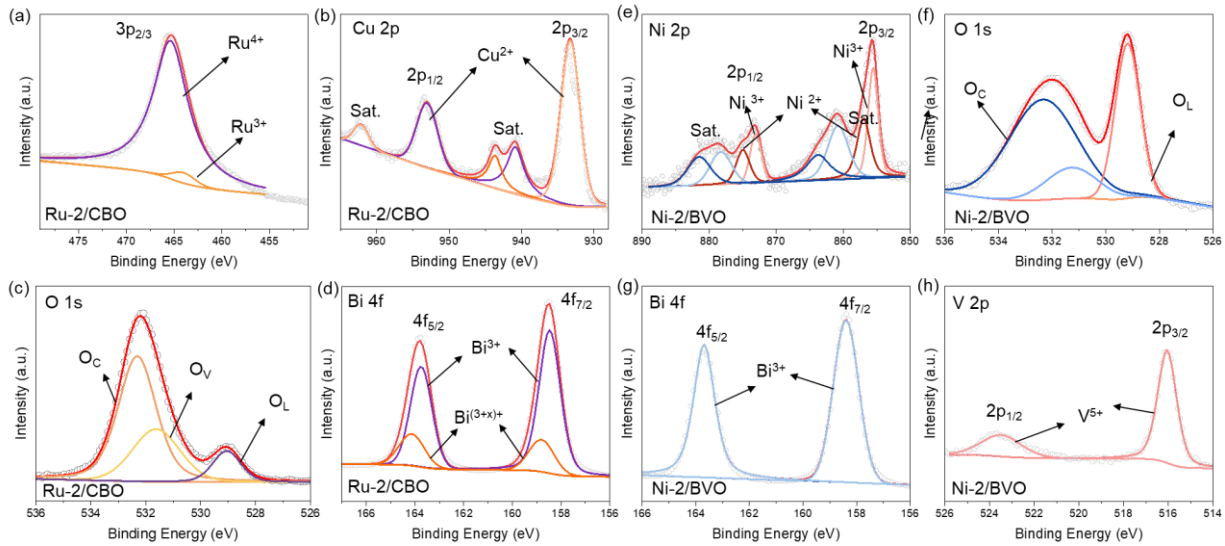

Figure 0-50. XPS spectra of (a-d) Ru-2/CBO and (e-h) NO-2/BVO after stability test.

3.3.5 Mechanistic insights

To elucidate the mechanism of PEC HMF oxidation, electron spin resonance (ESR) spectroscopy was employed with 5,5-dimethyl-1-pyrroline-N-oxide (DMPO) as a spin-trapping agent to identify reactive oxygen species on both photocathodes and photoanodes. When Ru-doped CBO (Ru-2/CBO) photocathodes were under illumination, a distinct superoxide radical ($\cdot O_2^-$) signal was detected, confirmed by the formation of the DMPO-$\cdot O_2^-$ adduct. This signal disappeared in the absence of light, underscoring the essential role of photoexcitation in $\cdot O_2^-$ generation (Figure 0-51a). Ru doping modulated the ESR signal intensity, suggesting enhanced kinetics of $\cdot O_2^-$ production, thereby increasing reactive oxygen species at the Ru-2/CBO surface (Figure 0-51b). *In-situ* XAS was further conducted to assess the structural evolution of Ru-2/CBO under operational PEC conditions, revealing a positive shift in the Ru K-edge XANES absorption onset with increasing bias voltage, which was absent under EC conditions (Figure 0-52 and Figure 0-53). This shift indicates that Ru doping facilitates electron transfer to O_2 during the ORR, enriching Ru sites with electron density, enhancing O_2 adsorption, and promoting HMF oxidation. A concomitant reduction in FT-EXAFS spectra of the Ru-O bond distance supports increased Ru-O interaction as electrons migrate from adsorbed O_2 to the catalyst surface. For the photoanode, NiOOH-modified BVO (NO-2/BVO) analyzed under light irradiation trapped hydroxyl radicals ($\cdot OH$) were identified by ESR, which were absent without illumination, confirming the light-driven generation of $\cdot OH$ (Figure 0-51c). NiOOH modifications further intensified the $\cdot OH$ radical signal, enhancing the catalytic microenvironment on the BVO surface. These findings reveal the

critical role of interfacial charge transfer at the NiOOH-BVO interface and the production of ·OH in the selective oxidation of HMF. The presence of DMPO-·OH adducts also indicates a hole-driven oxidation mechanism involving water molecules, supporting the role of ·OH radicals as active species in PEC HMF oxidation (Figure 0-51d). Ultimately, the ESR study highlights the synergistic 'dual-core processor' function of Ru doping in enhancing $\cdot O_2^-$ radicals and NiOOH modification in boosting ·OH radicals, thereby improving PEC HMF oxidation efficiency simultaneously at both photoelectrodes.

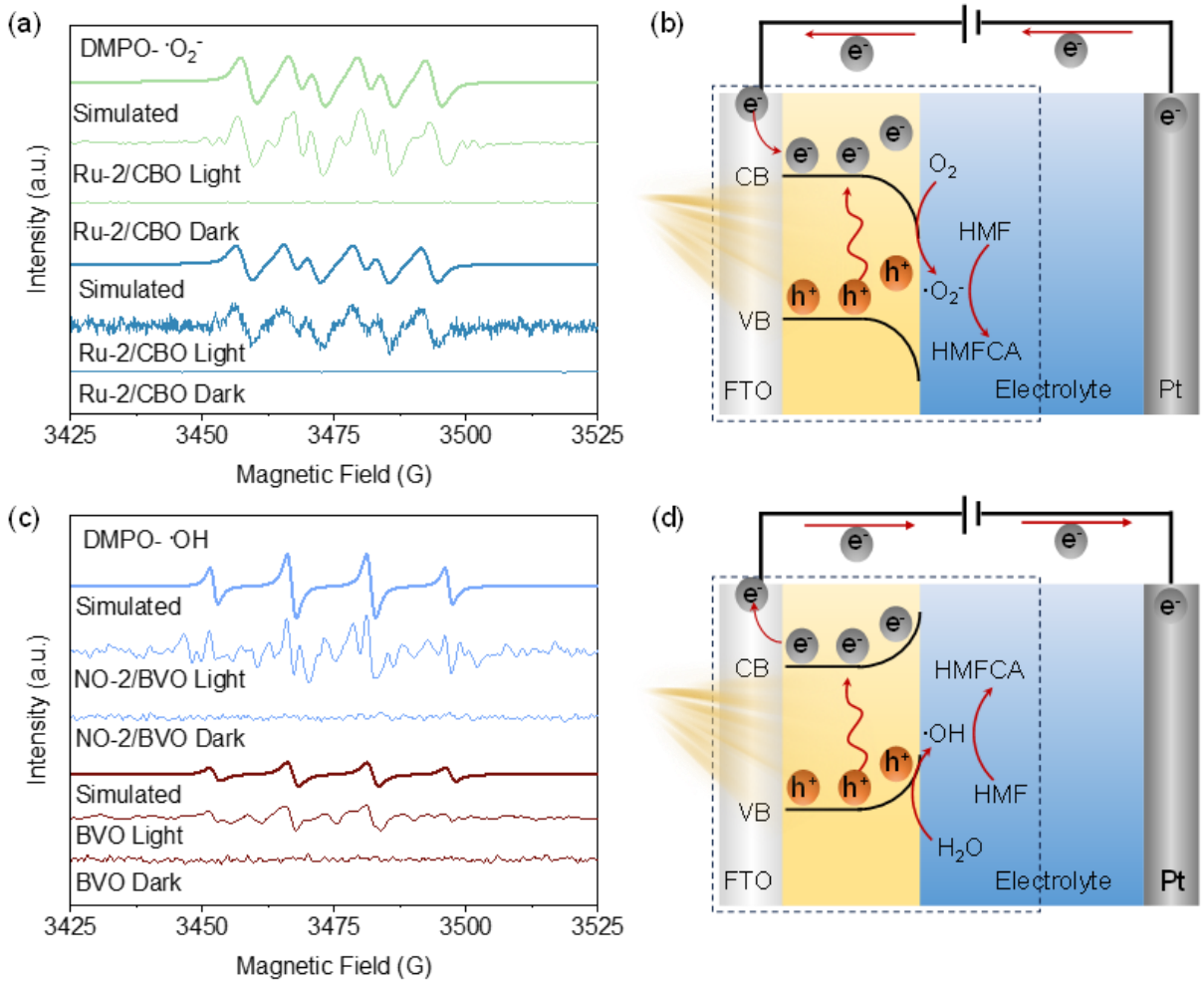

Figure 0-51. (a) DMPO-·O_2^- adduct spin-trap EPR spectra of the CBO and Ru-2/CBO. (b) proposed mechanism of PEC HMF oxidation at Ru-2/CBO photocathode. (c) DMPO-·OH adduct spin-trap EPR spectra of the BVO and NO-2/BVO. (d) proposed mechanism of PEC HMF oxidation at Ru-2/CBO photocathode.

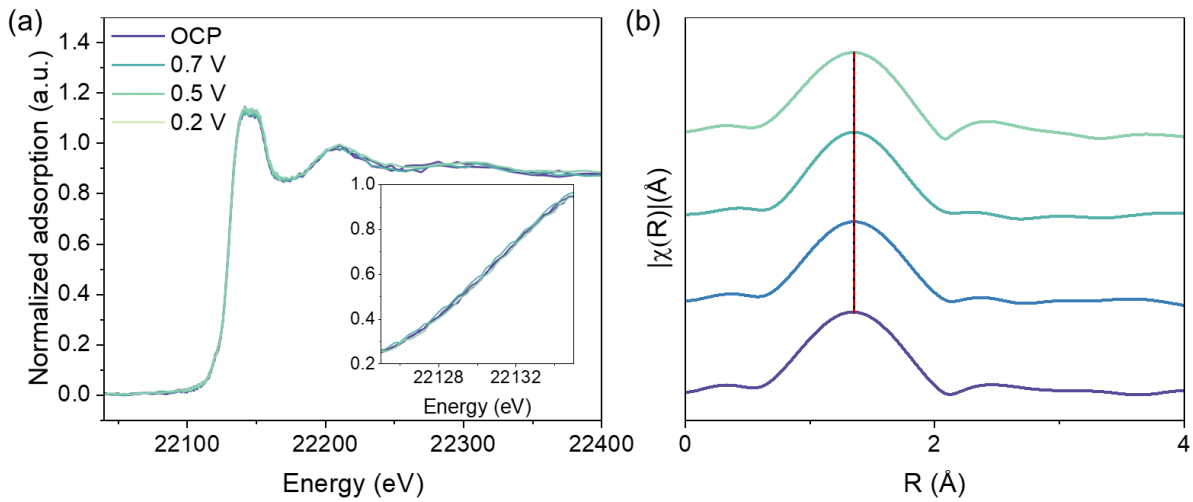

Figure 0-52. (a) *In-situ* Ru K-edge XANES of Ru-2/CBO under EC HMF oxidation. (b) FT-EXAFS spectra of Ru-2/CBO under EC HMF oxidation.

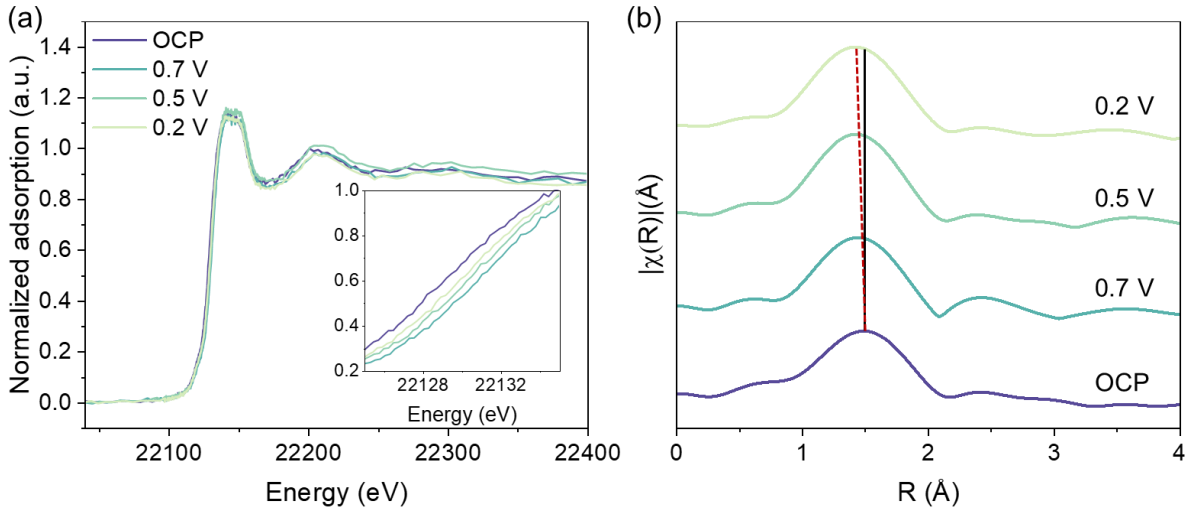

Figure 0-53. (a) *In-situ* Ru K-edge XANES of Ru-2/CBO under PEC HMF oxidation. (b) FT-EXAFS spectra of Ru-2/CBO under PEC HMF oxidation.

3.4 Conclusion

In this study, we present a ground-breaking unbiased tandem PEC system that achieves concurrent selective oxidation of 5- HMF to HMFCA at both photoelectrodes. By integrating a Ru-doped $CuBi_2O_4$ (Ru-2/CBO) photocathode and a NiOOH-modified $BiVO_4$ (NO-2/BVO) photoanode in a continuous-flow setup, the system effectively suppresses humin formation and maximizes HMFCA yield. Through a synergistic 'dual-core processor' mechanism, the system leverages NO-2/BVO at the photoanode to regulate the generation of ·OH radicals, enhancing oxidative reactivity, while Ru-2/CBO at the photocathode promotes ORR to generate $\cdot O_2^-$

radicals, as evidenced by ESR and in-situ XAS analyses. This tandem PEC system achieves an impressive stable photocurrent of 0.68 mA cm^{-2}, HMFCA selectivity exceeding 75% at both photoelectrodes and an ultrahigh FEHMFCA of 153.4%. Furthermore, the self-powered PEC configuration, driven entirely by solar energy, demonstrates industrial scalability, achieving an HMFCA yield of 355.2 mmol m^{-2}. These results not only underscore the potential of tandem PEC systems as a transformative platform for selective biomass conversion but also highlight their alignment with carbon-neutral and sustainable energy goals. The framework presented here offers a robust pathway for advancing PEC technology in biorefining, paving the way for scalable, efficient, and environmentally friendly biomass conversion.

Chapter 4 – Heterojunction-Engineered photoelectrocatalytic glycerol oxidation coupled with on-site H_2O_2 production

Abstract

The selective oxidation of biomass-derived compounds is a cornerstone of sustainable chemical production, offering pathways to integrate renewable energy into industrial processes. In this work, we present the first proton exchange membrane (PEM) photoelectrochemical (PEC) flow cell for simultaneous glycerol valorization and hydrogen peroxide (H_2O_2) production. Optimizing $Bi_2O_{2.33}/TiO_2$ (BO-*x*/TO, *x* = 1, 2, and 3) heterostructures as advanced photoanodes to achieve selective glycerol oxidation to dihydroxyacetone (DHA) at low bias of 0.45 V vs. RHE. The optimized BO-2/TO photoanode demonstrated a photocurrent density of 1.2 mA cm^{-2}, achieving a DHA yield of 1680 mmol m^{-2} h^{-1} with 49% selectivity. Mechanistic insights revealed that the incorporation of BO not only selectively activates the middle hydroxyl group of glycerol but also enhances the generation of hydroxyl radicals (·OH), which are critical for promoting selective oxidation to DHA while suppressing over-oxidation pathways. Simultaneously, the cathode yields H_2O_2 on-site and enhances overall system performance. This innovative integration of PEM technology with PEC systems establishes a scalable and energy-efficient platform for biomass valorization, bridging the gap between green chemistry and renewable energy, and setting a new benchmark for sustainable chemical transformation.

Keywords: Photoelectrocatalysis; glycerol oxidation; DHA; H_2O_2 production.

4.1 Introduction

The selective oxidation of biomass-derived compounds has gained significant attention due to its critical role in sustainable chemical production and renewable energy development.[31] Biomass oxidation not only valorizes renewable resources into high-value chemicals but also reduces dependence on fossil-based feedstocks, contributing to a circular economy.[50] Among various biomass derivatives, glycerol, a byproduct of biodiesel production, stands out as an attractive feedstock for oxidation due to its high availability, low cost, and potential to yield

value-added products such as dihydroxyacetone (DHA), glyceraldehyde (GLD), and formic acid (FA).[338,339] However, achieving efficient and selective glycerol oxidation remains a challenge due to its complex reaction pathways and the need for precise control over intermediate product formation.

The efficient oxidation of glycerol typically relies on noble-metal catalysts in thermocatalytic processes,[340] which operate at high temperatures and pressures and are economically prohibitive and environmentally taxing.[341] In contrast, the photoelectrocatalytic (PEC) strategy offers a green alternative by operating under ambient conditions, driven by solar energy, and providing enhanced control over reaction pathways through the application of an external bias. The PEC approach allows selective oxidation of glycerol to DHA, a valuable intermediate widely used in cosmetics, pharmaceuticals, and fine chemicals.[198,342] However, achieving high efficiency and selectivity in PEC glycerol oxidation remains challenging due to the intrinsic limitations of commonly used semiconductor photoanodes. TiO_2 (TO), one of the most extensively studied semiconductors for PEC applications, suffers from limited visible light absorption and rapid charge recombination, which impede its performance as a photoanode.[343] Consequently, there is a pressing need for improved photoanode materials that can overcome these limitations and achieve efficient PEC glycerol oxidation.[344] Among these, the design of heterostructures for photoanodes has demonstrated remarkable potential due to the unique properties of $Bi_2O_{2.33}$, including its narrow bandgap, high electron mobility, and ability to introduce oxygen vacancies that promote charge transport and surface reaction kinetics. These features make $Bi_2O_{2.33}/TiO_2$ a highly effective photoanode for selective glycerol oxidation.

Under typical photoelectrocatalytic reactions, the oxidation reaction at the photoanode is paired with hydrogen evolution at the photocathode.[227,345] While hydrogen production is an important goal for sustainable energy, its storage and transport remain significant challenges. To address this issue, hydrogen evolution can be replaced with the production of hydrogen peroxide (H_2O_2) at the photocathode.[346] H_2O_2 is a valuable chemical widely used in industries such as water treatment, paper bleaching, and disinfection.[347] By coupling glycerol oxidation at the $Bi_2O_{2.33}/TiO_2$ photoanode with H_2O_2 production at the cathode, this system not only enhances resource efficiency but also offers a practical solution for integrating PEC processes into industrial applications.

In this work, we designed $Bi_2O_{2.33}/TiO_2$ (BO-*x*/TO, *x* = 1, 2, and 3) heterostructures as efficient photoanodes for selective glycerol oxidation in PEC systems. By optimizing the BO-to-TO ratio, the BO-2/TO photoanode achieved a remarkable DHA yield of 1680 mmol m^{-2} h^{-1} with

49% selectivity, nearly doubling the performance of pristine TO. Mechanistic studies revealed that $Bi_2O_{2.33}$ enhances hydroxyl radical (·OH) generation and selectively interacts with glycerol intermediates to drive DHA formation. Coupled with a cathodic H_2O_2 yield of 0.083 mmol L^{-1}, this system demonstrates the potential of heterostructure photoanodes for integrating biomass valorization with solar energy harvesting, providing a scalable pathway for sustainable energy and chemical production.

4.2 Methods

4.2.1 Materials and reagents

Titanium butoxide ($C_{16}H_{36}O_4Ti$), bismuth nitrate pentahydrate ($Bi(NO_3)_3·5H_2O$), hydrochloric acid (HCl, 37 wt%), sulfuric acid (H_2SO_4) and Glycerol ($C_3H_8O_3$, ≥99%) were purchased from Sigma Co., Ltd. FTO substrates (FTO, 13-15 Ω) were received from Nippon Sheet Glass Co., Ltd.

4.2.2 Synthesis of TiO_2 Photoanode

TiO_2 nanorod arrays were prepared using a hydrothermal method. The FTO substrate was cleaned with acetone, isopropanol, and deionized water to eliminate impurities. Under constant stirring, 0.175 mL of titanium butoxide was added to a solution containing equal volumes of H_2O and HCl (6 mL each, 37 wt%). The mixture, along with the pretreated FTO substrate, was transferred into a Teflon-lined stainless-steel autoclave, sealed, and heated at 150 °C for 20 h. The resulting TiO_2 nanorod array was removed, washed with deionized water, and dried in air. The final product was annealed at 350 °C for 2 h with a heating rate of 10 °C min^{-1}.

4.2.3 Synthesis of $Bi_2O_{2.33}/TiO_2$ Photoanode

The $Bi_2O_{2.33}/TiO_2$ photoanode was fabricated in two steps. First, bismuth was electrodeposited onto the TiO2 nanorod array (denoted as Bi/TiO_2). Electrodeposition was performed at room temperature using a three-electrode setup, with the TiO_2 electrode rotated and held at -0.6 V (vs. Ag/AgCl) in an electrolyte containing 1 mmol $Bi(NO_3)_3·5H_2O$, 50 mL of water, and 100 mL of ethylene glycol. After deposition, the Bi-coated TiO_2 (Bi/TiO_2) was washed with ethanol. The second step involved calcining the Bi/TiO_2 at 450 °C for 2 h with a heating rate of 5 °C min^{-1}, converting the deposited Bi into Bi_2O_3 to form Bi_2O_3/TiO_2. Samples were prepared with varying electrodeposition times of 300 s, 600 s, and 1200 s, labeled as BO/TO-*x* (*x* = 1, 2, and 3).

4.2.4 Photoelectrochemical measurements

Photoelectrochemical measurements were conducted on an electrochemical workstation (CHI 660e, CH Instruments, Inc.) using a quartz cell (20 mL) in a three-electrode system (Ag/AgCl electrode as reference electrode and Pt foil as counter electrode). The simulated solar illumination was obtained from a 300 W Xenon lamp. The electrolyte contains 1 M Na_2SO_4 (pH = 2, adjusted by H_2SO_4) aqueous solution. The photocurrent was recorded at a scan rate of 10 mV s^{-1} with or without the presence of 0.1 M glycerol. All potentials mentioned in this work were converted to potentials versus RHE (in volts) according to equation 4-1:

$$E_{RHE} = E_{Ag/AgCl} + E_{Ag/AgCl\ vs\ NHE} + 0.059\ pH \qquad \text{(Equation 4-1)}$$

where $E_{Ag/AgCl\ vs\ NHE}$ in eq 1 is 0.197 V at 25 ºC.

According to the MS curves, the charge carrier density (Nd) can be calculated using the following equation:

$$N_d = \frac{2}{e\varepsilon_0\varepsilon} \times \left(\frac{d\left(\frac{1}{C^2}\right)}{dV_s} \right)^{-1} \qquad \text{(Equation 4-2)}$$

The electronic charge (e) is 1.6×10^{-19} C, vacuum permittivity (ε0) is 8.86×10^{-14} F m^{-1}, and relative permittivity (ε) is 68 for BVO.[313] C (F cm^{-2}) is the space charge capacitance in the semiconductor (obtained from MS curves), and Vs (V) is the applied potential for MS curves.

The ABPE can be calculated by the photocurrent-potential curves under simulated sunlight using the equation:

$$ABPE\ (\%) = [(1.23 - V) \times J / P_{light}] \times 100\% \qquad \text{(Equation 4-3)}$$

where V is the applied potential, J is the photocurrent density (mA cm^{-2}), and P_{light} is the power density of a 300 W Xe lamp.

The IPCE was obtained using a monochromator coupled with a 300 W Xe lamp as the simulated light source. An applied potential of 1.23 V vs. RHE was supplied by a CHI660e electrochemical workstation, and the power density at a specific wavelength was measured by a Newport power meter. IPCE values were calculated using the following equation:

$$IPCE\ (\%) = [1240 \times J_{light} / \lambda \times P_{light}] \times 100\% \qquad \text{(Equation 4-4)}$$

where J_{light} is the photocurrent density (mA cm^{-2}) obtained from the electrochemical workstation, λ is the wavelength (nm) of incident radiation, and P_{light} is the power density obtained at a specific wavelength (mW cm^{-2}).

4.2.5 PEC glycerol oxidation

PEC glycerol oxidation measurements Under general reaction conditions, the photoanode was immersed in 0.5 M Na_2SO_4 (pH = 2) containing 0.1 M glycerol in a quartz cell. The solution was stirred continuously at 500 rotations min^{-1}. Then, the PEC oxidation of glycerol was performed at a potential of 1.0 V vs. RHE for 1 h under AM 1.5G, 100 mW cm^{-2} illumination, and the temperature was maintained at room temperature (around 298 K). After the reaction, 1 mL of solution was taken out from the cell and analyzed using high-performance liquid chromatography (HPLC) to calculate the glycerol conversion and yields of the products using a Shimazu LC-20AD chromatograph equipped with an Aminex HPX-87H (300 mm, 7.8 mm) column and SPD and RID detector. The eluent was a 5 mM H_2SO_4 at a flow rate of 0.3 mL min^{-1}. The selectivity of DHA was calculated based on:

$$Selctivity_{DHA} = \frac{n_{DHA}}{n_{DHA}+n_{GLD}+n_{FA}} \qquad \text{(Equation 4-5)}$$

Where $n_{DHA} + n_{GLD} + n_{FA}$ are the yield of DHA, glyceraldehyde, and formic acid, respectively.

The Faradic efficiency is calculated based on the following equation:

$$Faradic\ efficiency_{DHA} = \frac{e_{DHA} \times n_{DHA} \times N}{Q/n} \qquad \text{(Equation 4-6)}$$

where e_{DHA} is the 2, N is Avogadro's constant, Q is the quantity of electric charge, and n is the elementary charge.

4.2.6 H_2O_2 quantification

The H_2O_2 concentration was detected by cerium sulfate ($Ce(SO_4)_2$) titration-based colorimetric method.[348] Early in the titration, the presence of Ce^{4+} can be easily observed by a yellowish solution color. While the product solution was added to the titration solution, Ce^{4+} would be bleached by H_2O_2 (equation 4-7), therefore the H_2O_2 concentration could be quantified according to the consumption of Ce4+ measured by ultraviolet-visible spectroscopy at the wavelength of 317 nm.

$$2Ce^{4+} + H_2O_2 \rightarrow 2Ce^{3+} + 2H^+ + O_2 \quad \text{(Equation 4-7)}$$

To prepare the standard $Ce(SO_4)_2$ titration solution (1 mM), 33.224 mg $Ce(SO_4)_2$ was dissolved in 100 mL 0.5 M sulfuric acid solution (H_2SO_4). Afterward, to fit the linear range of the calibration curve, the stock solution was further diluted 10 to 100 times with 0.5 M H_2SO_4. In the standardized analysis process, 500 μL sample electrolyte was added to 5 mL 0.1 mM $Ce(SO_4)_2$ solution and measured by ultraviolet-visible spectroscopy. Based on the fitting calibration curve, the mole of H_2O_2 can be determined by the mole of consumed Ce^{4+} (Equation 4-8).

$$mH_2O_2 = 1/2 \times mCe^{4+} \quad \text{(Equation 4-8)}$$

4.2.7 DFT calculation

All the spin-polarized density functional theory (DFT) calculations[314] were conducted as implemented in the Vienna ab initio simulation package (VASP).[236] The Perdew-Burke-Ernzerhof (PBE)[317] form of the generalized gradient approximation (GGA) was used for describing the exchange and correlation function, and the spin-orbit coupling (SOC) was included. The valence states and core-valence electron interactions were modeled using projector augmented wave (PAW) pseudopotentials,[316] with the plane-wave basis set cutoff energy of 500 eV. To accurately define geometries and electronic properties of the systems, the DFT-D3 scheme of Grimme was adopted for describing van der Waals (vdW) interactions.[315] The $Bi_2O_{2.33}$ (110) surface models were constructed by 3 × 3 slabs of 4 layers separated by 20 Å of vacuum in periodic cells. Surface calculations were performed with a Monkhorst–Pack sampling of 2 × 2 × 1 k-point grid. All the atomic positions were fully relaxed until the residual forces were less than 0.005 eV/Å.

4.3 Results

4.3.1 Morphology and composition

The $Bi_2O_{2.33}/TiO_2$ heterostructure photoanodes were synthesized by a two-step process: hydrothermal synthesis of TiO_2 nanorods on the fluorine-doped tin oxide (FTO), followed by electrodeposition of Bi onto the TiO_2 surface, then calcined and recorded as BO-*x*/TO (*x* = 1, 2, and 3).

Figure 0-1 shows an SEM micrograph of a hydrothermally prepared TO rod on the FTO

substrate, which exhibits a uniform rod-like structure and a tetragonal prism morphology. The top surface of these rods is uneven and contains many upper and lower edge points (Figure 0-2). The cross-section SEM image of the BO-2/TO sample shows that the BO-loaded TO nanorods still grow vertically on the substrate with a length of about 2.7 μm (Figure 0-3a). After supporting BO on the TO rods, BO spheres are observed to cover the TO rods. The spherical BO crystals were modified on the top and sidewall surfaces of the TO rods, resulting in an uneven morphology of the BO-*x*/TO (*x*=1, 2 and 3) composite rods (Figure 0-3b, Figure 0-4 and Figure 0-5). The spherical BO on the surface of the rod increased the specific surface area, which was beneficial to improve its photoactivity.

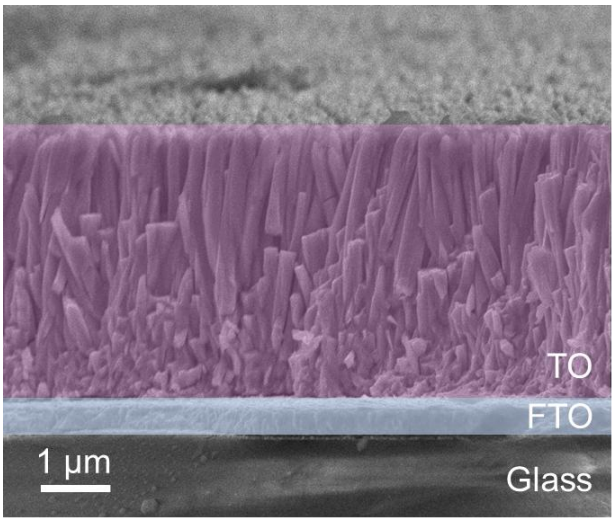

Figure 0-1. The cross-section SEM images of TO.

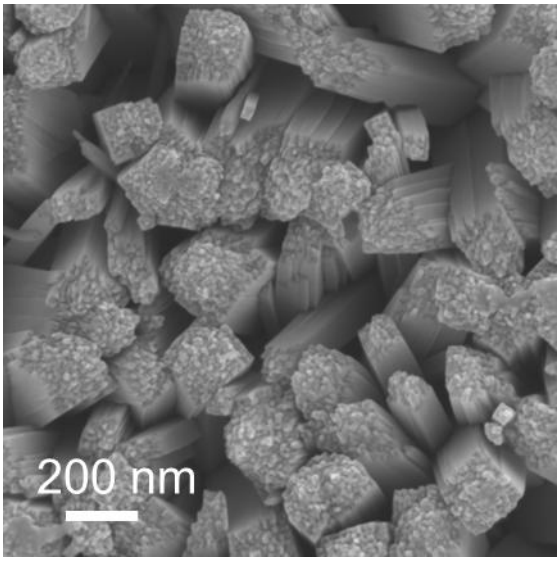

Figure 0-2. The top-view SEM images of TO.

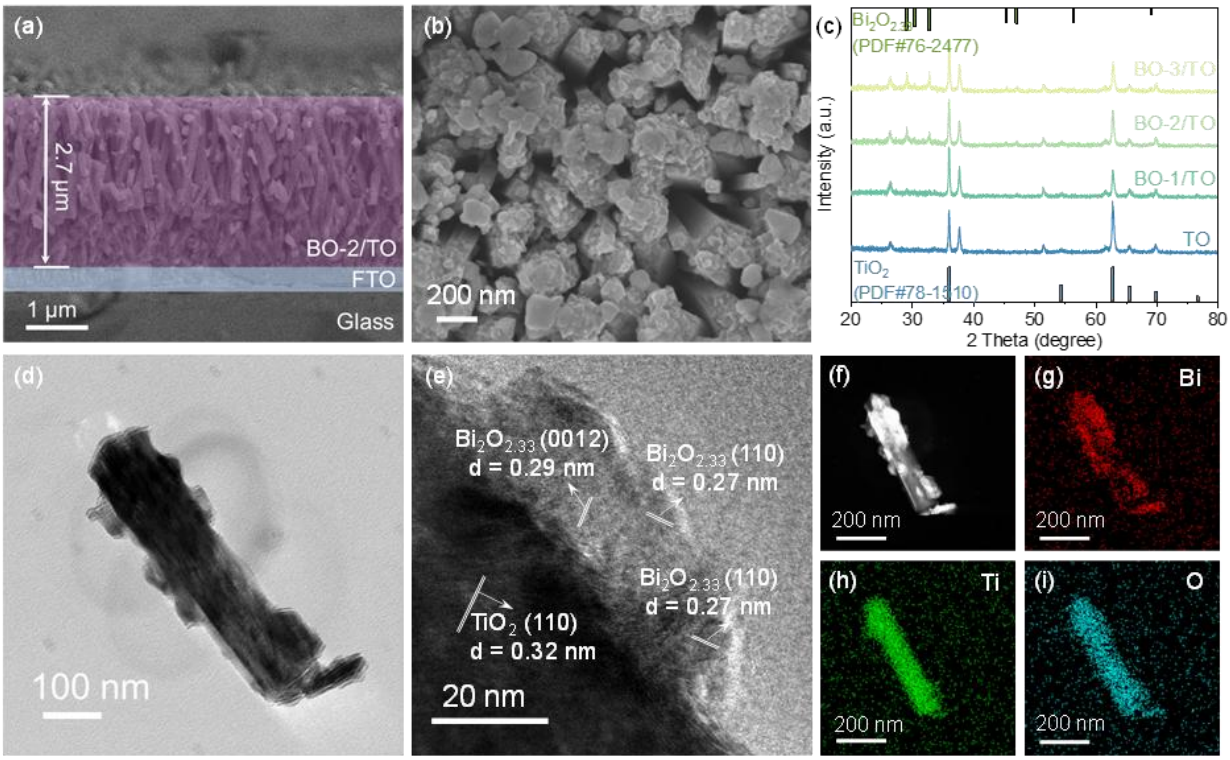

Figure 0-3. (a) The cross-section SEM image and (b) top-view SEM image of BO-2/TO. (c) XRD pattern of BO-*x*/TO (*x*=1, 2 and 3) and TO, (d) TEM image, (e) HR-TEM image, (f) STEM-HADDF image of BO-2/TO, and the corresponding element mapping of (g) Bi, (h) Ti and (i) O.

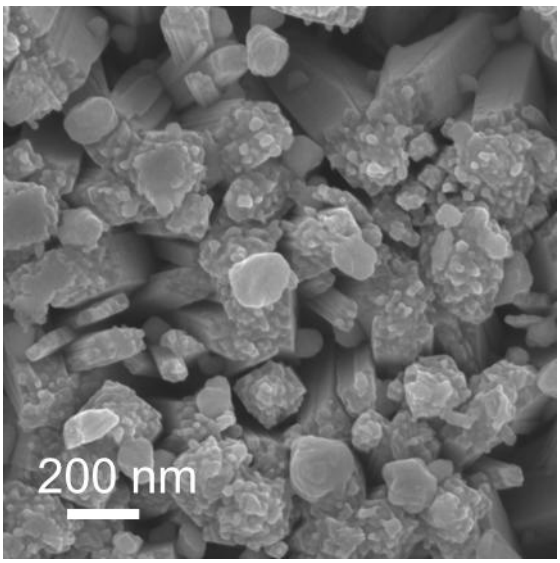

Figure 0-4. The top-view SEM images of BO-1/TO.

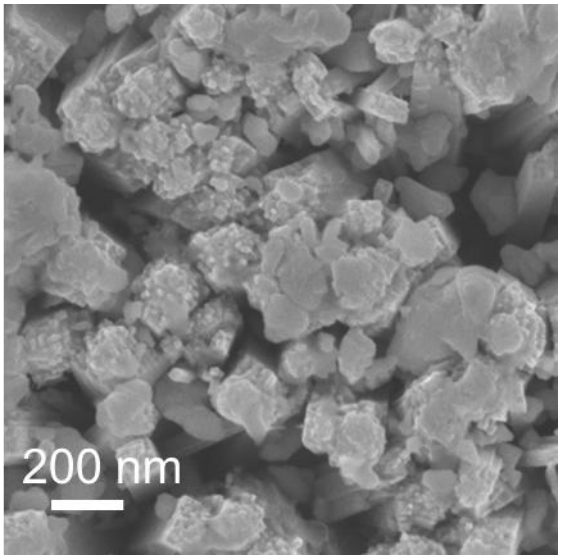

Figure 0-5. The top-view SEM images of BO-3/TO.

XRD has been used to understand the crystal structure of the photoanode (Figure 0-3c). The diffraction peaks of TO nanorods can be attributed to the anatase structure of TiO_2 (PDF# 78-1510), which has been shown to be beneficial for photocatalytic glycerol oxidation.[349,350] For BO-x/TO samples, in addition to the diffraction peaks attributed to anatase TiO_2, the peaks at about 32.88° and 47.16° can be attributed to the (110) and (200) planes of $Bi_2O_{2.33}$ (PDF# 76-2477). In addition, as the $Bi_2O_{2.33}$ content increases from BO-1 to BO-3, the diffraction peaks at around 25.35°, 26.38°, and 29.22° are slightly enhanced, corresponding to the (010), (105), and (107) planes of $Bi_2O_{2.33}$, respectively, indicating that the loading of $Bi_2O_{2.33}$ has an increasing trend. Transmission electron microscopy (TEM, Figure 0-3d) further supports that BO-2/TO still maintains the nanorod morphology of TO, and it can be clearly seen that BO is loaded on the nanorod surface. High-resolution TEM (HR-TEM, Figure 0-3e) further supports this finding, showing that BO-2/TO has clear lattice fringes, where the interplanar spacing of 0.32 nm corresponds to the (110) plane of TiO_2, and 0.27 nm and 0.29 nm correspond to the (1 1 0) and (0 0 12) planes of $Bi_2O_{2.33}$, respectively. The clear interface between the two can promote faster charge transfer and enhance electronic properties, which is crucial for the subsequent PEC catalytic efficiency. Element distribution mapping by scanning transmission electron microscopy (STEM) and corresponding EDS mapping (Figure 0-3f, Figure 0-3g, Figure 0-3h and Figure 0-3i) show that the Ti, O and Bi components are evenly distributed.

XPS analysis was conducted to determine the chemical composition and binding energy of the samples (Figure 0-6, Figure 0-7 and Figure 0-8). As shown in the high-resolution Ti 2p spectrum of the TO sample, two characteristic peaks are observed at 458.55 eV and 464.25 eV,

corresponding to Ti $2p_{3/2}$ and Ti $2p_{1/2}$, respectively, confirming the presence of Ti in the +4 state in the TO nanorod. Additionally, the presence of Bi 4f peaks in the BO-2/TO spectrum indicates that bismuth oxide has been successfully deposited onto the TO nanorod. In the high-resolution Bi 4f spectrum of BO-2/TO, two peaks are observed at binding energies of 164.33 eV and 159.13 eV, corresponding to Bi $4f_{5/2}$ and Bi $4f_{7/2}$, respectively. Notably, these binding energies are shifted to higher values compared to the BO sample, indicating electron transfer from BO to TO. This electron flow suggests a strong electronic interaction between the two components, which likely enhances charge separation and contributes to the improved performance of the BO-2/TO heterostructure.

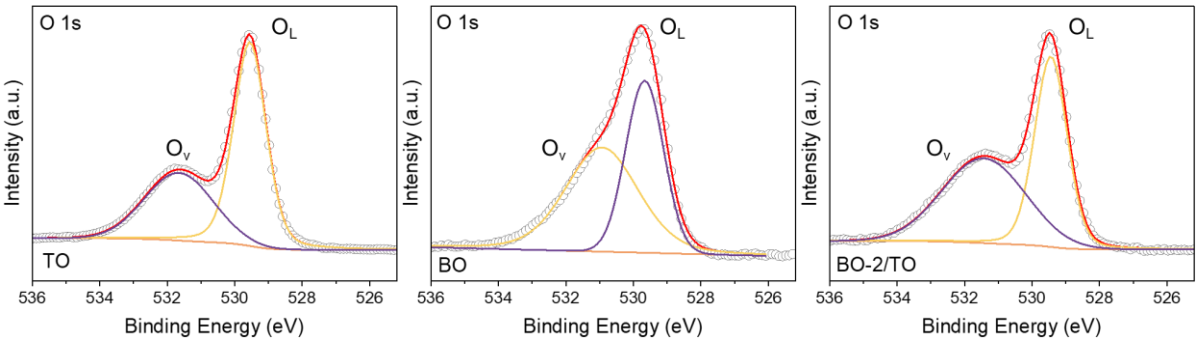

Figure 0-6. High-resolution XPS spectra of TiO_2, $Bi_2O_{2.33}$ and BO-2/TO for O1s.

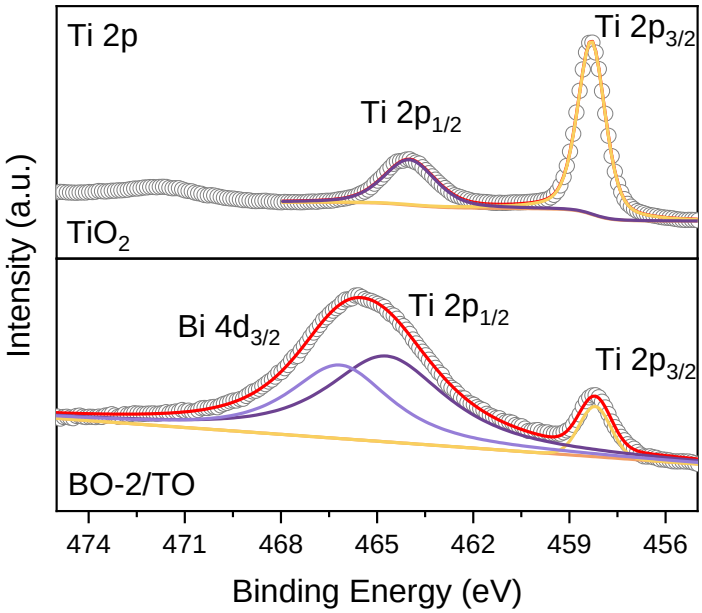

Figure 0-7. High-resolution XPS spectra of TiO_2 and BO-2/TO for Ti 2p.

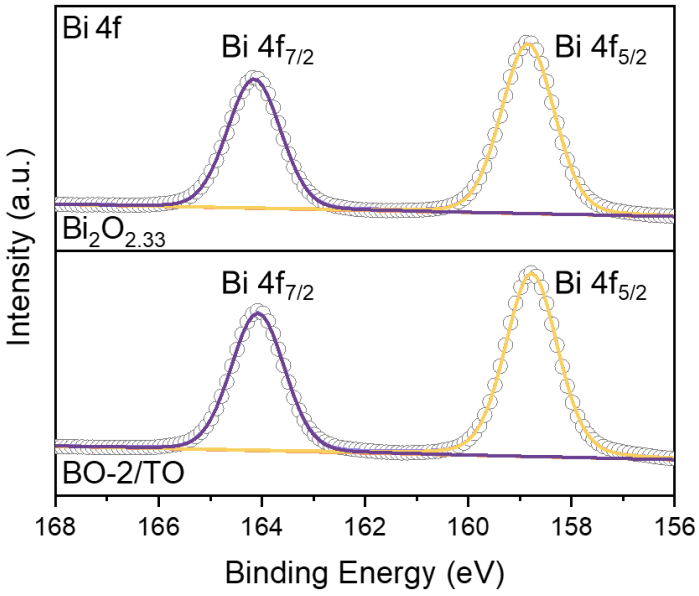

Figure 0-8. High-resolution XPS spectra of Bi2O2.33 and BO-2/TO for Bi 4 f.

4.3.2 Optical and Electronic Properties

Subsequently, we investigated the optical and electronic properties of the BO-*x*/TO (*x*=1, 2 and 3) heterostructure to elucidate its optical properties. The UV-visible absorption spectrum (Figure 0-9a) reveals that both TO and BO-*x*/TO photoanodes absorb light primarily around 420 nm. From the calculated Tauc plots, the band gap of TO is determined to be 3.08 eV, while the band gap of BO is narrower at 2.89 eV (Figure 0-9b and Figure 0-9c), indicating improved light-harvesting capabilities upon BO incorporation.

To further understand the charge dynamics, the photoluminescence (PL) spectra (Figure 0-9d) were analyzed. TO exhibits the highest PL intensity, indicating significant recombination of photoinduced electron-hole pairs. Upon BO doping, the PL intensity systematically decreases, with BO-2/TO showing the lowest emission rate. This suppression of PL intensity highlights enhanced charge separation and a reduced recombination rate, attributed to the improved interfacial charge transfer facilitated by BO doping. However, a slight increase in PL intensity is observed for BO-3/TO, suggesting that excessive BO doping introduces recombination centers, partially negating the benefits of enhanced charge transfer.

These results demonstrate that BO-2/TO achieves the most efficient carrier dynamics, striking an optimal balance between charge separation and recombination suppression. This improvement in carrier dynamics is critical for enhancing the photocatalytic performance of the BO-x/TO heterostructure.

4.3.3 Band Structure and Catalytic Mechanism

To further investigate the photoinduced carrier transfer behavior of the BO-2/TO catalyst, the energy band alignment between BO and TO was analyzed. The energy band positions of pristine TO and BO were determined using valence band-XPS (VB-XPS), as shown in Figures 2e and 2f, with recorded valence band maxima (E_{VB}) of 2.3 eV and 1.6 eV, respectively. Combining these values with the band gap values obtained from the Tauc plots, the conduction band (CB) positions were calculated using the formula $E_{CB}=E_{VB}-E_g$. The calculated CB positions for TO and BO are -0.8 eV and -1.3 eV, respectively.

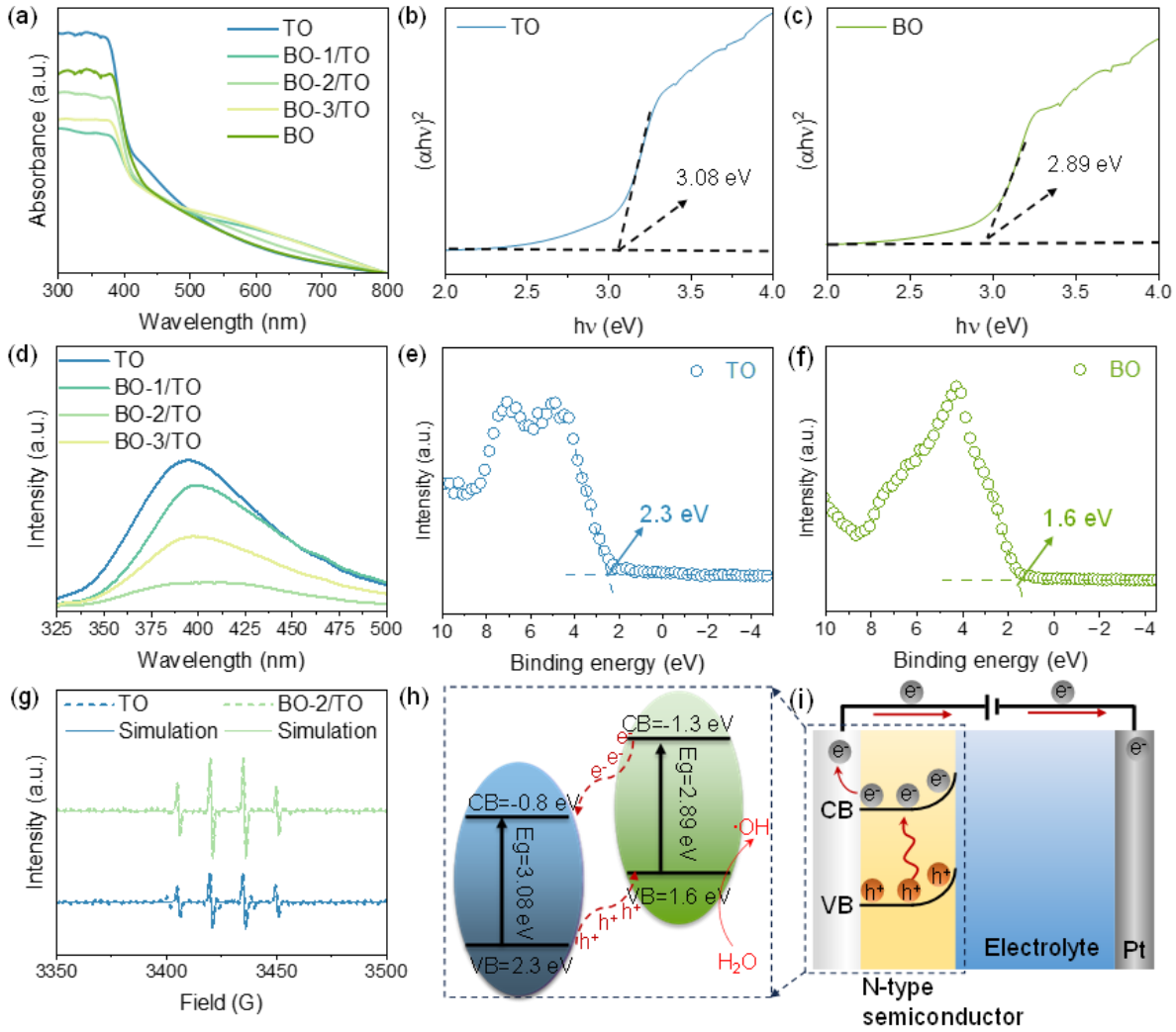

Figure 0-9. (a) UV-vis spectra of BO-*x*/TO (*x*=1, 2 and 3) and TO. Tacu plot of (b) TO and (c) BO, (d) PL spectra of BO-*x*/TO (*x*=1, 2 and 3) and TO. Valence band-XPS spectra of (e) TO and (f) BO. (g) EPR spectra of BO-2/TO and TO, (h) band gap structure of BO-2/TO.

The electron paramagnetic resonance (EPR) spectra in Figure 0-9g provide further insights into

the active species in the TO and BO-2/TO samples. TO exhibits a weak signal, corresponding to a low concentration of hydroxyl radicals (·OH), indicating limited charge transfer and radical generation. In contrast, the BO-2/TO sample shows a significantly stronger EPR signal, demonstrating that BO doping facilitates improved charge transfer and enhances the concentration of active radical species. This highlights the role of BO in boosting the catalytic efficiency of the BO-2/TO heterostructure.

The band alignment between BO and TO is depicted schematically in Figure 0-9h. The staggered type-II heterojunction formed between BO and TO enables efficient charge carrier transport across the interface. Photoinduced electrons generated in BO migrate to the conduction band of TO, while holes in TO transfer to the valence band of BO. This spatial charge separation minimizes recombination losses and facilitates the oxidation of water to generate hydroxyl radicals. The synergistic interactions between BO and TO enhance charge separation, transport, and redox reaction activation, resulting in significantly improved catalytic activity. These findings underscore the potential of the BO-2/TO heterostructure for efficient oxidation reactions and other catalytic applications.

Figure 0-10 provides a comprehensive analysis of the photoelectrochemical (PEC) performance of the BO-*x*/TO (*x*=1, 2 and 3) heterojunction structures, demonstrating their enhanced charge separation, transport, and light utilization properties. The linear sweep voltammetry (LSV) curves (Figure 0-10a and Figure 0-11) were measured under illumination in a 0.5 M Na_2SO_4 electrolyte (pH = 2) with and without 0.1 M glycerol. The baseline PEC performance was initially tested without glycerol in the electrolyte (Figure 0-11). In this case, the BO-*x*/TO (*x*=1, 2 and 3) photoanodes exhibited significantly higher photocurrent densities than the pristine TO photoanode within the potential window of 0.3V-1.4 V vs. RHE. This improvement is attributed to the enhanced light absorption and efficient charge transfer facilitated by the Type II heterojunction formed between BO and TO. Upon the addition of 0.1 M glycerol, the photocurrent densities of both TO and BO-*x*/TO (*x*=1, 2 and 3) were further enhanced. This enhancement occurs because glycerol oxidation has a lower reaction barrier compared to water oxidation (1.23 V vs. RHE).[198] Notably, the BO-2/TO photoanode exhibited the lowest onset potential and the highest photocurrent response, indicating that its optimized Type II heterojunction structure promotes more favorable reaction kinetics for glycerol oxidation. To further elucidate the electrode reaction process, amperometric I-t curves were recorded under chopped light illumination (Figure 0-10b). All photoanodes displayed clear

photocurrent responses corresponding to light on/off cycles, confirming good photoresponsivity. Consistent with the LSV results, BO-2/TO demonstrated the largest photocurrent density under glycerol oxidation conditions, which can be attributed to its superior Type II heterojunction structure, facilitating efficient charge transfer and oxidation kinetics. Importantly, the dark current density remained negligible compared to the photocurrent, confirming that the glycerol oxidation process is primarily driven by the PEC reaction rather than electrocatalysis. To probe the charge transfer kinetics, electrochemical impedance spectroscopy (EIS) measurements were conducted under illumination (Figure 0-12). Compared to TO, BO-*x*/TO (*x*=1, 2 and 3) photoanodes exhibited reduced charge transfer resistance, with BO-2/TO displaying the smallest resistance. This result indicates that the BO-2/TO heterojunction structure effectively improves conductivity and accelerates interfacial charge transfer, further enhancing PEC activity.

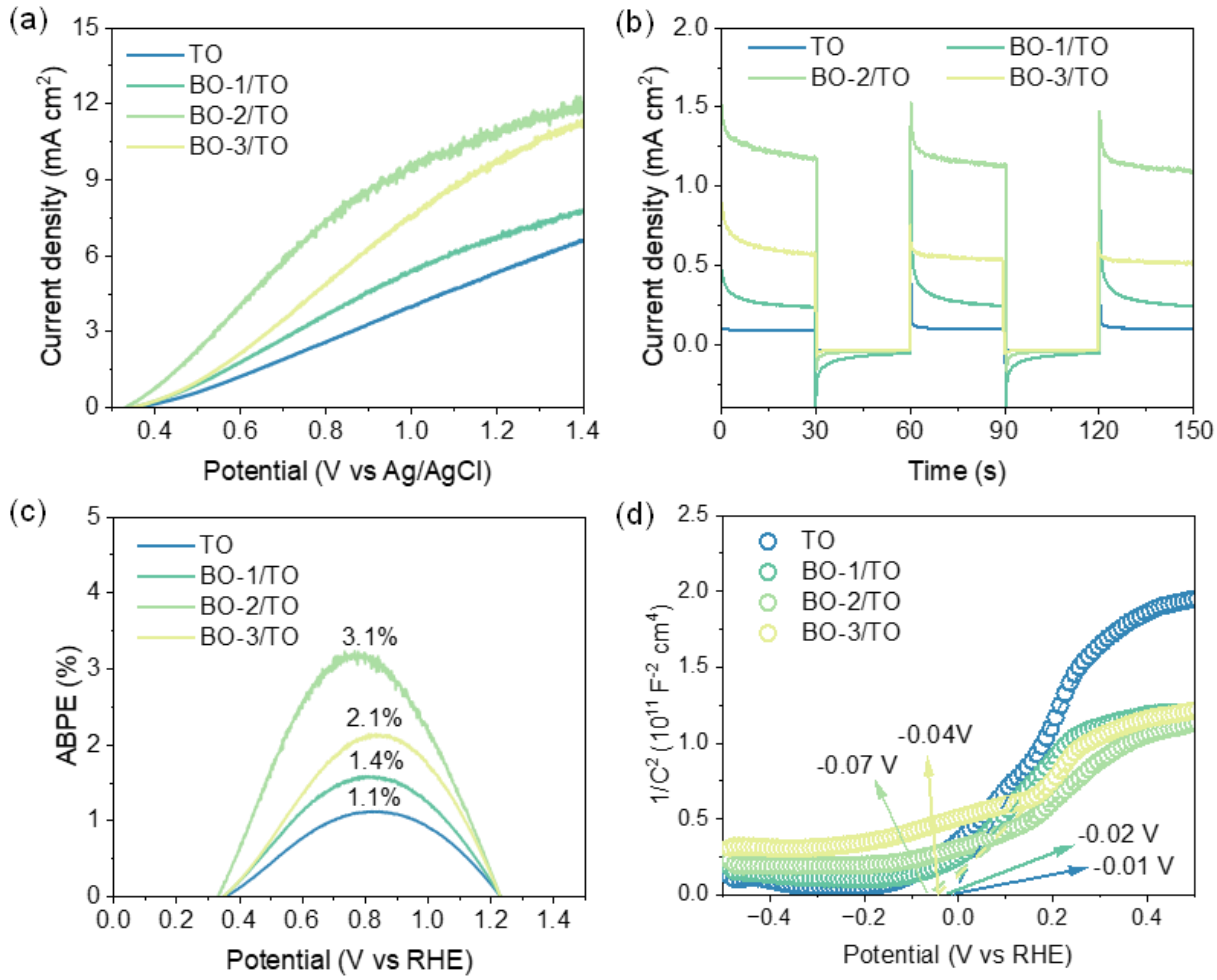

Figure 0-10. (a) LSV curve, (b) I-t curve. Reaction conditions: 0.1 M Na_2SO_4 (pH = 2) with 0.1 M glycerol under illumination (100 mW cm^{-2}). (c) ABPE, (d) MS plot of BO-2/TO.

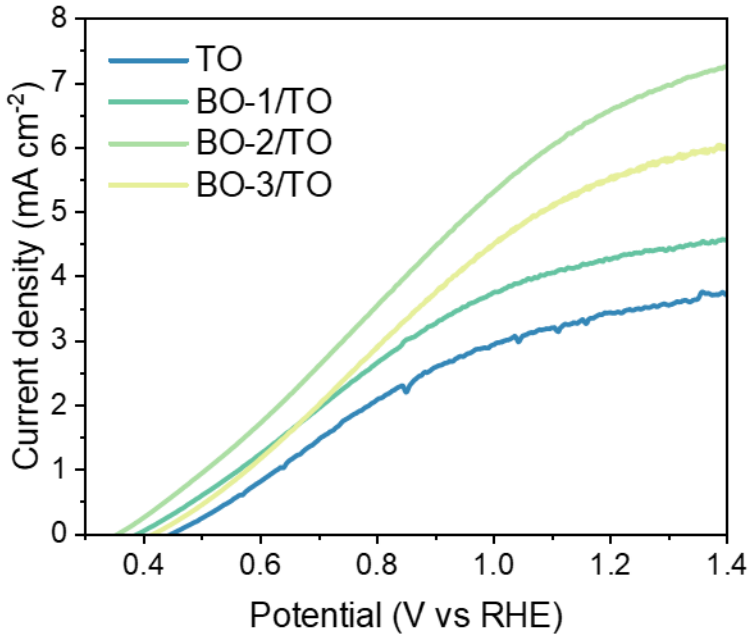

Figure 0-11. Linear sweep voltammetry curves of TO and BO/TO-*x* (*x*= 1, 2 and 3) samples in electrolyte without glycerol.

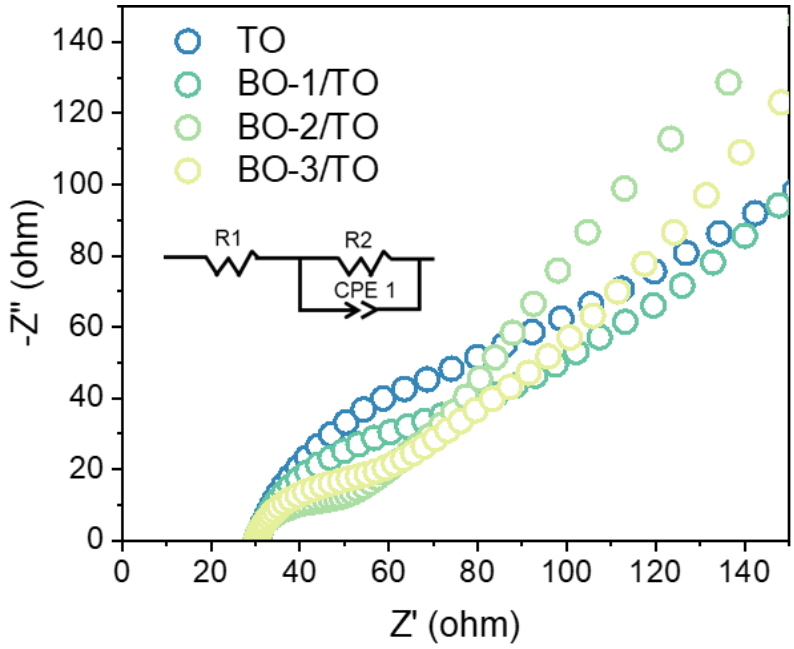

Figure 0-12. EIS plot of TO and BO/TO-*x* (*x*= 1, 2 and 3) samples.

In Figure 0-10c, the applied bias photon-to-current efficiency (ABPE) data provide a quantitative evaluation of the PEC performance of BO-x/TO samples under applied bias. The ABPE curves clearly demonstrate that BO-*x*/TO (*x*=1, 2 and 3) samples exhibit higher peak efficiencies compared to pure TO samples, underscoring their superior solar energy conversion

capability. Among the BO-*x*/TO (*x*=1, 2 and 3) series, BO-2/TO achieves the highest ABPE, reaching a maximum value of 3.1%, which represents an optimal balance between photogenerated charge carrier separation and the driving force provided by the applied bias. This significant enhancement compared to pure TO (1.1%) can be attributed to the incorporation of BO, which improves light absorption and facilitates charge transport across the BO/TO heterojunction, resulting in more efficient utilization of photogenerated carriers. In contrast, the ABPE for BO-3/TO shows a slight decline relative to BO-2/TO. This reduction is likely due to excessive BO loading, which introduces carrier recombination centers, partially hindering charge separation and transfer. These findings highlight that BO-2/TO achieves the most favorable compositional tuning, enabling superior PEC performance. The incident photon-to-current conversion efficiency (IPCE) results (Figure 0-13) further corroborate these observations. In the light absorption range of 400-500 nm, the BO-*x*/TO (*x*=1, 2 and 3) samples exhibit significant improvements in IPCE. For instance, under illumination in 0.5 M Na_2SO_4 electrolyte with 0.1 M glycerol (pH = 2), the IPCE of BO-2/TO reaches 68% at 450 nm, far exceeding that of pure TO (38% at 450 nm). This substantial improvement reflects the optimized electronic structure of the BO-2/TO heterostructure, which enhances light absorption, promotes efficient charge separation, and accelerates interfacial charge transfer. In summary, the ABPE and IPCE analyses collectively demonstrate that the BO-2/TO heterojunction structure achieves an optimal combination of enhanced light absorption, improved charge separation, and accelerated charge transfer, which are critical for high-efficiency glycerol oxidation reactions. These results emphasize the importance of compositional tuning in designing high-performance PEC systems.

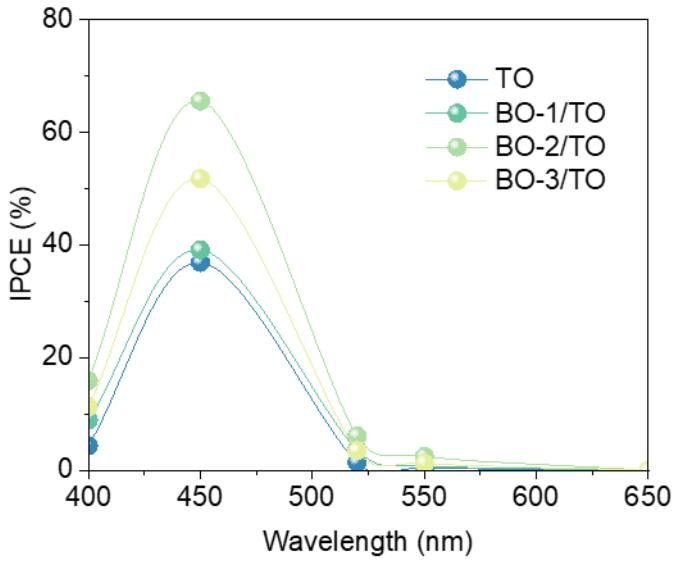

Figure 0-13. IPCE of TO and BO-*x*/TO (*x*=1, 2 and 3).

Mott-Schottky (MS) plots were subsequently collected to evaluate the carrier dynamics of the photoanodes (Figure 0-10d), providing critical insights into their carrier density and flat-band potential (E_{fb}). The positive slopes observed for all samples confirm their n-type semiconductor behavior.[351] Compared to pristine TO, the BO-*x*/TO (*x*=1, 2 and 3) heterostructures exhibit a clear negative shift in the E_{fb}, which suggests a more favorable band alignment for charge transfer. Additionally, the carrier densities, as extracted from the slopes of the Mott-Schottky plots and summarized in Table 0-1, show a significant improvement for the BO-*x*/TO (*x*=1, 2 and 3) samples. Among all samples, BO-2/TO demonstrates the steepest slope, indicating the highest carrier density.[352] This increased carrier density is critical for facilitating efficient charge separation and transfer, thereby enhancing the catalytic performance of the photoanode. In contrast, the slope for BO-3/TO decreases, suggesting a reduction in carrier density. This decline is likely due to excessive BO loading, which introduces recombination centers, thereby impeding charge transfer efficiency. The MS analysis reveals that BO-2/TO achieves an optimal balance of electronic properties, including enhanced carrier density and favorable band alignment, which are pivotal for improving charge transport and achieving superior photoelectrochemical performance.

Table 0-1. Summary of the carrier density for BO-*x*/TO (*x*=1. 2 and 3) and TO.

Anode	Nd (cm^{-3})

TO	6.3×10^{18}
BO-1/TO	6.7×10^{18}
BO-2/TO	2.3×10^{19}
BO-3/TO	1.8×10^{19}

To further understand the influence of BO-*x*/TO (*x*=1, 2 and 3) heterostructure on the carrier lifetime, the photo-induced carrier lifetime was calculated by the open circuit voltage (OCV) decay plots, which were deduced by the following equation:

$$\tau = \frac{k_B T}{e} \left(\frac{dV_{oc}}{dt} \right)^{-1} \qquad \text{(Equation 1)}$$

where k_B is the Boltzmann constant, e is the charge, and T is the temperature. To further investigate charge carrier dynamics, transient open circuit voltage decay (OCVD) measurements were conducted (Figure 0-14). The results reveal that the BO-*x*/TO (*x*=1, 2 and 3) catalysts exhibit shorter photo-induced carrier transient lifetimes compared to pristine TO. For example, BO-2/TO achieves a transient lifetime of 0.029 s, markedly shorter than the 0.260 s observed for TO. This reduction in lifetime indicates faster charge migration to the electrolyte, which is critical for enhancing PEC reaction.[353]

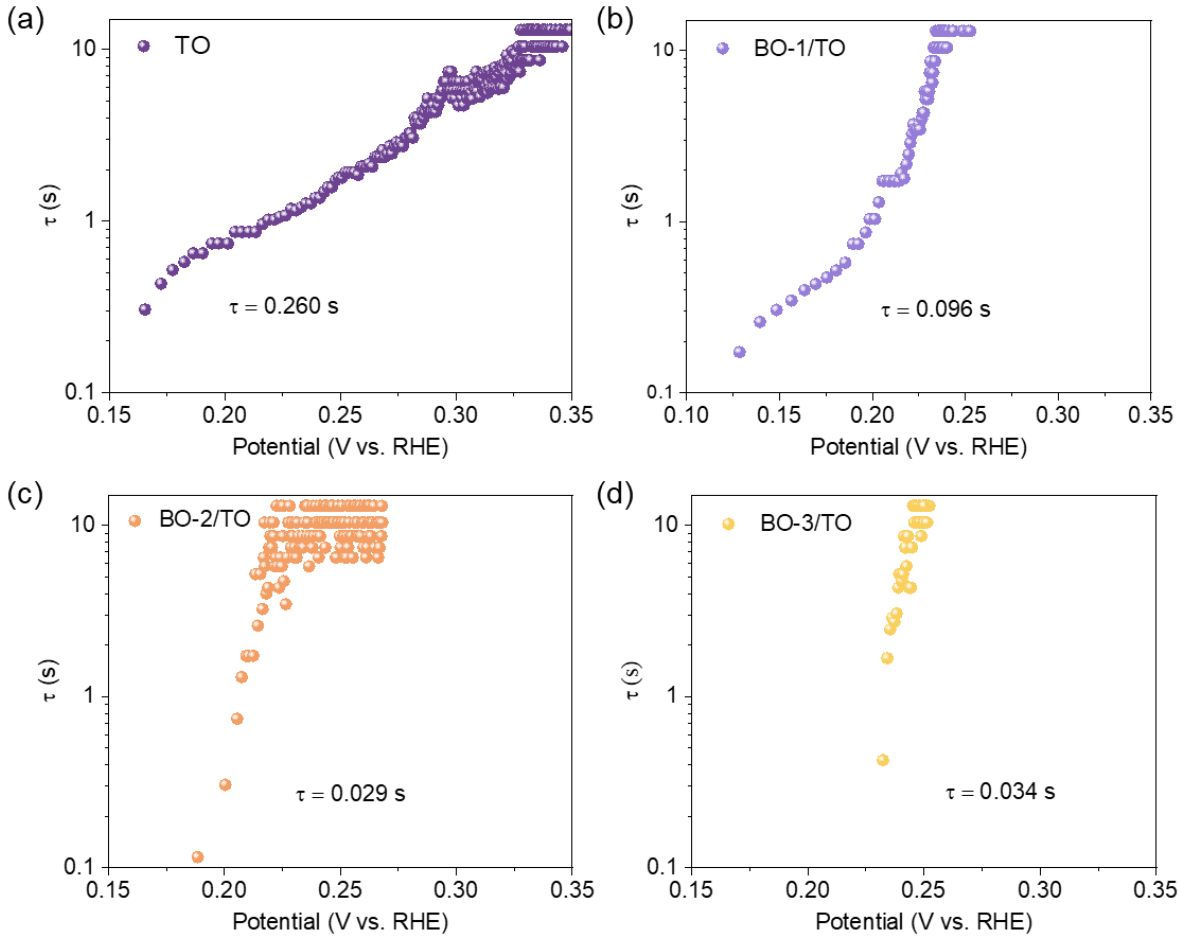

Figure 0-14. Average electron lifetime (τ) calculated from the open-circuit potential test of TO and BO-*x*/TO (*x*=1, 2 and 3) in glycerol electrolyte.

Based on the above-mentioned results, moderate BO loading (BO-2/TO) optimizes the carrier dynamics by extending carrier lifetime, enhancing charge separation, and promoting surface carrier injection, whereas excessive BO loading introduces limitations due to increased recombination. This balance highlights the critical role of compositional tuning in achieving optimal PEC performance.

4.3.4 PEC glycerol oxidation performance

Figure 0-15a compares the glycerol oxidation product yields for BO-*x*/TO (*x* = 1, 2, 3) catalysts and pure TO, illustrating their catalytic performance. Among them, BO/TO-2 achieves the highest product yields, attributed to its optimized electronic structure and efficient charge transfer, which significantly enhance glycerol oxidation. In contrast, BO/TO-1 shows minimal product formation due to inadequate interfacial charge transfer, while BO/TO-3 exhibits reduced yields likely caused by excess BO introducing recombination centers. These results

emphasize the critical role of BO loading in tuning the catalytic activity of BO-*x*/TO (*x*=1, 2 and 3) heterostructures.

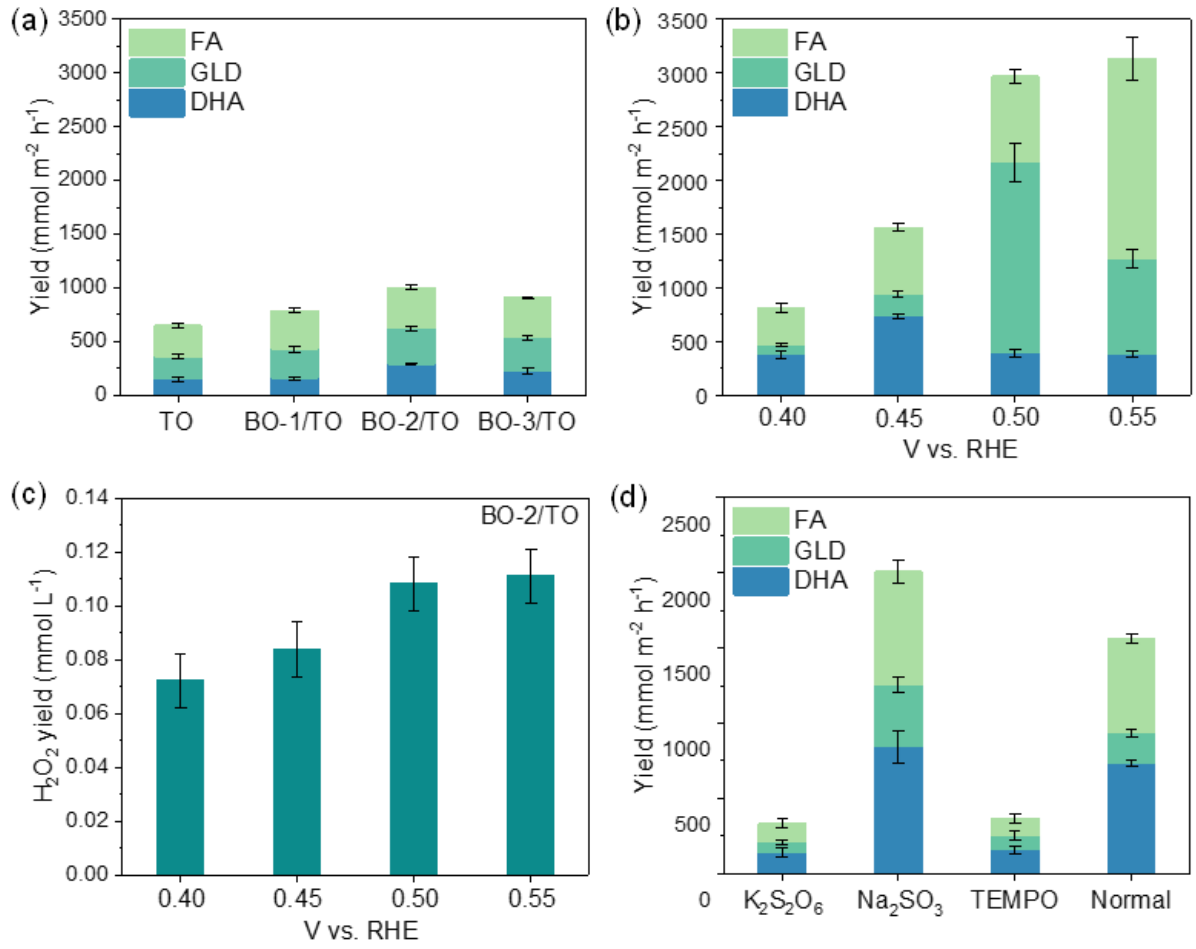

Figure 0-15. (a) The yield of glycerol oxidation on TO and BO-x/TO at 0.3 V vs RHE, (b) The yield of glycerol oxidation on BO-2/TO at different potential with 10 mL/min continuing flow of electrolyte. Reaction condition: 0.5 M Na_2SO_4 electrolyte (pH = 2) containing 0.1 M glycerol under illumination within 3 h. (c) The corresponding H_2O_2 production at the cathode for (b). (d) The yield of glycerol oxidation over BO-2/TO in the presence of various radical scavengers (5 mM) for 1 h (TEMPO as the ·OH radical scavenger, Na_2SO_3 as the hole scavenger, $K_2S_2O_8$ as the electron scavenger).

As shown in Figure 0-15a, FA is identified as the primary product of glycerol oxidation. This predominance is attributed to the oxidation mechanism in the solution, where the symmetrical structure of glycerol, with its two main -OH groups, makes it highly susceptible to attack by surface-adsorbed *OH radicals. To mitigate overoxidation and enhance the production of DHA as the main product, we optimized the electrolyte flow rate to 10 mL min^{-1} (Figure 0-16). At this optimal flow rate, the distribution of PEC glycerol oxidation products on BO-2/TO was analyzed under varying bias potentials. As illustrated in Figure 5b, glycerol undergoes

sequential oxidation to glyceraldehyde (GLD), glyceric acid (GLA), and glycolic acid (GA). GLD, being less stable, is readily oxidized to glyceric acid, which can further undergo C-C bond cleavage to form FA. Additionally, the conversion of glyceric acid to glycolic acid and subsequently to FA leads to the continuous accumulation of FA as the dominant product. Conversely, DHA, being more stable than GLD, accumulates as a significant intermediate, with its main byproducts derived from GLD. With increasing bias potential, the total product yield rises, and the highest DHA selectivity (49%) and yield (1680 mmol m^{-2} h^{-1}) were achieved at a bias of 0.45 V vs. RHE (Figure 0-15b). Furthermore, the Faradaic efficiency of DHA reached 53% (Figure 0-17), outperforming or matching recent benchmarks in glycerol oxidation research (Table 0-2). [342,354-357] Consequently, the glycerol oxidation reaction is predominantly governed by the PEC process, with minimal contributions from standalone electrocatalytic (EC) or photocatalytic (PC) pathways (Figure 0-18).

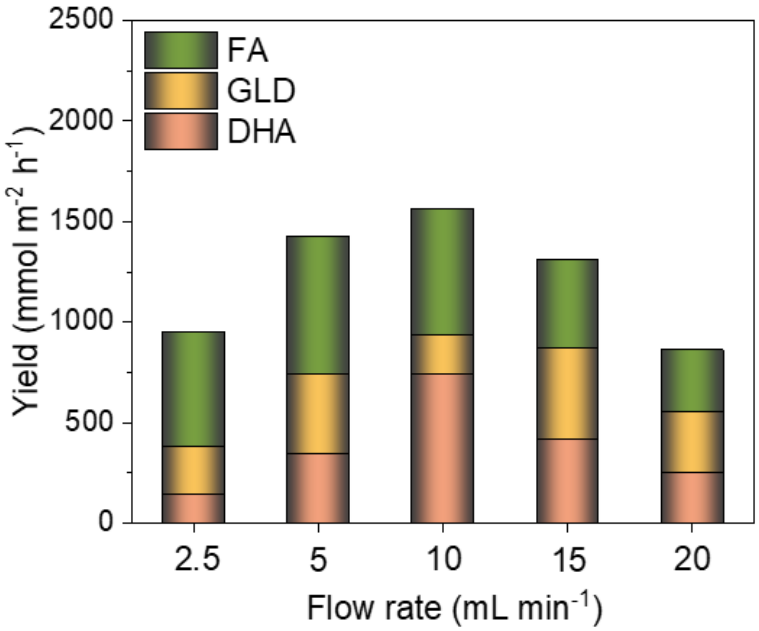

Figure 0-16. The yields of glycerol oxidation for BO-2/TO at different flow rates. Reaction condition: 0.5 M Na_2SO_4 electrolyte (pH = 2) containing 0.1 M glycerol under illumination within 3 h.

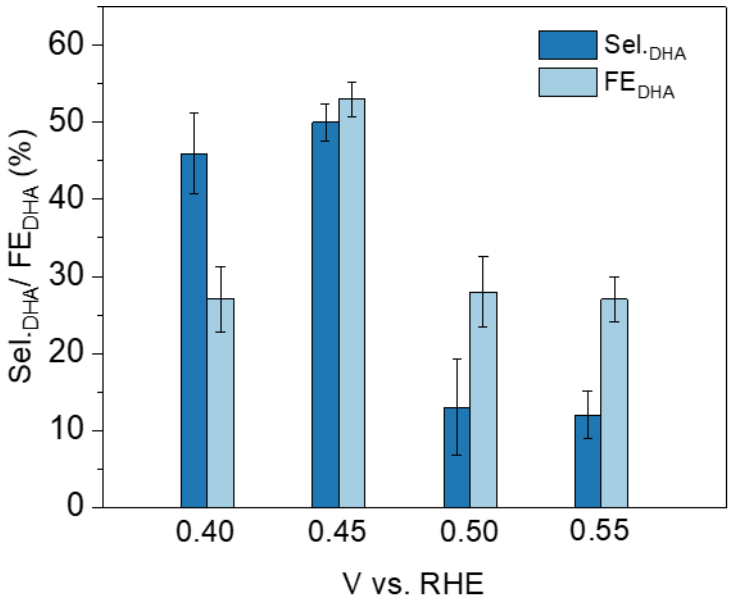

Figure 0-17. Selectivity and FE of DHA for BO-2/TO at different potentials with 10 mL/min continuing flow of electrolyte. Reaction condition: 0.5 M Na_2SO_4 electrolyte (pH = 2) containing 0.1 M glycerol under illumination within 3 h.

Table 0-2. Summary of PEC glycerol selective oxidation performance over different photoanodes.

Sample	electrolyte	DHA selectivity (%)	Bias	Reference
WO_3 / Carbon cloth	0.1 M Na_2SO_4	12	1.2V vs. RHE	[342]
$NiO_x(OH)_y$/W:$BiVO_4$	0.5 M Na_2SO_4	35	1.2 V vs. RHE	[354]
W:$BiVO_4$/NiOOH	0.5 M Na_2SO_4	19	1.2 V vs. RHE	[355]
NT-50V-3h-650	20 mM Na_2SO_4	19	1.50 V	[356]
$BiVO_4$	0.1 M $Na_2B_4O_7$	15	0.7 V vs. RHE	[357]
BO-2/TO	0.5 M Na_2SO_4	49	0.45 V vs. RHE	This work

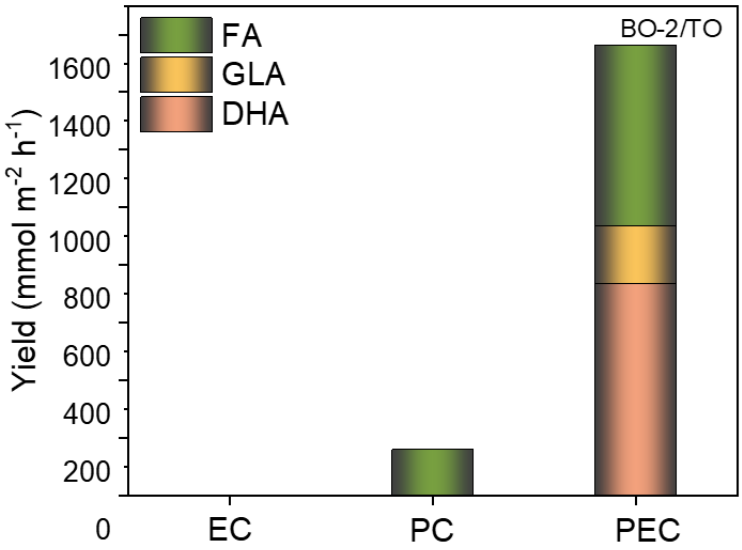

Figure 0-18. Glycerol oxidation product yields of BO-2/TO under PEC, photocatalytic (PC), and electrocatalytic (EC) conditions.

Glycerol oxidation at the anode is typically coupled with hydrogen generation at the cathode. However, in this system, oxygen reduction to hydrogen peroxide (H_2O_2) was selected for the cathode half-reaction due to its practical benefits for ease of transport. Figure 0-15c presents the H_2O_2 production performance of BO-*x*/TO (*x*=1, 2 and 3) heterostructures under catalytic conditions. The results reveal that BO/TO-2 achieves the highest H_2O_2 yield of 0.083 mmol L^{-1} at 0.45 V vs. RHE, significantly outperforming BO/TO-1 and BO/TO-3. This superior performance can be attributed to the optimized charge separation and transfer properties of BO/TO-2, which facilitate efficient electron migration to the cathode for the two-electron oxygen reduction reaction (ORR).

Figure 0-15d investigates the role of photogenerated holes and radicals in PEC glycerol oxidation by evaluating the effect of radical quenching on the performance of the BO-2/TO heterostructure. The addition of photogenerated hole scavenger (Na_2SO_3) and hydroxyl radical scavenger (TEMPO) nearly abolished glycerol conversion, indicating the essential involvement of both photogenerated holes and reactive radicals in the oxidation process. Interestingly, the addition of a photoelectron scavenger ($K_2S_2O_8$) slightly enhanced glycerol conversion, likely due to the increased availability of photogenerated holes for the oxidation reaction. This suggests that efficient hole utilization is a critical factor in improving the reaction performance. These observations indicate that PEC glycerol oxidation predominantly proceeds through the ·OH-radical-mediated mechanism, with photogenerated holes playing a pivotal

role in facilitating water oxidation to generate and stabilize adsorbed ·OH radicals. The results underscore the importance of the synergy between photogenerated holes and surface ·OH radicals in driving efficient glycerol oxidation.

The stability of the BO-2/TO photoanode was confirmed through I-t curves (Figure 0-19), which showed consistent current density over time. Structural and compositional analyses further validated its robustness. XRD indicated no significant changes in crystal structure or morphology (Figure 0-20), while XPS confirmed the stability of Ti and Bi oxidation states after the reaction (Figure 0-21). TEM and STEM images revealed that the BO and TO components retained their structural integrity, and their interface remained intact, ensuring efficient charge transfer (Figure 0-22, Figure 0-23 and Figure 0-24). These results demonstrate the excellent stability and durability of BO-2/TO, making it a promising material for long-term PEC applications.

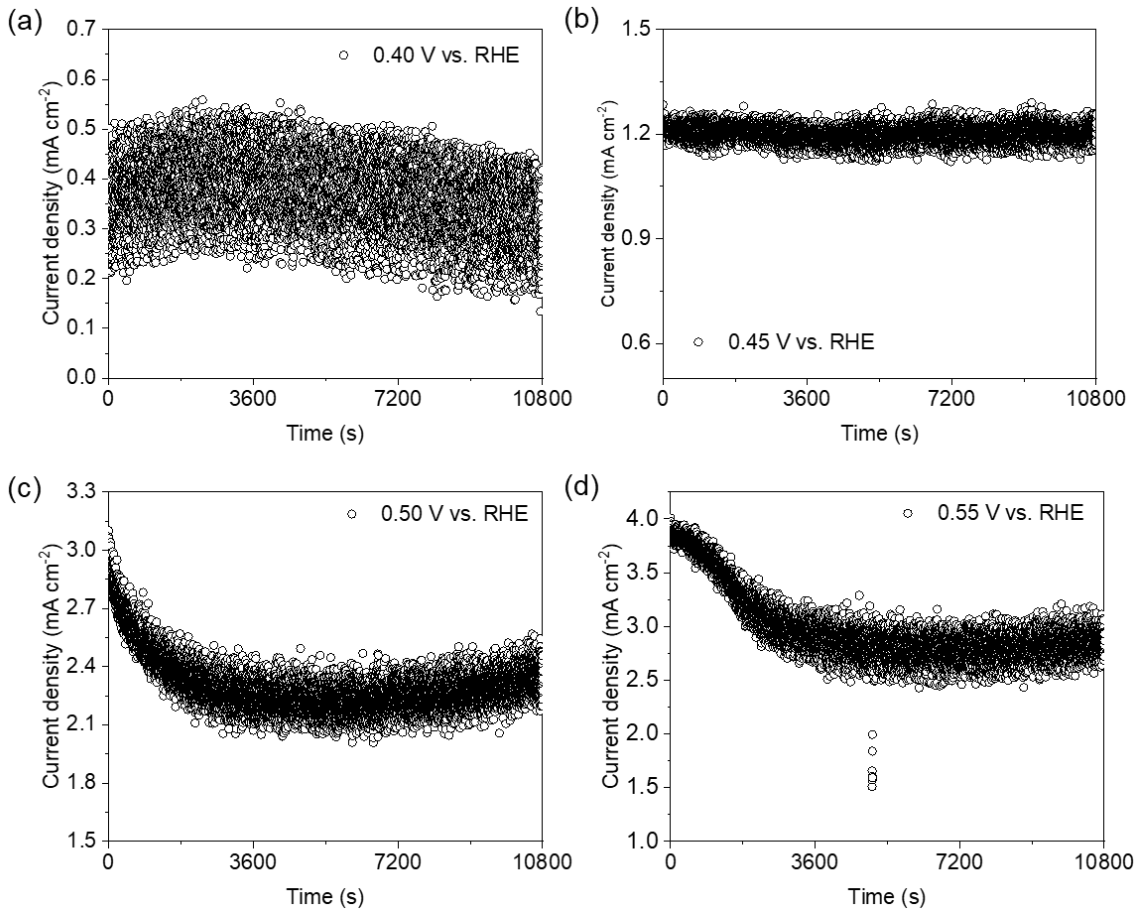

Figure 0-19. (a) I-t stability test of BO/TO for 3 h under different bias, (a) 0.40 V, (b) 0.45 V, (c) 0.50 V, and (d) 0.55 V vs. RHE.

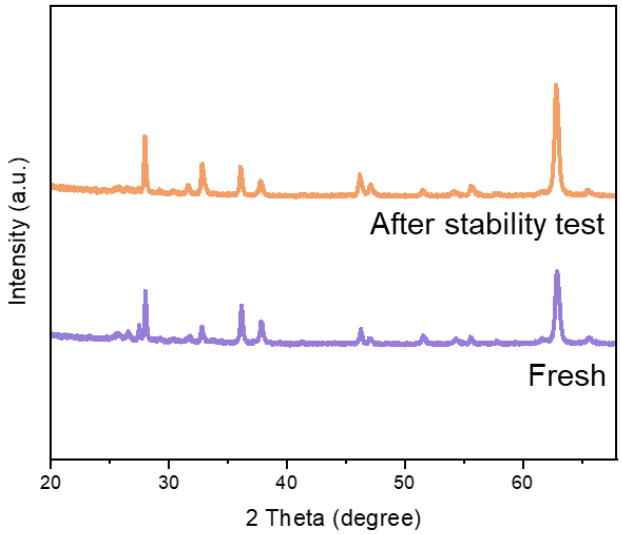

Figure 0-20. The XRD pattern of used BO-2/TO photoanode after 3h stability test.

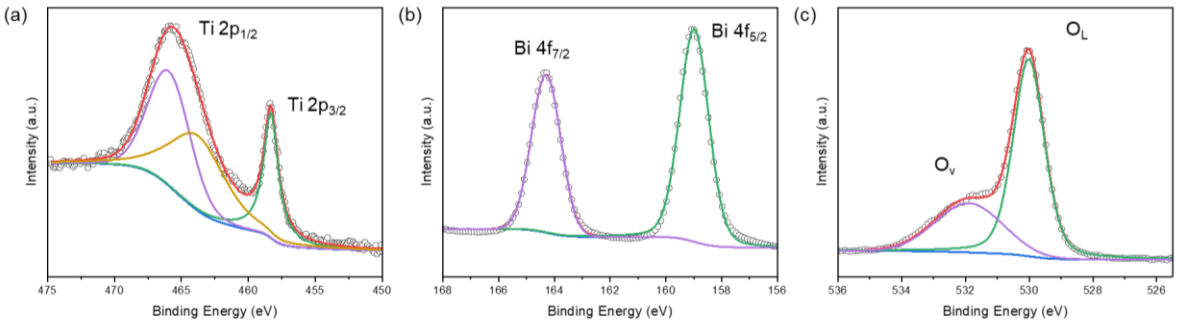

Figure 0-21. High-resolution (a) Ti 3d, (b) Bi 4f, (c) O 1s XPS spectra of BO-2/TO after stability test.

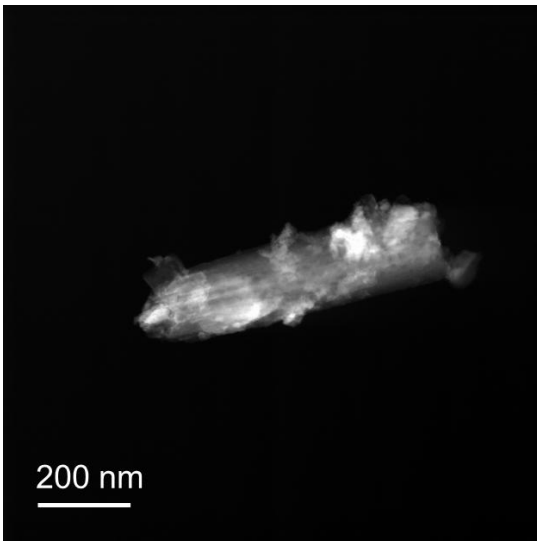

Figure 0-22. STEM HADDF image of BO-2/TO after stability test.

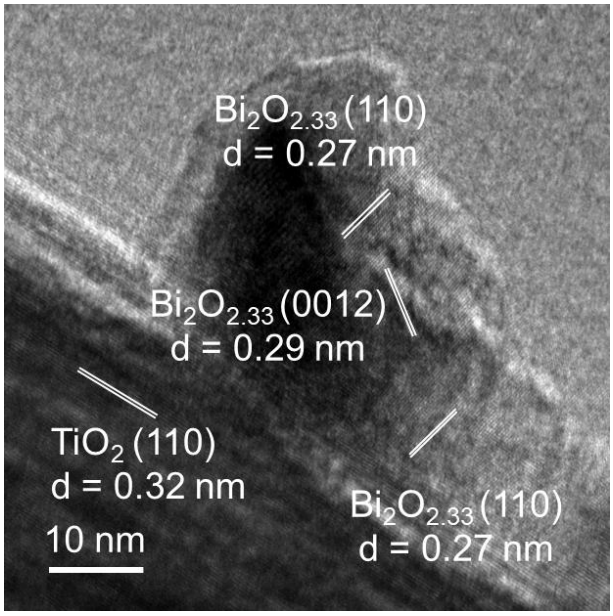

Figure 0-23. HR-TEM image of BO-2/TO after stability test.

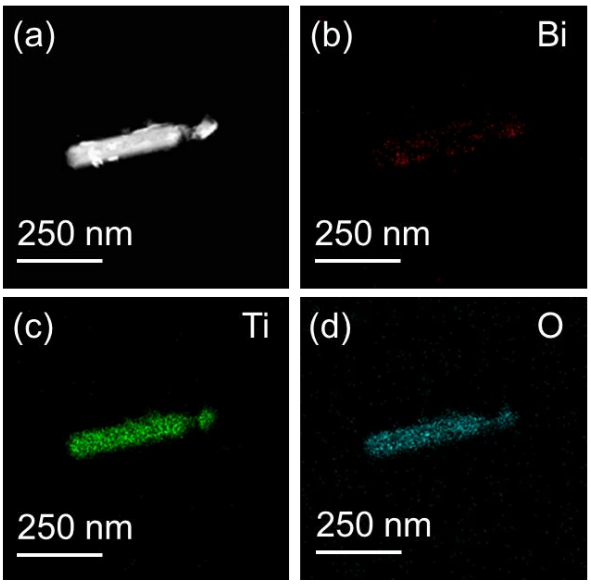

Figure 0-24. EDS mapping image of BO-2/TO after stability test.

To achieve the efficient conversion of glycerol to DHA, two fundamental processes play critical roles: the activation of surface-bound *OH groups on the catalyst and the selective adsorption and activation of hydroxyl groups (-OH) within the glycerol molecule. This dual mechanism ensures the precise transformation of glycerol into the desired product with high selectivity and efficiency. Density Functional Theory (DFT) calculations were employed to systematically analyze the differences in adsorption and cleavage of hydroxyl groups at distinct positions on the BO-*x*/TO (*x*=1, 2 and 3) surface. DFT calculations demonstrated that BO-2/TO

preferentially interacts with the intermediate hydroxyl group of glycerol (Figure 0-25a). Upon adsorption, the C-O bond of the intermediate hydroxyl group is elongated to 1.431 Å, signifying significant activation, whereas the C-O bond of the terminal hydroxyl group remains relatively shorter at 1.416 Å (Figure 0-25c). Furthermore, the adsorption energy of the intermediate hydroxyl group on BO/TO is -0.99 eV, markedly greater than the -0.59 eV for the terminal hydroxyl group (Figure 0-25b). These results underscore the strong interaction between BO-*x*/TO (*x*=1, 2 and 3) and the intermediate hydroxyl group, making it the primary site for activation and subsequent reaction.

The reaction mechanism for the photoelectrochemical (PEC) oxidation of glycerol to DHA was further elucidated using a Gibbs free energy diagram (Figure 0-25d). The process begins with the adsorption of glycerol onto the BO-2/TO surface. Under light irradiation, H_2O in the electrolyte is oxidized by photogenerated holes on the BO-x/TO surface, producing hydroxyl radical (·OH) species with a Gibbs free energy change of ΔG = -1.73 eV. These OH* radicals exhibit moderate oxidative power, initiating the oxidation of the α-H of glycerol to form a carbon radical ($\Delta G = -1.12$ eV). The subsequent interaction between a second OH* radical and the carbon radical results in the formation of a geminal diol intermediate (ΔG = 1.63 eV). This intermediate is inherently unstable in the acidic reaction environment and undergoes dehydration to yield DHA, with a Gibbs free energy change of ΔG = -0.70 eV. The final step involves the desorption of DHA from the BO-*x*/TO (*x*=1, 2 and 3) surface, which requires minimal energy (ΔG = -0.65 eV), completing the catalytic cycle (Figure 0-25e). The low energy barrier for desorption facilitates high DHA selectivity, as it minimizes further oxidation or degradation of the product. In parallel, the ORR occurs at the cathode, using a Pt electrode to generate H_2O_2. This reaction contributes to the overall system efficiency by co-producing a valuable chemical, H_2O_2, alongside DHA. Experimental results showed an H_2O_2 production rate of 0.083 mmol L^{-1} under standard PEC operating conditions (Figure 0-15c).

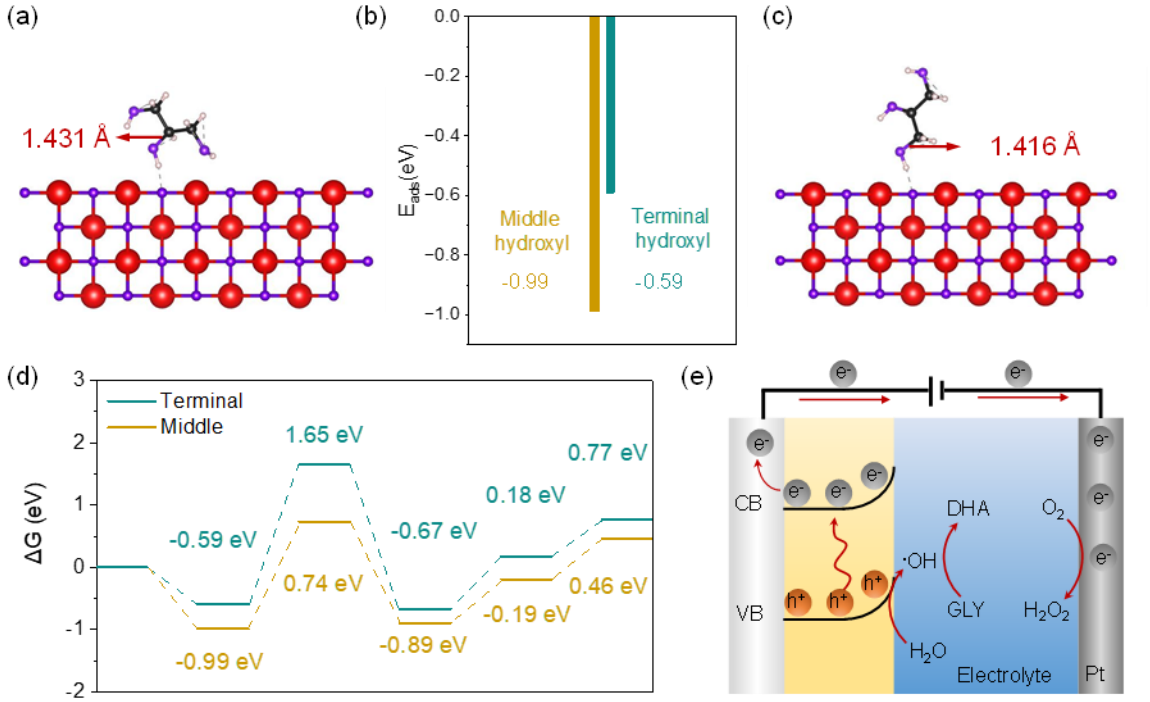

Figure 0-25. (a) and (c) DFT-optimized structures of the -OH group adsorbed on general BO/TO. (b) Adsorption energies of the glycerol with its middle hydroxyl or terminal hydroxyl adsorbed on Bi_2O_3 (201). The optimized adsorption geometries are also displayed. The color of each element is red for Bi, violet for O, white for H, and black for C, respectively. The dashed dark line represents the hydrogen bond between glycerol and BO. (d) Free energy profile of glycerol oxidation on the BO-x/TO model structure. (e) Schematic illustration showing PEC glycerol oxidation to DHA coupled with on-site H_2O_2 production.

4.4 Conclusion

In this study, $Bi_2O_{2.33}$ (BO) was successfully integrated onto a TiO_2 (TO) support to create heterostructured photoanodes, with the optimal configuration identified as BO-2/TO. This system achieved efficient PEC oxidation of glycerol to DHA under acidic conditions, coupled with the simultaneous production of H_2O_2 of 0.083 mmol L^{-1}. The formation of a type-II heterojunction between BO and TO suppressed bulk charge recombination, significantly enhanced light absorption, and improved charge transfer dynamics, collectively driving superior catalytic performance. Theoretical and experimental investigations revealed that BO plays a critical role in facilitating selective adsorption and activation of intermediate hydroxyl (-OH) groups in glycerol, promoting its preferential oxidation to DHA. This resulted in an impressive DHA yield of 1680 mmol m^{-2} h^{-1} with 49% selectivity. Moreover, the cathodic ORR effectively generated H_2O_2, demonstrating the practicality of biomass oxidation with

industrially valuable chemical production. The PEC system developed in this study highlights the potential of integrating selective glycerol oxidation with on-site H_2O_2 production, advancing sustainable chemical synthesis and biomass valorization.

Chapter 5 – Summary and outlook

5.1 Summary

This dissertation explores the development of green catalytic processes for sustainable chemical production, emphasizing the integration of light-enhanced catalysis into scalable technologies. The research systematically investigates different catalytic strategies for biomass valorization, aiming to improve efficiency, selectivity, and sustainability.

The study begins with an overview of biomass upgrading pathways, highlighting key platform chemicals and various catalytic approaches, including thermal, enzymatic, electrocatalytic, and photocatalytic methods (Chapter 1). A crucial aspect of this work is the application of light-assisted catalysis to enhance reaction performance. In Chapter 2, plasmonic photocatalysis was used to enhance the performance of conventional photocatalysis. The role of plasmon-enhanced electron transfer in the selective hydrogenation of unsaturated ketones using γ-Al_2O_3-supported AuPd nanoalloy catalysts (AuPd-γ-Al_2O_3) was investigated. The study demonstrates that the homogeneous Au-Pd alloy structure significantly enhances charge migration and hydrogen activation compared to the bimetallic Au@Pd core-shell structure. The LSPR excitation of Au nanoparticles plays a crucial role in electron transfer dynamics, facilitating selective C=O bond hydrogenation. DFT calculations confirm that the electron-enriched Au-Pd interface enhances catalytic performance by promoting selective adsorption and activation of ketone functional groups. Furthermore, *in situ* XAS and infrared spectroscopic analyses reveal that the photoinduced formation of AuPd-H species enables plasmon-driven hydrogenation under mild reaction conditions. These findings establish AuPd nanoalloys as highly efficient and sustainable catalytic systems for selective hydrogenation and provide a scientific framework for designing plasmonic alloy catalysts in green hydrogenation reactions.

Subsequently, we explore the PEC strategies to improve the solar-driven catalysis. Chapter 3 presents an unbiased tandem PEC system for the simultaneous selective oxidation of HMF to HMFCA at both photoelectrodes. This system integrates a Ru-doped $CuBi_2O_4$ (Ru-2/CBO) photocathode and a NiOOH-modified $BiVO_4$ (NO-2/BVO) photoanode in a continuous-flow configuration, effectively minimizing humin formation while maximizing HMFCA yield. A

key innovation of this system is its synergistic "dual-core processor" mechanism, where the NO-2/BVO photoanode regulates hydroxyl radical (·OH) generation to enhance oxidative reactivity, while the Ru-2/CBO photocathode promotes the ORR, producing $\cdot O_2^-$ to further drive selective biomass oxidation. ESR spectroscopy and in-situ XAS analysis confirm the pivotal role of these radical species in optimizing oxidation pathways. The system achieves an ultrahigh FE_{HMFCA} of 153.4%, an HMFCA selectivity exceeding 75%, and a stable photocurrent of 0.68 mA cm^{-2}, demonstrating its superior efficiency compared to conventional PEC systems. Furthermore, its self-powered PEC configuration, fully driven by solar energy, ensures industrial scalability, achieving an HMFCA yield of 355.2 mmol m^{-2}, making it a promising candidate for large-scale biomass valorization.

Chapter 4 explores the development of a heterojunction-engineered PEC system for the selective oxidation of glycerol to DHA, coupled with the on-site production of H_2O_2. In this study, BO was successfully integrated onto a TO support, forming a type-II heterojunction that enhances charge separation, light absorption, and charge transfer dynamics. The optimal heterostructure configuration, BO-2/TO, demonstrates superior PEC oxidation performance under acidic conditions, enabling efficient glycerol valorization while simultaneously facilitating cathodic ORR for H_2O_2 generation. Theoretical and experimental investigations confirm that BO plays a key role in the selective adsorption and activation of hydroxyl groups in glycerol, thereby promoting its preferential oxidation to DHA. This system achieves a DHA yield of 1680 mmol m^{-2} h^{-1} with 49% selectivity, demonstrating high catalytic efficiency. Simultaneously, the cathodic ORR produces H_2O_2 at a rate of 0.083 mmol L^{-1}, highlighting the dual functionality of the PEC system in generating both high-value chemicals and industrial oxidants. This integrated biomass oxidation and H_2O_2 production approach provides a cost-effective and environmentally sustainable alternative to conventional chemical processes.

Overall, this dissertation demonstrates the transformative potential of light-driven catalysis in advancing sustainable biomass conversion. By integrating plasmonic enhancement, tandem PEC oxidation, and heterojunction engineering, this work provides different strategies for energy-efficient and selective catalytic processes. The findings bridge fundamental catalysis research with practical industrial applications, offering scalable, green catalytic solutions for the production of renewable chemicals and fuels. This research contributes to the growing global efforts in carbon-neutral chemical synthesis, paving the way for future advancements in solar-driven biorefineries and sustainable catalysis.

5.2 Outlook

The development of green catalytic processes is crucial for achieving a carbon-neutral and sustainable future, particularly in the context of biomass valorization, selective hydrogenation, and oxidation. This dissertation has demonstrated solar-driven catalysis as a powerful approach to improving efficiency, selectivity, and scalability in catalytic reactions, paving the way for industrial applications in sustainable chemical synthesis.

A key point highlighted in this work is the application of plasmonic enhancement, tandem PEC cells, and heterojunction engineering, offering novel insights into how charge dynamics and reaction mechanisms can be optimized to achieve superior catalytic performance. By leveraging photo-induced charge transfer, synergistic radical-mediated oxidation, and type-II heterojunction architectures, this research has successfully demonstrated scalable catalytic platforms for producing high-value chemicals and fuels under mild and sustainable conditions.

However, the realization of large-scale adoption of green catalysis still faces multiple challenges. The primary bottlenecks are included below.

(1) Catalyst stability and longevity

Ensuring long-term operational stability in photo-driven catalytic systems remains a critical challenge, particularly for nanoscale metal catalysts and semiconductor-based PEC materials. Degradation of active sites, metal leaching, and photo-corrosion can hinder industrial viability.

(2) Economic feasibility

Many high-performance catalysts rely on noble metals (e.g., Au, Pd, Ru), which are expensive and have limited availability. The development of earth-abundant and low-cost alternatives is necessary for widespread adoption.

(3) Process integration and scale-up

While the current study has demonstrated promising lab-scale efficiencies, translating these findings to pilot-scale or industrial applications requires further investigation into reactor design, continuous-flow optimization, and energy input minimization.

(4) Selectivity and byproduct formation

Despite significant advances in biomass oxidation and hydrogenation, controlling reaction selectivity and minimizing side reactions remain crucial for maximizing the economic and environmental impact of these processes.

To accelerate the implementation of green catalytic processes for sustainable production, future research should focus on several key directions as follows.

1) Rational design of cost-effective and stable catalysts

The widespread adoption of PEC and plasmonic catalysts is currently limited by the reliance on noble metals such as Au, Pd, and Ru. Future research should prioritize the development of earth-abundant, low-cost alternatives without compromising catalytic efficiency. Transition metals (e.g., Fe, Co, Ni, Cu) and their oxide, sulfide, or phosphide derivatives hold great promise for biomass oxidation and hydrogenation reactions.

Furthermore, structural engineering of catalysts through core-shell architectures, intermetallic compounds, and high-entropy alloys can enhance stability, selectivity, and resistance to deactivation. The incorporation of oxygen vacancies, heteroatom doping, and defect engineering can further tailor electronic structures and reaction pathways, improving catalytic performance in light-assisted reactions. Developing scalable and reproducible synthesis methods will be essential for facilitating large-scale implementation of these materials.

2) Enhancing photoelectrochemical and plasmonic catalysis

While light-driven catalytic systems have demonstrated superior selectivity and efficiency, challenges remain in charge separation, energy conversion efficiency, and long-term stability. Heterojunction engineering, particularly through Z-scheme or S-scheme configurations, can optimize band alignment and charge carrier dynamics, thereby enhancing photoelectrochemical performance. The integration of plasmonic nanostructures with semiconductors offers an additional pathway for improving visible-light absorption and hot electron generation, leading to higher reaction rates and selectivity.

Future research should explore the use of hybrid PEC-electrocatalytic systems, where solar energy is utilized to drive electrochemical transformations. These hybrid approaches can reduce external energy inputs, making the process more economically feasible. Additionally, investigating solid-liquid interfacial charge dynamics using in situ spectroscopic techniques

(e.g., operando XAS spectroscopy, surface-enhanced Raman spectroscopy) will provide fundamental insights into catalytic mechanisms and active site evolution.

3) Expanding biomass valorization pathways

Beyond the selective oxidation of HMF and glycerol, future studies should focus on a broader range of biomass-derived feedstocks, including cellulose, hemicellulose, and lignin-derived intermediates. The development of catalytic strategies for C–C and C–O bond cleavage, as well as the functionalization of complex oxygenated molecules, will enable the production of a wider variety of bio-based chemicals and fuels.

Tandem catalytic processes, where multiple reaction steps occur sequentially or simultaneously within a single system, can increase process efficiency and eliminate the need for intermediate separation steps. Additionally, machine learning and computational screening of catalysts could accelerate the identification of optimal catalyst compositions and reaction conditions, driving more rapid advancements in biomass upgrading.

4) Scaling up and integrating with industrial processes

Translating photo-driven catalytic systems from laboratory-scale demonstrations to industrial applications requires significant advancements in reactor design, process integration, and energy optimization. Continuous-flow PEC reactors, designed with optimized light penetration, electrode configurations, and mass transport properties, will be critical for achieving high-throughput biomass conversion.

Furthermore, integrating PEC oxidation with renewable hydrogen production could create self-sustaining biorefinery systems that utilize solar energy for both oxidation and HER. Such integrated systems would enable co-production of biofuels, high-value chemicals, and green hydrogen, offering a holistic approach to sustainable energy and chemical manufacturing. Techno-economic analyses and life cycle assessments should be conducted to evaluate the cost-effectiveness, energy efficiency, and environmental impact of these emerging technologies.

5) Enabling a circular and carbon-neutral economy

The ultimate goal of green catalytic processes is to establish a circular and sustainable chemical industry that operates with minimal waste and maximum resource efficiency. Future research should focus on developing closed-loop catalytic cycles, where catalysts, solvents, and

reactants can be continuously recycled and reused.

Additionally, integrating CO_2 capture and conversion technologies into photoelectrocatalytic systems could enable the simultaneous utilization of biomass-derived feedstocks and atmospheric CO_2, further enhancing the sustainability of green chemical manufacturing. Collaboration between researchers, policymakers, and industry stakeholders will be essential in creating incentives and regulatory frameworks that promote the adoption of renewable catalytic technologies in commercial-scale applications.

The advancements in photoelectrochemical and light-driven catalysis demonstrated in this dissertation lay a strong foundation for next-generation green catalytic processes. By addressing challenges in catalyst design, reaction efficiency, process scalability, and sustainability, future research can accelerate the transition toward carbon-neutral and economically viable catalytic systems. These efforts will contribute to the global push for sustainable energy and chemical production, paving the way for a cleaner and more resource-efficient future.

Reference

1 Lin, J., Tian, W., Zhang, H., Sun, H. & Wang, S. Electronic Structure and Functions of Carbon Nitride in Frontier Green Catalysis. *Accounts of Chemical Research* **57**, 2303-2315, doi:10.1021/acs.accounts.4c00266 (2024).

2 Polshettiwar, V. & Varma, R. S. Green chemistry by nano-catalysis. *Green Chemistry* **12**, 743-754, doi:10.1039/B921171C (2010).

3 Jiménez-González, C. & Constable, D. J. *Green chemistry and engineering: a practical design approach*. (John Wiley & Sons, 2011).

4 Bilgen, S. Structure and environmental impact of global energy consumption. *Renewable and Sustainable Energy Reviews* **38**, 890-902, doi:https://doi.org/10.1016/j.rser.2014.07.004 (2014).

5 de Souza Mesquita, L. M. *et al.* Path2Green: introducing 12 green extraction principles and a novel metric for assessing sustainability in biomass valorization. *Green Chemistry* **26**, 10087-10106, doi:10.1039/D4GC02512A (2024).

6 Ghatak, H. R. J. R. & Reviews, S. E. Biorefineries from the perspective of sustainability: Feedstocks, products, and processes. **15**, 4042-4052 (2011).

7 Sheldon, R. A. J. C. S. R. Fundamentals of green chemistry: efficiency in reaction design. **41**, 1437-1451 (2012).

8 Panel, U. N. E. P. I. R., Consumption, U. N. E. P. S. & Branch, P. *Decoupling natural resource use and environmental impacts from economic growth*. (UNEP/Earthprint, 2011).

9 Olabi, A. G. *et al.* Green hydrogen: Pathways, roadmap, and role in achieving sustainable development goals. (2023).

10 Zhang, X., Fevre, M., Jones, G. O. & Waymouth, R. M. J. C. r. Catalysis as an enabling science for sustainable polymers. **118**, 839-885 (2018).

11 Gómez-López, P. *et al.* Nanomaterials and catalysis for green chemistry. **24**, 48-55 (2020).

12 Clark, J. H., Farmer, T. J., Herrero-Davila, L. & Sherwood, J. J. G. C. Circular economy design considerations for research and process development in the chemical sciences. **18**, 3914-3934 (2016).

13 Jenck, J. F., Agterberg, F. & Droescher, M. J. J. G. C. Products and processes for a sustainable chemical industry: a review of achievements and prospects. **6**, 544-556 (2004).

14 Silvestri, C., Silvestri, L., Forcina, A., Di Bona, G. & Falcone, D. J. J. o. C. P. Green chemistry contribution towards more equitable global sustainability and greater circular economy: A systematic literature review. **294**, 126137 (2021).

15 Qamar, O. A. *et al.* Feasibility-to-applications of value-added products from biomass: Current trends, challenges, and prospects. **454**, 140240 (2023).

16 Kumar, V., Malyan, S. K., Apollon, W. & Verma, P. J. R. E. Valorization of pulp and paper industry waste streams into bioenergy and value-added products: An integrated biorefinery approach. 120566 (2024).

17 Voukkali, I. *et al.* Fashioning the Future: Green chemistry and engineering innovations in biofashion. **497**, 155039 (2024).

18 Clarke, C. J., Tu, W.-C., Levers, O., Brohl, A. & Hallett, J. P. J. C. r. Green and sustainable solvents in chemical processes. **118**, 747-800 (2018).

19 Beller, M., Centi, G. & Sun, L. J. C. Chemistry future: priorities and opportunities from the sustainability perspective. **10**, 6-13 (2017).

20 Bordet, A. & Leitner, W. J. A. C. I. E. Adaptive catalytic systems for chemical energy conversion. **62**, e202301956 (2023).
21 Osman, A. I. *et al.* Cost, environmental impact, and resilience of renewable energy under a changing climate: a review. **21**, 741-764 (2023).
22 Amin, M. *et al.* Hydrogen production through renewable and non-renewable energy processes and their impact on climate change. **47**, 33112-33134 (2022).
23 Alok, A. *et al.* Technological advances in the transformative utilization of CO2 to value-added products. **10**, 106922 (2022).
24 Koytsoumpa, E. I., Bergins, C. & Kakaras, E. J. T. J. o. S. F. The CO2 economy: Review of CO2 capture and reuse technologies. **132**, 3-16 (2018).
25 Zhou, Y. J., Kerkhoven, E. J. & Nielsen, J. J. N. E. Barriers and opportunities in bio-based production of hydrocarbons. **3**, 925-935 (2018).
26 Becker, J. & Wittmann, C. J. A. C. I. E. Advanced biotechnology: Metabolically engineered cells for the bio-based production of chemicals and fuels, materials, and health-care products. **54**, 3328-3350 (2015).
27 Blum, C. *et al.* The concept of sustainable chemistry: Key drivers for the transition towards sustainable development. **5**, 94-104 (2017).
28 Baranzini, A. *et al.* Carbon pricing in climate policy: seven reasons, complementary instruments, and political economy considerations. **8**, e462 (2017).
29 Adun, H., Ampah, J. D., Bamisile, O., Hu, Y. J. S. P. & Consumption. The synergistic role of carbon dioxide removal and emission reductions in achieving the Paris Agreement goal. **45**, 386-407 (2024).
30 Abdmouleh, Z., Alammari, R. A., Gastli, A. J. R. & Reviews, S. E. Review of policies encouraging renewable energy integration & best practices. **45**, 249-262 (2015).
31 Wang, R., Feng, Y., Li, D., Li, K. & Yan, Y. Towards the sustainable production of biomass-derived materials with smart functionality: a tutorial review. *Green Chemistry* (2024).
32 Li, L., Lu, S., Fang, L., Wei, Y. & Yang, S. Review on biomass-derived carbon-based materials for electrocatalytic hydrogen production: state of the art and outlook. *Energy & Fuels* **37**, 18485-18501 (2023).
33 Belluati, M., Tabasso, S., Gaudino, E. C., Cravotto, G. & Manzoli, M. Biomass-derived carbon-based catalysts for lignocellulosic biomass and waste valorisation: a circular approach. *Green Chemistry* **26**, 8642-8668 (2024).
34 Chakraborty, R., Vilya, K., Pradhan, M. & Nayak, A. K. Recent advancement of biomass-derived porous carbon based materials for energy and environmental remediation applications. *Journal of Materials Chemistry A* **10**, 6965-7005 (2022).
35 Shaba, E. Y. *et al.* in *Biomass Valorization: A Sustainable Approach towards Carbon Neutrality and Circular Economy* 99-122 (Springer, 2025).
36 Okolie, J. A., Nanda, S., Dalai, A. K. & Kozinski, J. A. Chemistry and specialty industrial applications of lignocellulosic biomass. *Waste and Biomass Valorization* **12**, 2145-2169 (2021).
37 Singh, K., Mehra, S. & Kumar, A. Recent advances in catalytic conversion of lignin to value-added chemicals using ionic liquids and deep eutectic solvents: a critical review. *Green Chemistry* **26**, 1062-1091 (2024).
38 Di Fraia, A., Di Fraia, S. & Massarotti, N. Role of advanced oxidation processes in lignocellulose pretreatment towards biorefinery applications: a review on emerging trends and economic considerations. *Green Chemistry* (2024).
39 Tian, Q. *et al.* The driving force of biomass value-addition: Selective catalytic depolymerization of lignin to high-value chemicals. *Journal of Environmental Chemical Engineering* **11**, 109719 (2023).

40 Li, G. *et al.* Production of Renewable Hydrocarbon Biofuels with Lignocellulose and Its Derivatives over Heterogeneous Catalysts. *Chemical Reviews* **124**, 2889-2954 (2024).
41 Liu, Y. *et al.* Biofuels for a sustainable future. *Cell* **184**, 1636-1647 (2021).
42 Ding, W., Li, H., Zong, R., Jiang, J. & Tang, X. Controlled hydrodeoxygenation of biobased ketones and aldehydes over an alloyed Pd–Zr catalyst under mild conditions. *ACS Sustainable Chemistry & Engineering* **9**, 3498-3508 (2021).
43 Zeng, X. *et al.* Low-temperature degradation of lignin in aprotic solvent system for preparation of monophenolic platform chemicals. *Chemical Engineering Journal* **476**, 146466 (2023).
44 Soukup-Carne, D., Fan, X. & Esteban, J. An overview and analysis of the thermodynamic and kinetic models used in the production of 5-hydroxymethylfurfural and furfural. *Chemical Engineering Journal* **442**, 136313 (2022).
45 Messori, A., Fasolini, A. & Mazzoni, R. Advances in Catalytic Routes for the Homogeneous Green Conversion of the Bio-Based Platform 5-Hydroxymethylfurfural. *ChemSusChem* **15**, e202200228 (2022).
46 Liu, B. *et al.* Regulating the Transfer of Photogenerated Carriers for Photocatalytic Hydrogen Evolution Coupled with Furfural Synthesis. *ACS Nano* **18**, 17939-17949, doi:10.1021/acsnano.4c04562 (2024).
47 Osman, W. N. A. W., Rosli, M. H., Mazli, W. N. A. & Samsuri, S. Comparative review of biodiesel production and purification. *Carbon Capture Science & Technology* **13**, 100264 (2024).
48 Thanahiranya, P. *et al.* Sustainability assessment of dihydroxyacetone (DHA) production from glycerol: a comparative study between biological and catalytic oxidation routes. *ACS Sustainable Chemistry & Engineering* **11**, 17425-17439 (2023).
49 Qureshi, F. *et al.* Sustainable and energy efficient hydrogen production via glycerol reforming techniques: A review. *International Journal of Hydrogen Energy* **47**, 41397-41420 (2022).
50 Zhang, B., Biswal, B. K., Zhang, J. & Balasubramanian, R. Hydrothermal treatment of biomass feedstocks for sustainable production of chemicals, fuels, and materials: progress and perspectives. *Chemical Reviews* **123**, 7193-7294 (2023).
51 Fu, J., Shen, F., Liu, X. & Qi, X. Synthesis of MgO-doped ordered mesoporous carbons by Mg2+-tannin coordination for efficient isomerization of glucose to fructose. *Green Energy & Environment* **8**, 842-851, doi:https://doi.org/10.1016/j.gee.2021.11.010 (2023).
52 Cui, X., Zheng, L., Li, Q. & Guo, Y. A remarkable bifunctional carbon-based solid acid catalyst derived from waste bio-tar for efficient synthesis of 5-hydroxymethylfurfural from glucose. *Chemical Engineering Journal* **474**, 146006, doi:https://doi.org/10.1016/j.cej.2023.146006 (2023).
53 Vasconcelos, S. C. *et al.* Catalytic Upgrading of Lignocellulosic Biomass-Derived Compounds Using Hierarchical ZSM-5 Zeolites. *Energy & Fuels* **38**, 23823-23835, doi:10.1021/acs.energyfuels.4c04000 (2024).
54 Zhang, T., Wei, H., Jin, Y. & Xiao, H. Dehydration of glucose to 5-hydroxymethylfurfural over sn-containing dendritic mesoporous silica. *Chemical Engineering Journal* **454**, 140415, doi:https://doi.org/10.1016/j.cej.2022.140415 (2023).
55 Dharmapriya, T. N., Lin, K.-Y. A. & Huang, P.-J. Roles of Brønsted-Base and Brønsted-Acid Catalysts for Glucose Isomerization into Fructose and Fructose Dehydration into 5-Hydroxymethylfurfural. *Energy & Fuels* **38**, 16834-16852, doi:10.1021/acs.energyfuels.4c02551 (2024).

56 Ramesh, A., Rajesh, D., Shanthi, K., Bhargav, P. B. & Nguyen-Le, M.-T. Catalytic conversion of glucose to 5-hydroxymethylfurfural productions over sulphated Ti-Al2O3 catalysts. *Biomass and Bioenergy* **154**, 106261, doi:https://doi.org/10.1016/j.biombioe.2021.106261 (2021).
57 Ullah, N. *et al.* Metal–acid nanoplate-supported ultrafine Ru nanoclusters for efficient catalytic fractionation of lignin into aromatic alcohols. *Green Chemistry* **21**, 2739-2751, doi:10.1039/C8GC03440K (2019).
58 Xu, S., Yang, J., Li, J. & Shen, F. Highly Efficient Oxidation of Biomass Xylose to Formic Acid with CeOx-Promoted MnOx Catalyst in Water. *ACS Sustainable Chemistry & Engineering* **11**, 921-930, doi:10.1021/acssuschemeng.2c04940 (2023).
59 Wang, K., Liang, C., Zhang, Q. & Zhang, F. Synergistic Catalysis of Brønsted Acid and Lewis Acid Coexisted on Ordered Mesoporous Resin for One-Pot Conversion of Glucose to 5-Hydroxymethylfurfural. *ACS Omega* **4**, 1053-1059, doi:10.1021/acsomega.8b02982 (2019).
60 Qiu, G., Huang, C., Sun, X. & Chen, B. Highly active niobium-loaded montmorillonite catalysts for the production of 5-hydroxymethylfurfural from glucose. *Green Chemistry* **21**, 3930-3939, doi:10.1039/C9GC01225G (2019).
61 Qi, X. *et al.* Effect of CeO2 morphology on the catalytic properties of Au/CeO2 for base-free glucose oxidation. *Catalysis Science & Technology* **12**, 1313-1323, doi:10.1039/D1CY02078A (2022).
62 Wang, S., Eberhardt, T. L. & Pan, H. Efficient dehydration of fructose into 5-HMF using a weakly-acidic catalyst prepared from a lignin-derived mesoporous carbon. *Fuel* **316**, 123255, doi:https://doi.org/10.1016/j.fuel.2022.123255 (2022).
63 Luo, L. *et al.* Selective Photoelectrocatalytic Glycerol Oxidation to Dihydroxyacetone via Enhanced Middle Hydroxyl Adsorption over a Bi2O3-Incorporated Catalyst. *Journal of the American Chemical Society* **144**, 7720-7730, doi:10.1021/jacs.2c00465 (2022).
64 Sun, J. *et al.* Integration of Enzymatic and Heterogeneous Catalysis for One-Pot Production of Fructose from Glucose. **11**, 1157-1162, doi:https://doi.org/10.1002/cssc.201800015 (2018).
65 Zong, Z. *et al.* Mechanism and biomass association of glucuronoyl esterase: an α/β hydrolase with potential in biomass conversion. *Nature Communications* **13**, 1449, doi:10.1038/s41467-022-28938-w (2022).
66 Cristobal, J. R., Hegazy, R. & Richard, J. P. Glycerol 3-Phosphate Dehydrogenase: Role of the Protein Conformational Change in Activation of a Readily Reversible Enzyme-Catalyzed Hydride Transfer Reaction. *Biochemistry* **63**, 1016-1025, doi:10.1021/acs.biochem.3c00702 (2024).
67 Gao, D.-M. *et al.* Critical approaches in the catalytic transformation of sugar isomerization and epimerization after Fischer − History, challenges, and prospects. *Green Energy & Environment* **9**, 435-453, doi:https://doi.org/10.1016/j.gee.2023.02.003 (2024).
68 de Gonzalo, G., Colpa, D. I., Habib, M. H. M. & Fraaije, M. W. Bacterial enzymes involved in lignin degradation. *Journal of Biotechnology* **236**, 110-119, doi:https://doi.org/10.1016/j.jbiotec.2016.08.011 (2016).
69 Picart, P., Sevenich, M., Domínguez de María, P. & Schallmey, A. Exploring glutathione lyases as biocatalysts: paving the way for enzymatic lignin depolymerization and future stereoselective applications. *Green Chemistry* **17**, 4931-4940, doi:10.1039/C5GC01078K (2015).
70 Liu, P. *et al.* Upgraded cellulose and xylan digestions for synergistic enhancements of biomass enzymatic saccharification and bioethanol conversion using engineered

Trichoderma reesei strains overproducing mushroom LeGH7 enzyme. *International Journal of Biological Macromolecules* **278**, 134524, doi:https://doi.org/10.1016/j.ijbiomac.2024.134524 (2024).

71 Zanuso, E., Gomes, D. G., Ruiz, H. A., Teixeira, J. A. & Domingues, L. Enzyme immobilization as a strategy towards efficient and sustainable lignocellulosic biomass conversion into chemicals and biofuels: current status and perspectives. *Sustainable Energy & Fuels* **5**, 4233-4247, doi:10.1039/D1SE00747E (2021).

72 Pino, M. S., Rodríguez-Jasso, R. M., Michelin, M. & Ruiz, H. A. Enhancement and modeling of enzymatic hydrolysis on cellulose from agave bagasse hydrothermally pretreated in a horizontal bioreactor. *Carbohydrate Polymers* **211**, 349-359, doi:https://doi.org/10.1016/j.carbpol.2019.01.111 (2019).

73 Román, A. M. *et al.* Electro-oxidation of furfural on gold is limited by furoate self-assembly. *Journal of Catalysis* **391**, 327-335, doi:https://doi.org/10.1016/j.jcat.2020.08.034 (2020).

74 Bharath, G. & Banat, F. High-Grade Biofuel Synthesis from Paired Electrohydrogenation and Electrooxidation of Furfural Using Symmetric Ru/Reduced Graphene Oxide Electrodes. *ACS Applied Materials & Interfaces* **13**, 24643-24653, doi:10.1021/acsami.1c02231 (2021).

75 Wang, T. *et al.* Combined anodic and cathodic hydrogen production from aldehyde oxidation and hydrogen evolution reaction. *Nature Catalysis* **5**, 66-73, doi:10.1038/s41929-021-00721-y (2022).

76 Zhong, Y. *et al.* Grass-like NixSey nanowire arrays shelled with NiFe LDH nanosheets as a 3D hierarchical core–shell electrocatalyst for efficient upgrading of biomass-derived 5-hydroxymethylfurfural and furfural. *Catalysis Science & Technology* **12**, 201-211, doi:10.1039/D1CY01816G (2022).

77 Wang, T. *et al.* Transforming electrocatalytic biomass upgrading and hydrogen production from electricity input to electricity output. *Angewandte Chemie* **134**, e202115636 (2022).

78 Dai, Z., Liu, X., Liu, N., Zhang, Y. & Zhao, X. Upgrading biomass derived furan aldehydes by coupled electrochemical conversion over silver-based electrocatalysts. *Chemical Engineering Journal* **488**, 151001, doi:https://doi.org/10.1016/j.cej.2024.151001 (2024).

79 Wang, Y. *et al.* Efficient Electrocatalytic Oxidation of Glycerol via Promoted OH* Generation over Single-Atom-Bismuth-Doped Spinel Co3O4. *ACS Catalysis* **12**, 12432-12443, doi:10.1021/acscatal.2c03162 (2022).

80 Yu, H. *et al.* Pt single atom captured by oxygen vacancy-rich NiCo layered double hydroxides for coupling hydrogen evolution with selective oxidation of glycerol to formate. *Applied Catalysis B: Environmental* **330**, 122617, doi:https://doi.org/10.1016/j.apcatb.2023.122617 (2023).

81 Peng, T. *et al.* Electrocatalytic valorization of lignocellulose-derived aromatics at industrial-scale current densities. *Nature Communications* **14**, 7229, doi:10.1038/s41467-023-43136-y (2023).

82 Yuan, X., Lee, K., Eisenberg, J. B., Schmidt, J. R. & Choi, K.-S. Selective deoxygenation of biomass-derived carbonyl compounds on Zn via electrochemical Clemmensen reduction. *Nature Catalysis* **7**, 43-54, doi:10.1038/s41929-023-01066-4 (2024).

83 Tang, W. *et al.* Efficient Conversion of Biomass to Formic Acid Coupled with Low Energy Consumption Hydrogen Production from Water Electrolysis. **62**, e202305843, doi:https://doi.org/10.1002/anie.202305843 (2023).

84 Li, X. *et al.* in *Functional Materials for Electrocatalytic Energy Conversion* 509-537

(2025).
85 Qi, Y. *et al.* Simultaneous Oxidative Cleavage of Lignin and Reduction of Furfural via Efficient Electrocatalysis by P-Doped CoMoO4. **35**, 2208284, doi:https://doi.org/10.1002/adma.202208284 (2023).
86 Giannakoudakis, D. A., Colmenares, J. C., Tsiplakides, D. & Triantafyllidis, K. S. Nanoengineered Electrodes for Biomass-Derived 5-Hydroxymethylfurfural Electrocatalytic Oxidation to 2,5-Furandicarboxylic Acid. *ACS Sustainable Chemistry & Engineering* **9**, 1970-1993, doi:10.1021/acssuschemeng.0c07480 (2021).
87 Pang, X., Bai, H., Zhao, H., Fan, W. & Shi, W. Efficient Electrocatalytic Oxidation of 5-Hydroxymethylfurfural Coupled with 4-Nitrophenol Hydrogenation in a Water System. *ACS Catalysis* **12**, 1545-1557, doi:10.1021/acscatal.1c04880 (2022).
88 Ji, K. *et al.* Electrocatalytic Hydrogenation of 5-Hydroxymethylfurfural Promoted by a Ru1Cu Single-Atom Alloy Catalyst. **61**, e202209849, doi:https://doi.org/10.1002/anie.202209849 (2022).
89 Liu, S.-Q. *et al.* A coupled electrocatalytic system with reduced energy input for CO2 reduction and biomass valorization. *Energy & Environmental Science* **16**, 5305-5314, doi:10.1039/D3EE01999C (2023).
90 Patil, P. D., Karvekar, A., Salokhe, S., Tiwari, M. S. & Nadar, S. S. When nanozymes meet enzyme: Unlocking the dual-activity potential of integrated biocomposites. *International Journal of Biological Macromolecules* **271**, 132357, doi:https://doi.org/10.1016/j.ijbiomac.2024.132357 (2024).
91 Silva Almeida, C. *et al.* Enhancing Lipase Immobilization via Physical Adsorption: Advancements in Stability, Reusability, and Industrial Applications for Sustainable Biotechnological Processes. *ACS Omega* **9**, 46698-46732, doi:10.1021/acsomega.4c07088 (2024).
92 Do, V.-H. & Lee, J.-M. Surface engineering for stable electrocatalysis. *Chemical Society Reviews* **53**, 2693-2737, doi:10.1039/D3CS00292F (2024).
93 Allakhverdiev, S. I. Artificial photosynthesis: Powering a green new deal for sustainable energy. *International Journal of Hydrogen Energy* **90**, 199-209 (2024).
94 Das, B., Devi, M. & Dhar, S. S. in *Towards Sustainable and Green Hydrogen Production by Photocatalysis: Scalability Opportunities and Challenges (Volume 1)* 91-113 (ACS Publications, 2024).
95 Khan, M. A. *et al.* Recent advances over the doped g-C3N4 in photocatalysis: A review. *Coordination Chemistry Reviews* **522**, 216227 (2025).
96 Mohd, S. & Khan, A. M. Heterogeneous photocatalysis: Recent advances and applications. *Sustainable Green Catalytic Processes*, 141-163 (2024).
97 Vilanova, A., Dias, P., Lopes, T. & Mendes, A. The route for commercial photoelectrochemical water splitting: a review of large-area devices and key upscaling challenges. *Chemical Society Reviews* (2024).
98 Xu, J., Huang, X., Peng, J., Li, S. & Li, J.-F. Insights into plasmon-assisted chemical reactions: from fabrication to characterization. *eScience*, 100312 (2024).
99 Panda, S. *Green Horizons: Exploring Renewable Energy Technologies*. (Academic Guru Publishing House, 2024).
100 Sikiru, S. *et al.* Hydrogen-powered horizons: Transformative technologies in clean energy generation, distribution, and storage for sustainable innovation. *International Journal of Hydrogen Energy* **56**, 1152-1182 (2024).
101 Wang, M., Zhou, H. & Wang, F. Photocatalytic biomass conversion for hydrogen and renewable carbon-based chemicals. *Joule* **8**, 604-621 (2024).
102 Patel, J., Patel, A. R. & Tyagi, H. in *Challenges and Opportunities in Green Hydrogen Production* 239-267 (Springer, 2024).

103 Eswar, N., Singh, S. A. & Heo, J. Atomic layer deposited photocatalysts: comprehensive review on viable fabrication routes and reactor design approaches for photo-mediated redox reactions. *Journal of Materials Chemistry A* **7**, 17703-17734 (2019).
104 Bhattacharya, C. *et al.* Sustainable Nanoplasmon-Enhanced Photoredox Reactions: Synthesis, Characterization, and Applications. *Advanced Energy Materials* **10**, 2002402 (2020).
105 Hayati, F. *et al.* A novel, Z-scheme ZnO@ AC@ FeO photocatalyst, suitable for the intensification of photo-mediated peroxymonosulfate activation: Performance, reactivity and bisphenol A degradation pathways. *Journal of Environmental Management* **321**, 115851 (2022).
106 Colmenares, J. C. & Luque, R. Heterogeneous photocatalytic nanomaterials: prospects and challenges in selective transformations of biomass-derived compounds. *Chemical Society Reviews* **43**, 765-778 (2014).
107 Wu, X. *et al.* Photocatalytic transformations of lignocellulosic biomass into chemicals. *Chemical Society Reviews* **49**, 6198-6223 (2020).
108 Chen, H. *et al.* Mechanism insight into photocatalytic conversion of lignin for valuable chemicals and fuels production: A state-of-the-art review. *Renewable and Sustainable Energy Reviews* **147**, 111217 (2021).
109 Molinari, R., Lavorato, C. & Argurio, P. Visible-light photocatalysts and their perspectives for building photocatalytic membrane reactors for various liquid phase chemical conversions. *Catalysts* **10**, 1334 (2020).
110 Wang, F., Li, Q. & Xu, D. Recent Progress in Semiconductor-Based Nanocomposite Photocatalysts for Solar-to-Chemical Energy Conversion. *Advanced Energy Materials* **7**, 1700529, doi:https://doi.org/10.1002/aenm.201700529 (2017).
111 Xiong, L. & Tang, J. Strategies and Challenges on Selectivity of Photocatalytic Oxidation of Organic Substances. *Advanced Energy Materials* **11**, 2003216, doi:https://doi.org/10.1002/aenm.202003216 (2021).
112 Ma, J., Miao, T. J. & Tang, J. Charge carrier dynamics and reaction intermediates in heterogeneous photocatalysis by time-resolved spectroscopies. *Chemical Society Reviews* **51**, 5777-5794, doi:10.1039/D1CS01164B (2022).
113 Sun, H., Tang, R. & Huang, J. Considering single-atom catalysts as photocatalysts from synthesis to application. *iScience* **25**, doi:10.1016/j.isci.2022.104232 (2022).
114 Li, B. *et al.* Emerging multifunctional metal–organic framework materials. *Adv. Mater.* **28**, 8819-8860 (2016).
115 Jiao, L. & Jiang, H.-L. Metal-Organic-Framework-Based Single-Atom Catalysts for Energy Applications. *Chem* **5**, 786-804, doi:https://doi.org/10.1016/j.chempr.2018.12.011 (2019).
116 Sui, J. *et al.* A General Strategy to Immobilize Single-Atom Catalysts in Metal–Organic Frameworks for Enhanced Photocatalysis. *Adv. Mater.*, 2109203 (2021).
117 Li, J. *et al.* Metal-organic framework encapsulated single-atom Pt catalysts for efficient photocatalytic hydrogen evolution. *J. Catal.* **375**, 351-360, doi:https://doi.org/10.1016/j.jcat.2019.06.024 (2019).
118 Wei, S. *et al.* Atomically dispersed Fe atoms anchored on COF-derived N-doped carbon nanospheres as efficient multi-functional catalysts. *Chemical science* **11**, 786-790 (2020).
119 Zeng, L. & Xue, C. Single metal atom decorated photocatalysts: Progress and challenges. *Nano Research* **14**, 934-944, doi:10.1007/s12274-020-3099-8 (2021).
120 Dong, P. *et al.* Platinum Single Atoms Anchored on a Covalent Organic Framework: Boosting Active Sites for Photocatalytic Hydrogen Evolution. *ACS Catal.* **11**, 13266-

13279, doi:10.1021/acscatal.1c03441 (2021).
121 Kou, M. *et al.* Photocatalytic CO2 conversion over single-atom MoN2 sites of covalent organic framework. *Appl. Catal. B* **291**, 120146, doi:https://doi.org/10.1016/j.apcatb.2021.120146 (2021).
122 Hu, X. *et al.* Single-atomic Pt sites anchored on defective TiO2 nanosheets as a superior photocatalyst for hydrogen evolution. *Journal of Energy Chemistry* **62**, 1-10, doi:https://doi.org/10.1016/j.jechem.2021.03.003 (2021).
123 Li, W. *et al.* Pd single-atom decorated CdS nanocatalyst for highly efficient overall water splitting under simulated solar light. *Appl. Catal. B* **304**, 121000, doi:https://doi.org/10.1016/j.apcatb.2021.121000 (2022).
124 Fu, Q. & Draxl, C. Hybrid Organic-Inorganic Perovskites as Promising Substrates for Pt Single-Atom Catalysts. *Phys. Rev. Lett.* **122**, 046101, doi:10.1103/PhysRevLett.122.046101 (2019).
125 Wu, Y. *et al.* An organometal halide perovskite supported Pt single-atom photocatalyst for H2 evolution. *Energy & Environmental Science*, doi:10.1039/D1EE03679C (2022).
126 Hu, H. *et al.* Construction of Single-Atom Platinum Catalysts Enabled by CsPbBr3 Nanocrystals. *ACS Nano* **15**, 13129-13139, doi:10.1021/acsnano.1c02515 (2021).
127 Su, P. *et al.* Fe atoms anchored on defective nitrogen doped hollow carbon spheres as efficient electrocatalysts for oxygen reduction reaction. *Nano Research* **14**, 1069-1077, doi:10.1007/s12274-020-3151-8 (2021).
128 Su, P. *et al.* Exceptional electrochemical HER performance with enhanced electron transfer between Ru nanoparticles and single atoms dispersed on a carbon substrate. *Angew. Chem.* **133**, 16180-16186 (2021).
129 Tian, H. *et al.* Single-atom catalysts for high-energy rechargeable batteries. *Chemical Science* **12**, 7656-7676, doi:10.1039/D1SC00716E (2021).
130 Wang, X., Su, P., Duyar, M. S. & Liu, J. Microenvironment and Nanoreactor Engineering of Single-Site Metal Catalysts for Electrochemical CO2 Reduction. *Energy Fuels* **35**, 9795-9808, doi:10.1021/acs.energyfuels.1c00937 (2021).
131 Zhuo, H.-Y. *et al.* Theoretical understandings of graphene-based metal single-atom catalysts: stability and catalytic performance. *Chemical Reviews* **120**, 12315-12341 (2020).
132 Gao, C. *et al.* Heterogeneous single-atom catalyst for visible-light-driven high-turnover CO2 reduction: the role of electron transfer. *Adv. Mater.* **30**, 1704624 (2018).
133 Liu, Y. *et al.* Ni single atoms anchored on nitrogen-doped graphene as H2-Evolution cocatalyst of SrTiO3 (Al)/CoOx for photocatalytic overall water splitting. *Carbon* **183**, 763-773 (2021).
134 Zhao, Q. *et al.* Single Nickel Atoms Anchored on Nitrogen-Doped Graphene as a Highly Active Cocatalyst for Photocatalytic H2 Evolution. *ACS Catal.* **8**, 11863-11874, doi:10.1021/acscatal.8b03737 (2018).
135 Zhang, H. *et al.* Enhanced Charge Transfer Process and Photocatalytic Activity over a Phosphonate-based MOF via Amorphization Strategy. **63**, e202400965, doi:https://doi.org/10.1002/anie.202400965 (2024).
136 Sun, H. *et al.* Interfacial energy band engineered CsPbBr3/NiFe-LDH heterostructure catalysts with tunable visible light driven photocatalytic CO2 reduction capability. *Catalysis Science & Technology* **13**, 1154-1163, doi:10.1039/D2CY01982E (2023).
137 Wang, L. *et al.* Precisely Constructed Metal Sulfides with Localized Single-Atom Rhodium for Photocatalytic C−H Activation and Direct Methanol Coupling to Ethylene Glycol. **35**, 2205782, doi:https://doi.org/10.1002/adma.202205782 (2023).
138 Bao, X. *et al.* Photocatalytic Selective Oxidation of HMF Coupled with H2 Evolution on Flexible Ultrathin g-C3N4 Nanosheets with Enhanced N–H Interaction. *ACS*

Catalysis **12**, 1919-1929, doi:10.1021/acscatal.1c05357 (2022).
139 Zhang, M. *et al.* Selective Valorization of 5-Hydroxymethylfurfural to 2,5-Diformylfuran Using Atmospheric O2 and MAPbBr3 Perovskite under Visible Light. *ACS Catalysis* **10**, 14793-14800, doi:10.1021/acscatal.0c04330 (2020).
140 Xia, T. *et al.* Sunlight-Driven Highly Selective Catalytic Oxidation of 5-Hydroxymethylfurfural Towards Tunable Products. **61**, e202204225, doi:https://doi.org/10.1002/anie.202204225 (2022).
141 Luo, N. *et al.* Visible-light-driven coproduction of diesel precursors and hydrogen from lignocellulose-derived methylfurans. *Nature Energy* **4**, 575-584, doi:10.1038/s41560-019-0403-5 (2019).
142 Chang, J. N. *et al.* Covalent-Bonding Oxidation Group and Titanium Cluster to Synthesize a Porous Crystalline Catalyst for Selective Photo-Oxidation Biomass Valorization. *Angewandte Chemie* **134**, e202209289 (2022).
143 Li, L. *et al.* Photocatalytic Achmatowicz Rearrangement on Triphenylbenzene–Dimethoxyterephthaldehyde–Covalent Organic Framework-Mo for Converting Biomass-Derived Furfuryl Alcohol to Hydropyranone. *ACS Nano* **18**, 33142-33151, doi:10.1021/acsnano.4c10975 (2024).
144 Ma, J. *et al.* Photocatalytic conversion of biomass-based monosaccharides to lactic acid by ultrathin porous oxygen doped carbon nitride. *Applied Catalysis B: Environmental* **283**, 119520, doi:https://doi.org/10.1016/j.apcatb.2020.119520 (2021).
145 Wu, X. *et al.* Selectivity Control in Photocatalytic Valorization of Biomass-Derived Platform Compounds by Surface Engineering of Titanium Oxide. *Chem* **6**, 3038-3053, doi:https://doi.org/10.1016/j.chempr.2020.08.014 (2020).
146 Giannakoudakis, D. A. *et al.* Additive-free photo-assisted selective partial oxidation at ambient conditions of 5-hydroxymethylfurfural by manganese (IV) oxide nanorods. *Applied Catalysis B: Environmental* **256**, 117803, doi:https://doi.org/10.1016/j.apcatb.2019.117803 (2019).
147 Meng, S. *et al.* One-step synthesis of 2D/2D-3D NiS/Zn3In2S6 hierarchical structure toward solar-to-chemical energy transformation of biomass-relevant alcohols. *Applied Catalysis B: Environmental* **266**, 118617, doi:https://doi.org/10.1016/j.apcatb.2020.118617 (2020).
148 Kang, F. *et al.* Dual-functional marigold-like ZnxCd1-xS homojunction for selective glucose photoreforming with remarkable H2 coproduction. *Journal of Energy Chemistry* **79**, 158-167, doi:https://doi.org/10.1016/j.jechem.2022.11.043 (2023).
149 Wang, L. *et al.* Solar energy-driven C−H activation of methanol for direct C−C coupling to ethylene glycol with high stability by nitrogen doped tantalum oxide. *Chinese Journal of Catalysis* **42**, 1459-1467, doi:https://doi.org/10.1016/S1872-2067(21)63797-X (2021).
150 Zhou, P. *et al.* Partially reduced Pd single atoms on CdS nanorods enable photocatalytic reforming of ethanol into high value-added multicarbon compound. *Chem* **7**, 1033-1049, doi:10.1016/j.chempr.2021.01.007 (2021).
151 Song, H., Luo, S., Huang, H., Deng, B. & Ye, J. Solar-Driven Hydrogen Production: Recent Advances, Challenges, and Future Perspectives. *ACS Energy Letters* **7**, 1043-1065, doi:10.1021/acsenergylett.1c02591 (2022).
152 Edirisooriya, E. M. N. T. *et al.* Photo-reforming and degradation of waste plastics under UV and visible light for H2 production using nanocomposite photocatalysts. *Journal of Environmental Chemical Engineering* **11**, 109580, doi:https://doi.org/10.1016/j.jece.2023.109580 (2023).
153 Nguyen, T. K. A. *et al.* Understanding Structure-Activity Relationship in Pt-loaded g-C3N4 for Efficient Solar- Photoreforming of Polyethylene Terephthalate Plastic and

Hydrogen Production. **8**, 2300427, doi:https://doi.org/10.1002/smtd.202300427 (2024).
154 Uekert, T., Kuehnel, M. F., Wakerley, D. W. & Reisner, E. Plastic waste as a feedstock for solar-driven H2 generation. *Energy & Environmental Science* **11**, 2853-2857, doi:10.1039/C8EE01408F (2018).
155 Zhang, S. *et al.* Boosted Photoreforming of Plastic Waste via Defect-Rich NiPS3 Nanosheets. *Journal of the American Chemical Society* **145**, 6410-6419, doi:10.1021/jacs.2c13590 (2023).
156 Gong, X. *et al.* Photoreforming of plastic waste poly (ethylene terephthalate) via in-situ derived CN-CNTs-NiMo hybrids. *Applied Catalysis B: Environment and Energy* **307**, 121143, doi:https://doi.org/10.1016/j.apcatb.2022.121143 (2022).
157 Chen, Q. & Tan, Y. Enhanced plasmonic absorption of Pt cuboctahedra-WO3 nanohybrids used as visible light photocatalysts for overall water splitting. *Nano Research* **16**, 5919-5928, doi:10.1007/s12274-022-5175-8 (2023).
158 Wang, H. *et al.* Semiconductor heterojunction photocatalysts: design, construction, and photocatalytic performances. *Chemical Society Reviews* **43**, 5234-5244, doi:10.1039/C4CS00126E (2014).
159 Xiao, C., Zhang, L., Hao, H. & Wang, W. High Selective Oxidation of Benzyl Alcohol to Benzylaldehyde and Benzoic Acid with Surface Oxygen Vacancies on W18O49/Holey Ultrathin g-C3N4 Nanosheets. *ACS Sustainable Chemistry & Engineering* **7**, 7268-7276, doi:10.1021/acssuschemeng.9b00299 (2019).
160 Wu, H. *et al.* Construction of two-dimensionally relative p-n heterojunction for efficient photocatalytic redox reactions under visible light. *Applied Surface Science* **505**, 144638, doi:https://doi.org/10.1016/j.apsusc.2019.144638 (2020).
161 Shelake, S. P. *et al.* Emerging Photoreforming Process to Hydrogen Production: A Future Energy. **34**, 2403795, doi:https://doi.org/10.1002/adfm.202403795 (2024).
162 Kale, M. J., Avanesian, T. & Christopher, P. Direct Photocatalysis by Plasmonic Nanostructures. *ACS Catalysis* **4**, 116-128, doi:10.1021/cs400993w (2014).
163 Jain, V., Kashyap, R. K. & Pillai, P. P. Plasmonic Photocatalysis: Activating Chemical Bonds through Light and Plasmon. *Advanced Optical Materials* **10**, 2200463, doi:https://doi.org/10.1002/adom.202200463 (2022).
164 Dall'Osto, G. *et al.* Peeking into the Femtosecond Hot-Carrier Dynamics Reveals Unexpected Mechanisms in Plasmonic Photocatalysis. *Journal of the American Chemical Society* **146**, 2208-2218, doi:10.1021/jacs.3c12470 (2024).
165 Zhang, X. *et al.* Surface Plasmon Resonance-Mediated Photocatalytic H2 Generation. *ChemSusChem* **17**, e202400513, doi:https://doi.org/10.1002/cssc.202400513 (2024).
166 Chen, W. *et al.* Plasmonic tandem heterojunctions enable high-efficiency charge transfer for broad spectrum photocatalytic hydrogen production. *Journal of Energy Chemistry* **100**, 710-720, doi:https://doi.org/10.1016/j.jechem.2024.09.018 (2025).
167 Wang, Z. *et al.* Localized surface plasmon resonance-induced bidirectional electron transfer of formic acid adsorption for boosting photocatalytic hydrogen production on Ni/TiO2. *Chemical Engineering Journal* **482**, 148942, doi:https://doi.org/10.1016/j.cej.2024.148942 (2024).
168 Deka, T. & G Nair, R. Recent advancements in surface plasmon resonance and Schottky junction assisted photocatalytic water splitting of noble metal decorated Titania: A review. *International Journal of Hydrogen Energy* **59**, 322-342, doi:https://doi.org/10.1016/j.ijhydene.2024.02.002 (2024).
169 Han, C. *et al.* All-in-One: Plasmonic Janus Heterostructures for Efficient Cooperative Photoredox Catalysis. **63**, e202408527, doi:https://doi.org/10.1002/anie.202408527 (2024).
170 Tong, F., Liang, X., Bao, X. & Zheng, Z. Photocatalysis on Hybrid Plasmonic

Nanomaterials: From Catalytic Mechanism Study at Single-Particle Level to Materials Design. *ACS Catalysis* **14**, 11425-11446, doi:10.1021/acscatal.4c03566 (2024).
171 Xin, Y. *et al.* Copper-Based Plasmonic Catalysis: Recent Advances and Future Perspectives. **33**, 2008145, doi:https://doi.org/10.1002/adma.202008145 (2021).
172 Li, S. *et al.* Recent advances of non-noble metals based plasma materials in photocatalysis. *Coordination Chemistry Reviews* **510**, 215803, doi:https://doi.org/10.1016/j.ccr.2024.215803 (2024).
173 Bayles, A. *et al.* Al@TiO2 Core–Shell Nanoparticles for Plasmonic Photocatalysis. *ACS Nano* **16**, 5839-5850, doi:10.1021/acsnano.1c10995 (2022).
174 Sayed, M., Yu, J., Liu, G. & Jaroniec, M. Non-Noble Plasmonic Metal-Based Photocatalysts. *Chemical Reviews* **122**, 10484-10537, doi:10.1021/acs.chemrev.1c00473 (2022).
175 Ten, A., Lomonosov, V., Boukouvala, C. & Ringe, E. Magnesium Nanoparticles for Surface-Enhanced Raman Scattering and Plasmon-Driven Catalysis. *ACS Nano* **18**, 18785-18799, doi:10.1021/acsnano.4c06858 (2024).
176 Hopper, E. R. *et al.* Size Control in the Colloidal Synthesis of Plasmonic Magnesium Nanoparticles. *The Journal of Physical Chemistry C* **126**, 563-577, doi:10.1021/acs.jpcc.1c07544 (2022).
177 Zhu, P., Zhang, W., Li, Q. & Xia, H. Visible-Light-Driven Photocatalytic Oxidation of 5-Hydroxymethylfurfural to 2,5-Furandicarboxylic Acid over Plasmonic Au/ZnO Catalyst. *ACS Sustainable Chemistry & Engineering* **10**, 8778-8787, doi:10.1021/acssuschemeng.2c01143 (2022).
178 Zhang, W. *et al.* Photocatalytic Oxidation of 5-Hydroxymethylfurfural Over Interfacial-Enhanced Ag/TiO2 Under Visible Light Irradiation. **15**, e202102158, doi:https://doi.org/10.1002/cssc.202102158 (2022).
179 Sun, H. *et al.* Plasmon-enhanced alcohol oxidations over porous carbon nanosphere-supported palladium and gold bimetallic nanocatalyst. *Applied Catalysis B: Environmental* **292**, 120151, doi:https://doi.org/10.1016/j.apcatb.2021.120151 (2021).
180 Wang, A. *et al.* Plasmon-Enhanced 5-Hydroxymethylfurfural Production from the Photothermal Conversion of Cellulose in a Biphasic Medium. *ACS Sustainable Chemistry & Engineering* **9**, 16115-16122, doi:10.1021/acssuschemeng.1c04592 (2021).
181 Zhao, H. *et al.* Plasmon enhanced glucose photoreforming for arabinose and gas fuel co-production over 3DOM TiO2-Au. *Applied Catalysis B: Environmental* **291**, 120055, doi:https://doi.org/10.1016/j.apcatb.2021.120055 (2021).
182 Zhong, W. *et al.* Synergistic effect of photo-thermal catalytic glycerol reforming hydrogen production over 2D Au/TiO2 nanoflakes. *Chemical Engineering Journal* **446**, 137063, doi:https://doi.org/10.1016/j.cej.2022.137063 (2022).
183 Yang, Q. *et al.* Bimetal-modified g-C3N4 photocatalyst for promoting hydrogen production coupled with selective oxidation of biomass derivative. *Journal of Alloys and Compounds* **897**, 163177, doi:https://doi.org/10.1016/j.jallcom.2021.163177 (2022).
184 Yu, W. *et al.* Mechanistic Insights into the Selective Oxidation of 5-Hydroxymethylfurfural over Au/TiO2 Catalysts under Photoexcited and Dark States. *ACS Sustainable Chemistry & Engineering* **11**, 13116-13125, doi:10.1021/acssuschemeng.3c03289 (2023).
185 Liu, X., Zou, Y. & Jiang, J. Sunlight-driven selective oxidation of glycerol on formate oxidase mimicking AuPt/TiO2. *Applied Catalysis B: Environment and Energy* **350**, 123927, doi:https://doi.org/10.1016/j.apcatb.2024.123927 (2024).
186 Han, P. *et al.* Plasmonic silver nanoparticles promoted sugar conversion to 5-

hydroxymethylfurfural over catalysts of immobilised metal ions. *Applied Catalysis B: Environmental* **296**, 120340, doi:https://doi.org/10.1016/j.apcatb.2021.120340 (2021).
187 Bajpai, H., Nivedhitha, T. R., Dais, E., Kanungo, S. S. & Gopinath, C. S. Oxidative and selective C–C cleavage of glycerol to glycolaldehyde with atom-like Cu on Cu-TiO2: Photocatalytic water reduction with concurrent glycerol oxidation in sunlight. *Journal of Catalysis* **437**, 115644, doi:https://doi.org/10.1016/j.jcat.2024.115644 (2024).
188 Song, K. *et al.* Toward Efficient Utilization of Photogenerated Charge Carriers in Photoelectrochemical Systems: Engineering Strategies from the Atomic Level to Configuration. *Chemical Reviews* **124**, 13660-13680, doi:10.1021/acs.chemrev.4c00382 (2024).
189 Tang, B. & Xiao, F.-X. An Overview of Solar-Driven Photoelectrochemical CO2 Conversion to Chemical Fuels. *ACS Catalysis* **12**, 9023-9057, doi:10.1021/acscatal.2c01667 (2022).
190 Blaskievicz, S. F., Francisco, J. L., Marken, F. & Mascaro, L. H. Carbon Nitrides in Photoelectrochemistry: State of the Art and Perspectives Beyond Water Splitting. *ACS Applied Energy Materials* **7**, 3021-3038, doi:10.1021/acsaem.3c02623 (2024).
191 Liu, D. & Kuang, Y. Particle-Based Photoelectrodes for PEC Water Splitting: Concepts and Perspectives. *Advanced Materials* **36**, 2311692, doi:https://doi.org/10.1002/adma.202311692 (2024).
192 Toe, C. Y. *et al.* Recent advances and the design criteria of metal sulfide photocathodes and photoanodes for photoelectrocatalysis. *Journal of Materials Chemistry A* **9**, 20277-20319, doi:10.1039/D1TA05407D (2021).
193 Wang, Q., Liu, J., Li, Q. & Yang, J. Stability of Photocathodes: A Review on Principles, Design, and Strategies. *ChemSusChem* **16**, e202202186, doi:https://doi.org/10.1002/cssc.202202186 (2023).
194 Pattanayak, P. *et al.* Recent progress in perovskite transition metal oxide-based photocatalyst and photoelectrode materials for solar-driven water splitting. *Journal of Environmental Chemical Engineering* **10**, 108429, doi:https://doi.org/10.1016/j.jece.2022.108429 (2022).
195 Dong, X., Chen, X., Jiang, X. & Yang, N. Light-Assisted Energy Storage Devices: Principles, Performance, and Perspectives. *Advanced Energy Materials* **13**, 2301143, doi:https://doi.org/10.1002/aenm.202301143 (2023).
196 Li, S., Xu, W., Meng, L., Tian, W. & Li, L. Recent Progress on Semiconductor Heterojunction-Based Photoanodes for Photoelectrochemical Water Splitting. *Small Science* **2**, 2100112, doi:https://doi.org/10.1002/smsc.202100112 (2022).
197 Zuo, L. *et al.* Fundamental Insights into Photoelectrochemical Carbon Dioxide Reduction: Elucidating the Reaction Pathways. *ACS Catalysis* **14**, 16795-16833, doi:10.1021/acscatal.4c04795 (2024).
198 Liu, Y., Wang, M., Zhang, B., Yan, D. & Xiang, X. Mediating the Oxidizing Capability of Surface-Bound Hydroxyl Radicals Produced by Photoelectrochemical Water Oxidation to Convert Glycerol into Dihydroxyacetone. *ACS Catalysis* **12**, 6946-6957, doi:10.1021/acscatal.2c01319 (2022).
199 An, Y., Lei, T., Jiang, W. & Pang, H. Research progress on photocatalytic, electrocatalytic and photoelectrocatalytic selective oxidation of 5-hydroxymethylfurfural. *Green Chemistry* **26**, 10739-10773, doi:10.1039/D4GC03597F (2024).
200 Abbas, T., Yahya, H. S. M. & Amin, N. A. S. Insights and Progress on Photocatalytic and Photoelectrocatalytic Reactor Configurations and Materials for CO2 Reduction to Solar Fuels. *Energy & Fuels* **37**, 18330-18368, doi:10.1021/acs.energyfuels.3c02863 (2023).

201 Li, Z. *et al.* Roles of Cocatalysts in Biomass Photo(electro)refining. *Advanced Energy Materials* **14**, 2401838, doi:https://doi.org/10.1002/aenm.202401838 (2024).
202 Kong, H. *et al.* Electrolyte selection toward efficient photoelectrochemical glycerol oxidation on BiVO4. *Chemical Science* **15**, 10425-10435, doi:10.1039/D4SC01651C (2024).
203 Lu, Y. *et al.* Solar-driven highly selective conversion of glycerol to dihydroxyacetone using surface atom engineered BiVO4 photoanodes. *Nature Communications* **15**, 5475, doi:10.1038/s41467-024-49662-7 (2024).
204 Miao, Y. *et al.* Surface active oxygen engineering of photoanodes to boost photoelectrochemical water and alcohol oxidation coupled with hydrogen production. *Applied Catalysis B: Environmental* **323**, 122147, doi:https://doi.org/10.1016/j.apcatb.2022.122147 (2023).
205 Gao, Q. *et al.* Improved glyceraldehyde generation through FeOOH co-catalysts-modified BiVO4 featuring Bi-O-Fe active sites for photoelectrocatalytic glycerol oxidation. *Journal of Catalysis* **438**, 115709, doi:https://doi.org/10.1016/j.jcat.2024.115709 (2024).
206 Jakubow-Piotrowska, K., Witkowski, B. & Augustynski, J. Photoelectrocatalytic hydrogen generation coupled with reforming of glucose into valuable chemicals using a nanostructured WO3 photoanode. *Communications Chemistry* **5**, 125, doi:10.1038/s42004-022-00745-w (2022).
207 Wang, S. *et al.* A non-enzymatic photoelectrochemical glucose sensor based on BiVO4 electrode under visible light. *Sensors and Actuators B: Chemical* **291**, 34-41, doi:https://doi.org/10.1016/j.snb.2019.04.057 (2019).
208 Wang, Z. & Einaga, H. WO3-based Materials for Photocatalytic and Photoelectrocatalytic Selective Oxidation Reactions. *ChemCatChem* **15**, e202300723, doi:https://doi.org/10.1002/cctc.202300723 (2023).
209 Zheng, L. *et al.* Solar-driven upgrading of 5-hydroxymethylfurfural on BiVO4 photoanodes: Effect of TEMPO mediator and cocatalyst on reaction kinetics. *Applied Catalysis B: Environmental* **331**, 122679, doi:https://doi.org/10.1016/j.apcatb.2023.122679 (2023).
210 Sun, Y. *et al.* Photoelectrochemistry-driven selective hydroxyl oxidation of polyols: Synergy between Au nanoparticles and C₃N₄ nanosheets. *Chem Catalysis* **1**, 1260-1272, doi:10.1016/j.checat.2021.09.001 (2021).
211 Sun, H. *et al.* Vacancy-engineered bismuth vanadate for photoelectrocatalytic glycerol oxidation with simultaneous hydrogen production. *EES Catalysis*, doi:10.1039/D4EY00211C (2025).
212 Wu, P.-d., Li, L., Wang, K., Li, H. & Fang, Z. Non-quantum nanostructure-enabled hot carrier generation for enhancive photoelectrocatalytic oxidation of bio-alcohol in water coupled with hydrogen evolution. *Green Chemistry* **25**, 2771-2781, doi:10.1039/D3GC00226H (2023).
213 Zhou, Z. *et al.* Selective photoelectrocatalytic tuning of benzyl alcohol to benzaldehyde for enhanced hydrogen production. *Applied Catalysis B: Environmental* **286**, 119868, doi:https://doi.org/10.1016/j.apcatb.2020.119868 (2021).
214 Pahari, S. K. & Chen, Y.-T. In situ observation of photoelectrochemical water oxidation intermediates for selective biomass upgrading with simultaneous hydrogen production. *Chemical Engineering Journal* **473**, 145232, doi:https://doi.org/10.1016/j.cej.2023.145232 (2023).
215 Liu, W.-J. *et al.* Efficient electrochemical production of glucaric acid and H2 via glucose electrolysis. *Nature Communications* **11**, 265, doi:10.1038/s41467-019-14157-3 (2020).

216 Yuan, H. *et al.* α-Fe2O3/Nb2O5/C Nanorods for Selective Photoelectrocatalytic Oxidation of 5-Hydroxymethylfurfural under Solar Light. *ACS Applied Nano Materials* **7**, 10387-10395, doi:10.1021/acsanm.4c00798 (2024).
217 G, B. *et al.* Dual-functional paired photoelectrocatalytic system for the photocathodic reduction of CO2 to fuels and the anodic oxidation of furfural to value-added chemicals. *Applied Catalysis B: Environmental* **298**, 120520, doi:https://doi.org/10.1016/j.apcatb.2021.120520 (2021).
218 Pecoraro, C. M., Di Franco, F., Loddo, V., Bellardita, M. & Santamaria, M. Photoelectrolysis of glucose and fructose containing solution in PGM-free cells for hydrogen and valuable chemicals production. *International Journal of Hydrogen Energy* **87**, 1277-1287, doi:https://doi.org/10.1016/j.ijhydene.2024.09.124 (2024).
219 Stenuick, J.-Y. *What the EU's Pharmaceutical Strategy could mean for sustainability*, <https://noharm-europe.org/articles/blog/europe/what-eu%E2%80%99s-pharmaceutical-strategy-could-mean-sustainability> (2020).
220 Getty, M. R. v. *Path to net-zero: EU pharma accelerates pledges while US plays catch-up*, <https://www.spglobal.com/marketintelligence/en/news-insights/latest-news-headlines/path-to-net-zero-eu-pharma-accelerates-pledges-while-us-plays-catch-up-67928165> (2021).
221 Ren, Y., Yang, Y. & Wei, M. Recent Advances on Heterogeneous Non-noble Metal Catalysts toward Selective Hydrogenation Reactions. *ACS Catal.* **13**, 8902-8924, doi:10.1021/acscatal.3c01442 (2023).
222 Luneau, M. *et al.* Guidelines to Achieving High Selectivity for the Hydrogenation of α,β-Unsaturated Aldehydes with Bimetallic and Dilute Alloy Catalysts: A Review. *Chem. Rev.* **120**, 12834-12872, doi:10.1021/acs.chemrev.0c00582 (2020).
223 Racha, A., Samanta, C., Sreekantan, S. & Marimuthu, B. Review on Catalytic Hydrogenation of Biomass-Derived Furfural to Furfuryl Alcohol: Recent Advances and Future Trends. *Energy & Fuels* **37**, 11475-11496, doi:10.1021/acs.energyfuels.3c01174 (2023).
224 Kim, K. D. *et al.* Tailoring High-Performance Pd Catalysts for Chemoselective Hydrogenation Reactions via Optimizing the Parameters of the Double-Flame Spray Pyrolysis. *ACS Catal.* **6**, 2372-2381, doi:10.1021/acscatal.6b00396 (2016).
225 Wang, Z. *et al.* Influence of support acidity on the performance of size-confined Pt nanoparticles in the chemoselective hydrogenation of acetophenone. *Catal. Sci. Technol.* **5**, 2788-2797, doi:10.1039/C5CY00214A (2015).
226 Wang, Z. *et al.* Palladium-doped silica–alumina catalysts obtained from double-flame FSP for chemoselective hydrogenation of the model aromatic ketone acetophenone. *J. Catal.* **302**, 10-19, doi:https://doi.org/10.1016/j.jcat.2013.02.017 (2013).
227 Tang, R. *et al.* Fabrication of MOFs' derivatives assisted perovskite nanocrystal on TiO2 photoanode for photoelectrochemical glycerol oxidation with simultaneous hydrogen production. *Applied Catalysis B: Environmental* **296**, 120382 (2021).
228 Ma, X.-C., Dai, Y., Yu, L. & Huang, B.-B. Energy transfer in plasmonic photocatalytic composites. *Light: Science & Applications* **5**, e16017-e16017, doi:10.1038/lsa.2016.17 (2016).
229 Zhang, Y., Guo, W., Zhang, Y. & Wei, W. D. Plasmonic Photoelectrochemistry: In View of Hot Carriers. *Adv. Mater.* **33**, 2006654, doi:https://doi.org/10.1002/adma.202006654 (2021).
230 Li, H. *et al.* Facile interfacial synthesis of thin AuPd alloy nanowires for plasmon-enhanced selective photocatalytic oxidation of benzyl alcohol. *J. Catal.* **436**, 115588, doi:https://doi.org/10.1016/j.jcat.2024.115588 (2024).
231 Zhang, Y. *et al.* Surface-Plasmon-Driven Hot Electron Photochemistry. *Chem. Rev.* **118**,

2927-2954, doi:10.1021/acs.chemrev.7b00430 (2018).
232 Forcherio, G. T. *et al.* Single-Particle Insights into Plasmonic Hot Carrier Separation Augmenting Photoelectrochemical Ethanol Oxidation with Photocatalytically Synthesized Pd–Au Bimetallic Nanorods. *ACS Nano* **16**, 12377-12389, doi:10.1021/acsnano.2c03549 (2022).
233 Wang, H. *et al.* In-situ formation of electron-deficient Pd sites on AuPd alloy nanoparticles under irradiation enabled efficient photocatalytic Heck reaction. *Chinese Journal of Catalysis* **46**, 72-83, doi:https://doi.org/10.1016/S1872-2067(22)64192-5 (2023).
234 Xiao, Q. *et al.* Visible Light-Driven Cross-Coupling Reactions at Lower Temperatures Using a Photocatalyst of Palladium and Gold Alloy Nanoparticles. *ACS Catal.* **4**, 1725-1734, doi:10.1021/cs5000284 (2014).
235 Ravel, B. & Newville, M. ATHENA, ARTEMIS, HEPHAESTUS: data analysis for X-ray absorption spectroscopy using IFEFFIT. *J Synchrotron Radiat* **12**, 537-541, doi:10.1107/S0909049505012719 (2005).
236 Kresse, G. & Furthmüller, J. Efficiency of ab-initio total energy calculations for metals and semiconductors using a plane-wave basis set. *Computational Materials Science* **6**, 15-50, doi:https://doi.org/10.1016/0927-0256(96)00008-0 (1996).
237 Kohn, W. & Sham, L. J. Self-Consistent Equations Including Exchange and Correlation Effects. *Physical Review* **140**, A1133-A1138, doi:10.1103/PhysRev.140.A1133 (1965).
238 Perdew, J. P., Burke, K. & Ernzerhof, M. Generalized Gradient Approximation Made Simple. *Phys. Rev. Lett.* **77**, 3865-3868, doi:10.1103/PhysRevLett.77.3865 (1996).
239 Tkatchenko, A. & Scheffler, M. Accurate Molecular Van Der Waals Interactions from Ground-State Electron Density and Free-Atom Reference Data. *Phys. Rev. Lett.* **102**, 073005, doi:10.1103/PhysRevLett.102.073005 (2009).
240 Wang, V., Xu, N., Liu, J.-C., Tang, G. & Geng, W.-T. VASPKIT: A user-friendly interface facilitating high-throughput computing and analysis using VASP code. *Comput. Phys. Commun.* **267**, 108033, doi:https://doi.org/10.1016/j.cpc.2021.108033 (2021).
241 Park, J. *et al.* Compositional gradient induced enhancement of Dzyaloshinskii–Moriya interaction in Pt/Co/Ta heterostructures modulated by Pt–Co alloy intralayers. *Acta Mater.* **241**, 118383, doi:https://doi.org/10.1016/j.actamat.2022.118383 (2022).
242 Zou, H. *et al.* Pushing the limit of atomically dispersed Au catalysts for electrochemical H2O2 production by precise electronic perturbation of the active site. *Chem Catal.* **3**, doi:10.1016/j.checat.2023.100583 (2023).
243 Prytkova, A., Kirsanova, M. A., Kiiamov, A. G., Tayurskii, D. A. & Dimiev, A. M. Ni–Pd Nanocomposites on Reduced Graphene Oxide Support as Electrocatalysts for Hydrogen Evolution Reactions. *ACS Appl. Nano Mater.* **6**, 14902-14909, doi:10.1021/acsanm.3c02461 (2023).
244 Guo, B. *et al.* Bimetallic AuPd Nanoparticles Loaded on Amine-Functionalized Porous Boron Nitride Nanofibers for Catalytic Dehydrogenation of Formic Acid. *ACS Appl. Nano Mater.* **4**, 1849-1857, doi:10.1021/acsanm.0c03224 (2021).
245 Xie, M. *et al.* Intermetallic Single-Atom Alloy In–Pd Bimetallene for Neutral Electrosynthesis of Ammonia from Nitrate. *J. Am. Chem. Soc.* **145**, 13957-13967, doi:10.1021/jacs.3c03432 (2023).
246 Du, C. *et al.* Selectively Reducing Nitrate into NH3 in Neutral Media by PdCu Single-Atom Alloy Electrocatalysis. *ACS Catal.* **13**, 10560-10569, doi:10.1021/acscatal.3c01088 (2023).
247 Tofighi, G. *et al.* Microfluidic Synthesis of Ultrasmall AuPd Nanoparticles with a Homogeneously Mixed Alloy Structure in Fast Continuous Flow for Catalytic

Applications. *J. Phys. Chem. C* **122**, 1721-1731, doi:10.1021/acs.jpcc.7b11383 (2018).
248 Timoshenko, J. *et al.* Probing Atomic Distributions in Mono- and Bimetallic Nanoparticles by Supervised Machine Learning. *Nano Lett.* **19**, 520-529, doi:10.1021/acs.nanolett.8b04461 (2019).
249 Li, S. *et al.* Recent Advances in Plasmonic Nanostructures for Enhanced Photocatalysis and Electrocatalysis. **33**, 2000086, doi:https://doi.org/10.1002/adma.202000086 (2021).
250 Prada, S., Martinez, U. & Pacchioni, G. Work function changes induced by deposition of ultrathin dielectric films on metals: A theoretical analysis. *Phys. Rev. B: Condens. Matter* **78**, 235423, doi:10.1103/PhysRevB.78.235423 (2008).
251 Lee, Y.-S. *et al.* Charge redistribution and electronic behavior in Pd-Au alloys. *J. Korean Phys. Soc.* **37**, 451-455 (2000).
252 Gao, F. & Goodman, D. W. Pd–Au bimetallic catalysts: understanding alloy effects from planar models and (supported) nanoparticles. *Chem. Soc. Rev.* **41**, 8009-8020, doi:10.1039/C2CS35160A (2012).
253 Cheng, X. *et al.* Single-atom alloy with Pt-Co dual sites as an efficient electrocatalyst for oxygen reduction reaction. *Appl. Catal., B* **306**, 121112, doi:https://doi.org/10.1016/j.apcatb.2022.121112 (2022).
254 Ren, B. *et al.* Nano-crumples induced Sn-Bi bimetallic interface pattern with moderate electron bank for highly efficient CO2 electroreduction. *Nat. Commun.* **13**, 2486, doi:10.1038/s41467-022-29861-w (2022).
255 Liu, X. *et al.* Activation of Carbonyl Groups via Weak Interactions in Pt/COF/SiO2 Catalyzed Selective Hydrogenation. *ACS Catal.* **12**, 6618-6627, doi:10.1021/acscatal.2c00980 (2022).
256 Ning, F. *et al.* TiO2/graphene/NiFe-layered double hydroxide nanorod array photoanodes for efficient photoelectrochemical water splitting. *Energy Environ. Sci.* **9**, 2633-2643, doi:10.1039/C6EE01092J (2016).
257 Zhou, Y. *et al.* Amino Modified Carbon Dots with Electron Sink Effect Increase Interface Charge Transfer Rate of Cu-Based Electrocatalyst to Enhance the CO2 Conversion Selectivity to C2H4. *Adv. Funct. Mater.* **32**, 2113335, doi:https://doi.org/10.1002/adfm.202113335 (2022).
258 Tang, R. *et al.* Incorporating plasmonic Au-nanoparticles into three-dimensionally ordered macroporous perovskite frameworks for efficient photocatalytic CO2 reduction. *Chem. Eng. J.* **429**, 132137, doi:https://doi.org/10.1016/j.cej.2021.132137 (2022).
259 Yu, J. *et al.* Coalescence of Au–Pd Nanoropes and their Application as Enhanced Electrocatalysts for the Oxygen Reduction Reaction. **18**, 2203458, doi:https://doi.org/10.1002/smll.202203458 (2022).
260 Zhang, Y. & Park, S.-J. Bimetallic AuPd alloy nanoparticles deposited on MoO3 nanowires for enhanced visible-light driven trichloroethylene degradation. *J. Catal.* **361**, 238-247, doi:https://doi.org/10.1016/j.jcat.2018.03.010 (2018).
261 Ninakanti, R., Dingenen, F., Borah, R., Peeters, H. & Verbruggen, S. W. Plasmonic Hybrid Nanostructures in Photocatalysis: Structures, Mechanisms, and Applications. *Top. Curr. Chem.* **380**, 40, doi:10.1007/s41061-022-00390-w (2022).
262 Wu, Z. *et al.* A review of spectral controlling for renewable energy harvesting and conserving. *Mater. Today Phys.* **18**, 100388, doi:https://doi.org/10.1016/j.mtphys.2021.100388 (2021).
263 Shah, J., Gupta, S. K., Sonvane, Y. & Adhikari, K. Computational study of electronic and optical properties of p-group atomic adsorption on α-Al2O3 (0001). *Comput. Theor. Chem.* **1155**, 101-108, doi:https://doi.org/10.1016/j.comptc.2019.03.026 (2019).
264 Zhou, X. *et al.* Validating the efficiency of γ-Al2O3/La0.6Sr0.4Co0.2Fe0.8O3-δ

double-layer electrolyte for low temperature solid oxide fuel cell. *Int. J. Hydrogen Energy* **46**, 40014-40021, doi:https://doi.org/10.1016/j.ijhydene.2021.09.255 (2021).

265 Sarina, S. *et al.* Viable Photocatalysts under Solar-Spectrum Irradiation: Nonplasmonic Metal Nanoparticles. *Angewandte Chemie International Edition* **53**, 2935-2940, doi:https://doi.org/10.1002/anie.201308145 (2014).

266 Singh, S., Kumari, S., Ahlawat, M. & Govind Rao, V. Photocatalytic NADH Regeneration Employing Au–Pd Core–Shell Nanoparticles: Plasmonic Modulation of Underlying Reaction Kinetics. *J. Phys. Chem. C* **126**, 15175-15183, doi:10.1021/acs.jpcc.2c03998 (2022).

267 Zhang, L. *et al.* Plasmon-mediated activation of persulfate for efficient photodegradation of ionic liquids over Ag@Pd core–shell nanocubes. *Appl. Catal., B* **301**, 120751, doi:https://doi.org/10.1016/j.apcatb.2021.120751 (2022).

268 Yu, G. *et al.* Collective excitation of plasmon-coupled Au-nanochain boosts photocatalytic hydrogen evolution of semiconductor. *Nat. Commun.* **10**, 4912, doi:10.1038/s41467-019-12853-8 (2019).

269 Gao, Y. *et al.* The Polarization Effect in Surface-Plasmon-Induced Photocatalysis on Au/TiO2 Nanoparticles. *Angew. Chem.* **59**, 18218-18223, doi:https://doi.org/10.1002/anie.202007706 (2020).

270 Liu, X. *et al.* Activation of carbonyl groups via weak interactions in Pt/COF/SiO2 catalyzed selective hydrogenation. **12**, 6618-6627 (2022).

271 Sarina, S. *et al.* Enhancing Catalytic Performance of Palladium in Gold and Palladium Alloy Nanoparticles for Organic Synthesis Reactions through Visible Light Irradiation at Ambient Temperatures. *J. Am. Chem. Soc.* **135**, 5793-5801, doi:10.1021/ja400527a (2013).

272 Zhu, W., Kattel, S., Jiao, F. & Chen, J. G. J. A. E. M. Shape-controlled CO2 electrochemical reduction on nanosized Pd hydride cubes and octahedra. *Adv. Energy Mater.* **9**, 1802840, doi:https://doi.org/10.1002/aenm.201802840 (2019).

273 Sham, T. K. L-edge x-ray-absorption systematics of the noble metals Rh, Pd, and Ag and the main-group metals In and Sn: A study of the unoccupied density of states in 4d elements. *Phys. Rev. B* **31**, 1888-1902, doi:10.1103/PhysRevB.31.1888 (1985).

274 Müller, J. E. & Wilkins, J. W. Band-structure approach to the x-ray spectra of metals. *Phys. Rev. B* **29**, 4331-4348, doi:10.1103/PhysRevB.29.4331 (1984).

275 Hopkins, B. J. & Pender, K. R. The adsorption of hydrogen on (110), (100), (111), and (113) oriented tungsten single crystal surfaces. *Surf. Sci.* **5**, 316-324, doi:https://doi.org/10.1016/0039-6028(66)90030-6 (1966).

276 Ya, K. S. EFFECTIVE CHARGES AND ELECTRONEGATIVITY. *Russian Chemical Reviews* **31**, 197, doi:10.1070/RC1962v031n04ABEH001279 (1962).

277 Kepp, K. P. Chemical Causes of Metal Nobleness. *ChemPhysChem* **21**, 360-369, doi:https://doi.org/10.1002/cphc.202000013 (2020).

278 Xiao, Q. *et al.* Efficient photocatalytic Suzuki cross-coupling reactions on Au–Pd alloy nanoparticles under visible light irradiation. *Green Chem.* **16**, 4272-4285, doi:10.1039/C4GC00588K (2014).

279 Han, P. *et al.* Wavelength-Specific Product Desorption as a Key to Raising Nitrile Yield of Primary Alcohol Ammoxidation over Illuminated Pd Nanoparticles. *ACS Catalysis* **12**, 2280-2289, doi:10.1021/acscatal.1c05486 (2022).

280 Guo, M. *et al.* Improving Catalytic Hydrogenation Performance of Pd Nanoparticles by Electronic Modulation Using Phosphine Ligands. *ACS Catal.* **8**, 6476-6485, doi:10.1021/acscatal.8b00872 (2018).

281 More, S. R. & Yadav, G. D. Effect of Supercritical CO2 as Reaction Medium for Selective Hydrogenation of Acetophenone to 1-Phenylethanol. *ACS Omega* **3**, 7124-

7132, doi:10.1021/acsomega.8b00001 (2018).
282 Paul, R. *et al.* Realizing Catalytic Acetophenone Hydrodeoxygenation with Palladium-Equipped Porous Organic Polymers. *ACS Appl. Mater. Interfaces* **12**, 50550-50565, doi:10.1021/acsami.0c16680 (2020).
283 Saraeian, A. *et al.* Hydrogenation/Hydrodeoxygenation Selectivity Modulation by Cometal Addition to Palladium on Carbon-Coated Supports. *ACS Sustain. Chem. Eng.* **10**, 7759-7771, doi:10.1021/acssuschemeng.2c02399 (2022).
284 Buhaibeh, R. *et al.* Phosphine-NHC Manganese Hydrogenation Catalyst Exhibiting a Non-Classical Metal-Ligand Cooperative H(2) Activation Mode. *Angew. Chem. Int. Ed. Engl.* **58**, 6727-6731, doi:10.1002/anie.201901169 (2019).
285 Liu, B. & Liu, Q. A Pincer Cobalt Complex as Catalyst with Dual Hydrogenation Activities for Hydrodeoxygenation of Ketones with H2†. *Chin. J. Chem.* **n/a**, doi:https://doi.org/10.1002/cjoc.202300418.
286 Landry, M. J., Gellé, A., Meng, B. Y., Barrett, C. J. & Moores, A. Surface-Plasmon-Mediated Hydrogenation of Carbonyls Catalyzed by Silver Nanocubes under Visible Light. *ACS Catal.* **7**, 6128-6133, doi:10.1021/acscatal.7b02128 (2017).
287 Shabade, A. B. *et al.* Room temperature chemoselective hydrogenation of C C, C O and C N bonds by using a well-defined mixed donor Mn(i) pincer catalyst. *Chemical Science* **13**, 13764-13773, doi:10.1039/D2SC05274A (2022).
288 Ma, Y. *et al.* Cobalt Nanocluster Supported on ZrREnOx for the Selective Hydrogenation of Biomass Derived Aromatic Aldehydes and Ketones in Water. *ACS Catal.* **8**, 1268-1277, doi:10.1021/acscatal.7b03470 (2018).
289 Mendes-Burak, J., Ghaffari, B. & Copéret, C. Selective hydrogenation of α,β-unsaturated carbonyl compounds on silica-supported copper nanoparticles. *Chem. Commun.* **55**, 179-181, doi:10.1039/C8CC08457B (2019).
290 Kumar, A. *et al.* Wide spectral degradation of Norfloxacin by Ag@BiPO4/BiOBr/BiFeO3 nano-assembly: Elucidating the photocatalytic mechanism under different light sources. *J. Hazard. Mater.* **364**, 429-440, doi:https://doi.org/10.1016/j.jhazmat.2018.10.060 (2019).
291 Buhaibeh, R. *et al.* Phosphine-NHC Manganese Hydrogenation Catalyst Exhibiting a Non-Classical Metal-Ligand Cooperative H2 Activation Mode. *Angew. Chem. Int. Ed.* **58**, 6727-6731, doi:https://doi.org/10.1002/anie.201901169 (2019).
292 Liu, B. & Liu, Q. A Pincer Cobalt Complex as Catalyst with Dual Hydrogenation Activities for Hydrodeoxygenation of Ketones with H2†. *Chin. J. Chem* . **41**, 3528-3532, doi:https://doi.org/10.1002/cjoc.202300418 (2023).
293 He, M., Sun, Y. & Han, B. Green carbon science: efficient carbon resource processing, utilization, and recycling towards carbon neutrality. *Angewandte Chemie* **134**, e202112835 (2022).
294 Yang, Y. & Mu, T. Electrochemical oxidation of biomass derived 5-hydroxymethylfurfural (HMF): pathway, mechanism, catalysts and coupling reactions. *Green Chemistry* **23**, 4228-4254 (2021).
295 Xu, C., Paone, E., Rodríguez-Padrón, D., Luque, R. & Mauriello, F. Recent catalytic routes for the preparation and the upgrading of biomass derived furfural and 5-hydroxymethylfurfural. *Chemical Society Reviews* **49**, 4273-4306 (2020).
296 Wang, H. *et al.* Recent advances in catalytic conversion of biomass to 5-hydroxymethylfurfural and 2, 5-dimethylfuran. *Renewable and Sustainable Energy Reviews* **103**, 227-247 (2019).
297 Wang, T., Cao, X. & Jiao, L. Progress in hydrogen production coupled with electrochemical oxidation of small molecules. *Angewandte Chemie* **134**, e202213328 (2022).

298 Luo, H. *et al.* Progress and perspectives in photo-and electrochemical-oxidation of biomass for sustainable chemicals and hydrogen production. *Advanced Energy Materials* **11**, 2101180 (2021).
299 Vo, T. G., Gao, J. & Liu, Y. Recent Development and Future Frontiers of Oxygen Reduction Reaction in Neutral Media and Seawater. *Advanced Functional Materials*, 2314282 (2024).
300 Luo, Y. & Alonso-Vante, N. The effect of support on advanced Pt-based cathodes towards the oxygen reduction reaction. State of the art. *Electrochimica Acta* **179**, 108-118 (2015).
301 Zhang, B. *et al.* Simultaneous photoelectrocatalytic water oxidation and oxygen reduction for solar electricity production in alkaline solution. *ChemSusChem* **12**, 1026-1032 (2019).
302 Jeon, T. H., Kim, H., Kim, H.-i. & Choi, W. Highly durable photoelectrochemical H 2 O 2 production via dual photoanode and cathode processes under solar simulating and external bias-free conditions. *Energy & Environmental Science* **13**, 1730-1742 (2020).
303 Chen, C., Yasugi, M., Yu, L., Teng, Z. & Ohno, T. Visible light-driven H2O2 synthesis by a Cu3BiS3 photocathode via a photoelectrochemical indirect two-electron oxygen reduction reaction. *Applied Catalysis B: Environment and Energy* **307**, 121152 (2022).
304 Bruziquesi, C. G. *et al.* Cobalt as a sacrificial metal to increase the photoelectrochemical stability of CuBi2O4 films for water splitting. *International Journal of Hydrogen Energy* **48**, 3456-3465 (2023).
305 Lee, J. *et al.* Long-term stabilized high-density CuBi 2 O 4/NiO heterostructure thin film photocathode grown by pulsed laser deposition. *Chemical Communications* **55**, 12447-12450 (2019).
306 Meena, B. *et al.* Exploring CuBi2O4 as a promising photocathode material for PEC water splitting. *Energy & Fuels* **37**, 14280-14289 (2023).
307 Li, Z. *et al.* Gd-doped CuBi2O4/CuO heterojunction film photocathodes for photoelectrochemical H2O2 production through oxygen reduction. *Nano Research* **14**, 3439-3445 (2021).
308 Yang, W., Prabhakar, R. R., Tan, J., Tilley, S. D. & Moon, J. Strategies for enhancing the photocurrent, photovoltage, and stability of photoelectrodes for photoelectrochemical water splitting. *Chemical Society Reviews* **48**, 4979-5015 (2019).
309 Shi, H. *et al.* Visible light photoanode material for photoelectrochemical water splitting: a review of bismuth vanadate. *Energy & Fuels* **36**, 11404-11427 (2022).
310 Nair, V., Perkins, C. L., Lin, Q. & Law, M. Textured nanoporous Mo: BiVO 4 photoanodes with high charge transport and charge transfer quantum efficiencies for oxygen evolution. *Energy & Environmental Science* **9**, 1412-1429 (2016).
311 Gao, R. T. *et al.* Towards long-term photostability of nickel hydroxide/BiVO4 photoanodes for oxygen evolution catalysts via in situ catalyst tuning. *Angewandte Chemie* **132**, 6272-6277 (2020).
312 Ghamari Kargar, P., Shafiei, M. & Bagherzade, G. Transformation of 5-hydroxymethylfurfural to 5-hydroxymethyl-2-furan carboxylic acid mediated by silver nanoparticles biosynthesized from Spartium junceum flower extract. *Materials Today Sustainability* **25**, 100622, doi:https://doi.org/10.1016/j.mtsust.2023.100622 (2024).
313 Song, Y. *et al.* Engineering MoOx/MXene Hole Transfer Layers for Unexpected Boosting of Photoelectrochemical Water Oxidation. **61**, e202200946, doi:https://doi.org/10.1002/anie.202200946 (2022).
314 Kohn, W. & Sham, L. J. Self-consistent equations including exchange and correlation effects. *Physical review* **140**, A1133 (1965).
315 Grimme, S., Antony, J., Ehrlich, S. & Krieg, H. A consistent and accurate ab initio

parametrization of density functional dispersion correction (DFT-D) for the 94 elements H-Pu. *The Journal of chemical physics* **132** (2010).

316 Kresse, G. & Joubert, D. From ultrasoft pseudopotentials to the projector augmented-wave method. *Physical review b* **59**, 1758 (1999).

317 Perdew, J. P., Burke, K. & Ernzerhof, M. Generalized gradient approximation made simple. *Physical review letters* **77**, 3865 (1996).

318 Seo, G., Kim, B., Hwang, S. W., Shin, S. S. & Cho, I. S. High-performance bulky crystalline copper bismuthate photocathode for enhanced solar water splitting. *Nano Energy* **80**, 105568, doi:https://doi.org/10.1016/j.nanoen.2020.105568 (2021).

319 Derelli, D. *et al.* Photodegradation of CuBi2O4 Films Evidenced by Fast Formation of Metallic Bi using Operando Surface-sensitive X-ray Scattering**. **62**, e202307948, doi:https://doi.org/10.1002/anie.202307948 (2023).

320 Chu, S. *et al.* Revealing the Origin of Transition-Metal Migration in Layered Sodium-Ion Battery Cathodes: Random Na Extraction and Na-Free Layer Formation. *Angewandte Chemie* **135**, e202216174 (2023).

321 Xi, W. *et al.* Accelerating Ru0/Ru4+ Adjacent Dual Sites Construction by Copper Switch for Efficient Alkaline Hydrogen Evolution. *Advanced Energy Materials* **13**, 2302668, doi:https://doi.org/10.1002/aenm.202302668 (2023).

322 Wen, Y. *et al.* Stabilizing highly active Ru sites by suppressing lattice oxygen participation in acidic water oxidation. *Journal of the American Chemical Society* **143**, 6482-6490 (2021).

323 Yan, Y. *et al.* Ru doped graphitic carbon nitride mediated peroxymonosulfate activation for diclofenac degradation via singlet oxygen. *Chemical Engineering Journal* **430**, 133174, doi:https://doi.org/10.1016/j.cej.2021.133174 (2022).

324 Chen, D. *et al.* Ru-doped 3D flower-like bimetallic phosphide with a climbing effect on overall water splitting. *Appl. Catal., B* **279**, 119396, doi:https://doi.org/10.1016/j.apcatb.2020.119396 (2020).

325 Wang, C. *et al.* Ultralow Ru doping induced interface engineering in MOF derived ruthenium-cobalt oxide hollow nanobox for efficient water oxidation electrocatalysis. *Chem. Eng. J.* **420**, 129805, doi:https://doi.org/10.1016/j.cej.2021.129805 (2021).

326 Qin, X. *et al.* The Role of Ru in Improving the Activity of Pd toward Hydrogen Evolution and Oxidation Reactions in Alkaline Solutions. *ACS Catalysis* **9**, 9614-9621, doi:10.1021/acscatal.9b01744 (2019).

327 Huang, H. *et al.* Activation of inert copper for significantly enhanced hydrogen evolution behaviors by trace ruthenium doping. *Nano Energy* **92**, 106763, doi:https://doi.org/10.1016/j.nanoen.2021.106763 (2022).

328 Yu, Z. *et al.* Defective Ru-doped α-MnO2 nanorods enabling efficient hydrazine oxidation for energy-saving hydrogen production via proton exchange membranes at near-neutral pH. *Chemical Engineering Journal* **470**, 144050, doi:https://doi.org/10.1016/j.cej.2023.144050 (2023).

329 Wang, F., Chemseddine, A., Abdi, F. F., van de Krol, R. & Berglund, S. P. Spray pyrolysis of CuBi2O4 photocathodes: improved solution chemistry for highly homogeneous thin films. *Journal of Materials Chemistry A* **5**, 12838-12847, doi:10.1039/C7TA03009F (2017).

330 Wang, C. *et al.* Conformally Coupling CoAl-Layered Double Hydroxides on Fluorine-Doped Hematite: Surface and Bulk Co-Modification for Enhanced Photoelectrochemical Water Oxidation. *ACS Appl. Mater. Interfaces* **11**, 29799-29806, doi:10.1021/acsami.9b07417 (2019).

331 Leduc, J. *et al.* Electronically coupled uranium and iron oxide heterojunctions as efficient water oxidation catalysts. **29**, 1905005 (2019).

332 Wang, Z. *et al.* Identifying copper vacancies and their role in the CuO based photocathode for water splitting. *Angew. Chem.* **131**, 17768-17773 (2019).
333 Zhang, B. *et al.* Unveiling the Activity and Stability Origin of BiVO4 Photoanodes with FeNi Oxyhydroxides for Oxygen Evolution. **59**, 18990-18995, doi:https://doi.org/10.1002/anie.202008198 (2020).
334 Pan, J.-B. *et al.* Activity and Stability Boosting of an Oxygen-Vacancy-Rich BiVO4 Photoanode by NiFe-MOFs Thin Layer for Water Oxidation. **60**, 1433-1440, doi:https://doi.org/10.1002/anie.202012550 (2021).
335 Zhou, F., Min, Y., Fan, J. & Xu, Q. J. C. E. J. Reduced graphene oxide-grafted cylindrical like W doped BiVO4 hybrids with enhanced performances for photocatalytic applications. **266**, 48-55 (2015).
336 Pei, H. *et al.* A novel BiVO4/P3HT photoanode for highly efficient water oxidation and its hole energy offset effect with CuPc derivative. *Appl. Catal., B* **318**, 121865, doi:https://doi.org/10.1016/j.apcatb.2022.121865 (2022).
337 Tsilomelekis, G. *et al.* Molecular structure, morphology and growth mechanisms and rates of 5-hydroxymethyl furfural (HMF) derived humins. **18**, 1983-1993 (2016).
338 Kumar, M., Meena, B., Yu, A., Sun, C. & Challapalli, S. Advancements in catalysts for glycerol oxidation via photo-/electrocatalysis: a comprehensive review of recent developments. *Green Chemistry* **25**, 8411-8443 (2023).
339 Kongprawes, G. *et al.* Non-catalytic glycerol dehydrogenation to dihydroxyacetone using needle-in-tube dielectric barrier discharge plasma. *Scientific Reports* **14**, 31295 (2024).
340 Dodekatos, G., Schünemann, S. & Tüysüz, H. Recent advances in thermo-, photo-, and electrocatalytic glycerol oxidation. *ACS Catalysis* **8**, 6301-6333 (2018).
341 Moreira, R. *et al.* Oxidative steam reforming of glycerol. A review. *Renewable and Sustainable Energy Reviews* **148**, 111299 (2021).
342 Yu, J. *et al.* First PEM photoelectrolyser for the simultaneous selective glycerol valorization into value-added chemicals and hydrogen generation. *Applied Catalysis B: Environmental* **327**, 122465 (2023).
343 Zhang, W. *et al.* Visible-light responsive TiO2-based materials for efficient solar energy utilization. *Advanced Energy Materials* **11**, 2003303 (2021).
344 Ma, G. *et al.* Efficient strategies for designing photoanode toward selective photoelectrochemical glycerol upgrading: a review. *Journal of Materials Chemistry A* (2024).
345 Lin, J.-A., Roh, I. & Yang, P. Photochemical diodes for simultaneous bias-free glycerol valorization and hydrogen evolution. *Journal of the American Chemical Society* **145**, 12987-12991 (2023).
346 Sun, X. *et al.* Pairing Oxygen Reduction and Water Oxidation for Dual-Pathway H2O2 Production. *Angewandte Chemie International Edition* **63**, e202414417 (2024).
347 Xue, Y., Wang, Y., Pan, Z. & Sayama, K. Electrochemical and photoelectrochemical water oxidation for hydrogen peroxide production. *Angewandte Chemie International Edition* **60**, 10469-10480 (2021).
348 Lu, Z. *et al.* High-efficiency oxygen reduction to hydrogen peroxide catalysed by oxidized carbon materials. *Nature Catalysis* **1**, 156-162 (2018).
349 Pecoraro, C. M., Wu, S., Santamaria, M. & Schmuki, P. Bandgap Engineering of TiO2 for Enhanced Selectivity in Photoelectrochemical Glycerol Oxidation. *Adv. Mater. Interfaces* **n/a**, 2400583, doi:https://doi.org/10.1002/admi.202400583 (2024).
350 Wu, G., Liu, Y., He, Y., Feng, J. & Li, D. Reaction pathway investigation using in situ Fourier transform infrared technique over Pt/CuO and Pt/TiO2 for selective glycerol oxidation. *Appl. Catal., B* **291**, 120061,

doi:https://doi.org/10.1016/j.apcatb.2021.120061 (2021).
351 Zhou, M. *et al.* Constructing of n-Type Semiconductor Heterostructures for Efficient Hydrazine-Assisted Hydrogen Production. *Advanced Functional Materials*, 2415058 (2024).
352 Zhang, B. *et al.* Molecular and Heterojunction Device Engineering of Solution-Processed Conjugated Reticular Oligomers: Enhanced Photoelectrochemical Hydrogen Evolution through High-Effective Exciton Separation. *Advanced Science* **11**, 2308535 (2024).
353 Xiao, Y. *et al.* Selective Photoelectrochemical Oxidation of Glycerol to Glyceric Acid on (002) Facets Exposed WO3 Nanosheets. *Angewandte Chemie* **136**, e202319685 (2024).
354 Wu, Y.-H., Kuznetsov, D. A., Pflug, N. C., Fedorov, A. & Müller, C. R. Solar-driven valorisation of glycerol on BiVO4 photoanodes: effect of co-catalyst and reaction media on reaction selectivity. *J. Mater. Chem. A* **9**, 6252-6260, doi:10.1039/D0TA10480A (2021).
355 Wu, Y.-H., Kuznetsov, D. A., Pflug, N. C., Fedorov, A. & Müller, C. R. Solar-driven valorisation of glycerol on BiVO 4 photoanodes: effect of co-catalyst and reaction media on reaction selectivity. *Journal of Materials Chemistry A* **9**, 6252-6260 (2021).
356 Çetinkaya, S., Khamidov, G., Özcan, L., Palmisano, L. & Yurdakal, S. Selective photoelectrocatalytic oxidation of glycerol by nanotube, nanobelt and nanosponge structured TiO2 on Ti plates. *J. Environ. Chem. Eng.* **10**, 107210, doi:https://doi.org/10.1016/j.jece.2022.107210 (2022).
357 Huang, L.-W., Vo, T.-G. & Chiang, C.-Y. Converting glycerol aqueous solution to hydrogen energy and dihydroxyacetone by the BiVO4 photoelectrochemical cell. *Electrochimica Acta* **322**, 134725 (2019).